Improvement on the H→$\gamma\gamma$ mass measurement by constraining the photon energy scale uncertainty and search for Higgs boson pair production in the bb$\gamma\gamma$ final state with the ATLAS experiment using the full Run 2 at $\sqrt{s}$=13 TeV pp collision of LHC

Linghua Guo

To cite this version:

Linghua Guo. Improvement on the H→$\gamma\gamma$ mass measurement by constraining the photon energy scale uncertainty and search for Higgs boson pair production in the bb$\gamma\gamma$ final state with the ATLAS experiment using the full Run 2 at $\sqrt{s}$=13 TeV pp collision of LHC. High Energy Physics - Experiment [hep-ex]. Université Paris-Saclay, 2022. English. NNT : 2022UPASP096 . tel-03827309

HAL Id: tel-03827309
https://theses.hal.science/tel-03827309
Submitted on 24 Oct 2022

Improvement on the $H \to \gamma\gamma$ mass measurement by constraining the photon energy scale uncertainty and search for Higgs boson pair production in the $b\bar{b}\gamma\gamma$ final state with the ATLAS experiment using the full Run 2 at $\sqrt{s} = 13$ TeV pp collision of LHC

Amélioration de la mesure de la masse du boson de Higgs dans sa désintégration en deux photons en contraignant l'incertitude de l'échelle d'énergie des photons, et recherche de la production de paires de bosons de Higgs dans la désintégration en deux photons et deux quarks b avec le détecteur ATLAS et les données du Run 2 à $\sqrt{s} = 13$ TeV

Thèse de doctorat de l'université Paris-Saclay

École doctorale n°576 Particules, hadrons, énergie et noyau : instrumentation, imagerie, cosmos et simulation (PHENIICS)
Spécialité de doctorat : Physique des particules
Graduate School : Physique
Référent : Faculté des sciences d'Orsay

Thèse préparée dans l'unité de recherche **IJCLab** (Université Paris-Saclay, CNRS), sous la direction de **Marc ESCALIER**, Chargé de recherche

Thèse soutenue à Paris-Saclay, le 28 Septembre 2022, par

Linghua GUO

Composition du jury

Marie-Hélène SCHUNE Directrice de recherche, Université Paris-Saclay (IJCLab)	Présidente
Marie-Hélène GENEST Directrice de recherche, LPSC	Rapportrice & Examinatrice
Marco PIERI Directeur de recherche, Université de Californie San Diego	Rapporteur & Examinateur
Manuella VINCTER Professeure, Université de Carleton	Examinatrice
Paris SPHICAS Directeur de recherche, CERN et Professeur Université d'Athènes	Examinateur
Maarten BOONEKAMP Directeur de recherche, CEA Saclay	Examinateur
Guillaume UNAL Directeur de recherche, CERN	Examinateur
Marc ESCALIER Chargé de recherche, Université Paris-Saclay (IJCLab)	Directeur de thèse

THESE DE DOCTORAT

NNT : 2022UPASP096

universite PARIS-SACLAY

ÉCOLE DOCTORALE
Particules, hadrons, énergie et noyau :
instrumentation, imagerie, cosmos
et simulation (PHENIICS)

Titre: Amélioration de la mesure de la masse du boson de Higgs dans sa désintégration en deux photons en contraignant l'incertitude de l'échelle d'énergie des photons, et recherche de la production de paires de bosons de Higgs dans la désintégration en deux photons et deux quarks b avec le détecteur ATLAS et les données du Run 2 à $\sqrt{s} = 13$ TeV.

Mots clés: ATLAS, Higgs, Di-Higgs, calorimètre, étalonnage

Résumé: Après la découverte du boson de Higgs en 2012 par ATLAS et CMS au LHC, les mesures de précision et le couplage du Higgs sont importants pour la validation du modèle standard (SM), mais aussi pour la recherche de nouvelle physique au-delà du modèle standard (BSM), car toute déviation à la prédiction du SM peut indiquer la présence de nouvelle physique.

Cette thèse présente un travail sur l'étalonnage du calorimètre électromagnétique d'ATLAS. En utilisant la masse du boson Z connue, avec une précision de 2×10^{-5} autour de 91 GeV, l'énergie du calorimètre est calibrée avec un facteur d'échelle d'énergie et un terme constant de résolution. Ce travail contribue à la recommandation finale du Run 2 d'ATLAS, importante pour la mesure de la masse du Higgs dans sa désintégration en deux photons. La linéarité du calorimètre est mesurée, en tant que facteur d'échelle dépendant de l'énergie, qui est ensuite utilisée pour contraindre la systématique de l'échelle d'énergie. Sa performance est testée sur l'analyse de masse du Higgs avec le canal en deux photons. Les données de 139 fb^{-1} du Run 2 devraient mesurer la masse du boson de Higgs avec une incertitude statistique d'environ 125 MeV et une incertitude systématique expérimentale d'environ 260 MeV. Bénéficiant de cette contrainte de linéarité, l'incertitude systématique expérimentale est réduite d'un facteur de l'ordre de 1.5.

La recherche de la double production de Higgs permet de sonder le potentiel de Higgs et de l'auto-couplage du Higgs. Cette thèse exploite cette double production via la désintégration de HH en bbyy avec les données du Run 2 d'ATLAS. La limite observée (attendue) de la section efficace de production de di-Higgs est de 4,2 (5,7) fois la prédiction SM à un niveau de confiance de 95%. Le modificateur d'auto-couplage de Higgs κ_λ est contraint entre -1,5 et 6,7, tandis que la contrainte attendue est de $-2,4 < \kappa_\lambda < 7,7$.

ÉCOLE DOCTORALE
Particules, hadrons, énergie et noyau :
instrumentation, imagerie, cosmos
et simulation (PHENIICS)

Title: Improvement on the $H \to \gamma\gamma$ mass measurement by constraining the photon energy scale uncertainty and search for Higgs boson pair production in the $b\bar{b}\gamma\gamma$ final state with the ATLAS experiment using the full Run 2 at $\sqrt{s} = 13$ TeV pp collision of LHC.

Keywords: ATLAS, Higgs, Di-Higgs, calorimeter, calibration

Abstract: After the Higgs discovery in 2012 by ATLAS and CMS at LHC, precision measurements and Higgs couplings are important for validation of the Standard model (SM), but also for search of new physics Beyond the Standard Model (BSM), as any deviation from the SM prediction can indicate the presence of new physics.

This thesis presents a work on the calibration of the ATLAS electromagnetic calorimeter. Using the known lineshape of the Z boson peaked around 91 GeV with a precision of 2×10^{-5}, the energy response of the calorimeter is calibrated with an energy scale factor and resolution constant term. This work contributes to final calibration recommendation of ATLAS Run 2, which is important for the Higgs mass measurement with $H \to \gamma\gamma$ decay mode. The linearity of the calorimeter is measured, as energy-dependent scale factor, which is afterwards used to constrain the energy scale systematics. The performance of such constraint is tested on the $H \to \gamma\gamma$ mass analysis. The 139 fb^{-1} Run 2 data is expected to measure the Higgs boson mass with a statistical uncertainty around 125 MeV and an experimental systematic uncertainty around 260 MeV. Benefiting from the constraint with linearity, the experimental systematic uncertainty is reduced by around 1.5.

The search for the Di-Higgs production probes the Higgs potential and the Higgs self-coupling. This thesis exploits the Di-Higgs production via the $HH \to b\bar{b}\gamma\gamma$ decay with the ATLAS Run 2 data. The observed (expected) limit of the Di-Higgs production cross section is set to 4.2 (5.7) times the SM prediction at 95% confidence level. The Higgs self-coupling modifier κ_λ is constrained to be between -1.5 and 6.7, while the expected constraint is $-2.4 < \kappa_\lambda < 7.7$.

Contents

Acknowledgements

When I started my PhD in 2019, I was so excited to have this opportunity to work on particle physics within the ATLAS collaboration and CERN. This has been a really interesting and inspiring research experience. Although the world is suffering hardships in the past two years, with kind help from many people I am able to finish the PhD without delay. I have been very lucky to meet and work with so many talent scientists and warmhearted colleagues.
First of all, I would like to express my sincere thinks to my supervisor Marc Escalier and the "hidden" supervisor Louis Fayard.

Thank you Marc for your advice, patience and cares not only in the research activities but also on plenty of other stuffs. At the very beginning, I was slowed down by many technical problems, thank you for tolerating my low speed of understanding. I cannot imagine a more patient person to work during the PhD. Thank you for your expertise on the $H \to \gamma\gamma$ and the $HH \to b\bar{b}\gamma\gamma$ analyses, and for the very fruitful and detailed discussions.
Thank you Louis for your extensive knowledge and expertise on various topics, in particular on the electromagnetic calorimeter and the relevant analyses to photons. Thank you for making me to be a more open-minded person, you have known me the importance of harmonization into the group and the inspired me the way to work with different kinds of physicists.

Thank you David Delgove for all your help in the beginning and even after your departure. Thank you for your talent and inspirations. Thank you for attending my master defense.
Thank you Maarten Boonekamp and Ruggero Turra for the brilliant idea of the $Z \to ee$ linearity global fit model. This has been one of the most interesting studies I made during my PhD. Thank you Maarten for your unlimited ideas and all the help and discussions during the three years. Thank you Maarten for your kindness, I remember that you had came to our laboratory several times for in-person meetings.
Thank you Guillaume Unal for your intelligence and inspirations for analyzing and solving the issues in many topics. Thank you for all the help and discussions during the three years. It has been an really interesting experience to work with you.
Thank you Jean-Baptiste De Vivie for the help and support. Thank you for your suggestions about the egamma and HGam analyses.

Thank you to the egamma calibration group and the egamma calibration conveners: Narei Lorenzo Martinez, Yanping Huang, Stefano Manzoni, Ahmed Tarek and all the others.
Thank you to the $HH \to b\bar{b}\gamma\gamma$ group and group conveners: Elisabeth Petit, Valentina Cairo, Louis D'Eramo and all the others.
Thank you to the $H\gamma\gamma$ group and group conveners: Hongtao Yang, Ana Rosario Cueto Gomez, Stefano Manzoni, Davide Mungo and all the others.
Thank you to the IJCLab group, in the past years, I had received help from many experts in the laboratory.
Thanks to the PhD students: Aleksei Lukianchuk, Xiaowen Su, and others, thanks for the relaxing coffee time we spent together.
Thank you to the jury members, thank you to accept and correct my thesis and thanks for the fruitful discussion before defense.

Thank you to my classmates and best friends, Yonghui Xu, Hao Wei, Rui Yang who came to France together with me and have been accompanied with me during the past seven years.
Thank you to my friends Yali Wang and Yining Jiang. We have known each other just before around 9 months, but I would like to thank you for all the comforts and encourages.
Thank you to my girlfriend Ying An for having been accompanying the years. Thank you for tolerating my temple. Thank you for your suggestions on my thesis and defense. Thank you for coming to France to stay with me during the most difficult period.
Finally I would like to thank to my parents who always respect and support me even sometimes they suggested differently to what I decided.

Résumé étendu en français

Le modèle standard est une théorie décrivant les particules élémentaires et leurs interactions. Il comprend trois générations de quarks et de leptons, les bosons de jauge (gluon, bosons W et Z) et le boson de Higgs. Il comprend différentes théories, telles que la chromodynamique quantique et l'interaction électrofaible. Le mécanisme dit de Higgs prédit l'existence du boson de Higgs qui génère la masse des particules par une brisure spontanée de symétrie.

La découverte du boson de Brout-Englert-Higgs (boson de Higgs) d'une masse d'environ 125 GeV par les expériences ATLAS [1] et CMS [2] au Large Hadron Collider (LHC) constitue la pièce manquante de la génération de masse dans le modèle standard et inspire de nombreuses analyses pertinentes de physique.

Grâce aux performances impressionnantes des détecteurs ATLAS et CMS, la masse du boson de Higgs a été mesurée avec une précision d'environ 0,2%, en combinant les canaux $H \to \gamma\gamma$ et $H \to ZZ^* \to 4l$ en utilisant les données de Run 1 de LHC. L'une des étapes suivantes consiste à améliorer la précision des mesures du boson de Higgs, comme la masse, le couplage, etc. Ces mesures fournissent des informations pour tester le modèle standard et les modèles de physique au-delà du modèle standard.

Parmi les diverses propriétés du boson de Higgs, la masse est l'une des plus importantes à mesurer. La masse du boson de Higgs n'est pas prédite par le modèle standard, sa valeur est requise pour le calcul précis de la section efficace de production de Higgs et sa désintégration. Outre la masse, le boson de Higgs est une particule se couplant à elle-même. L'auto-couplage du Higgs est prédit par le potentiel de Higgs à travers le mécanisme de Brout-Englert-Higgs, qui joue un rôle important dans la stabilité de l'univers. Cette thèse contribue à un travail d'amélioration de la précision de la masse du boson de Higgs et à une recherche de double production du boson de Higgs permettant d'explorer son auto-couplage.

Le document est organisé comme suit :

Le chapitre 1 présente brièvement le modèle standard et le mécanisme de Brout-Englert-Higgs, avec un état des lieux des limites du modèle standard. La production, la désintégration et les mesures de la masse du boson de Higgs au LHC sont résumées.

Les méthodes statistiques sont présentées au chapitre 2, où les bases de la probabilité, de l'estimation des paramètres, des tests d'hypothèses et de la combinaison de données sont introduites. En particulier, la méthode asymptotique pour le test basé sur la vraisemblance est introduite, qui est une approche largement utilisée et puissante pour déterminer la fonction de densité de probabilité de la fonction statistique de test dans ATLAS.

Le chapitre 3 décrit le dispositif expérimental, notamment le LHC et le détecteur ATLAS, avec leur évolution pour le LHC à haute luminosité. La conception du détecteur ATLAS est introduite, avec la reconstruction, l'identification des électrons, des photons et des jets. Ce chapitre donne une description dédiée du calorimètre électromagnétique d'ATLAS, notamment la gerbe électromagnétique, l'électronique et la reconstruction des électrons et des photons.

Le cœur des analyses correspond aux chapitres 4, 5, 6. Le chapitre 4 décrit une recherche de la double production de Higgs dans le canal de désintégration $b\bar{b}\gamma\gamma$, où la stratégie de sélection et les résultats statistiques sont présentés. La combinaison avec d'autres canaux et les perspectives du LHC à haute luminosité sont données. Une étude de performance sur l'étalonnage du calorimètre électromagnétique d'ATLAS est décrite au chapitre 5. La dernière partie (chapitre 6) correspond à une analyse de la mesure de la masse du Higgs dans le canal diphotons, où l'incertitude systématique expérimentale dominante pour l'énergie du photon est résumée, et un modèle d'ajustement global lié au travail d'étalonnage du chapitre 5 est présenté.

Double production du boson de Higgs

Le mécanisme de Higgs prédit le boson de Higgs et aussi son autocouplage qui était mal connu avant les résultats de LHC. Explorer l'autocouplage du boson de Higgs permet d'étudier la forme réelle du potentiel de Higgs ainsi que la stabilité de l'univers. L'autocouplage du boson de Higgs est accessible grâce à la double production du boson de Higgs. Dans cette thèse, une recherche de cette production est effectuée où la section efficace de la production et le modificateur d'autocouplage de Higgs κ_λ sont étudiés. L'analyse explore l'état final $b\bar{b}\gamma\gamma$ où un boson de Higgs se désintègre en une paire de quarks b et l'autre se désintègre en deux photons. Par conséquent, les événements de collision avec deux photons de bonne qualité et deux jets de saveur b sont sélectionnés, bénéficiant des algorithmes efficaces de reconstruction, d'identification et d'étiquetage de saveur dans ATLAS.

Les événements sont également tenus de passer une sélection supplémentaire basée sur l'analyse multivariée (MVA). L'analyse utilise des arbres de décision boostés (BDT) pour mieux séparer le signal et le bruit de fond. Pour le signal, puisque la masse invariante du système des deux bosons de Higgs (m_{hh}) reconstruite avec les deux jets b et deux photons est très sensible au modificateur d'autocouplage de Higgs κ_λ, un BDT est utilisé dans la région de masse m_{hh} élevée pour cibler le signal avec de petites κ_λ, un autre à faible masse pour les grands κ_λ. Un tel algorithme d'optimisation améliore la sensibilité pour différents κ_λ. Finalement avec la masse m_{hh} et les scores de BDT, quatre catégories sont définies. Après toutes les sélections, le fond dominant est le processus avec deux photons et jets, le fond dit continu. Il y a aussi une contribution sous-dominante de la production d'un seule boson de Higgs.

L'ajustement de maximum de vraisemblance est effectué sur la variable de masse invariante des deux photons $m_{\gamma\gamma}$, où la section efficace de production de signal est ajustée, avec κ_λ fixé à la prédiction du modèle standard. Les données actuelles n'indiquent pas l'existence de signal. La limite supérieure observée (attendue) de la section efficace du signal est 4,2 (5,7) fois la prédiction du modèle standard à un niveau de confiance de 95%, en supposant que κ_λ est égal à 1. L'autocouplage de Higgs κ_λ est contraint entre -1,5 et 6,7 avec les données observées, et entre $-2,4 < \kappa_\lambda < 7,7$ pour les limites attendues.

Ce canal est combiné avec d'autres analyses portant sur différents états finaux, tels que $b\bar{b}b\bar{b}$ et $b\bar{b}\tau\bar{\tau}$. La limite supérieure combinée observée (attendue) de la section efficace du signal est 2,4 (2,9) fois la prédiction du modèle standard. L'intervalle limite combiné observé (attendu) est de $-0,6 < \kappa_\lambda < 6,6$ $(-2,1 < \kappa_\lambda < 7,8)$.

Outre la recherche directe de la double production de bosons de Higgs, l'autocouplage de Higgs peut apparaître dans la production d'un seul boson de Higgs via des boucles d'autocouplage de Higgs. Par conséquent, les productions de Higgs double et seule sont combinées pour améliorer la contrainte sur κ_λ.

De plus, l'analyse actuelle basée sur les données du Run 2 est extrapolée au futur LHC à haute luminosité où il est possible de trouver ce type du signal de double Higgs. Une significativité de 3,2 du signal de la double production du boson de Higgs dans le cas du modèle standard est attendue après combinaison des canaux de $b\bar{b}\gamma\gamma$ et $b\bar{b}\tau\bar{\tau}$ dans ATLAS. Le modificateur d'autocouplage de Higgs κ_λ devrait être mesuré avec une précision de 50%.

Étalonnage du calorimètre électromagnétique

Le calorimètre électromagnétique (ECAL) dans ATLAS est un calorimètre à échantillonnage utilisant du plomb comme absorbeur de la gerbe électromagnétique, et de l'argon liquide comme matière active pour le signal électronique. Il a une large couverture spatiale (2π dans l'angle azimutal ϕ, et jusqu'à 4,9 pour la pseudorapidité η). De plus, il est composé de plusieurs couches ce qui permet d'accéder aux informations longitudinales de la gerbe électromagnétique. L'ECAL est utilisé pour mesurer l'énergie des électrons et des photons. Un étalonnage précis de sa réponse énergétique est donc crucial pour les analyses utilisant des électrons ou des photons, comme la mesure de la masse du boson de Higgs dans l'état final à deux photons.

L'étalonnage est précédé de plusieurs étapes. La première étape est une régression multivariée, qui reconstruit l'énergie des particules à partir des informations enregistrées dans ECAL, telles que l'énergie mesurée dans chaque couche et les positions spatiales. Afin de maintenir la même réponse énergétique dans chaque couche du calorimètre, une intercalibration est effectuée. Au final, la réponse énergétique est enfin calibrée à l'aide du pic de résonance de masse bien connu du boson Z. En outre, les réponses des différents gains électroniques sont calibrées à l'aide de Runs spéciaux dédiés. Des corrections supplémentaires sont appliquées afin de couvrir l'étalonnage électronique résiduel et la non-uniformité de la réponse énergétique dans l'angle azimutal ϕ.

L'étalonnage basé sur la masse du boson Z est appelé étalonnage in-situ, en utilisant le pic de masse Z autour de 91 GeV comme référence. L'étalonnage se compose des facteurs d'échelle utilisés pour corriger la différence d'échelle d'énergie entre les données et la simulation, et du terme constant qui absorbe la différence de résolution d'énergie à l'aide d'un étalement gaussien. L'étalonnage in-situ se fait en fonction de η, pour chaque année des données collectées . Les facteurs d'échelle sont différents dans la région endcap d'une année à l'autre, ce qui est dû à l'évolution de la température de l'argon liquide et de la haute tension. Il existe des différences à termes constants dues à la mauvaise modélisation du bruit d'empilement dans le calorimètre.

La réponse énergétique des électrons d'impulsion transverse (E_T) proche de 40 GeV (moyenne de E_T des électrons issus de la désintégration du boson Z) est bien calibrée. Cependant, une erreur d'étalonnage est possible à une plage d'impulsion transverse différent de 40 GeV. Afin d'estimer un tel défaut d'étalonnage possible, le facteur d'échelle d'énergie est mesuré en fonction de E_T, appelé linéarité. Cette linéarité peut être due aux effets systématiques réels de l'énergie provenant du mauvais calibrage résiduel et de la modélisation des erreurs dans la simulation. Par conséquent, il peut être considéré comme une mesure des effets systématiques et utilisé comme données d'entrée d'un modèle d'ajustement global, qui donne l'estimation des systématiques et contraint les incertitudes.

Les contraintes obtenues sur les incertitudes systématiques peuvent être appliquées sur l'analyse de la mesure de la masse du boson de Higgs dans l'état final à deux photons, ce qui améliore la précision de la masse.

Masse du boson de Higgs mesurée dans le canal à deux photons

Dans le Run 1, avec les données 25 fb^{-1}, la masse de Higgs a été mesurée à $125,09 \pm 0,24$ GeV [3] avec la combinaison d'ATLAS et de CMS dans les canaux de two photons et de quatre leptons, où l'erreur statistique est 0,21 GeV, l'erreur systématique est 0,11 GeV.

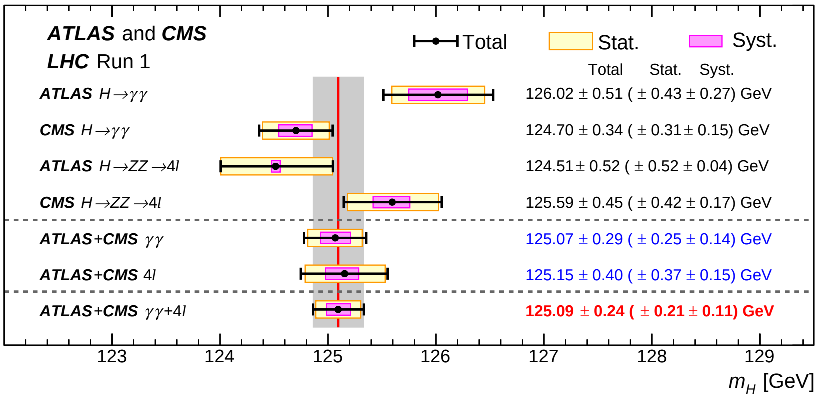

Figure 1: Résumé des mesures de masse du boson de Higgs à partir des analyses individuelles d'ATLAS et de CMS et de l'analyse combinée utilisant les données de 25 fb^{-1} du Run 1 [3].

Au début de Run 2, la masse du boson de Higgs publiée précédemment par ATLAS dans le canal à deux photons a été mesurée à $124,93 \pm 0,40$ GeV en utilisant les données de 36 fb^{-1}, où l'erreur statistique est 0,21 GeV, l'erreur systématique est 0,34 GeV. L'étude actuelle vise à améliorer la précision de la mesure en utilisant les données complètes de Run 2, ainsi que les contraintes sur les incertitudes systématiques provenant des mesures linéarité.

L'analyse cible le signal du boson de Higgs à partir de différents modes de production, tels que la fusion gluon gluon, la fusion du boson vecteur, la production associée avec deux quarks top, etc. Les événements sont d'abord filtrés par un ensemble de sélection de photons sur la qualité d'identification, d'isolement, d'impulsion transverse, etc. Ensuite, les événements sont divisés en quatorze catégories, afin de minimiser l'incertitude de masse mesurée. Un ajustement du maximum de vraisemblance est effectué simultanément avec les quatorze catégories, en utilisant la masse invariante du diphoton comme variable discriminante. Les formes de masse des signaux avec différentes masses de boson de Higgs sont modélisées par une fonction de Cristal-Ball, où le paramètre du pic μ_{CB} est déterminé en fonction de la masse du boson de Higgs.

L'analyse actuelle en cours pour l'ensemble du Run 2 montre une incertitude attendue de la masse du boson de Higgs de 209 MeV, qui comprend une incertitude statistique d'environ 124 MeV et une composante systématique d'environ 168 MeV. Bénéficiant d'une luminosité plus élevée et d'un calibrage amélioré par rapport à l'analyse avec les données de 36 fb^{-1} de Run 2, la précision de la masse est améliorée d'un facteur autour de 2. L'incertitude systématique sur la masse du boson de Higgs est dominée par les incertitudes sur l'échelle de l'énergie des photons, qui proviennent principalement de l'étalonnage du calorimètre électromagnétique, par exemple, l'incertitude due à la non-linéarité de la réponse énergétique du calorimètre, les fuites latérales de gerbe pour les photons, l'étalonnage des couches et les effets de matière.

Le modèle d'ajustement global donne une prédiction de l'échelle d'énergie résiduelle des photons dépendant de l'impulsion transverse et de la incertitude réduite correspondante à l'énergie des photons. La sortie d'ajustement global peut être directement appliquée à la vraisemblance de l'analyse de masse actuelle du boson de Higgs. Après l'avoir appliqué sur les photons, la composante systématique de l'incertitude de masse attendue est réduite de 168 MeV à 102 MeV, ce qui donne une amélioration d'un facteur de l'ordre de 1,7, la valeur centrale de la masse est décalée d'environ 130 MeV, ce qui est encore comparable à l'incertitude de masse.

L'analyse est encore préliminaire et doit encore être approuvée. Le modèle d'ajustement global va être vérifié avec les événements $J\psi \rightarrow ee$, où l'échelle d'énergie électronique est mesurée à faible impulsion transverse autour de 10 GeV. Les résultats seront extrapolés afin de vérifier la cohérence avec le facteur d'échelle mesuré avec $J\psi \rightarrow ee$. Une validation similaire sera également effectuée à l'aide d'événements $Z \rightarrow ll\gamma$.

Contribution de l'auteur

Le groupe ATLAS offre un merveilleux environnement enrichi d'une collaboration fructueuse dans les différents groupes d'analyse. Les analyseurs travaillent sur des sujets similaires ou différents et s'impliquent dans l'étude des autres par de communications régulières. La contribution personnelle de l'auteur est résumée ci-dessous :

Concernant l'analyse de production de double Higgs dans la désintégration $b\bar{b}\gamma\gamma$, l'auteur a travaillé sur l'interprétation statistique des résultats, qui inclut la construction de la fonction de vraisemblance préservée dans un workspace. Il a une contribution notamment à la définition de la limite pour la section efficace de di-Higgs et l'auto-couplage de Higgs, qui est dérivée à l'aide de deux méthodes différentes. L'une d'elles est une approche d'approximation, c'est-à-dire la formule dite asymptotique pour le test de maximum de vraisemblance, qui est une méthode puissante et validée dans de nombreux cas. L'autre est basée sur des pseudo-expériences (toys), qui sont censées donner des estimations plus précises des limites de cette analyse en raison du faible nombre d'événements observés.

L'auteur est l'un des principaux contributeurs pour l'étalonnage en énergie du calorimètre électromagnétique d'ATLAS. Le travail porte principalement sur l'étalonnage et la mesure in-situ du facteur d'échelle dépendant de l'énergie (linéarité). Il a étudié un modèle d'ajustement global avec les idées d'experts sur le calorimètre électromagnétique d'ATLAS. Ce modèle d'ajustement global aide à limiter l'incertitude de l'échelle d'énergie pour les électrons et les photons.

Pour l'analyse de la masse des bosons de Higgs dans le canal diphotons, l'auteur a contribué à l'application du modèle d'ajustement global afin d'améliorer encore la précision de la mesure de la masse des bosons de Higgs. Le résultat du modèle d'ajustement global est implémenté dans la vraisemblance de l'analyse de masse. La performance est estimée à l'aide de données Asimov attendues.

Introduction

The exciting discovery of the Brout-Englert-Higgs boson (Higgs boson) with a mass of around 125 GeV by the ATLAS [1] and CMS [2] experiments at the Large Hadron Collider (LHC), makes up the missing piece of mass generation in the Standard Model, and inspires enormous relevant physics analyses.

Thanks to the outstanding performance of the ATLAS and CMS detectors, the Higgs boson mass has been measured in the combination with a precision around 0.2% in the $H \to \gamma\gamma$ and $H \to ZZ^* \to 4l$ channels using the Run 1 data. One of the next steps is to improve the further precision on Higgs boson measurements, sush as mass, width, coupling, etc. These measurements provide useful information for testing the Standard Model and models of physics beyond the Standard Model.

Among the various Higgs boson properties, the mass is one of the most important to be measured. The Higgs boson mass is not predicted by the Standard Model, its value is required for the precise calculation of the Higgs production cross section and its decay. Apart from the mass, Higgs boson is a particular self-coupling particle. The Higgs self-coupling is predicted by the Higgs potential through the Brout-Englert-Higgs mechanism, which plays an important role in the stability of the universe. This thesis contributes to a work for improving the Higgs boson mass precision and a search of double Higgs boson production which can explore the Higgs boson self-coupling.

The document is organized as follows:

Chapter 1 gives a brief introduction of the Standard Model and the Brout-Englert-Higgs mechanism, with a debriefing on the limitations of the Standard Model. The Higgs boson production, decay and mass measurements at LHC are summarized. The basic statistical methods are presented in Chapter 2.

Chapter 3 describes the experimental setup, including the principle of the LHC and the ATLAS detector, with their upgrade for the high-luminosity LHC. The design of the ATLAS detector is introduced, with the reconstruction, identification of electrons, photons and jets. This chapter gives a dedicated description of the ATLAS electromagnetic calorimeter, including the electromagnetic shower, electronics and reconstruction of electrons and photons.

The core of analyses corresponds to Chapters 4, 5, 6. Chapter 4 describes a search for the double Higgs production in the $b\bar{b}\gamma\gamma$ decay channel, where the selection strategy and the statistical results are presented. The combination with other channels and the prospects for the high luminosity LHC are given. A performance study about the ATLAS electromagnetic calorimeter calibration is described in Chapter 5. The last part (Chapter 6) corresponds to an analysis of the Higgs mass measurement in the diphoton channel, where the dominant experimental systematic uncertainty for the photon energy is summarized, and a global fit model connected to the work of calibration in Chapter 5 is presented.

Contribution of Author

The ATLAS working group provides a wonderful environment enhanced with fruitful collaboration in the various patterns of analysis. Analysers are working on similar or different topics, and get involved to others' study through regular communications. Personal contribution of the author is summarized below:

For the $b\bar{b}\gamma\gamma$ double Higgs production analysis, the author has worked on the statistical interpretation of the results, which includes the construction of the full likelihood model stored in a so-called workspace, the maximum likelihood fit with the observed data and studies relevant to the impact of systematic uncertainty. He has a main contribution to the limit setting for the di-Higgs cross section and the Higgs self-coupling, which is derived using two different methods. One of them is an approximation and analytical approach, the so-called asymptotic formula for likelihood-based test, which is a powerful method validated in many cases. The other is based on pseudo-experiments (toys), which is supposed to give more accurate estimations of limits for this analysis due to the low observed number of events.

The author is one of the main contributors for the energy calibration of ATLAS electromagnetic calorimeter. The work is mainly about the in-situ calibration and measurement of the energy-dependent scale factor (so-called linearity). He has studied a global fit model with the ideas originated from experts on ATLAS electromagnetic calorimeter. This global fit model helps to constrain the energy scale uncertainty for electrons and photons.

For the Higgs bosons mass analysis in the diphoton channel, the author contributes to the application of the global fit model (described above) in order to further improve the precision of Higgs boson mass measurement. The output of the global fit model is implemented in the likelihood of the mass analysis, the performance is estimated using an expected Asimov data.

1 - Theoretical Aspects

1.1 Standard Model in a Nutshell

The Standard Model (SM) is the current paradigm describing particle physics in terms of fundamental particles and interactions. It is described by a theory containing the local symmetry

$$G = SU(3)_C \times SU(2)_L \times U(1)_Y \tag{1.1}$$

with $SU(3)_C$ for the strong interaction, and $SU(2)_L \times U(1)_Y$ for the electroweak interaction which is a unified theory of the weak and electromagnetic interactions developed by Glashow, Salam and Weinberg in the 1960s. The interactions are mediated by gauge bosons: the massless gluons (G^a_μ) for the strong interaction, with a running from 1 to 8; the gauge bosons (W^i_μ, B_μ) for the $SU(2)_L \times U(1)_Y$ electroweak interaction with i running from 1 to 3. After the spontaneous symmetry breaking $SU(2)_L \times U(1)_Y \to U(1)_{em}$, the ($W^i_\mu$, B_μ) gauge bosons are transformed into three massive vector bosons ($W^\pm, Z$) and a massless vector boson, the photon γ.

According to Noether's theorem, for each continuous symmetry, there is a corresponding conservation law. Hence the SM symmetry G corresponds to the conservation of the following quantum numbers: $SU(3)$ colour, $SU(2)$ weak isospin I and $U(1)$ weak hypercharge Y ($Q = T_3 + \frac{1}{2}Y$), where Q is the electrical charge and T_3 is the third component of the weak isospin.

In addition to the gauge bosons, the SM contains matter fermions and a scalar Higgs boson, which can be organized in the following representation:

$$\begin{aligned}
&\text{Leptons: } l_{iL} = \begin{pmatrix} \nu_i \\ e_i \end{pmatrix}_L : (1,2)_{Y=-1}, \quad e_{iR} : (1,1)_{Y=-2} \\
&\text{Quarks: } q_{iL} = \begin{pmatrix} u_i \\ d_i \end{pmatrix}_L : (3,2)_{Y=1/3}, \quad u_{iR} : (3,1)_{Y=4/3}, \quad d_{iR} : (3,1)_{Y=-2/3} \\
&\text{Higgs: } \Phi = \begin{pmatrix} \phi^+ \\ \phi^0 \end{pmatrix} : (1,2)_{Y=1}
\end{aligned}$$

where the first number (a) inside the bracket $(a,b)_c$ stands for the color triplet for quarks, singlet for leptons and Higgs; the second term (b) represents the weak isospin doublet for left-handed fermions and Higgs, while singlet for right-handed fermions; the lower number (c) is the weak hypercharge associated to the U(1) symmetry.

There are 3 generations for leptons (e, μ, τ) and $(\nu_e, \nu_\mu, \nu_\tau)$, and 3 generations for quarks (u, c, t) and (d, s, b), among those only the left-handed components are interacting with the $SU(2)$ weak gauge bosons W^i_μ, while the $U(1)$ gauge boson B_μ is coupling to both left-handed and right-handed particles. No evidence of the right-handed neutrino has yet been found, therefore they are ignored in the current formalism.

An overview of the particle content in the SM is presented in Fig. 1.1, including the spin-0 Higgs boson, spin-$\frac{1}{2}$ matter fermions and spin-1 gauge bosons (g, $W^\pm$, Z and γ).

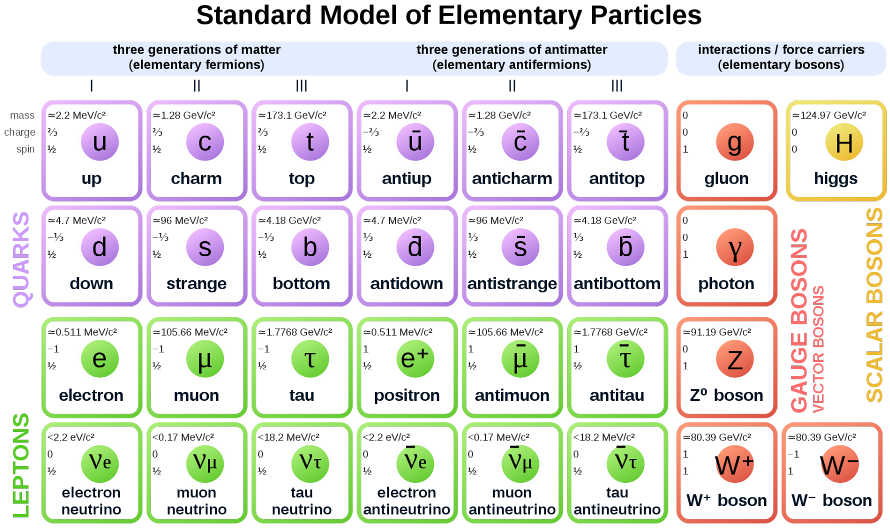

Figure 1.1: Particle content of the Standard Model [4].

In the following, the basic quantum field theories used to describe the SM particles and their interactions are briefly formulated, which involve the quantum chromodynamics (QCD), electroweak (EW) interaction, Higgs sector and Yukawa coupling. A historical review of the construction of the SM can be found in Ref. [5] (also in [6]).

Quantum chromodynamics is a Yang-Mills theory with $SU(3)_C$ symmetry described by the following Lagrangian[1]:

$$\mathcal{L}_{QCD} = -\frac{1}{4} G^a_{\mu\nu} G^{\mu\nu}_a + \bar{q}\gamma^\mu D_\mu q \tag{1.2}$$

with

$$G^a_{\mu\nu} = \partial_\mu G^a_\nu - \partial_\nu G^a_\mu + g_s f^{abc} G^b_\mu G^c_\nu, \quad D_\mu q = \left(\partial_\mu + i g_s \frac{\lambda_a}{2} G^a_\mu\right) q \tag{1.3}$$

The first term in Eq. 1.2 is the kinetic term for gluon fields, the second one is the Dirac Lagrangian for quarks and their interactions with gluons. $G^a_{\mu\nu}$ is the gluon field strength tensor, where index a runs from 1 to 8. g_s is the strong coupling constant. f^{abc} is the structure constant of $SU(3)$. q is the quark Dirac field for both left-handed and right-handed chiralities, and for all the six quark flavours. γ^μ are the Dirac matrices and D_μ is the gauge covariant derivative. $\frac{\lambda_a}{2}$ are the $SU(3)$ generators, with the Gell-Mann matrices λ^a. The strong coupling constant is vanishing at high energy or short distance according to the asymptotic freedom of QCD, which leads to the phenomenon of quark confinement.

The electroweak interaction is described by a $SU(2)_L \times U(1)_Y$ Yang-Mills theory with Lagrangian described as:

$$\mathcal{L}_{EW} = -\frac{1}{4} W^i_{\mu\nu} W^{\mu\nu}_i - \frac{1}{4} B_{\mu\nu} B^{\mu\nu} + \bar{\Psi}_L i\gamma^\mu D_\mu \Psi_L + \bar{\Psi}_R i\gamma^\mu D_\mu \Psi_R \tag{1.4}$$

---

[1] The convention of Minkowski metric $\eta = diag(1, -1, -1, -1)$ is used.

with

$$\begin{aligned} W^i_{\mu\nu} &= \partial_\mu W^i_\nu - \partial_\nu W^i_\mu + g\epsilon^{ijk} W^j_\mu W^k_\nu, \quad B_{\mu\nu} = \partial_\mu B_\nu - \partial_\nu B_\mu, \\ D_\mu \Psi_L &= \left(\partial_\mu + ig\frac{\sigma_i}{2} W^i_\mu + ig'\frac{Y}{2} B_\mu\right)\Psi_L, \quad D_\mu \Psi_R = \left(\partial_\mu + ig'\frac{Y}{2} B_\mu\right)\Psi_R. \end{aligned} \tag{1.5}$$

$-\frac{1}{4} W^i_{\mu\nu} W^{\mu\nu}_i - \frac{1}{4} B_{\mu\nu} B^{\mu\nu}$ represent the kinetic terms of the $SU(2) \times U(1)$ gauge fields, where $W^i_{\mu\nu}$ is the field strength density of $SU(2)$ gauge bosons, $B_{\mu\nu}$ is the one of $U(1)$. ϵ^{ijk} is the structure constant of $SU(2)$. g and g' are respectively the weak coupling constants associated with $SU(2)$ and $U(1)$ group. Ψ_L and Ψ_R correspond to the left-handed and right-handed components of leptons and quarks fields. σ_i are the Pauli matrices. Y stands for the weak hypercharge operator. As mentioned above, only Ψ_L is coupled to the $SU(2)$ fields W^i_μ, while B_μ interacts with both Ψ_L and Ψ_R.

The Higgs sector is expressed by a scalar Lagrangian including a quadratic potential $V(\Phi)$:

$$\mathcal{L}_{Higgs} = |D_\mu \Phi|^2 - V(\Phi) \tag{1.6}$$

with

$$D_\mu \Phi = \left(\partial_\mu + ig\frac{\sigma_i}{2} W^i_\mu + ig'\frac{Y_L}{2} B_\mu\right)\Phi \tag{1.7}$$

$$V(\Phi) = \mu^2 \Phi^\dagger \Phi + \lambda(\Phi^\dagger \Phi)^2 \tag{1.8}$$

The Higgs field Φ is a $SU(2)$ complex doublet, which includes a charged complex component ϕ^+, a neutral complex component ϕ^0.

$$\Phi = \begin{pmatrix} \phi^+ \\ \phi^0 \end{pmatrix} \tag{1.9}$$

Because of the negative sign of μ^2 in the SM, non-zero vacuum states emerge in the minimum of the Higgs potential, which violates the $SU(2) \times U(1)$ symmetry and predicts the existence of the Brout–Englert–Higgs boson (or Higgs boson as we call it from now on) and massive weak gauge bosons. This corresponds to the Brout–Englert–Higgs mechanism, which will be described in the next section.

On the other hand, as for fermion mass generation, a Yukawa term is used to describe the coupling between fermionic fields and the Higgs field:

$$\mathcal{L}_{Yukawa} = -y^u_{ij} \bar{q}_{iL} u_{jR} \tilde{\Phi} - y^d_{ij} \bar{q}_{iL} d_{jR} \Phi - y^e_{ij} \bar{l}_{iL} e_{jR} \Phi + h.c. \tag{1.10}$$

y^{ude}_{ij} are the Yukawa coupling matrices respectively for the up-type, down-type quarks and leptons (except for neutrinos). $\tilde{\Phi}$ is the charge-conjugate Higgs field defined as $\tilde{\Phi} = i\sigma_2 \Phi^* = \begin{pmatrix} \bar{\phi}^0 \\ -\bar{\phi}^+ \end{pmatrix}$.

1.2 Spontaneous Symmetry Breaking

According to the Goldstone theorem, if the vacuum state is not invariant under the action of symmetry, then the symmetry is broken along with the appearance of a massless Nambu-Goldstone boson for each broken generator. In the SM, the Higgs mechanism is a spontaneous symmetry breaking theory, which

predicts the Higgs bosons and generates the mass of particles.
As shown in Eq. 1.6, the SM Higgs potential reads as

$$V = \mu^2 \Phi^\dagger \Phi + \lambda(\Phi^\dagger \Phi)^2 \tag{1.11}$$

The Higgs scalar potential looks like a Mexican hat as sketched in Fig. 1.2 with non-zero and degenerate vacuum bound states lying on a ring in the horizontal plane. Each bound state is asymmetric under an arbitrary rotation along the z-axis, which indicates broken symmetry. If μ^2 were positive, the potential would be parabolic, subsequently, the global minimum would be null and the symmetry would be preserved.

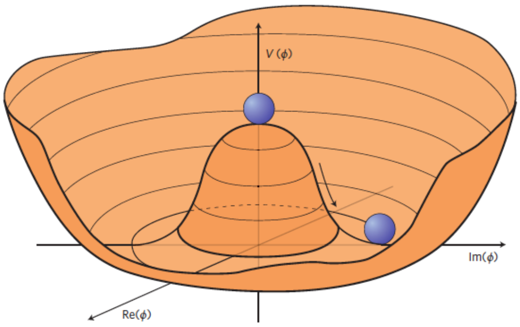

Figure 1.2: Higgs potential in SM [7].

With the choice of $\mu^2 < 0$ in the SM, the Higgs potential is minimized at

$$|\Phi| = \frac{v}{\sqrt{2}} = \sqrt{-\frac{\mu^2}{2\lambda}} \tag{1.12}$$

where v represents the vacuum expectation of Higgs field, that is fixed by the Fermi constant G_F with the relation $v = (\sqrt{2}G_F)^{-1/2} = 246$ GeV. Among the infinite set of vacuum states, once a vacuum is fixed, the $SU(2)_L \times U(1)_Y$ symmetry is broken to a $U(1)_{em}$ symmetry. In the following, the one with vanished charged component ($\phi^+ = 0$) is chosen:

$$\Phi_{\text{bound}} = \begin{pmatrix} 0 \\ \frac{v}{\sqrt{2}} \end{pmatrix} \tag{1.13}$$

Considering infinitesimal excitations around this vacuum, the field can be expanded as

$$\Phi = \exp\left(\frac{i\sigma_\mu \theta^\mu}{v}\right) \begin{pmatrix} 0 \\ \frac{1}{\sqrt{2}}(v+h) \end{pmatrix} \tag{1.14}$$

where μ runs from 1 to 3 corresponding to the three fields θ^1, θ^2 and θ^3, σ_μ are the Pauli matrices, h is a real scalar field. The θ and h correspond to the perturbations around the chosen vacuum.

If now we introduce this new form into the Higgs Lagrangian, by ignoring the gauge interactions and higher order terms, it gives

$$\mathcal{L}_{Higgs} = \frac{1}{2}\partial_\mu h \partial^\mu h - (-\mu^2)h^2 + \frac{1}{2}(\partial_\mu\theta^1\partial^\mu\theta^1 + \partial_\mu\theta^2\partial^\mu\theta^2 + \partial_\mu\theta^3\partial^\mu\theta^3) + ... \tag{1.15}$$

It reveals a massive scalar boson h of mass $\sqrt{2}|\mu|$ which is the Higgs boson, and three massless Goldstone bosons. As predicted by the Goldstone theory that the number of massless Goldstone bosons equals the number of broken generators, the $SU(2)_L \times U(1)_Y \to U(1)_{em}$ symmetry broken corresponds to three broken degrees of freedom, hence three Goldstone bosons appear.

1.3 Higgs Coupling, Weak Mixing Angle and Mass Generation

A gauge transformation is performed to eliminate the Goldstone bosons whose additional degrees of freedom are eaten by the electroweak gauge bosons, hence acquiring longitudinal polarization:

$$\Phi \to \Phi' = \exp(\frac{-i\sigma_\mu\theta^\mu}{v})\Phi = \frac{1}{\sqrt{2}}\begin{pmatrix} 0 \\ v+h \end{pmatrix} \tag{1.16}$$

Subsequently, the Higgs potential can be expressed with only one scalar field h:

$$\begin{aligned} V &= \mu^2\frac{(v+h)^2}{2} + \lambda\frac{(v+h)^4}{4} && (1.17)\\ &= \frac{\lambda v^4}{4} + \frac{\mu^2 v^2}{2} + (\mu^2 v + \lambda v^3)h + (\frac{\mu^2}{2} + \frac{3\lambda v^2}{2})h^2 + \lambda v h^3 + \frac{\lambda}{4}h^4 && (1.18)\\ &= -\frac{\lambda v^4}{4} - \mu^2 h^2 + \lambda v h^3 + \frac{\lambda}{4}h^4 && (1.19)\end{aligned}$$

Apart from the mass term $-\mu^2 h^2$, the Higgs potential predicts also tri-linear and quartic Higgs self-couplings, corresponding to the last two terms. Since the vacuum expectation value v is fixed by the Fermi constant G_F, in addition with the Higgs mass measured at LHC ($m_h = 125.09$ GeV) [3], the SM prediction of self-coupling constant λ is:

$$\left(\frac{v}{\sqrt{2}} = \sqrt{-\frac{\mu^2}{2\lambda}},\ -2\mu^2 = m_h^2\right) \xrightarrow{\text{SM}} \lambda = \frac{m_h^2}{2v^2} \approx 0.13 \tag{1.20}$$

By injecting Φ' in the covariant derivative in Eq. 1.7, this gives

$$\begin{aligned} D_\mu\Phi &= (\partial_\mu + ig\frac{\sigma_i}{2}W_\mu^i + ig'\frac{Y_L}{2}B_\mu)\frac{1}{\sqrt{2}}\begin{pmatrix} 0 \\ \frac{v+h}{\sqrt{2}} \end{pmatrix} \\ &= \begin{pmatrix} \partial_\mu + i\frac{g}{2}W_\mu^3 + i\frac{g'}{2}B_\mu & i\frac{g}{2}(W_\mu^1 - iW_\mu^2) \\ i\frac{g}{2}(W_\mu^1 + iW_\mu^2) & \partial_\mu - i\frac{g}{2}W_\mu^3 + i\frac{g'}{2}B_\mu \end{pmatrix}\begin{pmatrix} 0 \\ \frac{v+h}{\sqrt{2}} \end{pmatrix} \\ &= \begin{pmatrix} i\frac{g}{2}\frac{W_\mu^1 - iW_\mu^2}{\sqrt{2}}(v+h) \\ \frac{1}{\sqrt{2}}\partial_\mu h - \frac{i}{2}(gW_\mu^3 - g'B_\mu)\frac{v+h}{\sqrt{2}} \end{pmatrix} \end{aligned} \tag{1.21}$$

thus

$$|D_\mu\Phi|^2 = \frac{g^2}{8}(v+h)^2|W_\mu^1 - iW_\mu^2|^2 + \frac{1}{2}\partial_\mu h\partial^\mu h + \frac{1}{8}(v+h)^2(gW_\mu^3 - g'B_\mu)^2 \tag{1.22}$$

The Higgs Lagrangian is now re-expressed as

$$\begin{aligned}\mathcal{L}_{Higgs} &= \frac{1}{2}\partial_\mu h \partial^\mu h - (-\mu^2)h^2 + \frac{v^2}{8}\left[g^2|W_\mu^1 - iW_\mu^2|^2 + (gW_\mu^3 - g'B_\mu)^2\right] &(1.23)\\ &+ \frac{1}{8}(h^2 + 2vh)\left[g^2|W_\mu^1 - iW_\mu^2|^2 + (gW_\mu^3 - g'B_\mu)^2\right] &(1.24)\\ &- (\lambda v h^3 + \frac{\lambda}{4}h^4) &(1.25)\end{aligned}$$

The first line is interpreted as Lagrangian of Higgs bosons of mass $\sqrt{2}|\mu|$, plus additional terms of W and B fields. Rotation transformations are performed to obtain the mass eigen-fields $W_\mu^\pm$, Z_μ and A_μ. The gauge fields $W_\mu^\pm$ are defined as a combination of the first two charged gauge fields W_μ^1 and W_μ^2 of $SU(2)_L$, and neutral gauge fields A_μ and Z_μ are the two mixing states between W_μ^3 and B_μ.

$$\begin{aligned}W_\mu^\pm &= \frac{W_\mu^1 \mp iW_\mu^2}{\sqrt{2}} &(1.26)\\ A_\mu &= \frac{g'W_\mu^3 + gB_\mu}{\sqrt{g^2 + g'^2}} &(1.27)\\ Z_\mu &= \frac{gW_\mu^3 - g'B_\mu}{\sqrt{g^2 + g'^2}} &(1.28)\end{aligned}$$

The so-called Weinberg weak mixing angle θ_W is hence defined to describe the rotation between W_μ^3 and B_μ:

$$\begin{pmatrix} A_\mu \\ Z_\mu \end{pmatrix} = \begin{pmatrix} \cos\theta_W & \sin\theta_W \\ -\sin\theta_W & \cos\theta_W \end{pmatrix} \begin{pmatrix} B_\mu \\ W_\mu^3 \end{pmatrix} \tag{1.29}$$

such that

$$\cos\theta_W = \frac{g}{\sqrt{g^2 + g'^2}}, \quad \sin\theta_W = \frac{g'}{\sqrt{g^2 + g'^2}} \tag{1.30}$$

Hence the Higgs Lagrangian can be derived as

$$\begin{aligned}\mathcal{L}_{Higgs} &= \frac{1}{2}\partial_\mu h \partial^\mu h - (-\mu^2)h^2 + \frac{v^2 g^2}{4}W^+W^- + \frac{1}{2}\frac{v^2}{4}(g^2 + g'^2)|Z_\mu|^2 &(1.31)\\ &+ \frac{1}{8}(h^2 + 2vh)\left[2g^2W^+W^- + (g^2 + g'^2)|Z_\mu|^2\right] &(1.32)\\ &- (\lambda v h^3 + \frac{\lambda}{4}h^4) &(1.33)\end{aligned}$$

The spontaneous symmetry breaking gives three massive vector gauge bosons ($W^\pm$, Z^0), with masses:

$$m_W = \frac{gv}{2}, \, m_Z = \frac{v}{2}\sqrt{g^2 + g'^2} \tag{1.34}$$

The photon remains massless since the $U(1)_{em}$ symmetry is still preserved.

The second line of the Lagrangian represents the coupling between vector bosons and Higgs, which is proportional to the square of the vector boson mass and is crucial to maintain the unitarity of the theory. The coupling of weak bosons to Higgs mass is:

$$g_{WWh} = 16\frac{m_W^2}{v},\, g_{ZZh} = 8\frac{m_Z^2}{v} \tag{1.35}$$

$$g_{WWhh} = 8\frac{m_W^2}{v^2},\, g_{ZZhh} = 4\frac{m_Z^2}{v^2} \tag{1.36}$$

The gauge bosons masses are successfully generated by the Higgs mechanism, but the mechanism has no effect on fermions. The Yukawa interaction described in Eq. 1.10 is used to solve the fermion mass generation through interaction between fermions and the Higgs field. After symmetry breaking, the Yukawa term in Eq. 1.10 can be rewritten as:

$$\mathcal{L}_{Yukawa} = -\frac{v+h}{\sqrt{2}}(y_{ij}^u \bar{u}_{iL} u_{jR} + y_{ij}^d \bar{d}_{iL} d_{jR} + y_{ij}^e \bar{e}_{iL} e_{jR}) + h.c. \tag{1.37}$$

Hence the fermion mass is:

$$m_{ij}^{ude} = \frac{v}{\sqrt{2}} y_{ij}^{ude} \tag{1.38}$$

The coupling between Higgs boson and leptons is proportional to the fermion mass:

$$g_{llh} = \frac{m_l}{v} \tag{1.39}$$

Charged, Neutral and Electromagnetic Currents

Using the mass eigen-states $W_\mu^\pm$, Z_μ and A_μ, the interaction term of the electroweak Lagrangian can be derived to deduce the charged and neutral currents.

$$\begin{aligned}
\mathcal{L}_{EW}^{int} =& -\bar{\Psi}_L \gamma^\mu (g\frac{\sigma_i}{2} W_\mu^i + g'\frac{Y}{2} B_\mu)\Psi_L - \bar{\Psi}_R \gamma^\mu g' \frac{Y}{2} B_\mu \Psi_R \\
=& -\bar{\Psi}_L \gamma^\mu g \frac{\sigma_1 + i\sigma_2}{2\sqrt{2}} W_\mu^+ - \bar{\Psi}_L \gamma^\mu g \frac{\sigma_1 - i\sigma_2}{2\sqrt{2}} W_\mu^- \\
& - \bar{\Psi}_L \gamma^\mu (g\cos\theta_w \frac{\sigma_3}{2} - g'\sin\theta_w \frac{Y}{2})\Psi_L Z_\mu + \bar{\Psi}_R \gamma^\mu g' \sin\theta_w \frac{Y}{2} \Psi_R Z_\mu \\
& - \bar{\Psi}_L \gamma^\mu (g\sin\theta_w \frac{\sigma_3}{2} + g'\cos\theta_w \frac{Y}{2})\Psi_L A_\mu - \bar{\Psi}_R \gamma^\mu g' \cos\theta_w \frac{Y}{2} \Psi_R A_\mu
\end{aligned} \tag{1.40}$$

Let's define

$$\sigma_\pm = \sigma_1 \pm i\sigma_2 \tag{1.41}$$

$$e = g\sin\theta_w = g'\cos\theta_w \tag{1.42}$$

$$Q = T_3 + \frac{Y}{2} = \frac{\sigma_3}{2} + \frac{Y}{2} \tag{1.43}$$

where e is the elemental electric charge, Q is the electric charge operator.

Hence the Lagrangian can be rewritten as

$$\begin{aligned}\mathcal{L}_{EW}^{int} &= -\frac{g}{\sqrt{2}}\bar{\Psi}_L\gamma^\mu\frac{\sigma_\pm}{2}\Psi_L W_\mu^\pm - \frac{g}{\cos\theta_w}(\bar{\Psi}_L\gamma^\mu T_3\Psi_L - \sin^2\theta_w\bar{\Psi}_{LR}\gamma^\mu Q\Psi_{LR})Z_\mu - e\bar{\Psi}_{LR}\gamma^\mu Q\Psi_{LR}A_\mu \\ &= -\frac{g}{\sqrt{2}}j^\mu_{cc+}W^+_\mu - \frac{g}{\sqrt{2}}j^\mu_{cc-}W^-_\mu - \frac{g}{\cos\theta_w}j^\mu_{nc}Z_\mu - ej^\mu_{em}A_\mu\end{aligned} \tag{1.44}$$

where charged ($j^\mu_{cc\pm}$), neutral (j^μ_{nc}) and electromagnetic (j^μ_{em}) currents are defined below, which describes the fermion pairs that couple to weak gauge bosons.

$$j^\mu_{cc\pm} = \bar{\Psi}_L\gamma^\mu\frac{\sigma_\pm}{2}\Psi_L \tag{1.45}$$

$$j^\mu_{em} = \bar{\Psi}_{LR}\gamma^\mu Q\Psi_{LR} \tag{1.46}$$

$$\begin{aligned}j^\mu_{nc} &= \bar{\Psi}_L\gamma^\mu T_3\Psi_L - \sin^2\theta_w j^\mu_{em} \\ &= \bar{\Psi}\gamma^\mu(T_3 - Q\sin^2\theta_w)\frac{1-\gamma^5}{2}\Psi + \bar{\Psi}\gamma^\mu(-Q\sin^2\theta_w)\frac{1+\gamma^5}{2}\Psi \\ &= \frac{1}{2}\bar{\Psi}\gamma^\mu(C_V - C_A\gamma^5)\Psi\end{aligned} \tag{1.47}$$

$$\text{with} \quad C_V = T_3 - 2Q\sin^2\theta_w, \quad C_A = T_3 \tag{1.48}$$

For neutral current, C_V and C_A represent the vector and axial couplings of fermions to the Z boson.

1.4 Higgs Boson at the Large Hadron Collider

Since the discovery of the Higgs boson with a mass of $\approx$ 125 GeV by the ATLAS [1] and CMS [2] experiments at the Large Hadron Collider (LHC) in 2012, the various production and decay modes of the Higgs boson have been explored in order to measure its properties. The main production modes of the Higgs boson (Fig. 1.3) are the gluon-gluon fusion (ggF), vector boson fusion (VBF), associated production with a vector boson (VH), associated production with a pair of top or bottom quarks ($t\bar{t}H$ or $b\bar{b}H$) or with a single top quark tHq. The corresponding cross sections for the various Higgs productions are shown in Fig. 1.4a.

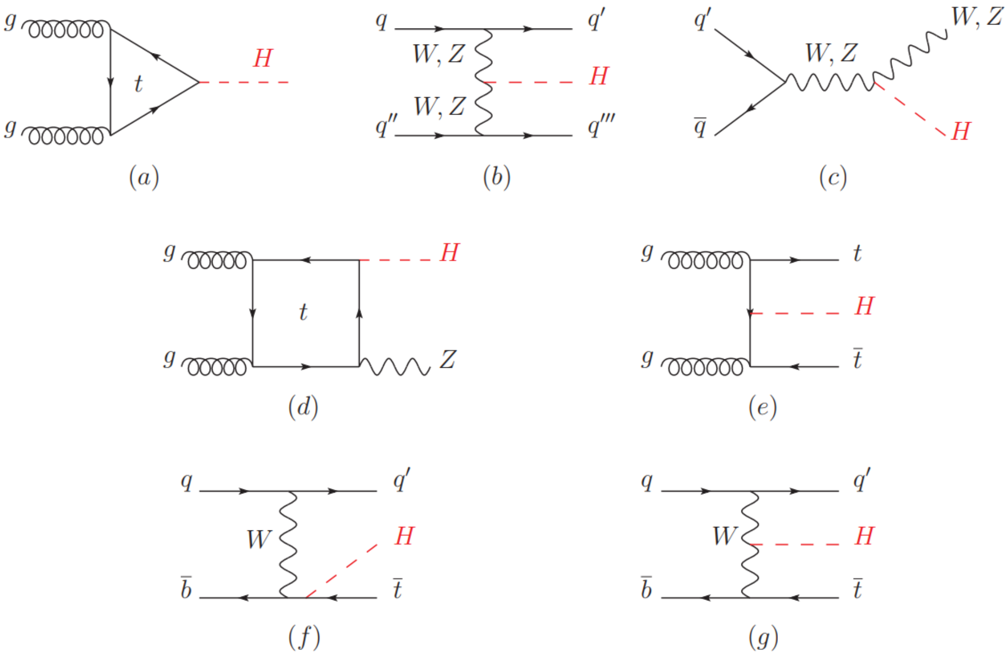

Figure 1.3: Main leading order Feynman diagrams for the Higgs production, via (a) ggF, (b) VBF, (c) VH from a quark-quark interaction, (d) ZH from a gluon-gluon interaction, (e) $t\bar{t}H$, (f-g) tHq processes [8].

The Higgs boson has a mean lifetime of $\sim 10^{-22}$ seconds, which will immediately decay into pair of final state fermions or bosons. For the Higgs boson with a mass of around 125 GeV, the main decay products are a pair of $b\bar{b}$ quarks with a branching ratio around 58.2% and W^+W^- bosons with a branching ratio around 21.4%, as illustrated in Fig. 1.4b. According to the evolution of branching ratio with the Higgs boson mass, one sees that the branching ratio BR($H \rightarrow ZZ$) is known with a relative uncertainty around 1%, if the Higgs boson mass is known with an uncertainty of 100 MeV. Hence a precise measurement of the Higgs boson mass is useful to have accurate theoretical prediction of the BR($H \rightarrow ZZ$) when comparing it to other decay modes.
The latest Run 2 combination results of the Higgs production cross section and branching ratio by the ATLAS experiment are presented in Fig. 1.5a, that observations for the main production and decay channels are all within 1σ standard deviation of the SM prediction.

The Higgs boson mass measured in the $H \rightarrow \gamma\gamma$ and $H \rightarrow ZZ \rightarrow 4l$ channels using the Run 1 and

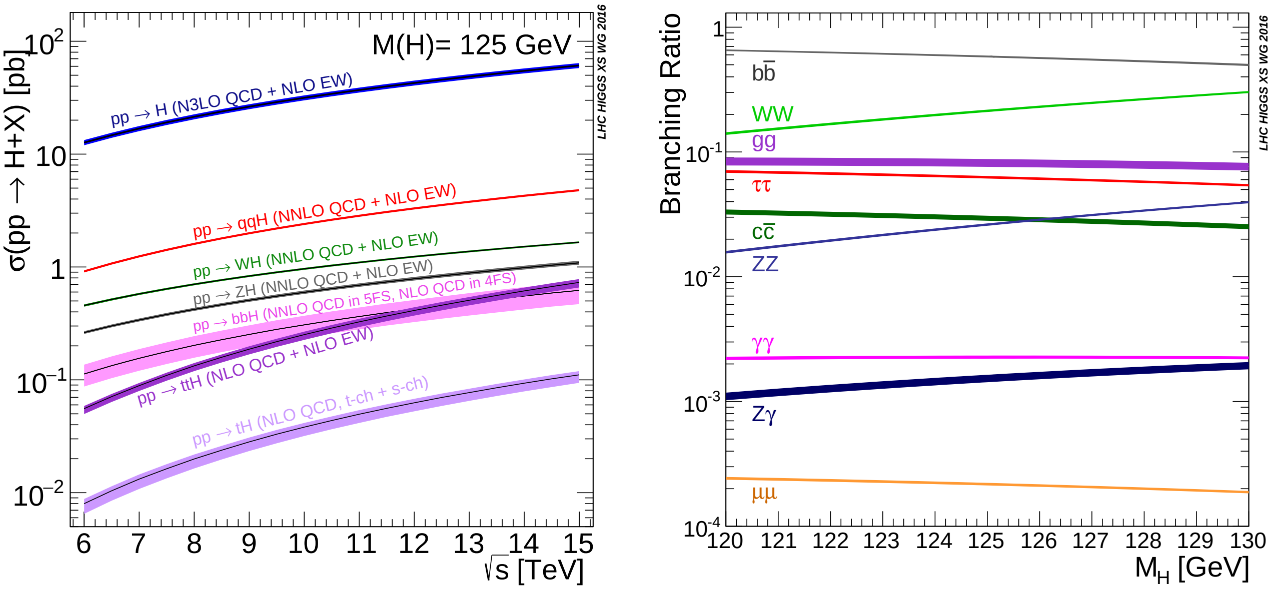

(a) *(b)*

Figure 1.4: (a) SM Higgs boson production cross section as a function of the center of mass energy $\sqrt{s}$ for pp collisions. The VBF production is labelled as $pp \to qqH$. (b) Branching ratios of the main decays of the SM Higgs boson near m_H=125 GeV. The error bands indicate the theoretical uncertainty. [9].

the latest Run 2 data by the CMS experiment is summarized in Fig. 1.5b, of which the current most precise measurement from CMS gives a central value of 125.38 GeV with a precision of 0.11%, after combining the Run 1 and 2016 results (see Appendix A for the Higgs boson mass measurement at LHC up to now).

1.5 Limitations of the Standard Model and Physics Beyond

As described in Eq. 1.31, the Higgs mechanism predicts the Higgs mass and its self-couplings.

$$\mathcal{L} = \frac{1}{2}\partial_\mu h \partial^\mu h - \frac{1}{2}m_h^2 h^2 - g_{hhh}h^3 - g_{hhhh}h^4 \tag{1.49}$$

In the case of the SM:

$$m_h^2 = -2\mu^2,\ g_{hhh} = \lambda v,\ g_{hhhh} = \frac{\lambda}{4} \tag{1.50}$$

The quartic coupling constant λ has an effect on the vacuum stability. Concerning the renormalized Higgs potential after countering for the corrections from $t\bar{t}H$ and HHH loops [12], it is possible that at some energy scale, λ will turn to be negative and lead to an unbounded vacuum. Fig. 1.6a shows the instability scale depending on the mass of the Higgs boson, calculated at top mass fixed at 173.1 GeV. With the current Higgs mass around 125 GeV, the vacuum starts to decay at a scale near $10^{10} \sim 10^{14}$ GeV. The instability energy scale as a function of the top mass and Higgs mass is presented in Fig. 1.6b, it tells that we are living in a meta-stable universe under the nature of SM. Optimistically, this meta-stability can be considered as an indication of new particles below the instability scale, which would regularize the vacuum to be stable. Because of this, the measurement of λ is not only important for proving the validity of the

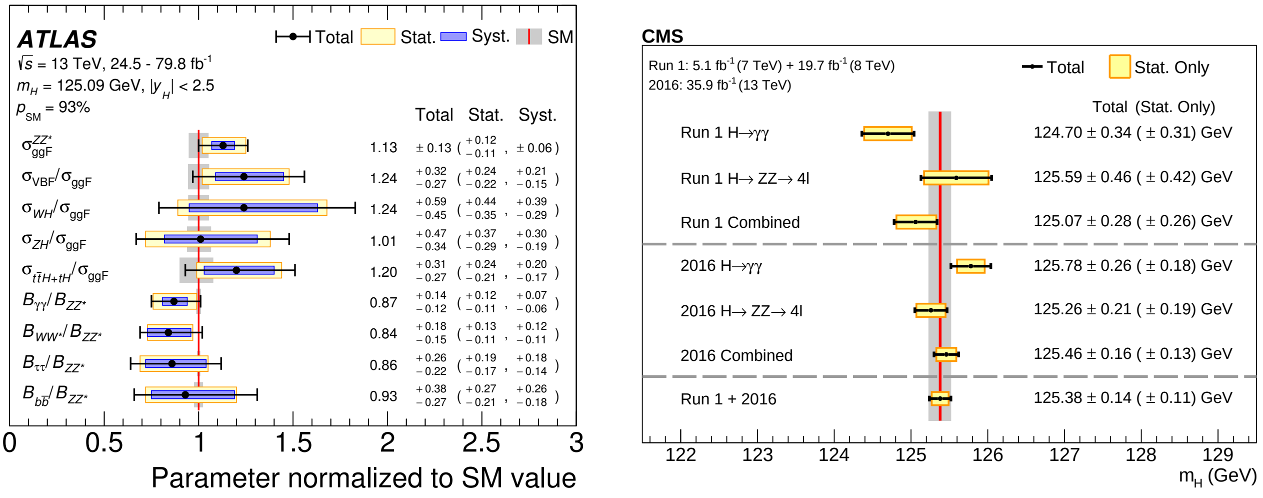

(a)

(b)

Figure 1.5: (a) Combined Higgs production cross sections and branching ratios by ATLAS, normalized to the SM predictions, for the main production and decay modes. The vertical red line with a grey band corresponds to the SM prediction with its theoretical uncertainty [10]. (b) Summary of the Higgs mass measurement in the $H \to \gamma\gamma$ and $H \to ZZ \to 4l$ channels and their combination by CMS using Run 1 and part of Run 2 data at LHC. The vertical red line with a grey band corresponds to the Run 1+2016 measurement [11].

SM, but also as a possible hint to new physics.

Another concern about the Standard Model is the hierarchy problem, that the electroweak scale of O(100) GeV is far away from the Plank scale of $M_P = \frac{1}{G} \simeq 1.22 \times 10^{19}$ GeV. Similar to Eq. 1.11, consider the bare Lagrangian as

$$\mathcal{L}_{\text{bare}} \subset -\mu^2_{\text{bare}}\Phi^\dagger\Phi - \lambda_{\text{bare}}(\Phi^\dagger\Phi)^2 \tag{1.51}$$

that the physical Higgs mass after renormalization is $m_h = -2\mu^2_{\text{bare}} - \Delta m_h^2$, where δm^2 is a counterterm representing the quantum radiative correction. A generic fermion loop as shown in Fig. 1.7 contributes to a correction as

$$\Delta m_h^2 = -\frac{y_f^2}{8\pi^2}\left[2\Lambda^2 + 6m_f^2 \ln(\Lambda/m_f)\right] + ... \tag{1.52}$$

where y_f is the Yukawa coupling to the fermion, and m_f is the fermion mass.

Such correction is quadratically divergent with the cutoff scale Λ, hence if the Standard Model remains valid at the Plank scale, the radiative correction would be $\simeq 10^{34}$ times larger than the square of the physical Higgs mass (around 125 GeV). The only solution is that the bare parameter μ^2_{bare} has a similar divergence with Λ as the radiative correction. This leads to the so-called fine-tuning problem.

Such kind of problem can be instead resolved by imaging that it exists other heavy particles at high energy that couple to the Higgs boson, for instance, a scalar boson S that is shown in Fig. 1.7b. It yields a

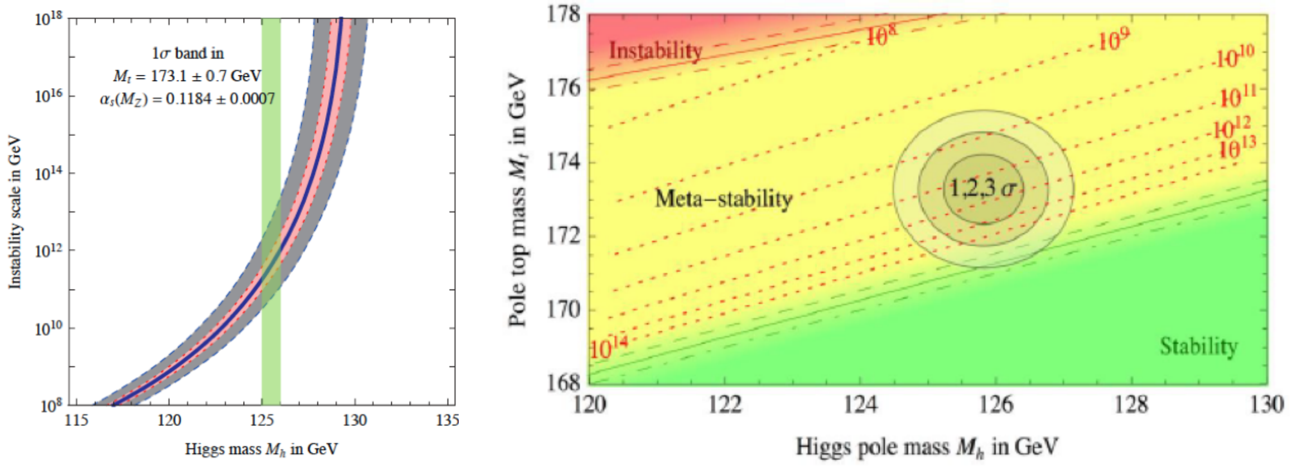

(a) *(b)*

Figure 1.6: Stability of vacuum. (a) Instability scale for different Higgs mass hypotheses of SM, the vacuum starts to decay at some scale from 10^{10} to 10^{14} GeV. (b) Meta-stability of the universe. Dotted lines show the instability scales [12].

correction similar to the fermions:

$$\Delta m_h^2 = \frac{\lambda_S}{16\pi^2}\left[\Lambda^2 + 2m_S^2 \ln(\Lambda/m_S)\right] + ... \tag{1.53}$$

where λ_S is the quartic coupling of S to Higgs.

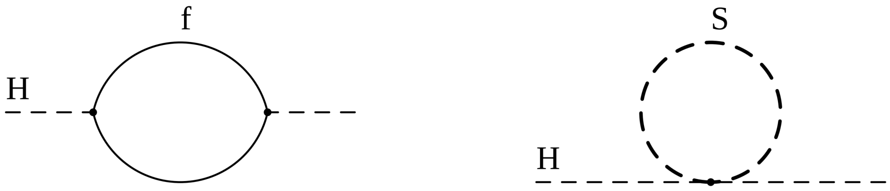

(a) (b)

Figure 1.7: One-loop quantum corrections to the mass-squared of the Higgs boson due to (a) the loop of a generic fermion f, (b) a generic scalar S [7].

The quadratic term of Λ can be cancelled for each fermion f, if there exists a scalar boson S satisfying the following relationship

$$\lambda_S = 2y_f^2 \tag{1.54}$$

The most popular theory having such kind of property is the supersymmetry theorem, which predicts a spin-0 sfermion as a superpartner of a fermion, for example, stop is the sfermion for the top quark.

There is also the problem of the unification of the gauge coupling constants (Fig. 1.8), where the unification is not reached for the SM but is obtained with the supersymmetric extension of the SM (MSSM).

As well, the neutrino is massless in the Standard Model, while the neutrino oscillation provides experimental evidence of its mass. Besides, the SM cannot explain the problem related to dark matter and dark energy.

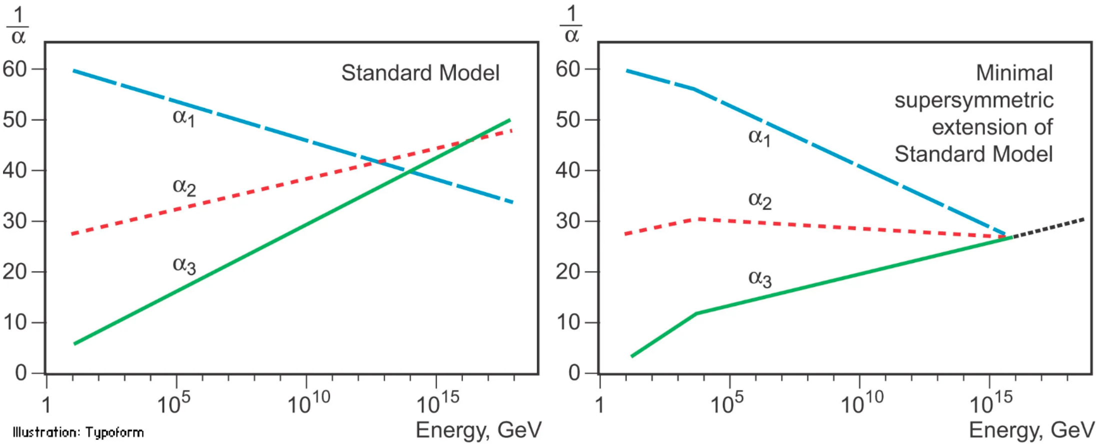

Figure 1.8: Evolution of the inverse of the three gauge coupling constants (α_1, α_2 and α_3 are respectively the electromagnetic, weak and strong coupling constants) in the Standard Model (left) and the supersymmetric extension of the SM (MSSM) (right). Only in the latter case unification is obtained [13].

All these problems imply the weakness of the Standard Model and motivate physicists to search for new physics beyond the Standard Model.

1.6 Conclusion

In this chapter, the aspects of the Standard Model are introduced, including quantum chromodynamics, electroweak theory and the Higgs mechanism. The so-called spontaneous symmetry breaking predicts the existence of massive vector bosons and the Higgs boson. The Higgs boson is crucial for the mass generation of particles, which can interact with massive particles including itself. Hence, the study of the Higgs boson is not only important for the validation of properties of the SM theory but also meaningful for the search for new physics.

2 - Statistical Methods

In this chapter, the statistical formalism used for data modelling, parameter estimation and hypothesis testing is introduced. All are based on a frequentist statistic approach. The conventions and notations follow the ones of the statistical data analysis book from G. Cowan [14] and the asymptotic formula paper [15].

2.1 Basic formalism

One could consider a set of data $\vec{x} = \{x_i\}$ collected with a given experiment and a given model or hypothesis H which predicts a probability density function (pdf) depending on a parameter θ:

$$x \sim P(x|\theta) \text{ or } P(x|H) \tag{2.1}$$

Typical implementation examples of pdfs are Gaussian or Poisson distributions, where θ are the parameters describing the average or spread of the distribution. There are also cases where the data points $\vec{x}$ are modelled by some functional forms, like polynomials and exponential functions. In practice, the objective of a statistical test is to estimate parameters or to test hypotheses, using the observed data. This is usually done by defining a test statistic

$$t_\theta(\vec{x}) = f(x_1, x_2, ..., x_n) \tag{2.2}$$

The test statistic $t_\theta(\vec{x})$ is a function of the measurements $\vec{x}$, where each x_i follows a probability density function $P(x|\theta)$. Consequently, the test statistic is also a random variable, usually with an unspecified analytical expression of probability. Some classic test statistic methods such as likelihood and least square are introduced in the following.

2.2 Parameter Estimation

The test statistic $t_\theta(\vec{x})$ that can be used to estimate the truth value θ_0 of a given parameter θ is called an estimator. It is quite often simply denoted as $\hat{\theta}$. A good estimator usually has several important properties:

- **unbiased**: the average of the estimator is equal to the truth value, i.e. $E\left[\hat{\theta}\right] = \theta_0 + b$ with $b = 0$.
- **efficient**: the variance of the estimator converges asymptotically to the minimum Cramér-Rao bound.
- **robust**: the estimator is insensitive to the dedicated choice of the probability density function.

One of the most wildly used estimators is the maximum likelihood estimator. The likelihood function is equal to the probability to observe a set of data $\vec{x}$ when the truth value of the parameter is θ, that is, the likelihood is a function of the parameter rather than a probability.

$$\mathcal{L}(\theta) = \prod_i^n P(x_i|\theta) \tag{2.3}$$

The maximum likelihood estimator (MLE) $\hat{\theta}$, is the value of θ which maximizes the likelihood function.

$$\hat{\theta} = \arg\max_\theta \mathcal{L}(\theta) \tag{2.4}$$

The MLE is unbiased if the likelihood has an exponential form. It is not robust since it requires the explicit form of the pdf, and it is asymptotically efficient. According to Cramér–Rao bound, the variance of an unbiased estimator satisfies the inequality

$$V(\hat{\theta}) \geq \frac{1}{I_\theta} \tag{2.5}$$

where $I(\theta)$ is the so-called Fisher information, which is expressed with the likelihood function at a large sample limit:

$$I_\theta = -n \cdot E\left[\frac{d^2 \ln P(x|\theta)}{d\theta^2}\Big|_{\theta_0}\right] \xrightarrow[n\to\infty]{} -\frac{\partial^2 \ln \mathcal{L}(\boldsymbol{\theta})}{\partial\theta_i \partial\theta_j}\Big|_{\hat{\theta}} \tag{2.6}$$

In the case of multi-dimensional parameters $\boldsymbol{\theta}$, the Fisher information appears as

$$I_{\boldsymbol{\theta}} = -E\left[\frac{\partial^2 \ln \mathcal{L}(\boldsymbol{\theta})}{\partial\theta_i \partial\theta_j}\Big|_{\hat{\boldsymbol{\theta}}}\right] \tag{2.7}$$

Because of the asymptotic minimum variance bound, for unbiased MLE, the covariance matrix of the estimators are converging to

$$V(\hat{\boldsymbol{\theta}}) = I_{\boldsymbol{\theta}}^{-1} = \left(-\frac{\partial^2 \ln \mathcal{L}(\boldsymbol{\theta})}{\partial\theta_i \partial\theta_j}\Big|_{\hat{\boldsymbol{\theta}}}\right)^{-1} \tag{2.8}$$

Another important estimator is the least square estimator, which is quite often used in regression analysis. Suppose that data $\vec{x}$ is modelled by a function $f(\boldsymbol{\theta})$, with uncertainty $\sigma(\boldsymbol{\theta})$, the least square function $\chi^2(\boldsymbol{\theta})$ is constructed as

$$\chi^2(\boldsymbol{\theta}) = \sum_i^n \left(\frac{x_i - f_i(\boldsymbol{\theta})}{\sigma_i(\boldsymbol{\theta})}\right)^2 \tag{2.9}$$

The least square estimator (LSE) is defined as the parameters which minimize the least square function.

$$\hat{\boldsymbol{\theta}} = \arg\min_{\boldsymbol{\theta}} \chi^2(\boldsymbol{\theta}) \tag{2.10}$$

The LSE is not always unbiased and efficient, except when the model $f(\boldsymbol{\theta})$ is linear as well as the uncertainties σ_i are independent on any hypothesis $\boldsymbol{\theta}$. We will keep this situation to ease the illustrations in the following. In the particular case of Gaussian, that is $x_i \sim \mathcal{G}(\mu, \sigma)$, with known σ, considering the model as $\mu(\boldsymbol{\theta})$, the least square is equivalent to a likelihood test, and in addition, it follows a chi-square law with the degree of freedom equal to $k = n - r$, where r is the dimension of $\boldsymbol{\theta}$:

$$\chi^2(\boldsymbol{\theta}) = \sum_i^n \left(\frac{x_i - \mu_i(\boldsymbol{\theta})}{\sigma}\right)^2 = -2\ln \mathcal{L}(\boldsymbol{\theta}) + \text{constant} \tag{2.11}$$

$$\chi^2(\boldsymbol{\theta}) \sim \chi^2(n-r) \tag{2.12}$$

If the data points are not independent but follow a multi-dimensional Gaussian distribution with a known covariance matrix V, the least square can be smoothly generalized to:

$$\chi^2(\boldsymbol{\theta}) = (\vec{x} - \vec{\mu}(\boldsymbol{\theta}))^T V^{-1} (\vec{x} - \vec{\mu}(\boldsymbol{\theta})) = -2\ln \mathcal{L}(\boldsymbol{\theta}) + \text{constant} \tag{2.13}$$

In the same principle, the covariance of LSE is defined with the second derivatives of least square similar to MLE

$$V(\hat{\boldsymbol{\theta}}) = 2\left(-\frac{\partial^2 \chi^2(\boldsymbol{\theta})}{\partial\theta_i \partial\theta_j}\Big|_{\hat{\boldsymbol{\theta}}}\right)^{-1} \tag{2.14}$$

2.3 Systematic Uncertainties and Profile Likelihood Ratio

An expression says that all the models are wrong, but some are useful. When fitting data using a specific model $f(\mu)$ with a parameter of interest μ, it is not surprising that with more and more data, the model is typically less and less accurate and the goodness-of-fit degrades. In this case, including nuisance parameters can improve the description of the model. In particle physics, nuisance parameters are often assigned to the systematic uncertainties, and they are constrained using auxiliary measurements independent of the primary ones.

The likelihood including nuisance parameters computed with both primary and auxiliary measurements is in the form as

$$\mathcal{L}(\mu, \boldsymbol{\theta}) = \prod_{i}^{n} P(x_i|\mu, \boldsymbol{\theta}) \cdot P(\boldsymbol{\theta_0}|\boldsymbol{\theta}) \tag{2.15}$$

where the first term represents the likelihood with the new model with the systematics effects, and the second is the auxiliary term for systematic uncertainties. They can be some experimental systematics, such as photon energy scale calibration, jet energy resolution, or some theoretical systematics, for example, the parton distribution function uncertainty, QCD renormalization and factorization scales. For some analyses, the auxiliary term can also be the background modelling constraint with measurements in specific control regions.

In order to deal with the additional degrees of freedom associated with the nuisance parameters, the widely used method is the profile likelihood ratio $\lambda(\mu)$, which maximizes the likelihood by profiling the nuisance parameters for each hypothetical value of the parameter of interest (POI) μ.

$$\lambda(\mu) = \frac{\mathcal{L}(\mu, \hat{\hat{\boldsymbol{\theta}}}(\mu))}{\mathcal{L}(\hat{\mu}, \hat{\boldsymbol{\theta}})} \tag{2.16}$$

where

- $\hat{\mu}$, $\hat{\boldsymbol{\theta}}$ are the maximum likelihood estimators for μ and $\boldsymbol{\theta}$.
- $\hat{\hat{\boldsymbol{\theta}}}(\mu)$ are the profiled values of $\boldsymbol{\theta}$ which maximize the likelihood for a fixed assumption of μ.

$$\hat{\hat{\boldsymbol{\theta}}}(\mu) = \arg\max_{\boldsymbol{\theta}} \mathcal{L}(\mu, \boldsymbol{\theta}) \tag{2.17}$$

The numerator is a conditional likelihood with fixed POI where nuisance parameters are profiled. The denominator is an unconditional likelihood with both POI and nuisance parameters inferred with data. It is often transformed to a slightly different function t_μ which has the advantage to be asymptotically distributed as a χ^2 distribution:

$$t_\mu = -2 \ln \lambda(\mu) \tag{2.18}$$

When t_μ=0, it implies a good agreement between data and the tested hypothesis μ.

The presence of systematic uncertainties degrades the sensitivity of POI as illustrated in Fig. 2.1. The t_μ scans over different Higgs masses for the combined Higgs mass measurement with $H \to \gamma\gamma$ and

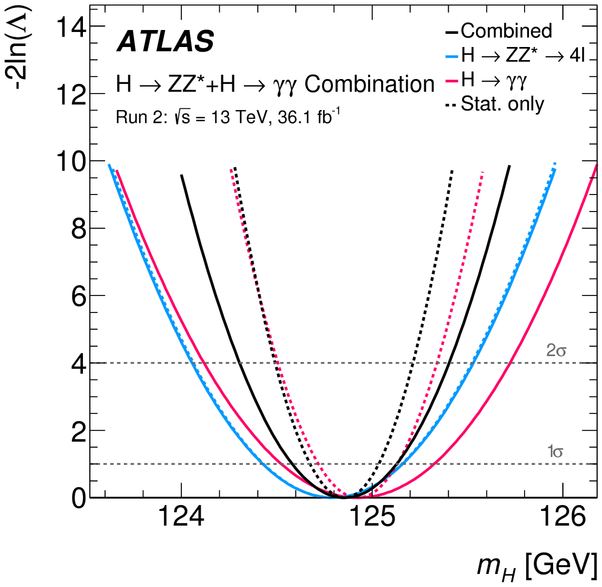

Figure 2.1: $t_\mu = -2\ln\lambda$ as a function of m_H for $H\to\gamma\gamma$, $H\to ZZ^*\to 4l$ and their combination using 36 fb^{-1} Run 2 data. The dashed lines show the mass measurement uncertainties assuming statistical uncertainties only. The dotted curves are the t_μ scan over different Higgs masses with fixed systematic nuisance parameters, such that all of the systematic effects are suppressed, with only statistical uncertainty remaining, while the solid curves represent a full model including systematics [16].

$H \to ZZ^* \to 4l$ channels using 36.1 fb^{-1} Run 2 data. Adding the systematic uncertainties increases the uncertainty of the measurement and degrades the sensitivity.

The separation between the statistical and systematic uncertainties can be realized by repeating the fit after fixing all the systematic nuisance parameters, which gives the statistical error. Subsequently, the systematic uncertainty is deduced to be the square root of the quadratic difference between the total and stat-only errors.

2.4 Hypothesis Testing

A statistical test can be used to evaluate the agreement between observation and a given hypothesis. Formally, the null hypothesis (H_0) and the alternative hypothesis (H_1) are always defined and assessed at the same time. The null hypothesis stands for the one to be tested and often to be tentatively excluded. The alternative hypothesis is defined as the one to be against the null hypothesis. One hypothesis can be not only one parameter value but also nested with a set of hypothetical values.

A typical example is the search of a new particle, with a parameter of interest μ representing the signal strength:

- H_0: background-only, i.e. $\mu = 0$.
- H_1: signal+background, i.e. $\mu > 0$.

In contrast, for the exclusion limit setting of a signal, the two hypotheses are:

- H_0: signal+background, i.e. $\mu > 0$.
- H_1: background-only, i.e. $\mu = 0$.

Let's consider a test statistic $t(\vec{x})$ defined in a phase space, and its probability density functions for the two hypotheses $f(t|H_0)$ and $f(t|H_1)$. According to Neyman, the critical region w is defined as the space where there is a low probability to be found if H_0 is true, but high if H_1 is true. The null hypothesis is rejected when observing $t(\vec{x})$ in the critical region with a given confidence level. Hence one could further define the size and the power of the test with the help of the critical region:

- **size of test**: $\alpha = P(t \in w|H_0)$, with α the type I error probability to wrongly reject H_0 when it's true.
- **power of test**: $1 - \beta = P(t \in w|H_1)$, with β the type II error probability to wrongly accept H_0 when it's false.

A test with a small size and a much larger power is usually a confident test for a physics discovery, which states a higher probability to reject H_0 when it is false than the case when it is true. Let's take the example of LEP as shown in Fig. 2.2a, where a log-likelihood ratio using Neyman-Pearson lemma is taken as the test statistic, the blue dotted curve is the pdf of the background-only hypothesis, the dotted brown is the signal+background hypothesis, and the data gives an observed test statistic value as shown by the red vertical line.

In order to claim a discovery, then H_0 is the background-only hypothesis, and H_1 is the signal+background hypothesis. Hence the critical region is located at a low value of the log-likelihood ratio where there is a higher probability to find the alternative than the null hypothesis. If we take the test statistic values lower than observation as the critical region, then the yellow area corresponds to the size of the test α, and the green area is the type II error probability β. For the purpose of discovery, the yellow area with a probability of α is also called the significance level of the test (consistent with the definition of p-value). The formal statement is that the null hypothesis is excluded at a significance level of α by the observed data.

If the purpose is to test the existence of a signal, then H_0 is signal+background, and H_1 is b-only, accordingly with the roles reversed between yellow and green areas. However, when the two hypotheses are similar to each other, as shown in Fig. 2.2b, the test statistic is not sensitive to distinguish the two hypotheses. Therefore when observing a small size test as shown in the green area, it is not convincing to exclude the null hypothesis. The alternative proposition is to use the CLs method [17], which is defined as

$$\mathrm{CL}_s = \frac{\mathrm{CL}_{s+b}}{\mathrm{CL}_b} \tag{2.19}$$

where

- CL$_{s+b}$: the size of the test α, referring to the green area.
- CL$_b$: the power of the test $1 - \beta$, referring to the complementary pattern of the yellow area.

The null hypothesis will be excluded when CL$_s$ is smaller than some threshold α', which defines the confidence level as $1 - \alpha'$. The typical choice in particle physics is $\alpha' = 0.05$, i.e. 95% confidence level (CL). The advantage of the CL$_s$ method is that in case of low sensitivity (H_0 similar to H_1), an observation in the critical region will exclude H_0 with the CL$_{s+b}$ method, but not with the CL$_s$ method. Explicitly it always requires a much larger probability to accept H_1 when considering rejecting H_0. More aspects of the limit setting will be introduced in the next section.

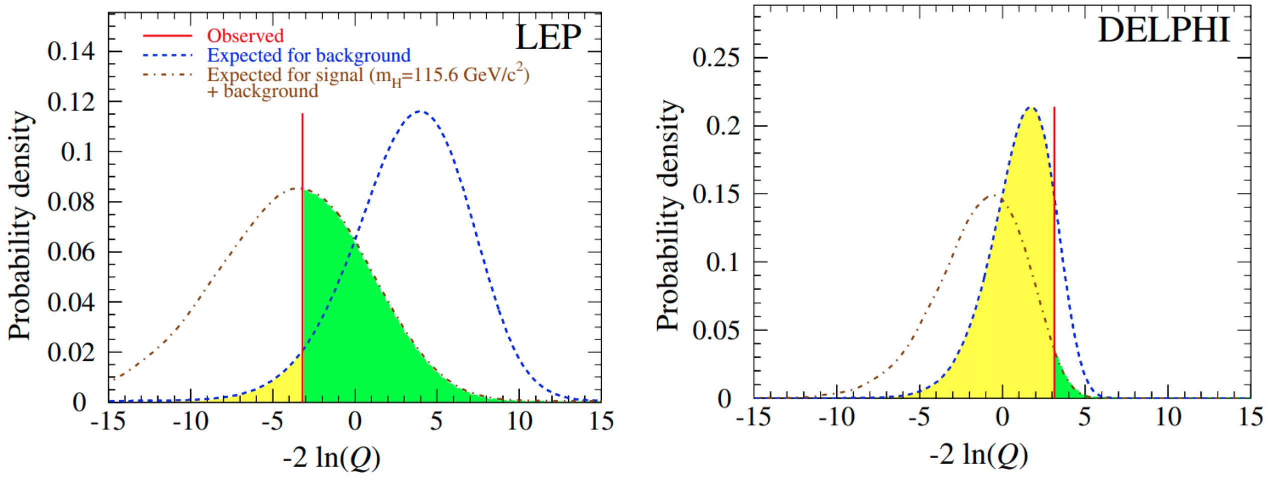

(a) (b)

Figure 2.2: (a) Results from the combined Higgs search with all the four experiments at LEP. Pdfs of the likelihood ratio for background-only hypothesis (blue) and signal+background hypothesis (brown) and observed value (red) are shown. (b) Separate contribution from the DELPHI experiment, where the two hypotheses are less discriminant [17].

2.5 Asymptotic formula for likelihood-based test

The remaining challenge is about how one could acquire the pdf $f(t|H)$ of a given test statistic t under a hypothesis H. Probably the most straightforward way is to generate a sufficient amount of pseudo-experiments (toys) under hypothesis H, with which we obtain a sampling distribution of t. Despite the that toys reflect realistic statistic behavior, however along with the increase of nuisance parameters, regions of interest and complexity of the model, the study can be very time-consuming. Alternatively, the most popular approach is the asymptotic formula for the likelihood-based test from Cowan, Cranmer, Gross and Vitells [15]. The method is based on Wald approximation and Wilks' theorem, which simplify the profile likelihood ratio and demonstrate that it follows a χ^2 law with the degree of freedom of 1.

- **Wald Approximation**:
$$t_\mu = \frac{(\mu - \hat{\mu})^2}{\sigma^2} + \mathcal{O}(1/\sqrt{N}) \tag{2.20}$$
with $\hat{\mu}$ follows a Gaussian distribution with a mean at truth value μ' and standard deviation σ.
- **Wilks' Theorem**: the pdf of t_μ is asymptotically a χ^2 distribution with a degree of 1.
$$t_\mu \sim \chi^2(1) \tag{2.21}$$

As that was fruitfully described in the asymptotic paper [15], only the main conclusions will be introduced in this thesis. The asymptotic paper introduces several powerful test statistics depending on the purpose of the analysis, considering the μ as the tested signal strength, and μ' as the true value associated to a given hypothesis.

2.5.1 Test statistic for the discovery of a positive signal

The purpose is to claim the significance of the discovery of a signal. In this case, H_0 is the background-only hypothesis ($\mu = 0$). The objective is to reject the $\mu = 0$ hypothesis, in presence of a positive signal. For that purpose, the q_0 test statistic is defined:

$$q_0 = \begin{cases} -2\ln\lambda(0) & \hat{\mu} \geq 0, \\ 0 & \hat{\mu} < 0, \end{cases} \tag{2.22}$$

The vanished value for $\hat{\mu} < 0$ is because typically only data with positive signal strength is concerned for discovery[1].
It could be simplified with Wald approximation:

$$q_0 = \begin{cases} \hat{\mu}^2/\sigma^2 & \hat{\mu} \geq 0, \\ 0 & \hat{\mu} < 0, \end{cases} \tag{2.23}$$

with $\hat{\mu}$ follows a Gaussian distribution centered at μ' and with a standard deviation σ.
The asymptotic pdf of q_0 under hypothetical value μ' is

$$f(q_0|\mu') = \left(1 - \Phi\left(\frac{\mu'}{\sigma}\right)\right)\delta(q_0) + \frac{1}{2}\frac{1}{\sqrt{2\pi}}\frac{1}{q_0}\exp\left[-\frac{1}{2}\left(\sqrt{q_0} - \frac{\mu'}{\sigma}\right)^2\right] \tag{2.24}$$

---

[1] Search for enhancement simplifies the problem, but deficit can be also adapted.

where $\Phi(\frac{\mu'}{\sigma})$ is the cumulative distribution function (cdf) of a normal random variable, $\delta(q_0)$ is a delta function at 0.
The corresponding cdf of q_0 is in a clear form as

$$F(q_0|\mu') = \Phi(\sqrt{q_0} - \frac{\mu'}{\sigma}) \tag{2.25}$$

The median of q_0 is thus equal to $(\frac{\mu'}{\sigma})^2$, corresponding to an observed $\hat{\mu} = \mu'$.
For the special case of the null hypothesis with $\mu' = 0$, it's simply

$$f(q_0|0) = \frac{1}{2}\delta(q_0) + \frac{1}{2}\frac{1}{\sqrt{2\pi}} \exp\left(-\frac{q_0}{2}\right) \tag{2.26}$$

$$F(q_0|0) = \Phi(\sqrt{q_0}) \tag{2.27}$$

where the pdf $f(q_0|0)$ is just a sum of a delta function and a χ^2 distribution with 1 degree of freedom, with half weight per each.
As presented by the light blue area in Fig. 2.3, for a given observed q_0, the p-value for the null hypothesis is

$$\text{p-value} = 1 - F(q_0|0) = 1 - \Phi(\sqrt{q_0}) \tag{2.28}$$

which corresponds to an observed significance of

$$Z = \Phi^{-1}(1 - \text{p-value})) = \sqrt{q_0} \tag{2.29}$$

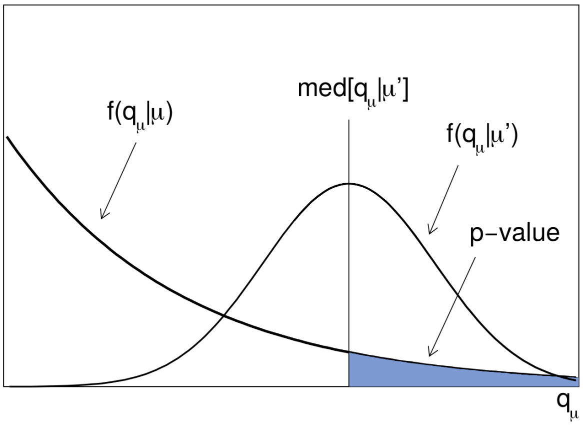

Figure 2.3: Illustration of p-value corresponding to the median of q_μ assuming a signal strength μ' [15].

One may notice that the observed significance can be sensitive to statistical fluctuation in data, therefore, a reference value is favoured for the reliable test, which is given by the expected significance. The expected value is determined by assuming data behaves exactly as the alternative hypothesis μ' (typically $\mu' = 1$). Thanks to the asymptotic formula, it's easy to deduce that there is a one-to-one mapping between the quantile of pdf of $\hat{\mu}$ and the quantile of pdf of q_0, between the quantile of pdf of q_0 and the one of pdf of

Z. According to Eq. 2.23 and Eq. 2.29, Z follows a normal distribution with a lower boundary at 0, that under the assumption of μ':

$$\mathrm{med}[Z|\mu'] = \frac{\mu'}{\sigma} \tag{2.30}$$

$$Z(\mu' + N\sigma) = \mathrm{med}[Z|\mu'] + N \tag{2.31}$$

$$Z(\mu' - N\sigma) = \max\big(\mathrm{med}[Z|\mu'] - N, 0\big) \tag{2.32}$$

where $\mathrm{med}[Z|\mu']$ is the median expected significance, $[Z(\mu' - N\sigma), Z(\mu' + N\sigma)]$ is the expected $N\sigma$ band of significance.

2.5.2 Test statistic for signal upper limit setting

The purpose is to derive a limit interval of μ such that the coverage probability for the truth value is equal to a given confidence level. For a typical limit setting, the null hypothesis is the S+B hypothesis with positive signal strength μ, and the alternative is the b-only hypothesis. An alternative test statistic $\tilde{q}_\mu$ is recommended

$$\tilde{q}_\mu = \begin{cases} -2\ln\frac{\mathcal{L}(\mu,\hat{\hat{\theta}}(\mu))}{\mathcal{L}(0,\hat{\hat{\theta}}(0))} & \hat{\mu} \le 0, \\ -2\ln\frac{\mathcal{L}(\mu,\hat{\hat{\theta}}(\mu))}{\mathcal{L}(\hat{\mu},\hat{\theta})} & 0 < \hat{\mu} \le \mu, \\ 0 & \hat{\mu} > \mu, \end{cases} \tag{2.33}$$

Since the objective to derive an upper limit after observing a measurement $\hat{\mu}$, the region of interest corresponds to the values of μ higher than $\hat{\mu}$. This is the reason why the test statistic vanishes when $\hat{\mu} > \mu$. The Wald approximation simplifies the statistic as:

$$\tilde{q}_\mu = \begin{cases} \frac{\mu^2}{\sigma^2} - \frac{2\mu\hat{\mu}}{\sigma^2} & \hat{\mu} < 0, \\ \frac{(\mu-\hat{\mu})^2}{\sigma^2} & 0 < \hat{\mu} \le \mu, \\ 0 & \hat{\mu} > \mu, \end{cases} \tag{2.34}$$

With the same principle as q_0, the pdf of $\tilde{q}_\mu$ under hypothetical value μ' is

$$\begin{aligned} f(\tilde{q}_\mu|\mu') &= \Phi(\frac{\mu'-\mu}{\sigma})\delta(\tilde{q}_\mu) \\ &+ \begin{cases} \frac{1}{2\sqrt{2\pi\tilde{q}_\mu}}\exp\left[-\frac{1}{2}\left(\sqrt{\tilde{q}_\mu} - \frac{\mu-\mu'}{\sigma}\right)^2\right] & 0 < \tilde{q}_\mu \le \mu^2/\sigma^2, \\ \frac{1}{\sqrt{2\pi}(2\mu/\sigma)}\exp\left[-\frac{1}{2}\frac{\left(\tilde{q}_\mu - (\mu^2-2\mu\mu')/\sigma^2\right)^2}{(2\mu/\sigma)^2}\right] & \tilde{q}_\mu > \mu^2/\sigma^2, \end{cases} \end{aligned} \tag{2.35}$$

One obvious feature is that the data in favor of a smaller $\hat{\mu}$ holds a larger $\tilde{q}_\mu$ value. Specifically, the delta function $\delta(\tilde{q}_\mu)$ corresponds to the case when $\hat{\mu} > \mu$, the second piece with $0 < \tilde{q}_\mu \le \mu^2/\sigma^2$ is mapped to $0 < \hat{\mu} \le \mu$, and the last piece is referring to negative $\hat{\mu}$, which leads to an enhanced tail at a large value of $\tilde{q}_\mu$.

The corresponding cdf of $\tilde{q}_\mu$ under hypothetical value μ' is

$$F(\tilde{q}_\mu|\mu') = \begin{cases} \Phi(\sqrt{\tilde{q}_\mu} - \frac{\mu-\mu'}{\sigma}) & 0 \le \tilde{q}_\mu \le \mu^2/\sigma^2, \\ \Phi(\frac{\tilde{q}_\mu - (\mu^2-2\mu\mu')/\sigma^2}{2\mu/\sigma}) & \tilde{q}_\mu > \mu^2/\sigma^2. \end{cases} \tag{2.36}$$

Using the mapping between $\hat{\mu}$ and $\tilde{q}_\mu$, the cdf can be reformulated in the function of $\hat{\mu}$:

$$F(\tilde{q}_\mu(\hat{\mu})|\mu') = \Phi(\frac{\mu' - \hat{\mu}}{\sigma}) \tag{2.37}$$

For typical positive signal hypothesis $\mu' \geq 0$, the median of $\tilde{q}_\mu$ is equal to $(\frac{\mu-\mu'}{\sigma})^2$.
For the special case of $\mu = \mu'$, the pdf and the cdf are:

$$f(\tilde{q}_\mu|\mu) = \frac{1}{2}\delta(\tilde{q}_\mu) + \begin{cases} \frac{1}{2\sqrt{\pi\tilde{q}_\mu}} \exp\left(-\tilde{q}_\mu/2\right) & 0 < \tilde{q}_\mu \leq \mu^2/\sigma^2, \\ \frac{1}{\sqrt{2\pi}(2\mu/\sigma)} \exp\left[-\frac{1}{2}\frac{(\tilde{q}_\mu+\mu^2/\sigma^2)^2}{(2\mu/\sigma)^2}\right] & \tilde{q}_\mu > \mu^2/\sigma^2, \end{cases} \tag{2.38}$$

$$F(\tilde{q}_\mu|\mu) = \begin{cases} \Phi(\sqrt{\tilde{q}_\mu}) & 0 < \tilde{q}_\mu \leq \mu^2/\sigma^2, \\ \Phi(\frac{\tilde{q}_\mu+\mu^2/\sigma^2}{2\mu/\sigma}) & \tilde{q}_\mu > \mu^2/\sigma^2, \end{cases} \tag{2.39}$$

For limit setting based on the CL$_s$ method, denoting $H_0 = \mu$ and $H_1 = \mu'$, with an observed test statistic $\tilde{q}_\mu$, the CL_s value is accordingly:

$$\mathrm{CL}_s = \frac{\mathrm{CL}_{s+b}}{\mathrm{CL}_b} = \frac{1 - F(\tilde{q}_\mu|\mu)}{1 - F(\tilde{q}_\mu|\mu')} \tag{2.40}$$

Presumably, when μ is close to μ', CL$_s$ is close to 1, that the null hypothesis μ is not excluded. As the tested μ varies far away from μ', the value of CL_{s+b} decreases more rapidly than CL_b, subsequently for a given confidence level $1 - \alpha$, the exclusion will be made when a hypothetical μ gives CL$_s \leq \alpha$.

Similar to the expected significance, the expected limit can be calculated within the same principle. Under an assumption of μ', the N-th quantile of pdf of $\hat{\mu}$ is bijective to minus N-th quantile of pdf of $\tilde{q}_\mu$, and bijective to N-th quantile of pdf of the upper limit $\mu_{\mathrm{up}+N}$. According to Eq. 2.37 and Eq. 2.40, $\mu_{\mathrm{up}+N}$ satisfies the relationship:

$$\mathrm{CL}_s(\mu_{\mathrm{up}+N}) = \frac{1 - \Phi\left(\frac{\mu_{\mathrm{up}+N}-\hat{\mu}}{\sigma}\right)}{1 - \Phi\left(\frac{\mu'-\hat{\mu}}{\sigma}\right)} \equiv \alpha \tag{2.41}$$

$$\text{with } \hat{\mu} = \mu' + N\sigma$$

$$\Rightarrow \mathrm{CL}_s(\mu_{\mathrm{up}+N}) = \frac{1 - \Phi\left(\frac{\mu_{\mathrm{up}+N}-\mu'}{\sigma} - N\right)}{\Phi(N)} \equiv \alpha \tag{2.42}$$

$$\Rightarrow \mu_{\mathrm{up}+N} = \mu' + \sigma\left(\Phi^{-1}\left(1 - \alpha\Phi(N)\right) + N\right) \tag{2.43}$$

In practice, the wildly studied situation is the limit when assuming the b-only hypothesis, i.e. $\mu' = 0$, thus

$$\mu_{\mathrm{up}+N} = \sigma\left(\Phi^{-1}\left(1 - \alpha\Phi(N)\right) + N\right) \tag{2.44}$$

One caveat is that this formula is based on the parabolic likelihood assumption, however for a realistic test, this is not always held, often one needs to run over different values of μ to construct a CL$_s$ scan for different quantile of the alternative hypothesis pdf $f(\tilde{q}_\mu|\mu')$, and obtain the expected limit and its variance bands as the intersection to the threshold α.

Asimov data for expected results

For determination of the expected results, the so-called Asimov data is studied. As one may notice, the remaining missing material of a test with asymptotic formula is the standard deviation σ for $\hat{\mu}$. And the Asimov data provides an estimation. Consider a signal region with $\mu' S(\boldsymbol{\theta_s})$ expected signal and $B(\boldsymbol{\theta_b})$ expected background, an observable x is chosen to be the discriminator and its pdf for signal and background are respectively $f_s(x;\boldsymbol{\theta_s})$ and $f_b(x;\boldsymbol{\theta_b})$, where $\boldsymbol{\theta_s}$ and $\boldsymbol{\theta_b}$ are nuisance parameters. The Asimov data is a binned dataset for which each bin yields exactly the same events as the model prediction. Suppose a histogram $\boldsymbol{n} = (n_1, ..., n_N)$ arranged in x stores the Asimov data, the histogram values n_i are defined as

$$n_i = \mu' S_i(\boldsymbol{\theta_s}) + B_i(\boldsymbol{\theta_b}) \tag{2.45}$$

where $S_i(\boldsymbol{\theta_s})$ and $B_i(\boldsymbol{\theta_b})$ are respectively the expectation values of signal and background in i-th bin of x:

$$S_i(\boldsymbol{\theta_s}) = S(\boldsymbol{\theta_s}) \cdot \int_{\text{bin } i} f_s(x;\boldsymbol{\theta_s}) dx, \tag{2.46}$$

$$B_i(\boldsymbol{\theta_b}) = B \cdot \int_{\text{bin } i} f_b(x;\boldsymbol{\theta_b}) dx \tag{2.47}$$

Therefore, the model consists of one parameter of interest μ' and nuisance parameters $(B, \boldsymbol{\theta_s}, \boldsymbol{\theta_b})$.
In practice, for a pure frequentist approach, the Asimov data should also involve the auxiliary observations $\boldsymbol{\theta_0}$ which are defined as the same values of $\boldsymbol{\theta}$ in the definition of n_i. Presumably, if fitting the model with the Asimov data, the inferred parameters will exactly equal to the same values as those used for generation.

$$\hat{\mu} = \mu', \tag{2.48}$$

$$\hat{B} = B, \hat{\boldsymbol{\theta}}_{\boldsymbol{s}} = \boldsymbol{\theta_s}, \hat{\boldsymbol{\theta}}_{\boldsymbol{b}} = \boldsymbol{\theta_b} \tag{2.49}$$

In order to estimate the standard deviation of the estimator $\hat{\mu}$, the classical way is passing to the Fisher information. While thanks to the asymptotic formula, the profile likelihood ratio t_μ is simply written as $t_\mu = \frac{(\mu - \hat{\mu})^2}{\sigma^2}$. Accordingly, the estimate of σ is given by

$$\sigma_A^2 = \frac{(\mu - \mu')^2}{t_{\mu,A}} \tag{2.50}$$

where $\hat{\mu} = \mu'$ by definition of Asimov data, $t_{\mu,A} = -2 \ln \lambda_A(\mu)$ is the profile likelihood ratio computed with the Asimov data.

One important point is about the validity of the asymptotic formula. The approach has its successful and powerful usage to ease the definition of the pdf of likelihood-based statistic and the calculations of the p-value. Still, one needs to pay attention to when the Gaussian approximation would potentially fail in case of low number of events. In order to justify the accuracy of the asymptotic results, usually toy MC is proposed, by generating pseudo-experiments to obtain a more realistic pdf of the test statistic. According to Ref. [15], the asymptotic approximation remains to have good description with at least five events.

The asymptotic formula is a useful and powerful approach for hypothesis testing, it significantly eases the implementation and stays with its validity in most practical cases. On the other hand, pseudo-experiments (toys) preserve their reliability once the asymptotic formula becomes risky in situations with few events. For this thesis, the toy-based test is implemented for the $HH \to b\bar{b}\gamma\gamma$ analysis for the limit setting, which will be introduced in Ch. 4.

2.6 Data Combination

Once several results are available for a given interesting physics parameter, a combination of these results can be used to further improve the accuracy of the measurement. The best way is to combine the original data of each result, using a likelihood-based method, which includes the full data information and the correlations of the systematic uncertainties. This corresponds to the case of the Higgs mass combination using the $H \to \gamma\gamma$ and $H \to ZZ^* \to 4l$ data as shown in Fig. 2.1. However, combining the full likelihoods can be a lot of work and sometimes unfeasible, in particular when combining across different experiments. In the following, other methods for data combination are introduced.

In the simple case of uncorrelated measurements, the least square method can be used for combination. Assuming n measurements $y_i \pm \sigma_i$ for a physical quantity y, the combination corresponds to one which minimizes the least square defined as

$$\chi^2(y) = \sum_i \left(\frac{y - y_i}{\sigma_i} \right)^2 \tag{2.51}$$

The combined value $\hat{y}_{\text{comb}}$ is expressed as a weighted average of every single measurement:

$$\hat{y}_{\text{comb}} = \frac{\sum_i w_i y_i}{\sum_i w_i} \tag{2.52}$$

where the weights w_i are obtained by minimizing the $\chi^2(y)$

$$w_i = \frac{1}{\sigma_i^2} \tag{2.53}$$

Hence the combined uncertainty σ_{comb} satisfying the relationship

$$\frac{1}{\sigma_{\text{comb}}^2} = \sum_i \frac{1}{\sigma_i^2} \tag{2.54}$$

which is at least as good as the best individual uncertainty.
The method assumes no correlation between the various y_i, i.e. uncorrelated uncertainty, the typical example is when σ_i are the statistical uncertainties. However, when a systematic effect is presented, for instance, when combining two results from two different experiments, combining with only the statistical errors can lead to wrongly estimated combined uncertainty. Also, the presence of systematic uncertainty can induce potential correlation, which is not taken into account by this method.

In the case of correlated measurements, the method of best linear unbiased estimate (BLUE) [18] can be considered, which is interpreted as

- **Best**: smallest variance after combination.
- **Linear**: the combination $\hat{y}_{\text{BLUE}}$ has a linear dependence on the inputs, i.e. $\hat{y}_{\text{BLUE}} = \sum_i w_i y_i$.
- **Unbiased**: the sum of weight w_i is equal to one, i.e. $\sum_i w_i = 1$.

Assuming the measurements y_i is related by a covariance matrix V, hence the variance of the BLUE combination is derived as

$$\sigma^2_{\hat{y}} = \boldsymbol{w}^T \cdot V \cdot \boldsymbol{w} \tag{2.55}$$

where $\boldsymbol{w}$ is the vector of BLUE weights.

The weights can be deduced using the Lagrangian multiplier method, in which the Lagrangian function is constructed as

$$\mathcal{L}(\boldsymbol{w}, \lambda) = \boldsymbol{w}^T \cdot V \cdot \boldsymbol{w} + \lambda \cdot \left(\sum_i w_i - 1 \right) \tag{2.56}$$

where the first term is the combined variance to be minimized, and the second one is the constraint on the sum of weights.

Hence the weights are obtained as

$$w_i = \frac{\sum_j V^{-1}_{ij}}{\sum_{ij} V^{-1}_{ij}} \tag{2.57}$$

where V^{-1} is the inverse matrix of the covariance matrix V.

It is equivalent to minimize the least square function, since the least square estimator reaches the minimum variance band for a linear model:

$$\chi^2(y) = \sum_{ij} (y - y_i)\, V^{-1}_{ij}\, (y - y_j) \tag{2.58}$$

$$\hat{y}_{\text{LSE}} = \sum_i \frac{\sum_j V^{-1}_{ij}}{\sum_{ij} V^{-1}_{ij}} \cdot y_i \tag{2.59}$$

The variance of the BLUE estimator is hence equal to

$$\sigma^2_{\hat{y}} = \left(\sum_{ij} V^{-1}_{ij} \right)^{-1} \tag{2.60}$$

A similar example as Ref. [18] is used to illustrate the simple BLUE combination of two measurements $Y_A = 1.007 \pm \sigma_A$ and $Y_B = 1.005 \pm \sigma_B$ of a single quantity Y, where σ_A and σ_B are respectively the corresponding uncertainties. The covariance matrix V is defined with the correlation ρ between the two uncertainties:

$$V = \begin{pmatrix} \sigma_A^2 & \rho\sigma_A\sigma_B \\ \rho\sigma_A\sigma_B & \sigma_B^2 \end{pmatrix} \tag{2.61}$$

According to the BLUE method, the combination $\hat{Y} = w_A Y_A + w_B Y_B$ are given by

$$w_A = \frac{\sigma_B^2 - \rho\sigma_A\sigma_B}{\sigma_A^2 + \sigma_B^2 - 2\rho\sigma_A\sigma_B} \tag{2.62}$$

$$w_B = \frac{\sigma_A^2 - \rho\sigma_A\sigma_B}{\sigma_A^2 + \sigma_B^2 - 2\rho\sigma_A\sigma_B} \tag{2.63}$$

The combined variance is

$$\sigma^2_{\hat{Y}} = \frac{\sigma^2_A \sigma^2_B (1-\rho^2)}{\sigma^2_A + \sigma^2_B - 2\rho\sigma_A\sigma_B} \tag{2.64}$$

Respectively for the uncertainty ratio $\sigma_B/\sigma_A = 1, 1, 1, 2, 10$, the evolution of w_B, $\sigma^2_{\hat{Y}}/\sigma^2_A$ and $\hat{Y}$ in function of the correlation ρ is shown in Fig. 2.4.

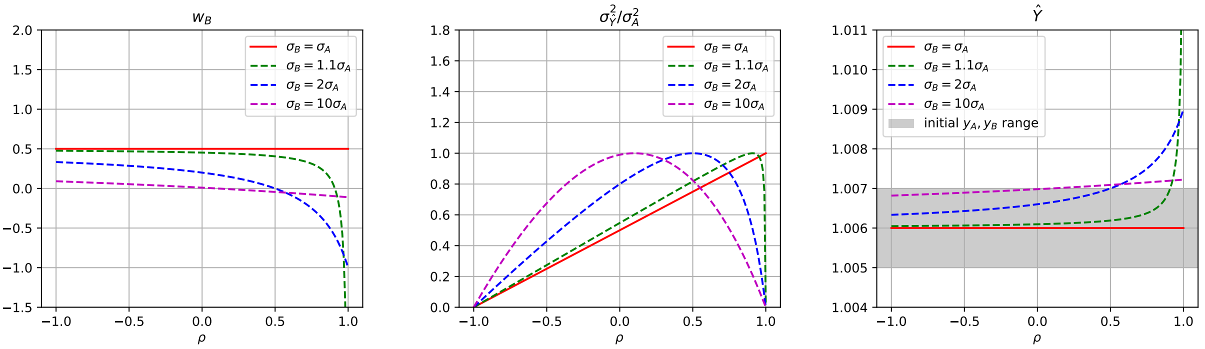

Figure 2.4: Evolution of BLUE weight w_B (left), combined variance normalized to the one of measurement A $\sigma^2_{\hat{Y}}/\sigma^2_A$ (middle), and the BLUE weighted average $\hat{Y}$ (right) as a function of the introduced correlation ρ, for different ratios of σ_B/σ_A. The grey band in the right plot indicates the range $[Y_B, Y_A]$ of the initial measurements before the combination.

The combined variance is bounded up to the lowest one among the initial measurements ($\sigma_{\hat{Y}} \leq \sigma_A$), and the maximum bound is reached when the correlation satisfies $\rho = \sigma_A/\sigma_B$. It also corresponds to the case that w_B is null and the combined $\hat{Y}$ is equal to the Y_A, the one with smaller initial uncertainty. And when $\rho > \sigma_A/\sigma_B$, w_B starts to be negative, and the strong correlation extrapolates the combination to be outside the range of the initial measurements, i.e. $\hat{Y} \notin [Y_B, Y_A]$. For the special case when $\sigma_A = \sigma_B$, the obtained weights are always equal to one half, hence the combined value is centered between the two initial ones.

The BLUE method can also manage the combination of correlated measurements of several physical quantities.
Consider N physical quantities (observables) $X_\alpha = \{X_1, X_2, ..., X_N\}$ with n measurement y_i with covariance V. Each y_i corresponds to the measurement of one of the quantities X_α, and each quantity is measured at least once.

Let's define the identification matrix $\mathcal{U}$, which is a $n \times N$ matrix used to match each y_i to the corresponding quantity:

$$\mathcal{U}_{i\alpha} = \begin{cases} 1, & \text{if } y_i \text{ is a measurement of } X_\alpha \\ 0, & \text{else} \end{cases} \tag{2.65}$$

Subsequently, the least square function is expressed as

$$\chi^2(X) = \sum_{ij}^{n} \left(y_i - \sum_{\alpha}^{N} \mathcal{U}_{i\alpha} X_\alpha \right) V^{-1}_{ij} \left(y_j - \sum_{\alpha}^{N} \mathcal{U}_{j\alpha} X_\alpha \right) \tag{2.66}$$

Then the BLUE estimate of each physical quantity $X\alpha$ is given by

$$\hat{X}_\alpha = \sum_i^n w_{\alpha i} y_i \tag{2.67}$$

where the weights are calculated as

$$w_{\alpha i} = \sum_\beta^N \left(\mathcal{U}^T V^{-1} \mathcal{U}\right)^{-1}_{\alpha\beta} \left(\mathcal{U}^T V^{-1}\right)_{\beta i} \tag{2.68}$$

with $\mathcal{U}^T$ the transpose of the identification matrix, V^{-1} the inverse of the covariance matrix.

The covariance for the BLUE estimates is

$$\operatorname{cov}\left(\hat{X}_\alpha, \hat{X}_\beta\right) = \left(\mathcal{U}^T V^{-1} \mathcal{U}\right)^{-1}_{\alpha\beta} \tag{2.69}$$

The BLUE method is a powerful tool for data combination, which is fast and friendly to be implemented by providing the single measurements and their uncertainties, although it is highly sensitive to the assumptions on correlations, which may be poorly known in practice.

2.7 Conclusion

In this chapter, some basic notations about frequentist statistic have been introduced, including parameter estimation, hypothesis testing, asymptotic formula for likelihood-based test and data combination. These are the crucial elements for the statistical interpretation of most of the analyses.

3 - Experimental Aspects

Benefiting from the high center-of-mass energy at 13 TeV, the Large Hadron Collider (LHC) and ATLAS detector provide a great platform to investigate general physics programs. The experimental setup used in the offline physics analysis is introduced in this chapter including the description of the LHC and the ATLAS experiment.

3.1 Large Hadron Collider

The Large Hadron Collider (LHC) is a proton double-ring superconducting collider integrating the functions of accelerating and colliding particles, located on the border of Switzerland and France. It is the most energetic and powerful collider in the field of particle physics research. Based on the hadron-hadron collisions, there are four main experiments making use of different detectors with different functionalities for different physical goals. The physics goals of the ATLAS and CMS experiments are to improve the understanding of the Standard Model and to search for new physics beyond the Standard Model. After the discovery of the Higgs, another important physics motivation of these experiments is to study the Higgs physics. The main physics goal of the LHCb experiment is to measure the charge and parity (CP) violation and to search for new physics with B hadrons. The main goal of the ALICE experiment is dedicated to heavy-ion physics, for the purpose of studying the physics of strongly interacting matter at an extreme energy density, where a phase of matter called quark-gluon plasma appears.

The construction of the LHC collider [19] uses the tunnel of the previous LEP [20] collider, which is about 26.7 kilometers long and installed about 100 meters underground. The basic structure is shown in Fig. 3.1. The perimeter of the LHC can be divided into eight arcs and eight straight lines, where each arc is about 2.8 kilometers long, and each straight line is about 528 meters long. The straight line area is used to install detectors and control systems. It undertakes the role of hadron beam input and output which is usually called IR (insertion region) or IP (interaction point). The ATLAS and CMS detectors are installed at IP1 and IP5; while IP2 and IP8 are not only installed with the LHCb and ALICE detectors but also serve as injection areas for the two proton beams, one is in a clockwise direction and the other is in a counterclockwise direction; two collimation systems designed to protect the machine from the damaging beam loss are installed at IP3 and IP7; two radio frequency systems (RF) for two beams are installed at IP4, which mainly focus on providing RF power to the beam for acceleration to the highest energy and tightly gathering protons to form proton bunches ensuring the high luminosity at the collision point; IP6 is the beam recovery area called beam dumping system.

The protons needed for the LHC collider are produced with the ionization of hydrogen in a device called Duoplasmatron, where an electrical filed breaks down hydrogen gas into protons and electrons. In order to achieve the target instantaneous luminosity (as will be defined later) of 10^{34} cm^{-2}s^{-1}, the number of protons contained in each bunch N_b is designed to be about 1.15$\times10^{11}$, with a time interval of 25 ns between the adjacent proton bunches, which corresponds to a spatial distance near 3×10^{8}m/s $\times 25 \times 10^{-9}$s $= 7.5$m for protons with 6.5 TeV energy close to the speed of light. In the LHC ring with a circumference of $27\,$km, a maximum of $27 \times 10^3/7.5 = 3600$ proton bunches can be injected. However, in the actual operation, it is necessary to reserve a certain space for the purpose of beam stability, so the number

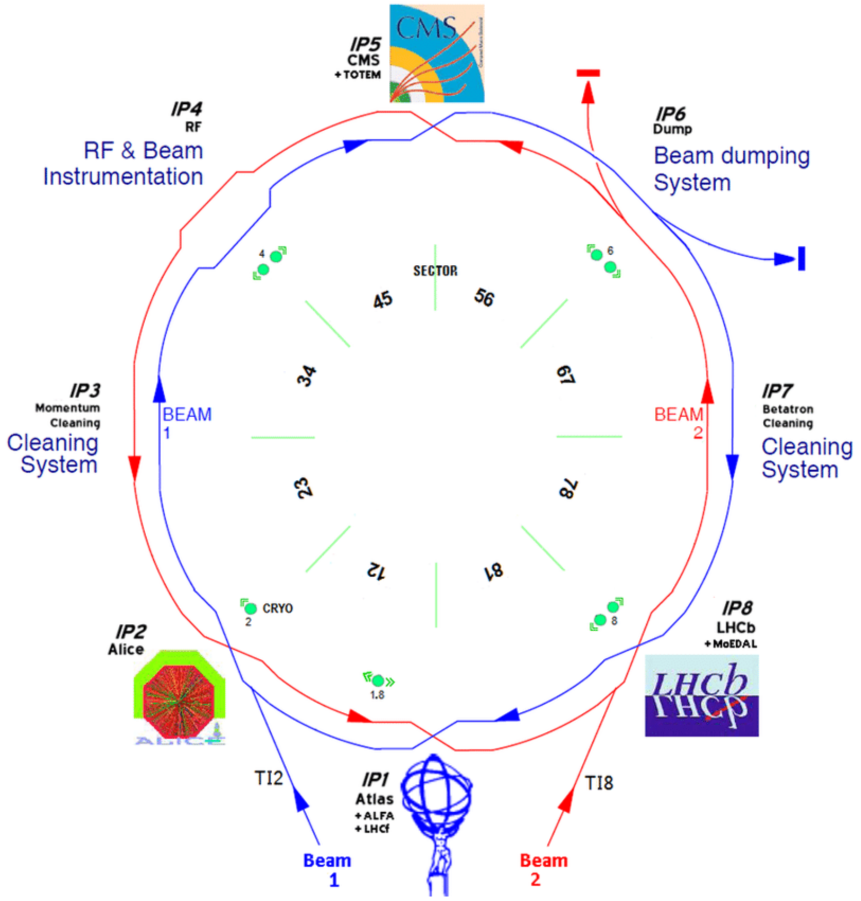

Figure 3.1: Layout of the Large Hadron Collider, including the four main experiments and the two proton rings (red and blue lines). The arrows of the rings indicate the direction of the proton beam.

of proton bunches in each beam is designed to be approximately 2808, and the two proton beams contain $2808 \times 1.15 \times 10^{11} \times 2 \approx 6 \times 10^{14}$ protons in total. A small hydrogen cylinder contains about $5\,\mathrm{kg}$ hydrogen (2500 moles), and the number of hydrogen atoms is $2 \times 2500 \times N_A \approx 3 \times 10^{27}$ (N_A is Avogadro constant). Considering the efficiency of hydrogen ionization of around 70%, and the proton bunches in the LHC ring being filled every 10 hours, then this $5\,\mathrm{kg}$ hydrogen can be theoretically used for $3 \times 10^{27} \times 0.7/(6 \times 10^{14} \times 24 \times 365/10) \approx 4 \times 10^{9}$ years without recycling of the used protons.

Before protons are accelerated and collided in the 27 km LHC ring, they need to pass through several pre-acceleration rings to form a bunch of protons at certain energy:

- Through the RF four-dipole system [21] (QRF), the protons are tightly bunched together to form a proton bunch, and a certain speed is obtained;
- Through the linear accelerator LINAC2, the proton bunches with a certain primary velocity reach an energy of 50 MeV;
- Through the Proton Synchrotron Booster (PSB), the proton bunches reach the energy of 1.4 GeV ;

- Through the Proton Synchrotron (PS), the proton bunches reach the energy of 26 GeV;
- Through the Super Proton Synchrotron (SPS), The proton bunches reach the energy of 450 GeV.

The relative positions of each acceleration system are shown in Fig. 3.2.

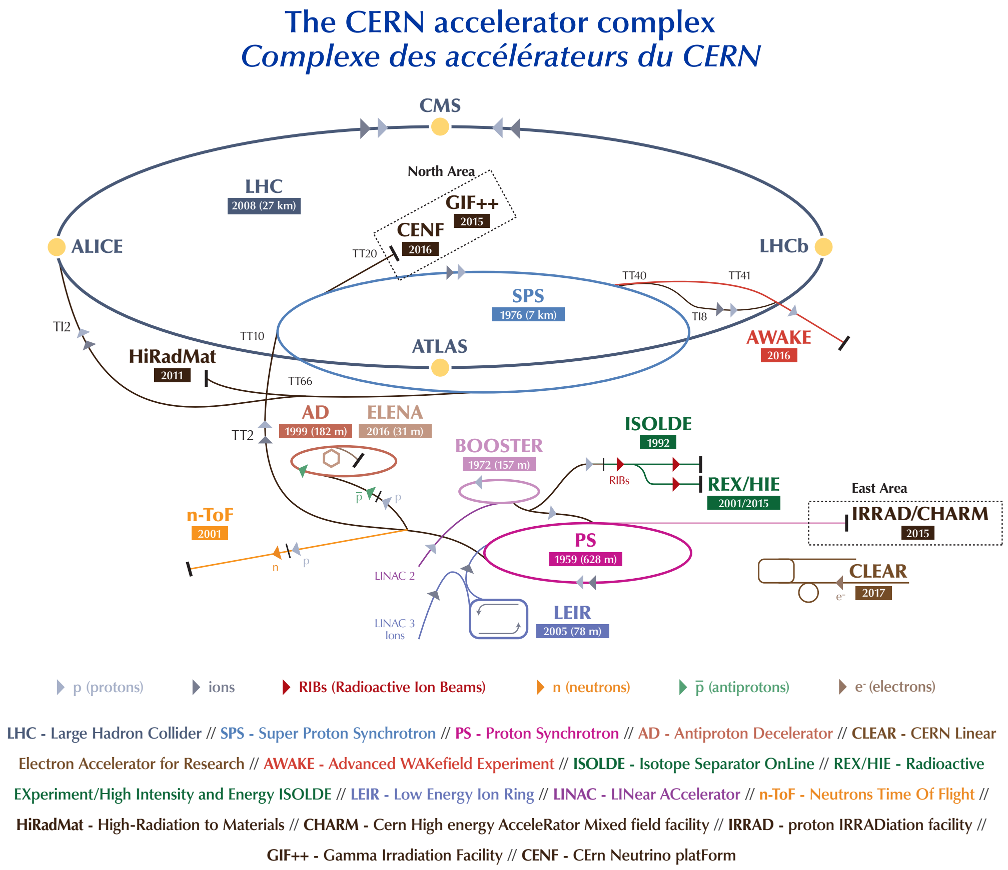

Figure 3.2: An overview of the structure of the accelerator complex at CERN. Protons pass through the linear accelerator LINAC2, the Proton Synchrotron Booster (PSB), the Proton Synchrotron (PS), the Super Proton Synchrotron (SPS), and finally enter the LHC [22].

Such a chain of proton injectors allows the flexibility of the proton bunch structure [23, 24]. The main bunching filling scheme used in LHC Run 2 is the so-called batch-compression-merging-splitting (BCMS) beam with trains of 48 bunches at extraction from the SPS. It starts with 8 bunches in the PSB, which are injected into the PS, where the RF manipulations are performed to merge compress and split the bunches. Pairs of bunches are merged together, following a triple splitting at 2.5 GeV then twice double splitting at 26 GeV extracted from the PS, hence the total number of bunches is $8/2 \times 3 \times 2 \times 2 = 48$. BCMS is the main bunch filling scheme used in Run 2, except in the fall of 2017, where the alternative 8b4e (8 bunches $\oplus$ 4 empty buckets) beams were used mainly to reduce the electron cloud effects.This scheme allows mitigating the electron cloud effect since every 8 bunches are spaced by 4 empty buckets. Different to BCMS, 7 bunches are filled from PSB to PS, which pass a double splitting at 2.5 GeV and then twice double splitting at 26 GeV. Hence the total number for 8b4e is $7 \times 2 \times 2 \times 2 = 56$. A sketch of the BCMS and 8b4e bunch filling schemes is shown in Fig. 3.3.

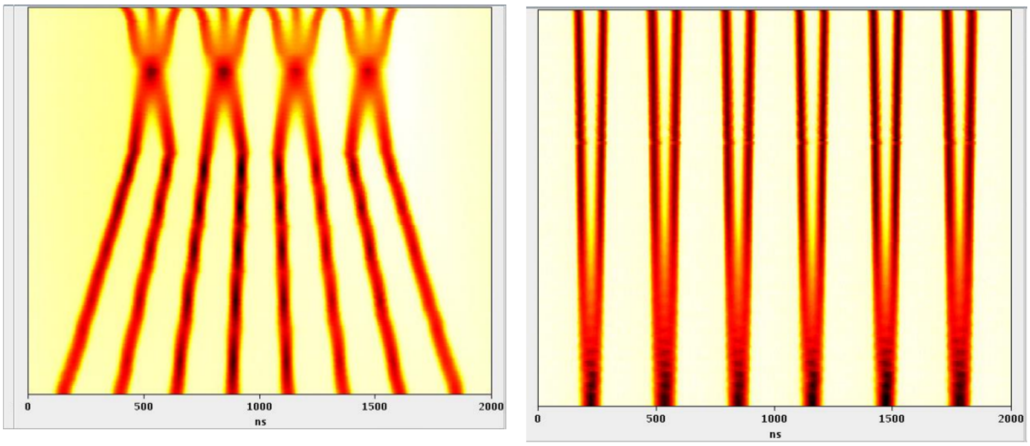

25 ns BCMS

8b4e standard

Figure 3.3: BCMS and 8b4e bunching filling schemes at the LHC. The x-axis represents the bunching spacing time, y-axis shows the bunch evolution from the PSB 1.4 GeV bunches to the 2.5 GeV splitting in PS [23].

In order to make the proton bunches run according to the pre-determined orbit when entering the LHC collider, a magnetic dipole that is used to generate a magnetic field [25]. A total of 1232 magnetic dipoles are installed on the eight arcs of the LHC ring, each dipole is about 14.7 meters long, and its cross section is shown in Fig. 3.4. At $11800\,\text{A}$, these magnetic dipoles can generate a uniform magnetic field of about 8.3 T in the ring, working at a temperature of 1.9 K using superfluid helium. In addition to these dipoles, there are some quadripoles (392) to focus the proton beam, accelerate and stabilize the proton energy, hexapoles to correct the energy-magnetic field dependence, and octopoles to stabilize the cluster are also included. In total, more than 8000 magnetic multipoles are used in the LHC to control the energy and trajectory of the proton bunches in the beam. These magnetic multipoles work at a temperature of about $1.9\,\text{K}$ through a cryostat system, making the proton beams enter the LHC ring and reach the target energy of $6.5\,\text{TeV}$ after about 20 minutes of acceleration. The speed of the protons after the acceleration is close to the speed of light, so each proton bunch has an energy of about 1.29×10^5 J, and each beam has an energy of 360 MJ.

Luminosity (L) is an important quantity to evaluate the performance of the collider machine. Its value is a measurement of the number of collisions per square centimeter per second in the detector. The larger the value of L, the larger the number of collisions. Collision here refers to deep inelastic scattering that creates new particles or new physics processes. The total cross section of pp collisions on the LHC is $110\,\text{mbarns}$, of which the one for the inelastic collisions is $60\,\text{mbarns}$, and the one for elastic collisions are $40\,\text{mbarns}$, the rest corresponds to single diffraction. Luminosity and cross section have the following relationship:

$$N_{\text{event/sec}} = L(t) \cdot \sigma_{\text{event}}, \tag{3.1}$$

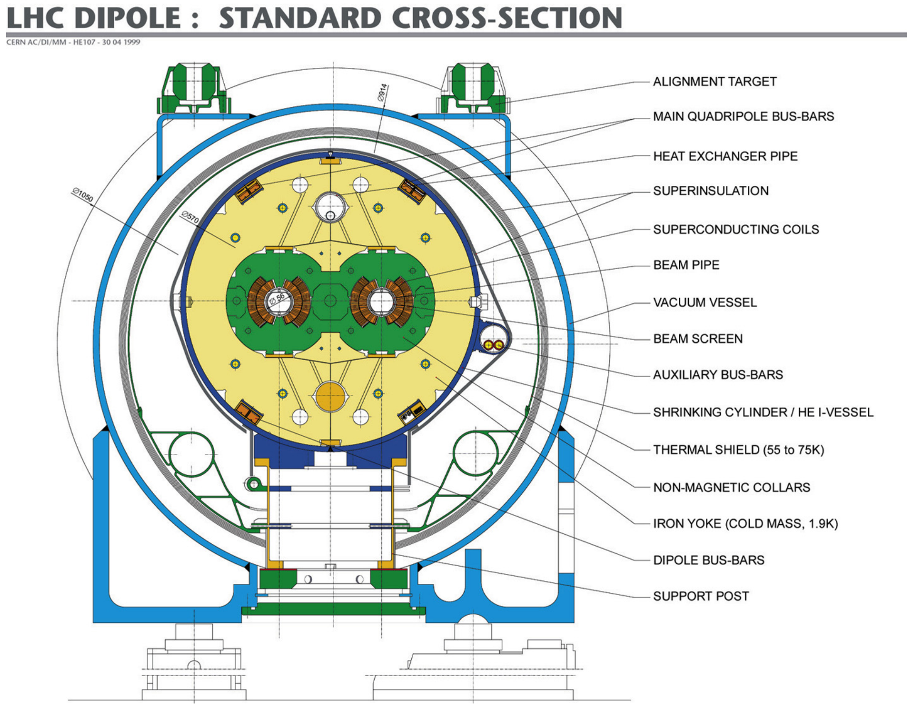

Figure 3.4: Schematic cross section of a magnetic dipole at the Large Hadron Collider [26].

where $L(t)$ is the instantaneous luminosity, with a designed value of $10^{34}\ \mathrm{cm}^{-2}\mathrm{s}^{-1}$ at the LHC, characterized by the beam structures:

$$L = \frac{N_b^2 n_b f_{\text{rev}} \gamma}{4\pi \epsilon_n \beta^*} F, \tag{3.2}$$

with N_b the number of protons in each proton bunch, n_b the number of proton bunch per proton beam, f_{rev} the LHC revolution frequency, γ the Lorentz boost factor, ϵ_n the normalized emittance, β^* the β function at the collision point, and F the geometric luminosity reduction factor derived from the crossing angle between the beams at the interaction point.

The accumulated luminosity is the integral of the instantaneous luminosity within a certain period of time, expressed as

$$\mathcal{L} = \int_{t_0} L(t)\mathrm{d}t. \tag{3.3}$$

At the target luminosity of the LHC, on average, about 20-40 inelastic scattering processes are generated for each collision (up to around 70), which means that the physics processes we are interested in are often accompanied by about 30 other processes. This value is called pileup (PU).

The total luminosity integrated on the LHC running time and the profile of the average pileup are shown for Run 2 (2015-2018) in Fig. 3.5: a total integrated luminosity of 147 fb^{-1} is recorded by ATLAS, which corresponds to a mean number of pileup of around 34.

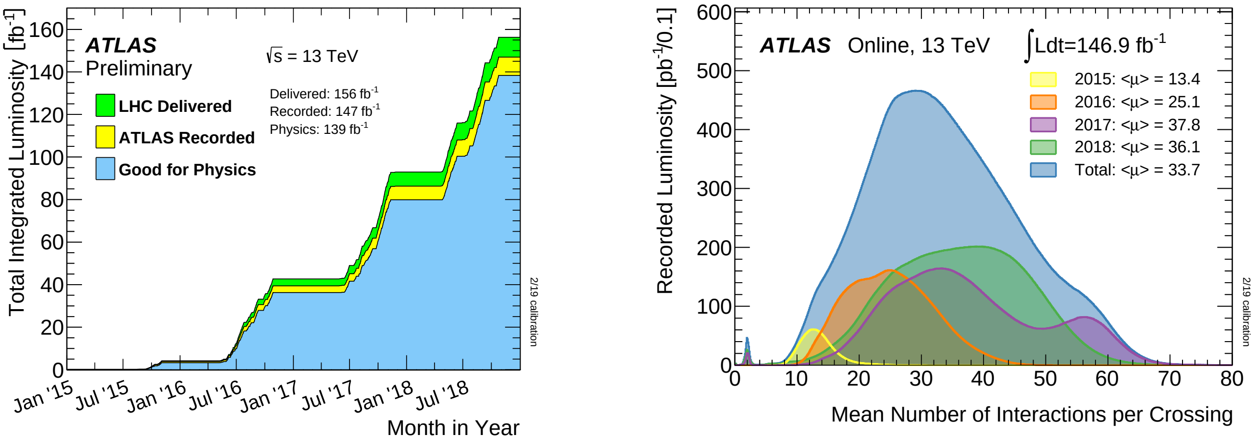

(a) (b)

Figure 3.5: (a) Cumulative luminosity at LHC Run 2. (b) Average interactions per bunch crossing (pileup) for the full Run 2 and individual years [27].

A detailed drawing which shows the past and future evolution of the run conditions in LHC and the so-called high-luminosity LHC (HL-LHC) can be found in Fig. 3.6. The LHC started to work at Run 1 (2010-2012) with a center of mass energy of 7 or 8 TeV, corresponding to a total integrated luminosity of 30 fb^{-1}; The Run 2 (2015-2018) was operated at a higher center of mass energy of 13 TeV and yielded a cumulative luminosity of 156 fb^{-1}; After several upgrades on both accelerators and detectors, the Run 3 has been started from the spring of 2022, which is designed to be running at 13.6 TeV and expected to arrive a cumulative luminosity of 450 fb^{-1}.

After Run 3, in order to further increase the discovery potential, an upgrade project called high-luminosity LHC is proposed to construct a more powerful LHC with a ten times larger luminosity around 3000-4000 fb^{-1}. The HL-LHC will allow more accurate physics measurements and improve the sensitivity to rare events, for instance, the rare decays of the Higgs boson (Higgs boson into light quarks and leptons) and the double Higgs production.

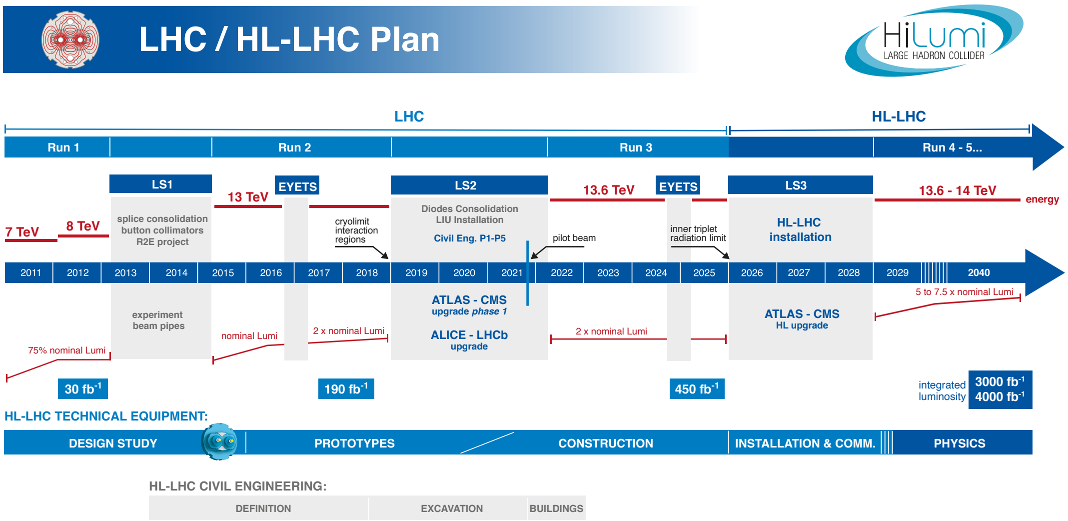

Figure 3.6: LHC/HL-LHC run conditions plan [28].

3.2 ATLAS detector

A Toroidal LHC ApparatuS, abbreviated as ATLAS [29], is one of the general experiments having a high luminosity in the LHC (the other one is CMS), which has multi-physics motivations to exploit the operation of the LHC as much as possible. In order to solve or pave the way for many aspects of the physics projects including the high precision tests of QCD, electroweak interactions, and flavour physics, ranging from measurements of Standard Model parameters to the search of the Beyond Standard Model, the ATLAS detector should meet many strict requirements as follows:

- Require high detector granularity with large acceptance in pseudorapidity with almost full azimuthal angle coverage, fast response of the electronics, and radiation-hard sensors aiming at a large amount of the particle fluxes;
- Require good momentum precision and reconstruction for charged particles, and good position resolution to measure the secondary vertices reconstructed by the vertex detector for offline tagging of τ-leptons and jets from b quark;
- Require an excellent electromagnetic calorimeter to reconstruct and identify the electron and photon with high efficiency, and a full-coverage hadronic calorimeter for accurate jet and missing transverse energy measurements;
- Require accurate muon measurements including good momentum precision over a wide range of momenta and the capability to discriminate the muon charge with high p_{T};
- Require adequate background rejection for objects with low p_{T} to reach high trigger efficiency and to achieve an acceptable trigger rate for interesting physics processes.

The ATLAS detector has a nominally symmetric structure surrounding the interaction point, consisting of different sub-detectors with different functionalities. The overall layout of the ATLAS detector slice is shown in Figure 3.7. The dimensions are 25 m in height and 44 m in length. The total weight of the detector is approximately 7000 tons, where the shielding and magnet systems occupy most of the weight. The magnetic field is 2 T corresponding to the axial direction provided by a solenoid for the inner detector and is about 0.5 and 1 T with toroidal direction provided by a barrel toroid and two endcap toroids for the muon detectors in the central and endcap regions, respectively.

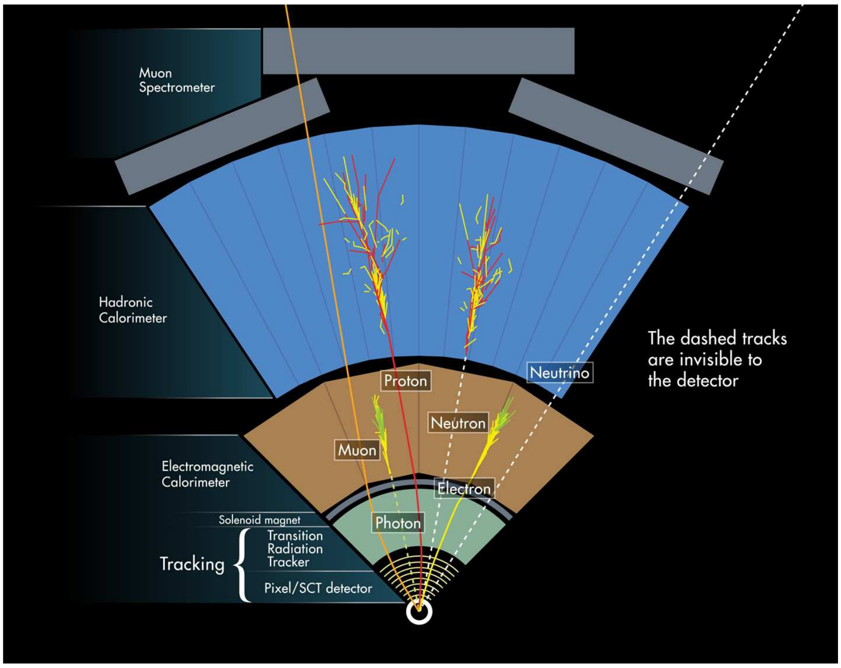

Figure 3.7: Schematic of the profile slice of the ATLAS detector [30].

The x-y-z coordinate can be built in the ATLAS detector system, where the nominal interaction point is defined as the origin of the coordinate and the z-axis is along the beam direction, pointing counter-clockwise. The $x - y$ plane is perpendicular to the z-axis, where the y-axis is upward, and the x-axis corresponds to the direction from the interaction point to the center of the LHC ring.

The azimuth angle ϕ in the polar coordinate system is in the x-y plane where $\phi = 0$ corresponds to the positive direction of the x-axis and $\phi = \frac{\pi}{2}$ corresponds to the positive direction of the y-axis. The polar angle θ is the angle from the z axis. In order to describe the angle between the direction of particle motion and beams, the pseudorapidity $\eta = -\ln\left[\tan\left(\frac{\theta}{2}\right)\right]$ is used. For example, the variation of η is from $+\infty \rightarrow$0, when θ from 0$\rightarrow$ $\frac{\pi}{2}$. More important, in the direction of the beams, the difference of pseudorapidity is Lorentz invariant for massless particles. The rapidity $y = \frac{1}{2}\ln\left(\frac{E+p_z}{E+p_z}\right)$ is also used for massive objects, such as jets, with E and p_z respectively the energy and the longitudinal momentum along the beam axis. The distance ΔR in the pseudorapidity-azimuthal angle space is defined as $\Delta R = \sqrt{\Delta\eta^2 + \Delta\phi^2}$, where $\Delta\eta$ and $\Delta\phi$ are respectively the angular difference in the η and ϕ direction. The widely used variables, such as the transverse momentum p_{T}, the transverse energy E_{T}, and the missing transverse energy $E_{\mathrm{T}}^{\mathrm{miss}}$ are defined in the x-y plane unless specified otherwise.

From inside to outside, the sub-detectors making up the ATLAS detector are the Inner Detector, Electromagnetic Calorimeter, Hadronic Calorimeter, and Muon Spectrometer. These sub-detectors and the magnet and trigger systems are introduced in the following sections.

3.2.1 Inner Detector

The inner detector (ID) is located in the center of the ATLAS detector, that is the nearest to the interaction point, which suffers very large particle fluxes. The main goal of the ID is to measure the tracks left by the charged particles bending in the magnetic field, which are used for momentum measurement and vertex reconstruction. As far as the physics motivations of the ATLAS detector are concerned, the ID needs to guarantee the good precision of the momentum and vertex measurements that are used in the combination of different types of sub-detectors. As shown in Fig. 3.8 and Fig. 3.9, in the inner region with small radii (up to 514 mm) of the ID, silicon pixel layers (Insertable B-Layer and pixel detector) and stereo pairs of silicon microstrip (SCT) layers make use of the discrete space-points to achieve high-resolution pattern recognition capabilities. At larger radii (from 554 mm to 1082 mm) is located the transition radiation tracker (TRT), which includes many layers of gaseous straw tube elements interleaved with transition radiation material. The ID is immersed in a 2 T magnetic field generated by the central solenoid magnets, which extends over a length of 5.3 m with a diameter of 2.5 m.

The Insertable B-Layer (IBL) is closest to the beam pipe where particle collisions occur in the very heart of ATLAS. In fact, it is an additional pixel layer installed in May 2014 during the first time long shutdown prepared for the higher instantaneous and integrated luminosity to maintain and improve the robustness and performance of the ATLAS tracking system. IBL consists of 14 carbon fibre staves whose width and length are respectively 2 cm and 64 cm. The locations of these 14 staves face the beam pipe and are inclined in ϕ by 14°, with a radius of 33.5 mm and coverage of $|\eta| < 3$. In order to satisfy the required radiation tolerance and read-out efficiency in an environment of much intensive hit rate and radiation doses, the new front-end read-out chip, the FE-I4 was developed, which is different from the FE-I3 front-end chip of the Pixel detector. Two types of sensors (planar and 3D) are installed in the IBL as shown in Figure 3.10. In these sensors, a total of 32 FE-I4 read-out chips are equipped, in which 24 FE-I4 read-out chips are bump-bonded to 12 double-chip planar n-in-n sensors and 8 FE-I4 read-out chips are bump-bonded to 8 single-chip 3D sensors. The detailed parameters of the IBL are shown in Tab. 3.1. Taking the stave tilt and the overlap between staves into account, the IBL radiation length averaged over ϕ is estimated to be 1.88% X_0 for tracks produced in the x-y plane at $z = 0$.

By providing more accurate hit information near the interaction point, the mitigation of the effect of the multiple scattering in the detector material on the track extrapolation improves the measurement of the impact parameter resolution in both the transverse (d_0) and longitudinal (z_0) projections, which is particularly important for the tagging of jets from b-quark, in which the long lifetime B meson usually leaves a displaced vertex. On the other hand, the smaller pixel pitch of the IBL in the longitudinal direction contributes to the resolution in z_0 throughout a pretty complete p_{T} range.

Outside the IBL, there are the pixel and SCT trackers comprising many layers of silicon pixels and strips, covering the region $|\eta| < 2.5$. In the barrel region, they are arranged on concentric cylinders around the

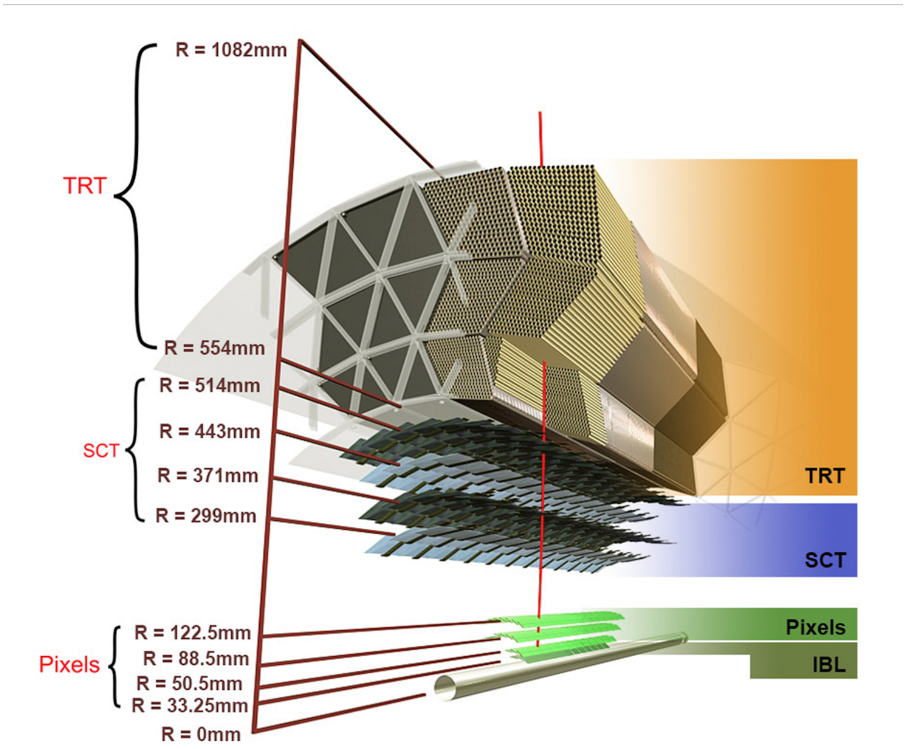

Figure 3.8: Layout of the Inner Detector in the ATLAS [31].

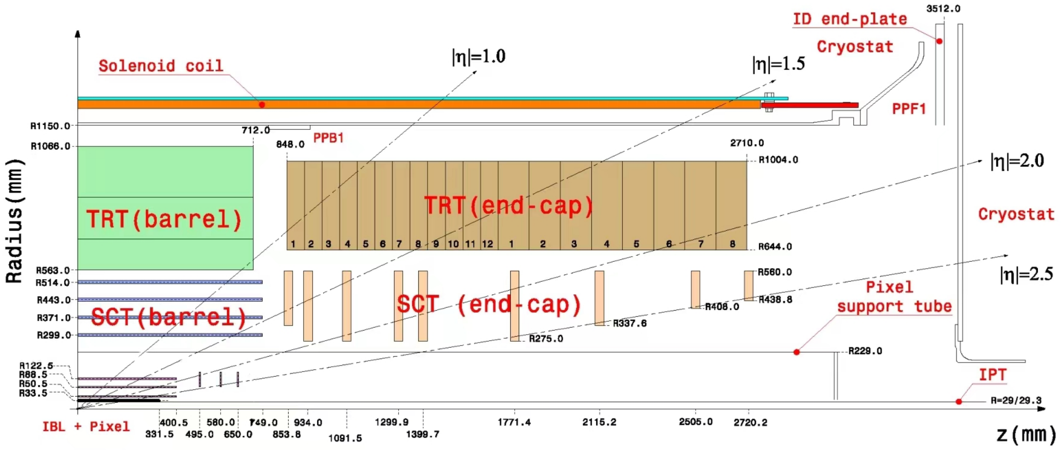

Figure 3.9: Layout of the ATLAS inner tracking detector position. According to the position in the pseudorapidity, the various ID components are divided into a barrel and two endcaps regions. [32].

z-axis (beam direction) while in the endcap regions they are located on disks perpendicular to the z-axis. There are 1744 sensors in the pixel detector and every sensor is made up of 47232 pixels with a pitch of

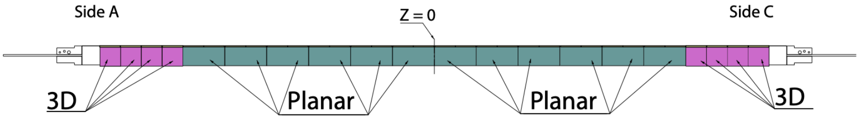

Figure 3.10: Longitudinal layout of planar and 3D modules on a stave for the IBL[32].

Item	Value
Number of staves	14
Number of physical modules per stave	20 (12 planar, 8 3D)
Number of FEs per stave	32
Coverage in η, no vertex spread	$\lvert\eta\rvert$ <3.0
Coverage in η, 2σ (122 mm) vertex spread	$\lvert\eta\rvert$< 2.58
Active $\lvert z\rvert$ stave length (mm)	330.15
Stave tilt in ϕ (degree)	14
Overlap in ϕ (degree)	1.82
Center of the sensor radius (mm)	33.5

Table 3.1: Main layout parameters for the IBL detector [32].

50 μm in the R-ϕ direction and 400 μm in the z direction, which corresponds to a total of 46080 readout channels. There are 4088 sensors in the SCT tracker where 2112 of them are in the barrel with 80 μm pitch micro-strip and the remaining 1976 are in the endcaps with a variable pitch of 70 μm to 95 μm, which leads to 6.2 million readout channels. The pixel tracker consists of 3 cylindrical layers in barrel and 2×3 disks in the two endcaps regions, and the SCT involves 4 cylindrical layers in barrel and 2×9 disk in endcap.

Outside the pixel and SCT trackers, the TRT detector, containing polyimide drift (straw) tubes of 4 mm diameter filled with a Xe/CO_2/O_2 gas mixture (in design condition), is installed up to $|\eta| = 2.0$. The TRT contains up to 73 layers of straws interleaved with fibres (barrel) and 160 straw planes interleaved with foils (end-cap). The barrel TRT is divided into three rings of 32 modules each. The TRT endcaps each consist of two sets of independent wheels with 12 and 8 wheels from inside to outside.

All tracks with $|\eta| < 2.5$ are measured with six precision space-points and about 36 straws, except for a slight degradation across the barrel to the endcap transition region $(0.8 < |\eta| < 1.0)$ with $p_{\mathrm{T}} > 0.5$ GeV, where this number decreases to a minimum of 22 crossed straws. The total number of TRT readout channels is approximately 351000. Although the precision is lower than the inner pixel and SCT, with the largely increased number of hits and longer measured track length, the TRT also contributes significantly to the momentum measurements. The particular function of the TRT is to enhance the electron identification by the detection of transition radiation photons in the straw tubes, which allows discriminating between electrons and charged pions [33].

3.2.2 LAr Electromagnetic Calorimeter

The essential objective of the electromagnetic calorimeter (ECAL) is to measure the total energy of electrons and photons, part of the energy of jets and contribute to the particle identification and the measurement of $E_{\mathrm{T}}^{\mathrm{miss}}$. The measurement is based on the electromagnetic interactions with dense matters, that generates electromagnetic showers as cascades of electrons and photons produced in the calorimeter. The measured energy is then used to reconstruct the particle decaying to an electron or a photon. For instance, the processes relevant to the Higgs boson $H \to \gamma\gamma$ and $H \to ZZ$ in which at least one of the Z bosons decays to dielectron, are very important to characterize the production and decay of the Higgs boson. Therefore, the accuracy of basic quantities measurement of these elementary particles is important to reach the goods of the ATLAS experiment.

In general, the segmentation of the ECAL should be as fine as possible, the typically achieved energy resolution has to reach the level of $\Delta E/E = 11.5\%/\sqrt{E} \oplus 0.5\%$ (E in GeV) and the resolution on the polar direction of a shower should meet the requirement of $\Delta\theta = 50\,\mathrm{mrad}/\sqrt{E}$ (E in GeV).

The energy measurement of e/γ exploits the characteristic interaction with the material of the detector constituting the key to detection and identification. When particles pass through the detector, four main kinds of electromagnetic interaction could happen: interaction with atomic electrons, interaction with the atomic nucleus, and two long-range collective effects, Cherenkov and transition radiations. Interactions with atomic electrons lead to ionization and excitation, and interactions with the nucleus lead to Compton scattering, bremsstrahlung, and pair production (for photons). Mostly, the principal source of energy loss for electrons and photons with energy of more than several MeV is the bremsstrahlung and pair production, respectively. Through these interactions, one incoming particle can produce many secondary and tertiary particles which are called particle showers. Fig. 3.11 illustrates the electromagnetic shower development for an incoming electron, which is similar to the shower development for incoming photons.

The shower composition and dimension depend on the particle type and the detector material. The radiation length X_0 is usually used to estimate longitudinal shower length. The definition is the length that an electron passes through when the electron energy is 1/e of its primary energy:

$$\frac{dE}{dX} = -\frac{E}{X_0} \tag{3.4}$$

For photons, the mean free path is 9/7 X_0, over which the probability of converting a photon into a e^+e^- pair is 1-1/e and the probability of not converting is 1/e.

The radiation length depends on the properties of material, and satisfying the following relationship for material with a given atomic number Z and mass number A:

$$X_0 = \frac{716.4A}{Z(Z+1)\ln(287/\sqrt{Z})}\ \mathrm{g}\cdot\mathrm{cm}^{-2} \tag{3.5}$$

The shower development continues until the critical energy E_c, below which the dominating process is ionization. Hence for an electron with initial energy E_0, the maximum longitudinal shower depth is given by

$$X = X_0 \frac{\ln(E_0/E_c)}{\ln 2} \tag{3.6}$$

The shower depth increases logarithmically with initial energy E_0 and linearly with radiation length X_0. The crucial energy E_c is basically decreasing with the increase of atomic number Z.

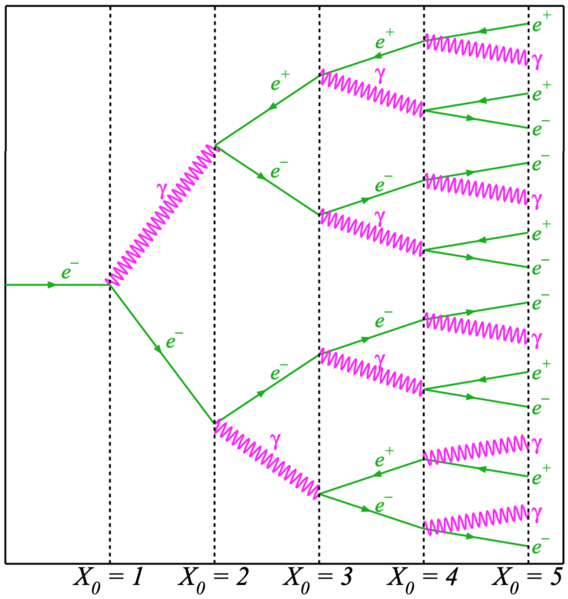

Figure 3.11: Electromagnetic shower development for a high-energetic electron in radiation length X_0 [34].

With the electron continuously losing its energy, the effect of the Coulomb scattering becomes dominant which leads to the shower expanding in the transverse dimension. The Molière Radius R_M is used to estimate the transverse shower length. By definition, it is the radius of a cylinder containing on average 90% of the shower's energy deposition. Two Molière radii contain 95% of the shower's energy deposition. It is related to the X_0 by the approximate relation:

$$R_M = 0.0265 X_0 (Z + 1.2) \tag{3.7}$$

The X_0 and R_M are related to the intrinsic characteristic of the detector material. A smaller X_0 means strong stopping power and fully energy deposition. A smaller R_M represents better shower position resolution and better shower separation due to a smaller degree of shower overlaps. Tab. 3.2 shows the values of X_0, R_M, and E_c for different materials, where lead shows an excellent radiation length and small Molière Radius, hence it is chosen as the dense material in the ATLAS ECAL.

The ATLAS ECAL is a sampling calorimeter consisting of plates of dense, passive material alternating with layers of sensitive material. The whole calorimeter is globally divided into four main layers (Fig. 3.12), with one Presampler layer in front of the three accordion-like layers which contain most of the EM shower.
In front of the accordion, a thin Presampler (PS) detector is suited in the range of $|\eta| < 1.8$ for correcting energy losses due to the upstream material from ID, solenoid magnets, cryostats, cables, etc.). The PS is a 1 cm (5 mm) liquid argon (LAr) active layer instrumented with electrodes roughly perpendicular (parallel) to the beam axis in the barrel (endcap). The PS plays a very important role in the transition region of $1.37 < |\eta| < 1.52$ between the two cryostats, due to the impact of more material in front of the calorimeter. Above $|\eta| = 1.8$, the PS is no longer necessary given the limited amount of dead material and the higher

material	X_0/cm	R_M/cm	E_c/MeV
Cu	1.43	1.5	24.8
Pb	0.56	1.6	9.51
Liquid Ar	14.2	9.5	30.5
Fe	1.76	1.7	21
Plastic	42.9	-	100

Table 3.2: X_0, R_M, and E_c for different materials.

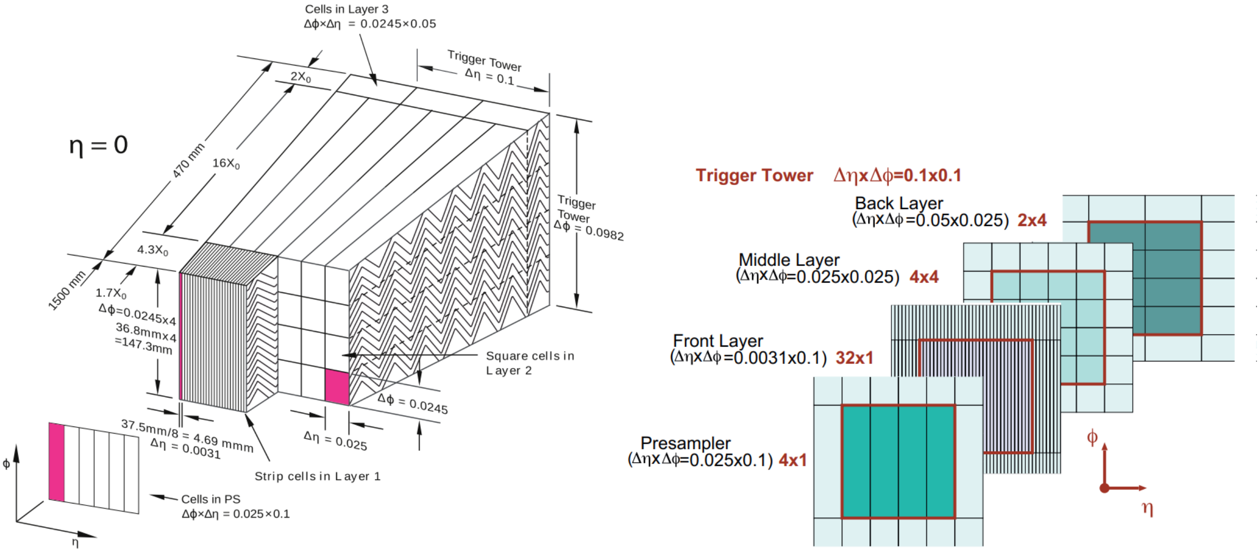

Figure 3.12: Schematic representation of the ATLAS liquid argon calorimeter (left). The segmentation of the super-cells of the EM calorimeter (right) [35].

energy of particles for a given p_{T}. The PS is made of 32 sectors in ϕ, and two sectors are fixed to one calorimeter module.

The main body of ECAL is installed behind the PS, for which the lead is used as the dense and passive absorber because of its large atomic number and density, and the liquid argon (LAr) is used as the active sampling material for its intrinsic linear behaviour, stability of response over time, and intrinsic radiation-hardness. Fig. 3.13 shows the lead absorbers in a Liquid Argon bath at an operating temperature of 88K (-185°C), which is glued between two stainless steel, and the cooper electrodes at high voltage (HV) located in the middle of 2×2 mm gap between two absorbers.

The absorbers and electrodes have an accordion geometry (Fig. 3.12 left) which guarantees a full ϕ coverage, following an original idea of D. Fournier [38]. The absorbers made of lead plates are glued to two stainless-steel sheets of 0.2 mm thickness. The lead plates in the barrel have a thickness of 1.53 mm for $|\eta| < 0.8$ and 1.13 mm for $|\eta| > 0.8$, where the change in lead thickness at $|\eta| = 0.8$ limits the decrease of the sampling fraction as $|\eta|$ increases. In the endcaps, the plates have a thickness of 1.7 mm for $|\eta| < 2.5$

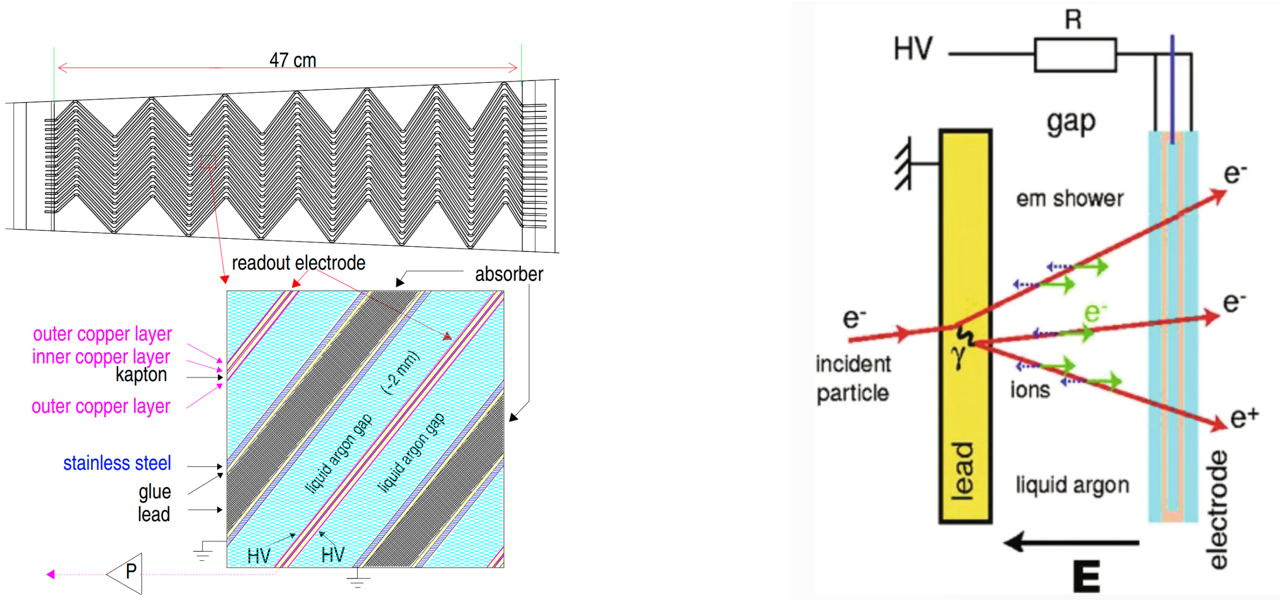

Figure 3.13: (left) Accordion structure with a small sector of the barrel calorimeter in a plane transverse to the LHC beams, and a zoom on the electrode structure in the bottom showing the liquid argon, lead absorber and copper electrode [36]. (right) Illustration of shower development and ionisation collection [37].

and 2.2 mm for $|\eta| > 2.5$. The readout electrodes are located in the gaps between the absorbers and consist of three conductive copper layers separated by insulating polyimide sheets where the two outer layers are at the high-voltage potential and the inner one is used for reading out the signal via capacitive coupling. Each barrel gap between two absorbers is equipped with two electrodes, one type for $|\eta| < 0.8$ and another for $|\eta| > 0.8$. Similarly, each endcap gap between two absorbers is equipped with one type of electrode for $|\eta| < 2.5$ and another for $|\eta| > 2.5$.

The total ECAL can be divided into one barrel ($|\eta| < 1.475$) and two endcaps ($1.375 < |\eta| < 3.2$) covering the pseudorapidity range of $|\eta| < 3.2$ contained in their corresponding cryostats. The barrel cryostat is 6.8 m long, with an outer radius of 2.25 m, and an inner radius of 1.15 m. The vessels are made of aluminium with vacuum insulation. The solenoid, sharing the vacuum insulation, has 44 mm thickness and amounts to 0.63 X_0. The endcap cryostats are built out of aluminium and are vacuum insulated. The outer radius of the cylindrical warm shell is the same as the barrel (2.25 m), and the length of one cryostat is 3.17 m.

The barrel ECAL is made of two half-barrels with each one made up of 1024 accordion-shaped absorbers centred around the z-axis and interleaved with readout electrodes. One half-barrel covers the region with $z > 0$ $(0 < \eta < 1.475)$ and the other one covers the region with $z < 0$ $(-1.475 < \eta < 0)$. The length of each half-barrel is 3.2 m with weighs 57 tons and the inner and outer diameters of 2.8 m and 4 m. As mentioned above, the barrel ECAL is complemented with a liquid-argon PS detector, placed in front of its inner surface, over the full barrel η range. Each half-barrel has been divided into 16 modules, and each module is segmented in longitudinal dimension with three sampling layers, which covers a $\Delta\phi = 22.5°$.

A module with three layers in depth is depicted in Fig. 3.12. The first layer (front) is made of narrow strips corresponding to a very fine granularity in η which provides precise position measurements and γ/π^0 separation contributing to the high jet rejection capability required to obtain a very pure $\gamma\gamma$ spectrum for Higgs studies. The front layer is read out at the low-radius side of the electrode. The second layer (middle) consists of quadratic cells (squares) of 0.025 in both η and ϕ. As the layer with the longest length of approximately 16-18 X_0, it absorbs most of the shower energy of the particles. The third layer (back) is arranged in larger towers of 0.05 in η and 0.025 in ϕ used to recover high energy tails and helps to separate hadronic to electromagnetic particles. Both the middle and back layers are read out at the high-radius side of the electrode. The fine granularity in η of the ECAL enables a measurement of the angle of the incoming electromagnetic particle and hence the primary vertex using the pointing method [39, 40].

The endcap ECAL has two parts covering the region of $1.375 < |\eta| < 3.2$, one on each side of the barrel ECAL. Each endcap ECAL consists of two co-axial wheels corresponding to an inner wheel with a radius of 330 mm and an outer wheel with a radius of 2098 mm and both wheels are 63 cm thick with a weight of 27 tons. There are 768 absorbers interleaved with readout electrodes in the outer wheel and 256 absorbers in the inner wheel. The boundary between the inner and the outer wheel is 3 mm wide and located at $|\eta| = 2.5$ with the filling of mostly low-density material. Each endcap wheel is further divided into eight wedge-shaped modules without introducing any discontinuity along the ϕ thanks to the accordion geometry. The electrodes are positioned in the middle of the gaps by honeycomb spacers. As for the barrel ECAL, the precision region in the endcap ECAL ($1.5 < |\eta| < 2.5$) is divided in depth into three longitudinal layers. The front layer, about 4.4 X_0 thick, is segmented with strips along the η direction. The transverse size of the projective cell in the middle layer is the same as defined in the barrel ECAL, $\Delta\eta \times \Delta\phi = 0.025 \times 0.025$. The back layer has a twice coarser granularity in η. The outermost region $|\eta| < 1.5$ of the outer wheel and the inner wheel ($2.5 < |\eta| < 3.2$) are segmented in only two longitudinal layers and have a coarser transverse granularity. The η-granularity in the front layer varies with η in order to keep the copper strip width larger than a few mm. The ϕ-granularity is obtained by collecting the signals from adjacent electrodes. Each module contains 3984 readout channels, including the 96 channels in the PS.

The readout granularity of the different layers, the number of layers, and the number of readout channels, are summarized in Table 3.3.

The input electron passes through a plate of the lead absorbers, making an EM shower in the calorimeter which then produces ionisation electrons (green arrows in Fig. 3.13 right). These ionisation electrons are drifted by the HV and induce an electric current, which is transferred from the electrodes to the electronic readout. In total, taking the PS cells into consideration, there are 173312 channels to be read out.

Fig. 3.14 shows the cumulative material up to a given layer of the ECAL. The depth of the front layer ends up being 6 X_0 (including dead material and PS). The end of the middle sampling is 24 X_0. The depth of the back layer varies from 2 to 12 X_0 (for $|\eta|$ less than about 0.6, the depth of the second sampling is limited to 22 X_0, in order to have at least 2 X_0 in the third sampling). So the total thickness of a module is at least 22 X_0, increasing from 22 X_0 to 30 X_0 between $|\eta| = 0$ and $|\eta| = 0.8$ and from 24 X_0 to 33 X_0 between $|\eta| = 0.8$ and $|\eta| = 1.3$. The total active thickness of an endcap ECAL is greater than 24 X_0 except for $|\eta| < 1.475$. The thickness increases from 24 to 38 X_0 as $|\eta|$ increases from 1.475 to 2.5 (outer wheel) and from 26 to 36 X_0 as $|\eta|$ increases from 2.5 to 3.2 (inner wheel).

Detector	Barrel		Endcap	
	$\lvert\eta\rvert$ coverage	Number of layers	$\lvert\eta\rvert$ coverage	Number of layers
Presampler	$\lvert\eta\rvert < 1.52$	1	$1.5 < \lvert\eta\rvert < 1.8$	1
ECAL	$\lvert\eta\rvert < 1.35$	3	$1.375 < \lvert\eta\rvert < 1.5$	2
	$1.35 < \lvert\eta\rvert < 1.475$	2	$1.5 < \lvert\eta\rvert < 2.5$	3
			$2.5 < \lvert\eta\rvert < 3.2$	2
	$\lvert\eta\rvert$ coverage	$\Delta\eta \times \Delta\phi$	$\lvert\eta\rvert$ coverage	$\Delta\eta \times \Delta\phi$
Presampler	$\lvert\eta\rvert < 1.52$	0.025×0.1	$1.5 < \lvert\eta\rvert < 1.8$	0.025×0.1
Front layer	$\lvert\eta\rvert < 1.40$	$0.025/8 \times 0.1$	$1.375 < \lvert\eta\rvert < 1.425$	0.050×0.1
	$1.40 < \lvert\eta\rvert < 1.475$	0.025×0.025	$1.425 < \lvert\eta\rvert < 1.5$	0.025×0.1
			$1.5 < \lvert\eta\rvert < 1.8$	$0.025/8 \times 0.1$
			$1.8 < \lvert\eta\rvert < 2.0$	$0.025/6 \times 0.1$
			$2.0 < \lvert\eta\rvert < 2.4$	$0.025/4 \times 0.1$
			$2.4 < \lvert\eta\rvert < 2.5$	0.025×0.1
			$2.5 < \lvert\eta\rvert < 3.2$	0.1×0.1
Middle layer	$\lvert\eta\rvert < 1.40$	0.025×0.025	$1.375 < \lvert\eta\rvert < 1.425$	0.050×0.025
	$1.40 < \lvert\eta\rvert < 1.475$	0.075×0.025	$1.425 < \lvert\eta\rvert < 2.5$	0.025×0.025
			$2.5 < \lvert\eta\rvert < 3.2$	0.1×0.1
Back layer	$\lvert\eta\rvert < 1.35$	0.05×0.025	$1.5 < \lvert\eta\rvert < 2.5$	0.050×0.025
	Number of readout channels			
Presampler	7808		1536	
ECAL	101760		62208	

Table 3.3: Main parameters of the electromagnetic calorimeter system [29].

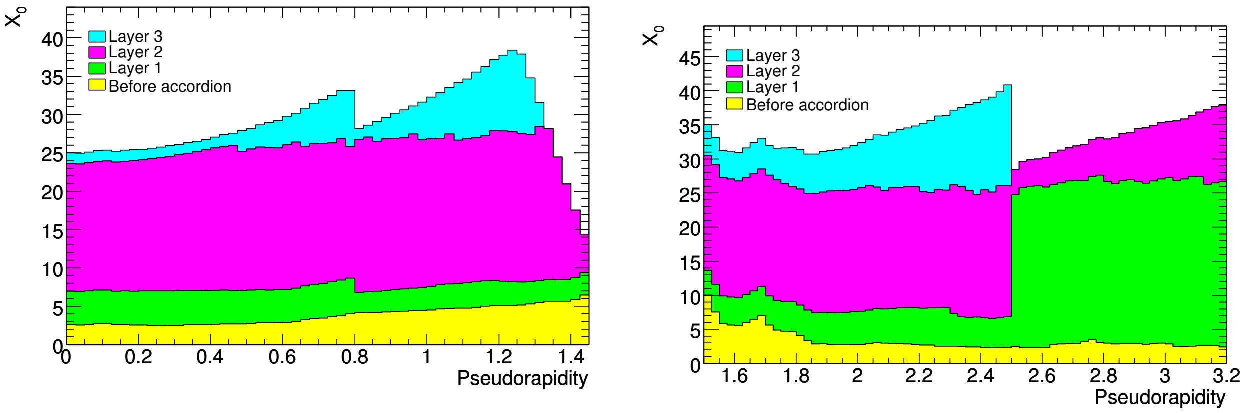

(a) barrel

(b) endcap

Figure 3.14: Cumulative amount of passive material, in units of radiation length X_0 and as a function of $|\eta|$, in front of and in the electromagnetic calorimeter. [41].

The ECAL energy resolution σ_E can be parametrized as

$$\frac{\sigma_E}{E} = \frac{a}{\sqrt{E}} \oplus \frac{b}{E} \oplus c \tag{3.8}$$

where the symbol $\oplus$ indicates that the terms are added quadratically, a is the sampling term which corresponds to the stochastic nature of an EM shower, b is the noise term that describes the contribution of electronic noise of the readout electronics and of the pileup noise, and c is the constant term arising from spatial inhomogeneities of the LAr calorimeter structure or of dead material. The term b depends on the cluster size and its typical value is from 200 to 300 MeV. All of them are η-dependent parameters.

The sampling term a covers stochastic fluctuations of the electromagnetic cascade during energy deposition. It is the leading term in the resolution for electrons with low or medium energy. It can be measured using the J/ψ width where $J/\psi \to e^+e^-$ provides low-energy electrons whose energy measurement resolution is completely dominated by a. The sampling term spreads mostly from 10% to 15% with η. The sampling term depends on the choice of the material used for the absorber and the active material as well as the thickness of the sampling layers. The sampling fluctuations can be reduced by increasing the sampling fraction f_{samp}:

$$f_{\text{samp}} = \frac{E_{\text{mip}}^{\text{active}}}{E_{\text{mip}}^{\text{active}} + E_{\text{mip}}^{\text{absorber}}} \tag{3.9}$$

where $E_{\text{mip}}^{\text{active}}$ and $E_{\text{mip}}^{\text{absorber}}$ denote the energy deposited by a minimum ionizing particle in the active and absorber materials, which means that the increase of the amount of active material for the shower development can reduce the sampling fraction and hence the sampling term. Most sampling calorimeters with a resolution better than $10\%/\sqrt{E}$ have a large sampling fraction exceeding 15%. Alternatively, the homogeneous calorimeter (for example, lead tungstate scintillating crystals in CMS ECAL) usually has a better energy resolution because of the full shower collection, although no information on the longitudinal shower shape is recorded.

The noise contribution $\frac{b}{E}$ increases with the decrease of the energy of the incident particles, which means that this term may become dominant at energies below a few GeV. Therefore, the noise equivalent energy is usually required to be much smaller than 100 MeV per channel. On the other hand, in sampling calorimeters, the noise term can be decreased by increasing the sampling fraction, because the larger sampling fraction corresponds to the larger signal from the active medium, therefore, a higher signal-to-noise ratio can be obtained.

The constant term c includes contributions which do not depend on the energy of the particle. For example, the non-uniformity of the calorimeter response caused by instrumental effects induces additional smearing to the measured energy. Non-uniformity can also originate from the detector geometry, such as the irregular shapes of the absorber and active layers, imperfections in the detector containing the mechanical structure and readout system, temperature gradients, detector ageing, radiation damage, boundary effect between modules, etc. All these effects are supposed to be manifested in the constant term. With the increase of energy, the constant term becomes more and more dominant. Tight construction tolerances are therefore imposed on the mechanics and readout system of modern calorimeters, for instance, LHC calorimeters. Typically the constant term of an ECAL should be within the level of 1% .

3.2.3 Hadronic Calorimeter

In order to measure the energy of hadrons with good resolution ($\Delta E/E = 50\%/E \bigoplus 3\%$) and linearity (1–2% up to TeV scale), the Hadronic Calorimeter (HCAL), a sampling calorimeter was developed using the iron (passive) and plastic scintillator (active material) in the ATLAS detector. It is driven by the aim to reconstruct the decay $W \to$ jet+jet at high p_{T}, therefore, the transverse granularity of HCAL is designed to be $\Delta\eta \times \Delta\phi = 0.1 \times 0.1$ in the range of $|\eta| < 2.5$ and $\Delta\eta \times \Delta\phi = 0.2 \times 0.2$ beyond the range of $|\eta| = 2.5$. The total HCAL can be divided into three parts including the tile calorimeter, the liquid-argon hadronic endcap calorimeter (HEC), and the liquid-argon forward calorimeter (FCal) corresponding to different pseudorapidity coverage shown in Figure 3.15.

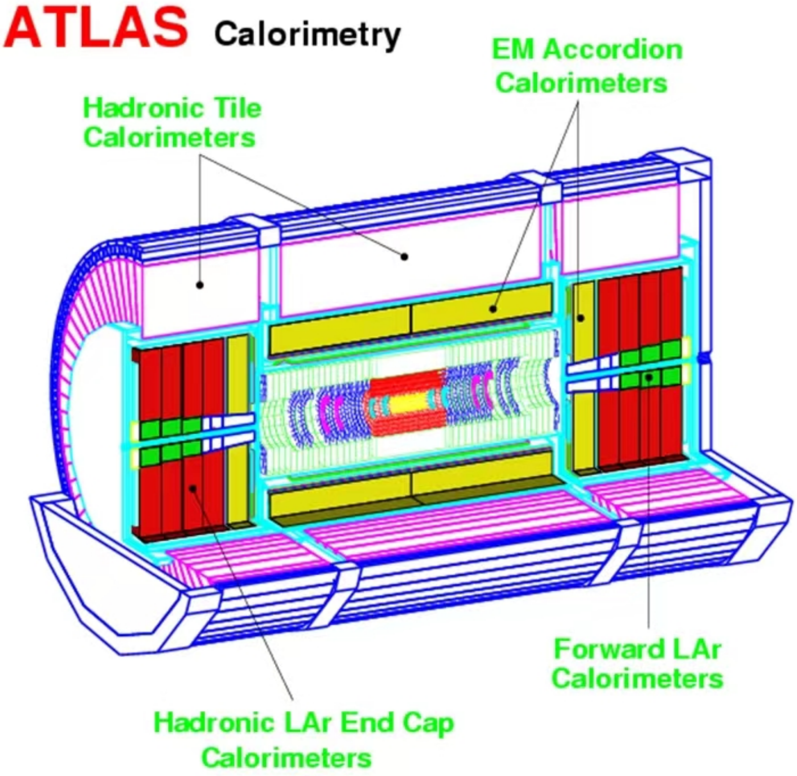

Figure 3.15: Schematic view of the calorimeters in the ATLAS detector [42].

The tile calorimeter is installed in the barrel region of $|\eta| < 1.7$ containing three parts, in which two parts are located symmetrically in the region of $1.55 < |\eta| < 1.7$ with the length of 2.6 m, the inner radius of 2.28 m, and the outer radius of 4.25 m. The third part is in the central barrel covering $|\eta| < 1.55$ with 5.8 m in length. Each barrel tile HCAL consists of 64 modules or wedges of size $\Delta\phi \approx 0.1$, made of steel plates and scintillating tiles. In the longitudinal direction, the calorimeter modules are segmented into three layers of 1.5, 4.1 and 1.8 λ (effective nuclear interaction length) in the central barrel and 1.5, 2.6, 3.3 λ in the extended two barrels, which corresponds a total radial depth approximately of 7.4λ. There are approximately 5000 cells and 10000 channels in the tile calorimeter.

The Hadronic Endcap Calorimeter (HEC) is made up of flat copper as absorber plates and liquid-argon as active medium for its robustness against the high radiation levels in the pseudorapidity range of $1.5 < |\eta| < 3.2$. There are two wheels with 32 identical modules contained in the HEC. The front HEC1 and rear HEC2 wheels are placed in the cryostat for each endcap, where the cryostat is shared with the electromagnetic endcap (EMEC) and forward (FCal) calorimeters. The length of HEC1 (HEC2) is 0.82 m (0.96 m). The thickness of the copper absorber plates is 25 mm for HEC1 and 50 mm for HEC2, with the first plate being half of this normal thickness in either case which is at least 10 interaction lengths (λ) including the ECAL in front of the HEC, in order to satisfy the requirement of the linearity of the energy response measured has to stay within 2%.

The forward calorimeters (FCal) are located in the same cryostats as the endcap calorimeters and provide coverage over $3.1 < |\eta| < 4.9$, which is at a distance of approximately 4.7 m from the interaction point with the exposure of high particle fluxes. The FCal thus consists of three layers (Fig. 3.16), where the layer closest to the interaction point called FCal1 is a Cu/LAr calorimeter designed for electromagnetic calorimetry, FCal2 and FCal3 are hadronic W/LAr calorimeters, and behind FCal3 is a passive layer of brass.

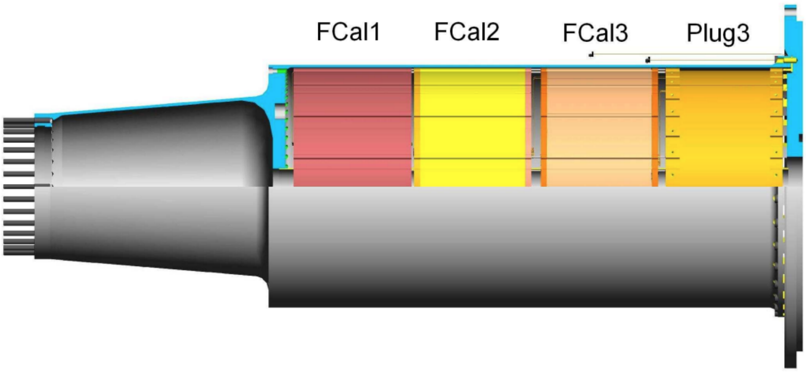

Figure 3.16: The cut-away view of the FCAL installation with multi-layers [43].

The choice of tungsten as the absorber in the hadronic FCal2 and FCal3 modules limits the transverse hadronic shower spread, which is especially important for η determination in the forward region since a fixed distance here covers a larger η interval. An FCal readout cell consists of several neighbouring FCal electrodes read out together. Fewer electrodes are grouped close to the inner edge, which ensures an η-ϕ granularity of about 0.1×0.1 or better for most of the electromagnetic layer.

3.2.4 Muon Spectrometer

The muon spectrometer is the outermost sub-detector of ATLAS. As the name implies, it is designed to detect the muon with two purposes: an independent muon trigger and high-quality standalone muon reconstruction over a wide range in transverse momentum, pseudorapidity, and azimuthal angle, where the muon p_{T} should be measured in the pseudorapidity range of $|\eta|$ <2.7 and the triggers should be fired in the region $|\eta| < 2.4$. The driving performance goal is a standalone transverse momentum resolution of approximately 10% for 1 TeV track, which translates into a sagitta along the z-axis of about 500 μm, to be measured with a resolution less than 50 μm. Based on these goals and the condition of the muon spectrometer, it was devised to include three large superconducting air-core toroids, the precision-tracking chambers for accurate momentum resolution, and an effective trigger system based on chambers with fast response. Fig. 3.17 shows the cross-section of the muon system.

The toroid in the barrel is formed by eight superconducting coils, each of them with a coil area of 5×26m^2. The magnetic field extends between the inner and the outer tracking stations, and is in the range of 0.5

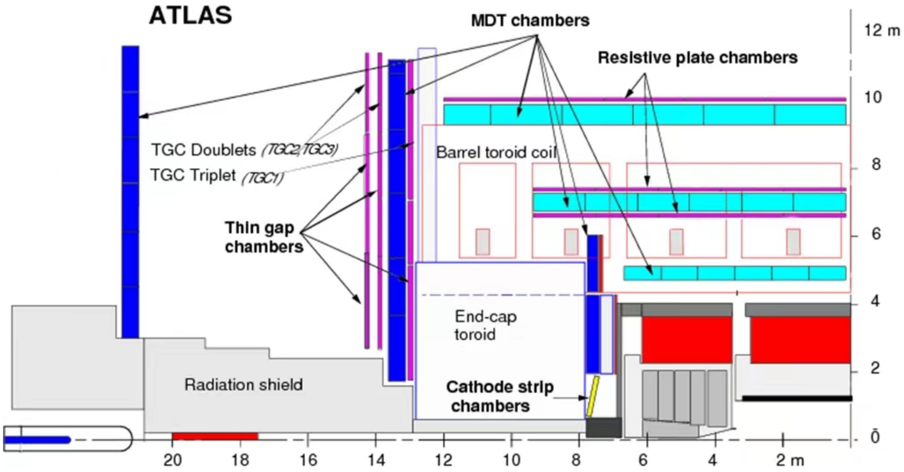

Figure 3.17: Cross-section of the muon system in a plane containing the beam axis (bending plane) [44].

to 2 T. In each endcap, the magnetic field is provided by eight superconducting coils, located between the first and the second station of tracking chambers. The field is in the range of 1 to 2 T. The performance of the toroid in terms of bending power is characterised by the field integral $\int \mathrm{B}\mathrm{d}l$, where B is the field component normal to the muon direction and the integral is computed along an infinite-momentum muon trajectory, between the innermost and outermost muon chamber planes. The barrel toroid provides 1.5 to 5.5 Tm of bending power in the pseudorapidity range $0 < |\eta| < 1.4$, and the endcap toroids approximately 1 to 7.5 Tm in the region $1.6 < |\eta| < 2.7$. The bending power is lower in the transition regions where the two magnets overlap $(1.4 < |\eta| < 1.6)$.

For the precision-tracking chambers, because of the different rates in the barrel and in the endcap, two different detectors have been designed. In the barrel region, there are three layers of stations arranged in three concentric cylindrical shells around the beam axis at radii of approximately 5 m, 7.5 m, and 10 m. The innermost stations consist of the Monitored Drift Tube (MDT) directly after the HCAL. The stations of the second layer are composed of one MDT chamber and two Resistive Plate Chambers (RPC) on each side of the MDT. The outer stations are outside the magnetic field and composed of an MDT chamber and an RPC on the outer side of the MDT. the first layer of stations sits in front of the magnet. In the two endcaps, there are also three layers perpendicular to the z-axis and located at distances of $|z|$ ≈7.4 m, 10.8 m, 14 m, and 21.5 m from the interaction point. The stations of the inner layer are in front of the magnet, where multi-wire proportional chambers Cathode Strip Chambers (CSC) are installed in the region closest to the beam pipe with $2 < |\eta| < 2.7$ and MDT chambers provide the remaining coverage. The second layer is installed behind the endcap magnet where stations are one layer of MDT chambers and two layers of Thin Gap Chambers (TGC) that can provide the trigger signal. The outer station layer is equipped with MDT chambers.

The trigger chambers of the muon system provide fast information on muon tracks traversing the detector, allowing the L1 trigger logic to recognise their multiplicity and approximate energy range. The trigger system should satisfy requirements as follows:

- discrimination on muon transverse momentum;

- bunch-crossing identification;
- fast and coarse tracking information to be used in the high-level trigger stages;
- second coordinate measurement in the non-bending ϕ-projection to complement the MDT measurement;
- robustness towards random hits due to n/γ-background in the experimental hall.

Two different types detectors have been used for barrel ($|\eta| \leq 1.05$) and endcap ($1.05 \leq |\eta| < 2.4$) regions. In the barrel, RPCs are used due to good spatial and temporal resolution as well as adequate rate capability. In the endcap regions, TGCs are selected, operating on the same principle as multi-wire proportional chambers, which provides good time resolution and high rate capability.

3.2.5 Magnet system

The magnet system in the ATLAS detector consists of one solenoid and three toroids (one barrel and two endcaps). In total, four superconducting magnets provide the magnetic field over a volume of approximately 12000 m^3 in the areas of the four main sub-detectors of the ALTAS. In order to reach the strict environment of superconducting, and in the condition of very high energy stored in the magnet with the nominal operating current of more than several kA, the cold mass and cryostat integration is necessary. On the other hand, an outside return yoke is used to strengthen the magnetic field and confine it to a definite region. The overall spatial arrangement of the coil windings is shown in Fig. 3.18.

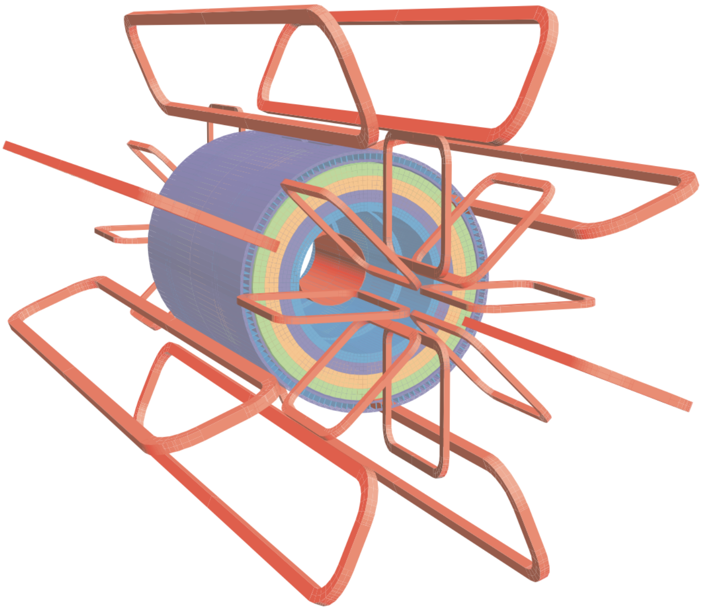

Figure 3.18: Geometry of magnet windings and tile calorimeter steel [29].

The central solenoid is aligned on the beam axis and provides a 2 T axial magnetic field for the inner detector while it also needs to minimize the radiative thickness in front of the barrel ECAL. Therefore, it was carefully optimised to keep the material thickness in front of the calorimeter as low as possible. In order to reach this criterion, the solenoid windings and LAr calorimeter share a common vacuum vessel, thereby eliminating two vacuum walls. An additional heat shield consisting of 2 mm thick aluminium panels is installed between the solenoid and the inner wall of the cryostat. The solenoid assembly contributes a total of ≈0.66 radiation lengths at normal incidence. The inner and outer diameters of the solenoid are 2.46 m and 2.56 m with an axial length of 5.8 m. The single-layer coil is wound with a high-strength Al-stabilised NbTi conductor, specially developed to achieve a high field with low thickness, inside a 12 mm thick support cylinder of Al. The coil mass is 5.4 tons and the stored energy is 40 MJ. The stored-energy-to-mass ratio of only 7.4 kJ/kg at the nominal field, clearly demonstrates the compliance with the requirement of design for an extremely lightweight structure successfully. The flux is returned by the steel of the ATLAS HCAL and its girder structure. The solenoid is charged and discharged in about 30 minutes. In the case of a quench, the stored energy is absorbed by the enthalpy of the cold mass which raises the cold mass temperature to a safe value of 120 K maximum. Re-cooling to 4.5 K is achieved within one day.

A barrel toroid and two endcap toroids produce a toroidal magnetic field of approximately 0.5 T and 1 T for the muon detectors in the central and endcap regions, respectively, with a working point temperature of 4.7 K. The barrel toroid consists of eight coils encased in individual racetrack-shaped, stainless-steel vacuum vessels. The coil assembly is supported by eight inner and eight outer rings of struts. The overall size of the barrel toroid system as installed is 25.3 m in length, with inner and outer diameters of 9.4 m and 20.1 m, respectively. The conductor and coil-winding technology are based on winding a pure Al-stabilised Nb/Ti/Cu conductor into pancake-shaped coils, followed by vacuum impregnation. The two endcap toroids are used to generate the magnetic field required for optimising the bending power in the endcap regions of the muon spectrometer system. They are supported off and can slide along the central rails, which facilitates the opening of the detector for access and maintenance. Each endcap toroid consists of a single cold mass built up from eight flat, square coil units and eight keystone wedges, bolted and glued together into a rigid structure to withstand the Lorentz forces. The conductor and coil-winding technology are the same as the barrel toroids.

3.2.6 Trigger system

With the high luminosity of the LHC (up to $2.1 \times 10^{34}\ \mathrm{cm^{-2}s^{-1}}$) and the high bunch crossing rate (40 MHz), it is difficult to save all events information, the trigger is thus important to filter events and decrease the event rate. The trigger system [45] has been substantially upgraded with respect to Run 1, and it consists of two levels of event selection: Level-1 (L1) and High-Level Trigger (HLT) as shown in Fig. 3.19. The L1 trigger is hardware-based, implemented using custom-made electronics, while the HLT is almost entirely based on commercially available computers and networking hardware.

The L1 trigger searches for signatures from high-p_{T} muons, electrons/photons, jets, and τ-leptons decaying into hadrons. It also selects events with large missing transverse energy ($E_{\mathrm{T}}^{\mathrm{miss}}$) and large total transverse energy. The L1 trigger uses reduced-granularity information from a subset of detectors: the RPC and TGC for high-p_{T} muons, and all the calorimeter sub-systems for electromagnetic clusters, jets, τ-leptons, $E_{\mathrm{T}}^{\mathrm{miss}}$. The L1 trigger decision is formed by the central trigger processor (CTP in Fig. 3.19). The maximum L1-accepted event rate is reduced to 100 kHz in Run 2 within a latency of 2.5 μs.

The HLT proceeds the signatures accepted by the L1 trigger, benefiting from further information from ID, calorimeters and MS. The HLT reconstruction can be seeded by either Regions-of-Interest (RoI) from

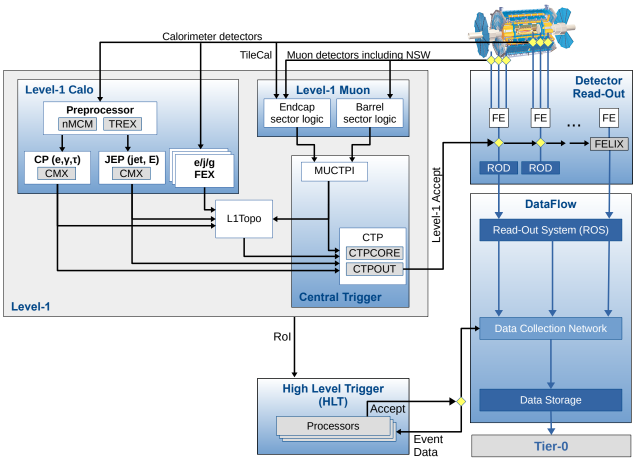

Figure 3.19: Schematic of the ATLAS Trigger system [46].

L1 or the full detector space.

3.3 Object Reconstruction and Identification in ATLAS

Most of the particles produced by the proton-proton collisions of the LHC have a limited lifetime, which means only a fraction of them live long enough to be detected by ATLAS. Actually, most of them decay or cascade into lighter and more stable particles before interacting with the detector. Based on the well-known particle characteristics, the elementary or composite particles having a mean free path greater than 500 μm, which can interact with the detector material and be detected, are muons (μ^+, μ^-), electrons (e^+, e^-), photons (γ), π mesons (π^+, π^-), K mesons (K^+, K^-, K_L^0), protons (p^+, p^-), neutrons (n), and other hadrons. Besides, quarks and gluons hadronize to produce color-neutral hadron bound states (some of which are mentioned above), producing a highly collimated conical particle shower in the detector, called a jet. Jet containing b hadrons can be identified through unique properties as b-jet. For neutrinos, since they are only involved in the weak interactions corresponding to extremely small cross sections, their existence can only be detected by a specific detector, such as Super-Kamiokande, rather than ATLAS or CMS. Their transverse energy is denoted as $E_{\mathrm{T}}^{\mathrm{miss}}$ in the ATLAS experiment, inferred by the conservation of transverse momentum. In order to perform analyses with high accuracy, the reconstruction and identification of these basic objects are important. The following sections 3.3.1 and 3.3.2 will introduce the techniques and methods used in the object reconstruction and identification of electrons, photons and jets.

3.3.1 Electron and Photon

Electrons and photons interact with the lead absorber of the LAr calorimeter to form an EM shower. The EM shower ionizes the LAr between the absorbers, and the ionized electronic signal is proportional to the energy deposition of the physics object. The energy deposited is measured by the signal amplitude in the calorimeter unit. The calorimeter cells forming the clusters of deposited energy serve as seeds for the cluster reconstruction algorithm in the ATLAS experiment.

ECAL electronics and cell energy estimate

During an EM shower, the ionization current received in the electrodes (Fig. 3.13 right) is sent to the electronic readout. A schematic of the the electronic readout of the ATLAS LAr calorimeters is shown in Fig. 3.20, which is divided into a Front End (FE) system of circuit boards mounted on the detector cryostats, and a Back End (BE) system of VME-based boards located outside the detector hall.

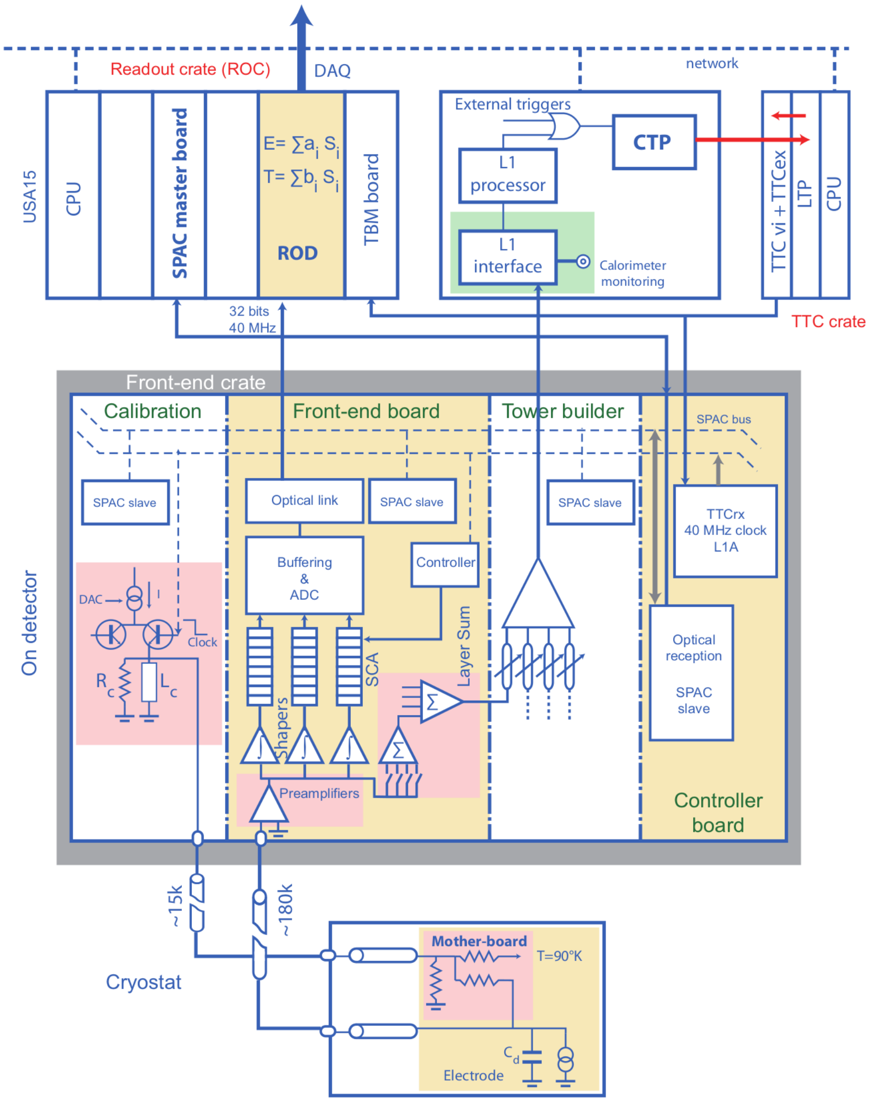

Figure 3.20: Schematic of the overall architecture of the ATLAS LAr readout electronics, the LAr detectors are located at the bottom [36].

The FE system includes Front-end boards (FEB), which are used to amplify, shape and digitize the received raw electric current in the electrodes. Three versions of preamplifiers with different impedance and maximum input currents are used to match the detector capacitances and dynamic ranges of the calorimeter sections. The amplified signal is then passed through the shaper chips to produce three overlapping linear gain scales, which is 1 for low gain (LG), 9.9 for medium gain (MG) and 93 for high gain (HG). The different gains with a ratio $\sim$ 10 is used to recover the full dynamical range.

The input electric current has a triangle shape with a maximum drift time $t_d \approx 450$ ns (Fig. 3.21). Since this charge collection time of 450 ns is longer than the time difference between two bunch crossings at the LHC (25 ns), it will integrate several bunch crossings and include a lot of pileup events. In order to mitigate such an effect, the signals are passed through a bipolar filter which shapes them to a more peaked pulse (Fig. 3.21 curve with dots). The bipolar filter decreases the long tails at large drift time and reduces the bandwidth of the pulse, hence brings larger tolerance to pileup noise.

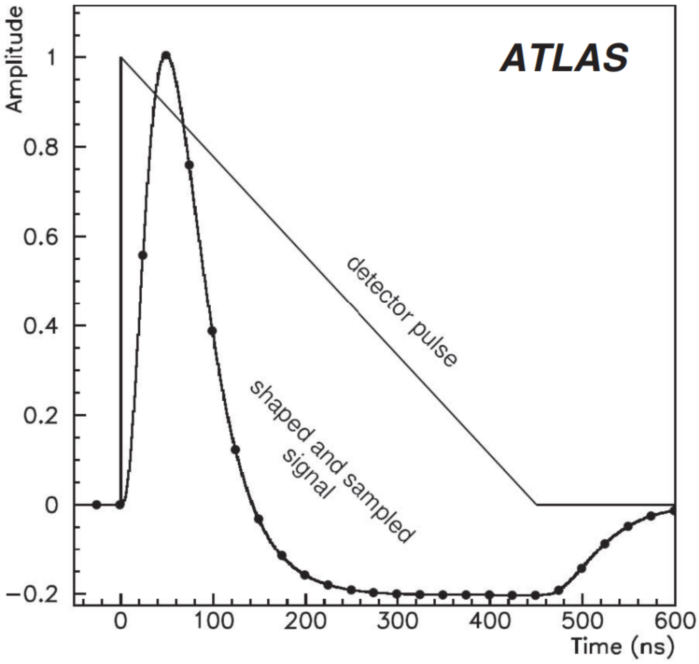

Figure 3.21: Typical triangle and shaped electronic pulse signal in one LAr cell. The dotted curve is the shaped signal pulse, after sampled with a separation of 25 ns [37].

The shaped signals are sampled at the LHC bunch crossing frequency of 40 MHz (25 ns) and stored in analog in the switched-capacitor array (SCA) analog pipeline chips. The analog signal is then digitized using a 12-bit Analog to Digital Converter (ADC), based on which the Gain Selector chips choose the relevant gain for each channel. Specifically, a high gain, medium gain, and low gain are used respectively for ADC counts lower than 1300, between 1300 and 3900 and very high ADC.

Read Out Driver (ROD), the primary component of the Back End electronics, is used to reconstruct the pulse amplitude A in unit of ADC:

$$A = \sum_i a_i \left(ADC_i - P\right) \tag{3.10}$$

where ADC_i is the ADC counts of recorded sample i, P is the pedestal defined as the mean value of the sample when no signal is presented, a_i are the optimal filter coefficients (OFCs) [47] used to estimate the pulse amplitude, which is optimized with minimum electronic and pileup noise, depending on the choosen gain in the cell.

The total energy deposited in a LAr calorimeter cell is then reconstructed as

$$E = F_{\mu A \to MeV} \cdot \frac{M_{cal}}{M_{phy}} \cdot R \cdot \sum_i a_i \left(ADC_i - P\right) \tag{3.11}$$

where

- R is the the electronic gain from ADC counts to ionization current $(ADC \to \mu A)$, which is determined with dedicated electronics calibration runs.
- $\frac{M_{cal}}{M_{phy}}$ corrects for bias due to the different shapes between calibration and physics signals.
- $F_{\mu A \to MeV}$ converts the ionization current to the total deposited cell energy.

Definition and reconstruction of the topo-cluster

The reconstruction algorithm making use of the clusters of energy deposits measured in topologically connected EM and hadronic calorimeter cells has been developed and used since 2017, where these clusters are denoted as topo-clusters [48]. Before 2017, cluster reconstructions used a fixed energy window algorithm due to technical limitations. The topo-cluster reconstruction relies on the cell energy significance denoted as $\zeta_{\text{cell}^{\text{EM}}}$ and computed as,

$$\zeta^{\text{EM}}_{\text{cell}} = \left|\frac{E^{\text{EM}}_{\text{cell}}}{\sigma^{\text{EM}}_{\text{noise,cell}}}\right|, \tag{3.12}$$

where $|E_{\text{cell}}|$ is the absolute energy of the calorimeter cell and $\sigma^{\text{EM}}_{\text{noise,cell}}$ is the cell noise including the electronics and pileup noises. In general, the definition of the topo-cluster obeys the following steps:

- Form the proto-clusters which is the collection of cells with $\zeta^{\text{EM}}_{\text{cell}} \geqslant 4$;
- Add neighbouring cells with $\zeta^{\text{EM}}_{\text{cell}} \geqslant 2$ where the qualified neighbour cell becomes a seed cell in the next iteration, collecting each of its neighbours in the proto-cluster.
- Combine nearby cells with $\zeta^{\text{EM}}_{\text{cell}} \geqslant 0$ into the clusters built in the above two steps.

The topo-cluster algorithm is the default ATLAS software. In practice, the reconstruction of the topo-cluster is not limited to one region of the detector: cells of a single topo-cluster could be from both the LAr and Tile calorimeters. In order to allow for future improvements to topo-cluster-based isolation calculations, as well as the potential for adoption of a detector-wide particle flow reconstruction algorithm, the same topo-cluster is commonly used as the initial cluster in different object reconstruction algorithms such as the jet, leptons, and etc. Therefore, in the reconstruction of electron and photon whose workflow is shown in

Fig 3.22, these initial clusters must be modified to consider cells from the EM calorimeter only. The initial cut on the cluster energy within the EM calorimeter for each cluster on the EM fraction, f_{EM}, is applied and calculated as

$$f_{\text{EM}} = \frac{E_{L_1} + E_{L_2} + E_{L_3} + w \cdot (E_{E4} + E_{\text{PS}})}{E_{\text{cluster}}}, \quad w = \begin{cases} 1, & 1.37 < |\eta| < 1.63 \\ 0, & \text{otherwise} \end{cases} \tag{3.13}$$

where the $E_{L_{1,2,3}}$ is the cluster energy in layers 1, 2 or 3 of the calorimeter. The term $(E_{E_4} + E_{\text{PS}})$ is only considered for clusters within the transition region of $1.37 < |\eta| < 1.63$, since electrons and photons in that η region tend to deposit non-negligible amounts of energy in the pre-sampler and E4 scintillators. The latter term is excluded in other detector regions to decrease noise. Hadronic contributions to the cluster are suppressed by removing the hadronic calorimeter cells from each cluster, leaving only cells belonging to the LAr calorimeter, the presampler, and the E_4 scintillators. The threshold of the f_{EM} is determined by the simulation and optimised at a value of 0.5 which can reject 60% of pileup clusters without limiting the efficiency for selecting true electron topo-clusters. Moreover, only clusters with deposit energy of more than 400 MeV are considered to reject clusters from pileup interaction or $\pi^0 \to \gamma\gamma$.

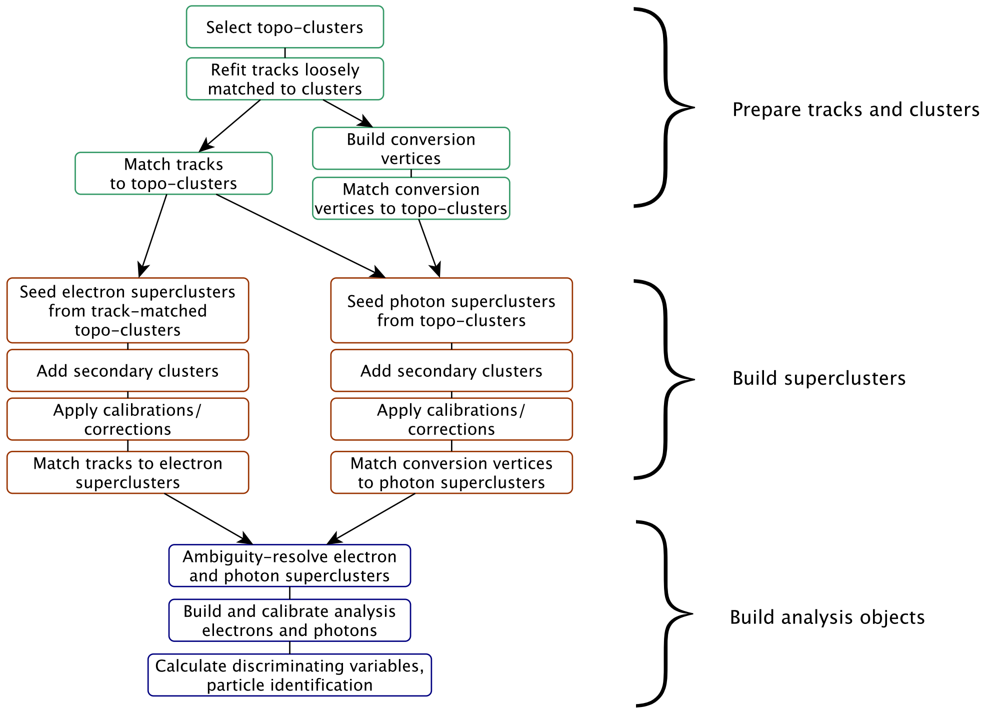

Figure 3.22: Algorithm workflow diagram for the electron and photon reconstruction [49].

The main advantage of topo-clusters in the latest algorithm is its ability to recover the low-energy deposition of bremsstrahlung photons and associate them with electron clusters to form the so-called superclusters (Fig. 3.23).

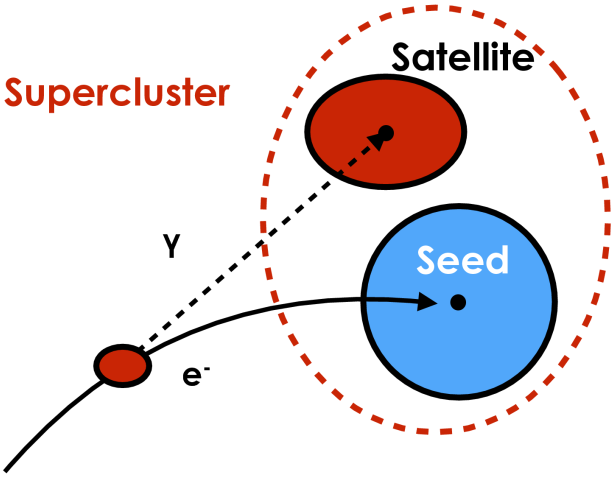

Figure 3.23: The illustration of an example supercluster showing an electron (blue) and bremsstrahlung photon (red) [49].

Supercluster reconstruction

Based on the topo-clusters and reconstructed track, the matching can be done by extrapolating the track to the cluster in the second layer of the ECAL. If the η and ϕ of the track and cluster satisfy $\Delta\eta < 0.05$, and $-0.1 < q_{\text{charge}} \cdot (\phi_{\text{track}} - \phi_{\text{cluster}}) < 0.05$, the match is successful. In some cases, electrons have large energy loss due to the bremsstrahlung, and momentum correction is needed to improve the track-cluster matching efficiency. On the other hand, if multiple tracks match the same cluster, the track with the smallest ΔR to the cluster is selected. Meanwhile, the vertices from photon conversion are also reconstructed by the algorithm using tracks with silicon hits (denoted Si tracks) and tracks reconstructed only in the TRT (denoted TRT tracks). Two-track conversion vertices are reconstructed from two tracks forming a vertex consistent with that of a massless particle, while single-track conversion vertices are essentially tracks without hits in the innermost sensitive layers. If multiple conversion vertices are matched to a cluster, double-track conversions with two silicon tracks are preferred over other double-track conversions, followed by single-track conversions. Within each category, the vertex with the smallest conversion radius is preferred. According to the track-cluster matching, the electron, the converted photon, and the unconverted photon are classified in the ATLAS experiment.

The next step is the reconstruction of "superclusters", which is independently applied for photons and electrons with different requirements. In summary, there are two stages: In the first stage, topo-clusters are used for evaluation as seed cluster candidates, which are the cornerstone of superclusters; in the second stage, clusters near the seed candidates are identified as satellite cluster candidates, which may emerge from bremsstrahlung radiation or topo-cluster splitting as shown in Fig 3.24.

If satellite clusters pass the necessary selection criteria, they are added to the seed candidates to form the final superclusters. The electron seed cluster candidates from a list of topo-clusters are required $E_{\text{T}} > 1$ GeV, and could be matched to a track having more than 4 hits in the silicon tracking detector. The seed cluster with higher energy deposits is preferred if there is more than one candidate. The photon seed cluster candidates must have an energy greater than 1.5 GeV, due to the absence of a matching track. Then for the satellite finding stage, it aims to add all possible idle clusters that are from the same initial electron or photon to the seed cluster. This step proceeds in the window of $\Delta\eta \times \Delta\phi = 0.075 \times 0.125$ around the seed cluster barycenter for both electron and photon, as these cases tend to represent secondary EM showers originating from the same initial electron or photon. There are two extra criteria for electron and photon, respectively. For electrons, a larger window $\Delta\eta \times \Delta\phi = 0.125 \times 0.3$ around the seed cluster barycenter is also used to perform the satellite finding. In this strategy, a cluster is considered a satellite if it has more than one matched track, which means that this satellite and its seed cluster share the same best-matched track. This special step in the electron supercluster reconstruction relies more on tracking information to discriminate distant radiative photons from pile-up noise, or other unrelated clusters.

For converted photons, the conversion vertices are used to test if a cluster can be matched to a track that is one track of the conversion vertex associated with the seed cluster, or if this cluster has the same matched conversion vertex as the seed cluster. The conversion vertex is built before the supercluster construction. By default, only the best-matched tracks and conversion vertices are used for the matching. Furthermore, only tracks that contain silicon hits, and conversion vertices made up only of tracks containing silicon hits, are used for satellite cluster matching. The iteration of the satellite finding is applied in the cluster list in the order of the cluster p_{T} to seek all clusters that are possible to be satellites, where one cluster can be regarded as a satellite once. The iteration continues until all available clusters have been examined.

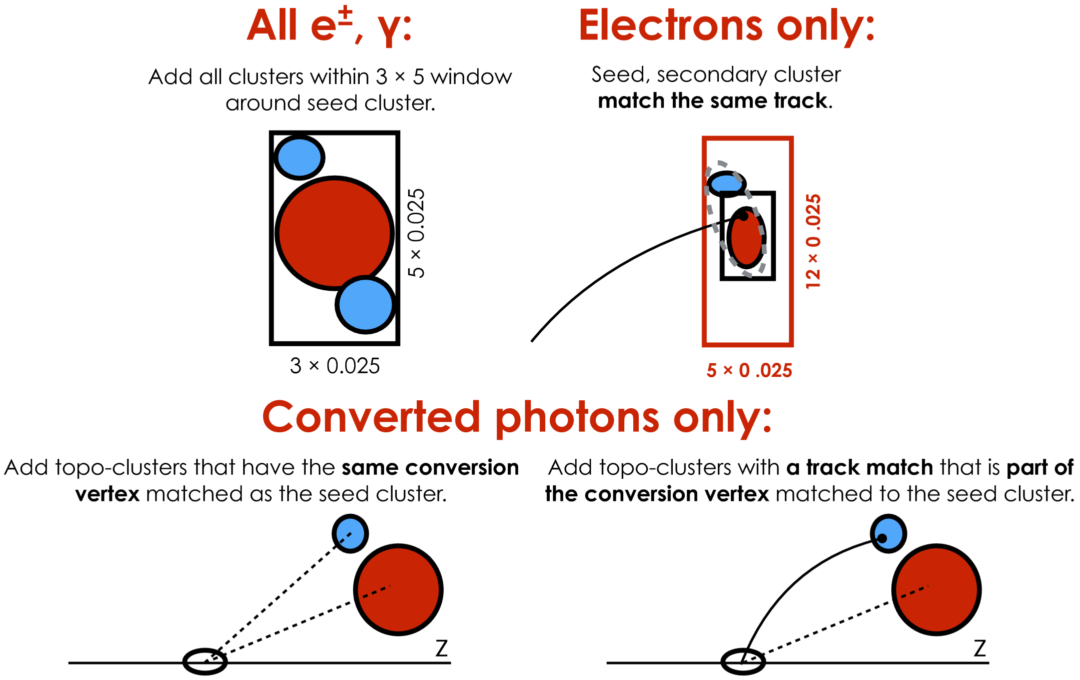

Figure 3.24: Diagram of the superclustering algorithm for electrons and photons. Seed clusters are shown in red, and satellite clusters in blue [49].

After superclusters are formed by all seed clusters and their associated satellites, the final step is to select the cells of a supercluster by combining the list of cells associated with each individual cluster to make a final list for the supercluster, denoted as "cell summation". This step only includes cells from the first three LAr calorimeter layers, as well as the pre-sampler, and the E4 scintillators in the transition region. It is well known that the electron or photon shower tends to have a shape with narrow η and wide ϕ. So as a final step prior to calibration, the size of each constituent topo-cluster is restricted to three (five) cells across in the η direction in the barrel (end-cap) region, with respect to the cluster barycenter by removing cells from the cluster falling in a region outside of the threshold in η. However, in order to include cells containing energy from interactions between the primary electron or photon, and the detector material, no restrictions are applied in the ϕ-direction. The η-restriction does not significantly have an impact on the electron and converted photon reconstruction, as the magnetic field in the ID ensures that the separation of the electron and bremsstrahlung photons (or the converted photon tracks) occurs mainly in the ϕ direction. As shown in Fig. 3.25, the change in the average shower containment for η-restricted superclusters is equivalent to clusters built using the sliding window algorithm. As the calibration will be introduced in Chapter 6, no further details are given here.

Ambiguity Resolution for Electron and Photon

After the electron and photon superclusters are built, initial energy calibration and position correction are applied to them. But since electron and photon superclusters are built independently, a given seed cluster can produce both an electron and a photon. In such cases, as shown in Fig. 3.26, the ambiguity resolution procedure for the electron and photon should be applied where the trajectory information from the tracker can be used. Tracks are matched to electron superclusters and conversion vertices to photon superclusters. The matching is performed in the same way that the matching to EM topo-clusters was performed, but using the superclusters instead. The final output is that if a particular object can be easily identified only as a photon (a cluster with no good track attached) or only as an electron (a cluster with a good track attached and no good photon conversion vertex), then only a photon or an electron object is created. Otherwise, both an electron and a photon object are created and these cases are marked explicitly as ambiguous, allowing the final classification of these objects to be determined based on the specific requirements of each analysis. It means that the sample of electron or photon candidates is still highly contaminated with photon conversions or low p_{T} electrons. Dedicated cuts to reject the latter are necessary which can be achieved by the foundation of electron and photon identification.

Electron and photon identification

The purpose of electron and photon identification is to select pure primary electron and photon samples from collision vertices. The identification algorithm should be able to suppress the radiated particles from the hadronic process. The algorithm makes use of the longitudinal and transverse shower profiles of the candidate particles that are consistent with the expected EM showers of electron photons. The input variables for electron and photon identification are summarized in Tab. 3.4.

The identification of electrons relies on a likelihood discriminant constructed from quantities based on the ID track and lateral/longitudinal development of the EM shower [50].

$$\mathcal{L}_{\mathcal{S}(\mathcal{B})} = \prod_{i=1}^{n} P_{s(b),i}(x_i), \tag{3.14}$$

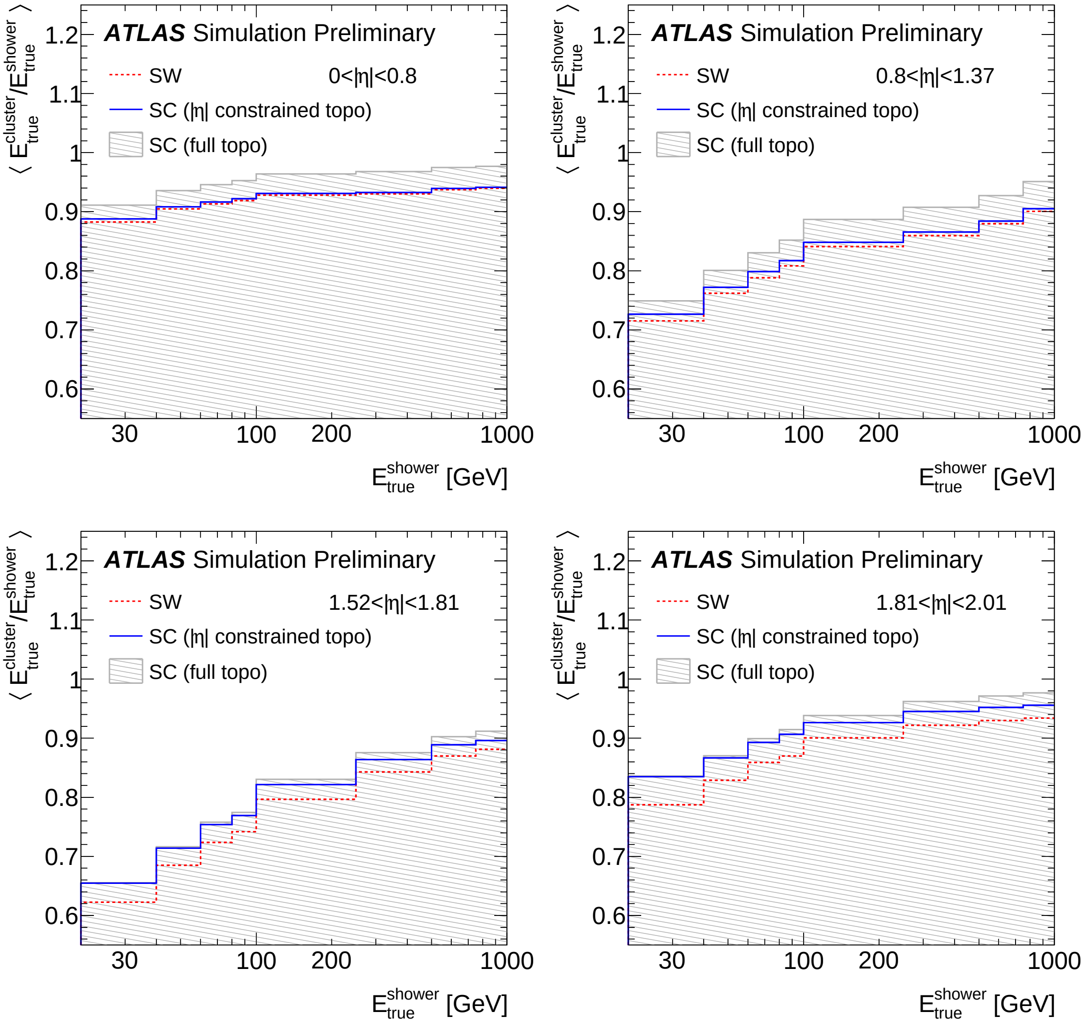

Figure 3.25: Average shower containment as a function of true shower energy for simulated electrons reconstructed via a sliding window and supercluster-based approaches. Included also are superclusters built using topo-clusters which are allowed unrestricted growth in the η-direction [49].

where $\vec{x}$ is the vector of discriminating variable values and $P_{s,i}(x_i)$ is the value of the signal probability density function of the i^{th} variable evaluated at x_i. In the same way, $P_{b,i}(x_i)$ refers to the background probability function. Then the signal and the background are fitted by using the Kernel Density Estimation method [51] included in the TMVA software package [52], and finally, a discriminative variable $d_{\mathcal{L}} = \frac{\mathcal{L}_S}{\mathcal{L}_S + \mathcal{L}_B}$ that can distinguish the signal and the background is obtained. Samples of MC simulation of dijet, Z→ ee, and W→ $e\nu_e$ are used to determine likelihood function and extract electron efficiencies in bins of p_{T} and η as shown in Fig. 3.27, which are measured with samples of Z→ ee and $J/\psi \rightarrow ee$. Based on these efficiencies, three working points are defined as Tight, Medium, and Loose, corresponding to 80%, 90% and 98% efficiencies, respectively. The uncertainties of the electron identification efficiency are $\pm 7\%$ at $E_{\mathrm{T}} = 4.5$ GeV and decrease with transverse energy, reaching better than $\pm 1\%$ for $30 < E_{\mathrm{T}} < 250$ GeV. The systematic uncertainties in the measurements are dominated by background subtraction uncertainties

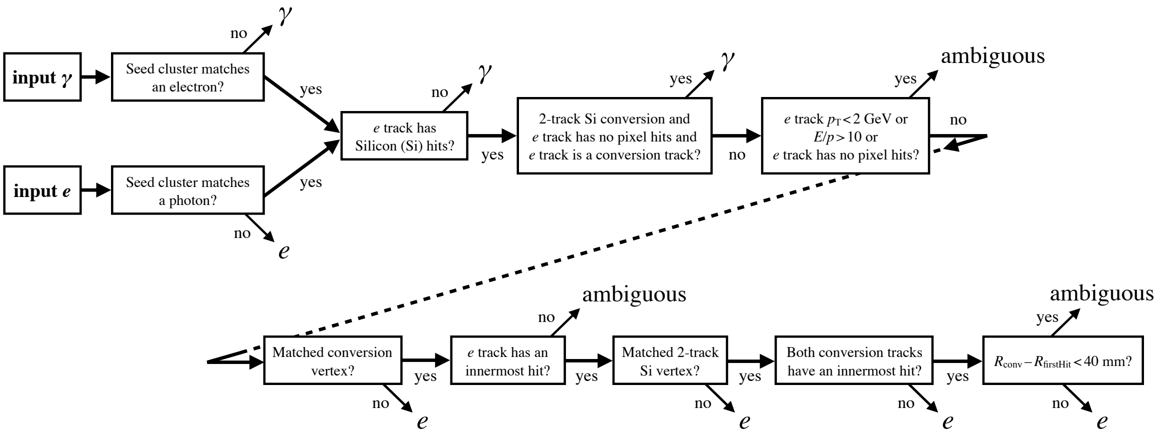

Figure 3.26: Flowchart showing the logic of the ambiguity resolution for particles initially reconstructed both as electrons and photons [49].

Category	Description	Name	Usage
Hadronic leakage	Ratio of E_T in the first layer of HCAL to the one of EM cluster ($\vert\eta\vert < 0.8$ and $\vert\eta\vert > 1.37$)	R_{had_1}	e/γ
	Ratio of E_T in HCAL to the one of EM cluster ($0.8 < \vert\eta\vert < 1.37$)	R_{had}	e/γ
EM third layer	Ratio of energy in the third layer to the total energy in ECAL	f_3	e
EM second layer	Ratio of sum of energies in the 3×7 to the one in the 7×7 $\eta \times \phi$ rectangle centered around the most energetic cell	R_η	e/γ
	Lateral shower width $\sqrt{(\sum E_i\eta_i^2)/(\sum E_i) - ((\sum E_i\eta_i)/(\sum E_i))^2}$, within a window of 3×5 cells	w_{η_2}	e/γ
	Ratio of sum of energies in the 3×3 to the one in the 3×7 $\eta \times \phi$ rectangle centered around the most energetic cell	R_ϕ	e/γ
EM first layer	Total lateral shower width $\sqrt{(\sum E_i(i - i_{\mathrm{max}})^2)/(\sum E_i)}$, within a window of $\Delta\eta \approx 0.0625$ where i_{max} is the index of the highest-energy cell	w_{stot}	e/γ
	Lateral shower width $\sqrt{(\sum E_i(i - i_{\mathrm{max}})^2)/(\sum E_i)}$, within a window of 3 cell around the most energetic	w_{s3}	γ
	Energy fraction outside core of three central cells, within seven cells	f_{side}	γ
	Difference between the energy of the second maximum cell, and the energy of the smallest cell between the first and second maxima	ΔE_s	γ
	Ratio of the energy difference between the first and second maximum cells in clusters to the sum of theses energies	E_{ratio}	e/γ
	Ratio of the energy measured in the first layer to the total energy of the ECAL	f_1	e/γ
Track conditions	Number of hits in the innermost pixel layer	$n_{\mathrm{innermost}}$	e
	Number of hits in the pixel detector	n_{Pixel}	e
	Total number of hits in the pixel and SCT	n_{Si}	e
	Transverse impact parameter relative to the beam-line	d_0	e
	Significance of transverse impact parameter w.r.t. its uncertainty	$\vert d_0/\sigma(d_0)\vert$	e
	Momentum loss by the track between the perigee and the last measurement point divided by the momentum at perigee	$\Delta p/p$	e
	Likelihood probability based on transition radiation in the TRT	$\mathrm{eProbabilityHT}$	e
Track-cluster matching	$\Delta\eta$ between cluster position in the first layer of ECAL and the extrapolated track	$\Delta\eta_1$	e
	$\Delta\phi$ between the cluster position in the second layer of ECAL and the momentum-rescaled track	$\Delta\phi_{\mathrm{res}}$	e
	Ratio of the cluster energy to the measured track momentum	E/p	e

Table 3.4: Discriminating variables used for electron and photon identification. The usage column indicates if the variables are used for the identification of electrons, photons, or both [49].

at low E_{T}. For larger values of E_{T}, additional systematic uncertainties of $\pm 0.5\%$, $\pm 1.0\%$, $\pm 1.5\%$ assigned due to variations in the electron efficiency with E_{T} for Loose, Medium and Tight identification, respectively, limiting the precision. Besides, the ratio of efficiency measured by data and simulation is calculated as scale factors to be applied in the offline analysis.

The identification of photon is based on a set of selection on several discriminating variables related to the longitudinal and lateral shower development in the EM calorimeter, and the shower leakage to the hadronic calorimeter. These variables take advantage of the fact that prompt photons tend to produce a narrower shower and smaller leakage to the HCAL compared to photons from hadronic jets and $\pi^0 \to \gamma\gamma$. The photon identification criteria are optimized using MC simulation of γ+jet, $\gamma\gamma$, H$\to$ $\gamma\gamma$, as well as the sample of background photons in QCD dijets events. Three working points defined as Tight, Medium, and Loose are provided by the ATLAS experiment. The Loose working points are typically used for one-photon and two-photon triggering and are defined by several shower shape variables. The Medium working

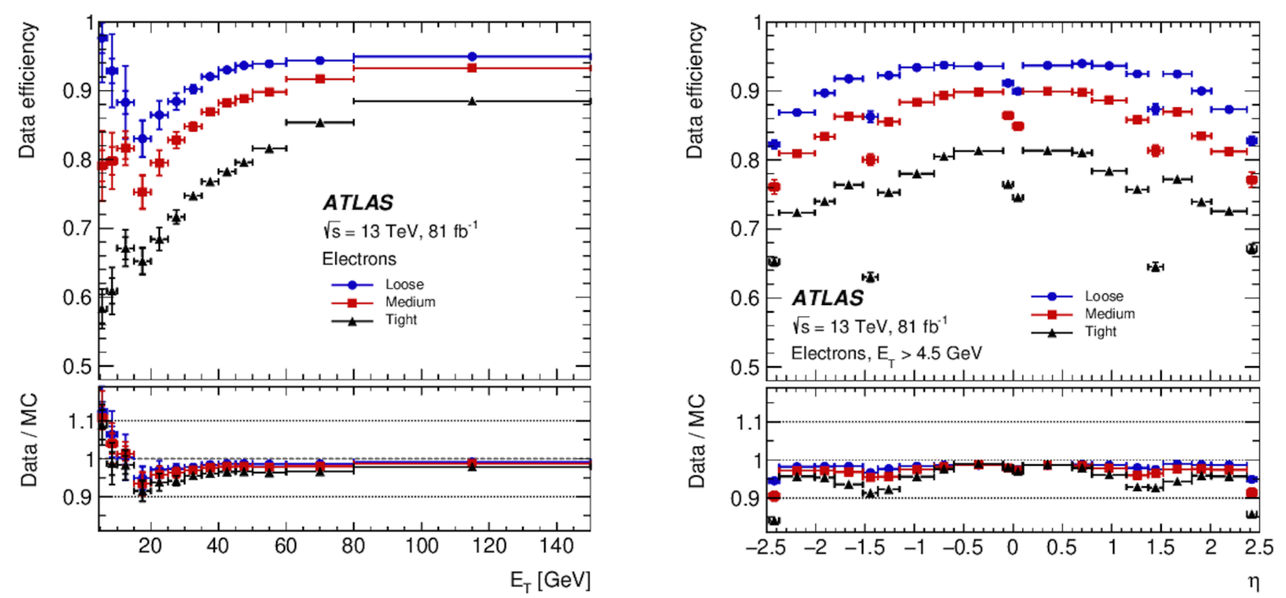

Figure 3.27: The electron identification efficiency in Z→ ee events in data as a function of E_{T} (left) and as a function of η (right) for the Loose, Medium and Tight operating points. The efficiencies are obtained by applying data-to-simulation efficiency ratios measured in $J/\psi \to ee$ and Z→ ee events to Z→ ee simulation. The inner uncertainties are statistical and the total uncertainties are the statistical and systematic uncertainties in the data-to-simulation efficiency ratio added in quadrature. For both plots, the bottom panel shows the data-to-simulation ratios [49].

points include all selection requirements of the Loose working point in addition to a loose choice of E_{ratio} (the ratio of the energy difference between the largest energy deposition and the second largest energy deposition in the cluster to the sum of the two energies) for triggering, which is mainly used in the case of the high pileup. The Tight working points are mainly used for the offline analysis. It uses the full granularity information of the calorimeter including the fine structure information of the first sampling layer. Moreover, a multivariate algorithm is used to optimize the power of the discrimination and the optimization is applied separately for both converted and unconverted photons (the Loose and Medium working treat the converted and unconverted photons identically). The main difference between the shower shapes of the converted and unconverted photon is the opening angle of the converted $e^{+}e^{-}$ pair, which is amplified under the magnetic field and also has additional reactions with the upstream material of the calorimeter. The efficiency of photon identification is measured by using data and simulated samples with three different methods: photons from final state radiation of the Z boson decay (Z→ $\ell\ell\gamma$); photons from an exclusive photon sample with a matrix method; photons emulated by the electron shower shape of Z→ ee. These three methods of efficiency measurement are performed using different processes, with different event topologies that may impact the photon efficiency. Fig. 3.28 shows the Tight identification efficiencies for unconverted and converted photons for these three methods. The data to MC scale factors are also shown for each measurement separately. Within their statistical and systematic uncertainties, results agree with each other.

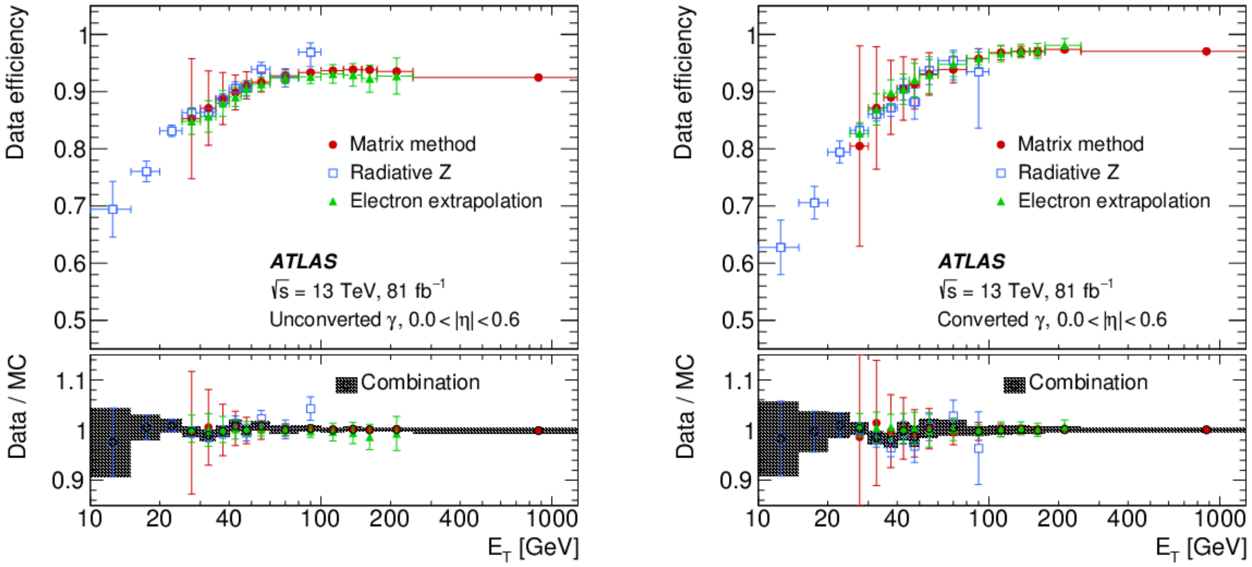

Figure 3.28: Photon identification efficiency, and the ratio of data to MC efficiencies, for unconverted photons (left) and converted photons (right) with the requirement of Loose isolation applied as pre-selection, as a function of E_T in the region of $|\eta| < 0.6$. The combined scale factor obtained using a weighted average of scale factors from the individual measurements is also presented; the band represents the total uncertainty [49].

Electron and photon isolation

Hadrons in jets which leave active signal in the detector, can be misidentified as electrons or photons, while the signature from real electrons and photons is more discrete and clean. In order to further improve the false signal rejection rate, the candidates are required to have less surrounded activities, which are quantifies by the isolation variables.

The isolation variables are generally defined with the charged tracks or calorimeter clusters near the candidate. The calorimeter isolation $E_{\mathrm{T}}^{\text{cone20}\,(40)}$ represents the sum of transverse energy of the clusters in the cone size of $\Delta R = 0.2\,(0.4)$ around the electron or photon, and the track isolation $p_{\mathrm{T}}^{\text{cone20}}$ represents the sum of the transverse momentum of the tracks in the cone size of $\Delta R = 0.2$ around the electron or photon where tracks matched to the electron or converted photon are excluded, and $p_{\mathrm{T}}^{\text{varcone20}}$ represents the sum of the transverse momentum of the tracks in the cone size of $\Delta R = \text{min}(10/p_{\mathrm{T}}, 0.2)$ around the electron or photon. They are computed as follows:

$$E_{\mathrm{T}}^{\text{cone20}} = E_{\mathrm{T,raw}}^{\text{iso20}} - E_{\mathrm{T,core}} - E_{\mathrm{T,leakage}}(E_{\mathrm{T}}, \eta, \Delta R) - E_{\mathrm{T,pileup}}(\eta, \Delta R) \tag{3.15a}$$

$$p_{\mathrm{T}}^{\text{cone20}} = \sum_{t \in cone} p_{\mathrm{T}}^{t} - p_{\mathrm{T}}^{e,\text{track}} / p_{\mathrm{T}}^{\text{converted}\,\gamma,\text{cluster}} \tag{3.15b}$$

where the $E_{\mathrm{T,raw}}^{\text{iso}}$ is the raw calorimeter isolation, $E_{\mathrm{T,core}}$ is the energy of the EM calorimeter cells contained in a $\Delta\eta \times \Delta\phi = 5 \times 7$ (in EM-middle-layer units) rectangular cluster around the barycentre of the EM particle cluster.

For electrons, different isolation working points are shown in Table 3.5. For photons, the requirements of different isolation working points are shown in Table 3.6. The working point of most of the photon analyses is the loose.

Working point	Calorimeter isolation	Track isolation
Gradient	$\epsilon = 0.1143 \times p_{\mathrm{T}} + 92.14\%$ (with $E_{\mathrm{T}}^{\text{cone20}}$)	$\epsilon = 0.1143 \times p_{\mathrm{T}} + 92.14\%$ (with $p_{\mathrm{T}}^{\text{varcone20}}$)
HighPtCaloOnly	$E_{\mathrm{T}}^{\text{cone20}} < \text{max}(0.015 \times p_{\mathrm{T}}, 3.5\,\text{GeV})$	-
Loose	$E_{\mathrm{T}}^{\text{cone20}}/p_{\mathrm{T}} < 0.20$	$p_{\mathrm{T}}^{\text{varcone20}}/p_{\mathrm{T}} < 0.15$
Tight	$E_{\mathrm{T}}^{\text{cone20}}/p_{\mathrm{T}} < 0.06$	$p_{\mathrm{T}}^{\text{varcone20}}/p_{\mathrm{T}} < 0.06$

Table 3.5: Definition of the electron isolation working points and isolation efficiency ϵ. In the Gradient working point definition, the unit of p_{T} is GeV. All working points use a cone size of $\Delta R = 0.2$ for calorimeter isolation and $\Delta R_{\text{max}} = 0.2$ for track isolation.

Working point	Calorimeter isolation	Track isolation
Loose	$E_{\mathrm{T}}^{\text{cone20}} < 0.065 \times E_T$	$p_{\mathrm{T}}^{\text{cone20}}/E_T < 0.05$
Tight	$E_{\mathrm{T}}^{\text{cone40}} < 0.022 \times E_T + 2.45\,\text{GeV}$	$p_{\mathrm{T}}^{\text{cone20}}/E_T < 0.05$
TightCaloOnly	$E_{\mathrm{T}}^{\text{cone40}} < 0.022 \times E_T + 2.45\,\text{GeV}$	-

Table 3.6: Definition of the photon isolation working points.

The efficiencies of the corresponding isolation working points for electrons and photons are shown in Fig. 3.29, where the electrons are required to fulfil the Medium selection from the likelihood-based electron identification.

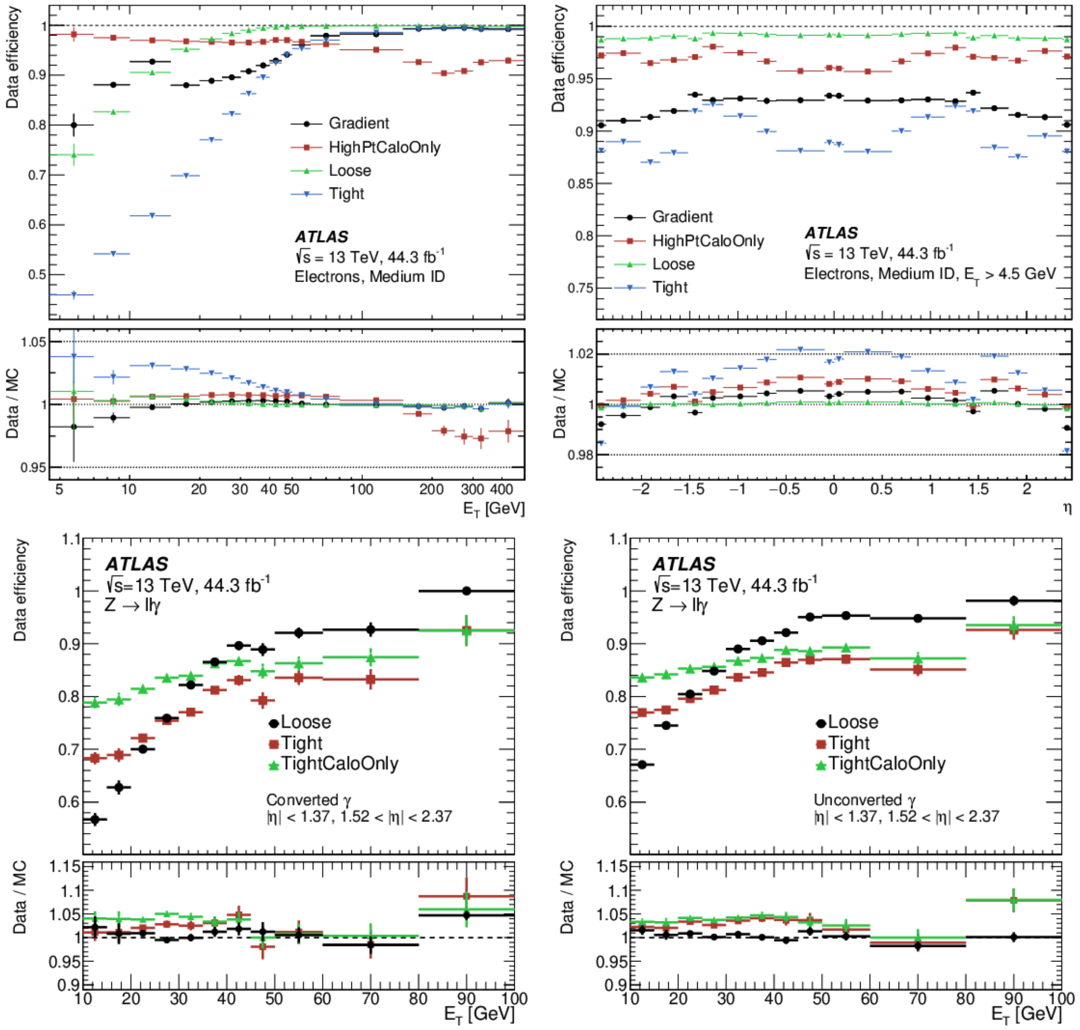

Figure 3.29: Efficiency of the different isolation working points for electrons and photons from inclusive Z$\rightarrow ee$ and Z$\rightarrow \ell\ell\gamma$ events as a function of the electron E_T (top left), electron η (top right), and converted or unconverted photon E_T (bottom). The lower panel shows the ratio of the efficiencies measured in data and in MC simulations. The total uncertainties are shown, including the statistical and systematic components [49].

3.3.2 Jet Reconstruction and Flavour Tagging

Jets, as the product of the hadronization of quarks or gluons, consist of collimated charged and neutral hadrons. It is an essential piece of the physics program due to its frequent presence in signal processes and various backgrounds. A jet has fruitful activity in both the inner detector and the calorimeters, where the charged hadrons deposit energies in ID, and the hadronic shower is in the calorimeters with most of them in HCAL.

In order to reconstruct the jet, calorimeter cells are first clustered into topo-clusters (similar to electron and photon in Sec. 3.3.1) and the anti-k_t algorithm [53] with a radius parameter of $R = 0.4$. The anti-k_t algorithm relies in the distance measures:

$$d_{ij} = \min\left(\frac{1}{k_{ti}^2}, \frac{1}{k_{tj}^2}\right)\frac{\Delta_{ij}^2}{R} \tag{3.16a}$$

$$d_{iB} = \frac{1}{k_{ti}^2} \tag{3.16b}$$

where d_{ij} and d_{iB} are respectively the distance between entities (particles, pseudo-jets) and the one between entity i and the beam (B), $\Delta_{ij}^2 = (y_i - y_j)^2 + (\phi_i - \phi_j)^2$ and k_{ti}, y_i and ϕ_i are respectively the transverse momentum, rapidity and azimuthal of entity i.

According to the definition of d_{ij}, between hard and soft particles, its value is exclusively determined by the transverse momentum of the hard one, hence the two particles will be combined if they are within the same core of a given radius R (i.e. $d_{1j} < d_{1B}$ where index 1 corresponds to the hard particle). Such kind of jets exploring only the calorimeter information is called EMtopo jets.

Then combining both the tracking and calorimeter information, the PFlow jets are reconstructed based on the particle flow algorithm [54]. Specifically, energy deposited in the calorimeter by charged particles is subtracted from the observed topo-clusters and replaced by the momenta of tracks that are matched to those topo-clusters [55]. For all tracks up to $p_T^{\mathrm{trk}} = 100$ GeV, the subtraction is performed unless the energy E^{clus} in a cone of size $\Delta R = 0.15$ around the extrapolated particle satisfies

$$\frac{E^{\mathrm{clus}} - < E_{\mathrm{dep}} >}{\sigma(E_{\mathrm{dep}})} > 33.2 \times \log_{10}(40\ \mathrm{GeV}/p_T^{\mathrm{trk}}) \tag{3.17}$$

where $< E_{\mathrm{dep}} >$ is the expected mean energy deposit by pions and $\sigma(E_{\mathrm{dep}})$ its expected standard deviation.

Consequently, for low track momenta, where the track resolution is supposed to be better than the one of the calorimeter, the subtraction is often performed, unless the deposited energy in the calorimeter is very high. While with the increased calorimeter resolution at large momenta, the algorithm slowly tends to retain the calorimeter information. Above $p_T^{\mathrm{trk}} = 100$ GeV, the subtraction is no longer performed which makes the PFlow identical to EMtopo one.

Such treatment improves the jet energy and angular resolution, reconstruction efficiency and stability with respect to pileup.

Jets (with $|\eta| < 2.5$) can be classified as light flavour (light quarks and gluon) jets, c-jets or b-jets. The b-jet can be used to study some specific processes, for instance, the Higgs to $b\bar{b}$ decay. The b-hadrons from the b-jet usually lead to displaced vertices and significant features on the impact parameters of tracks. The jet flavour is determined using a deep-learning neural network named as DL1r, which is trained with fruitful features from tracks and calorimeters, such as jet transverse momentum and pseudorapidity, likelihood ratios between different flavour hypotheses (b, c, light), variables associated to a secondary vertex (number of tracks, invariant mass of tracks, distance between secondary and primary vertices, etc.).

The performance of the b-tagging is evaluated with an inclusive $t\bar{t}$ MC. Fig. 3.30 shows the b-tagging efficiency versus the rejection rate for light flavour and c-jets. Different working points are thus defined as the thresholds on the DL1r output discriminant, which give fixed b-tagging efficiency, for instance, 85%, 77%. 70% and 60%.

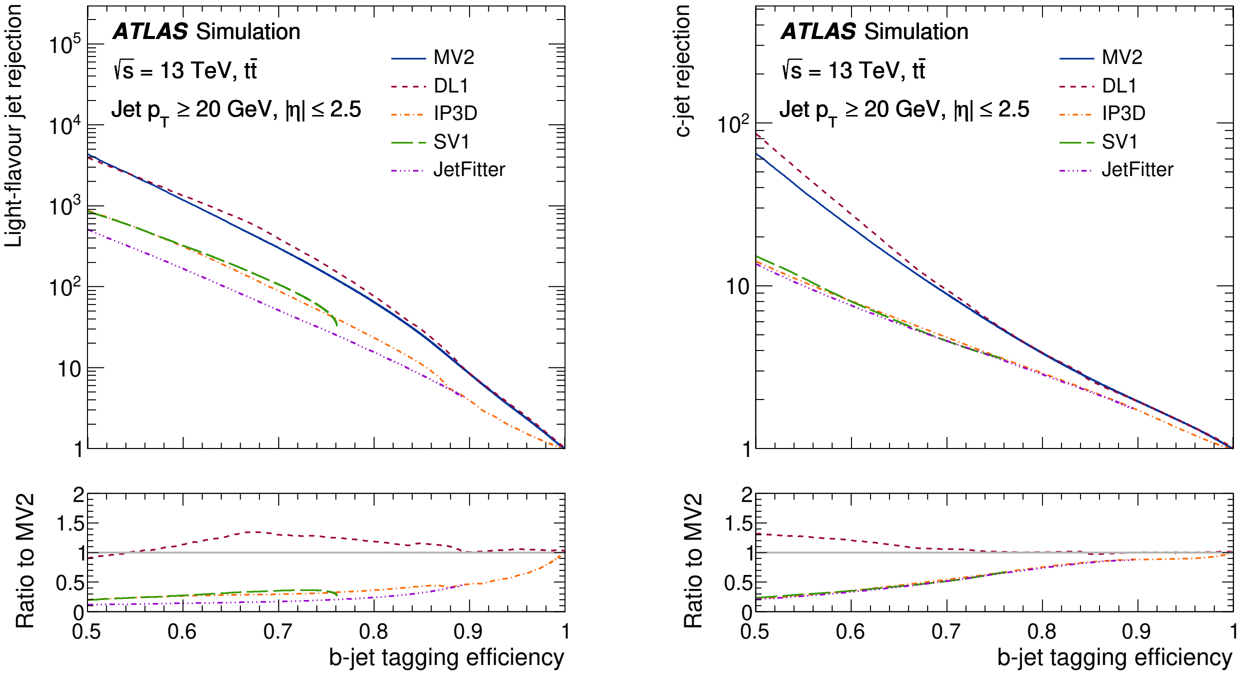

Figure 3.30: (left) light-flavour jet and (right) c-jet rejections versus the b-jet tagging efficiency for the various b-tagging algorithms evaluated on the baseline $t\bar{t}$ events [56].

The state-of-art DL1r algorithm achieves a better b-tagging performance with a higher rejection on other flavours at the same efficiency for b-jets, with respect to the others used in the past.
The working point used in the $HH \to b\bar{b}\gamma\gamma$ analysis [57] corresponds to an efficiency of 77% for jets containing b-hadrons, and the mis-identification rate is 1/130 (1/4.9) for light flavour (charm) jets. Scale factors are applied to the simulated events, to correct for differences in b-tagging efficiency between data and simulation. There scale factors are measured as a function of the jet p_T using a likelihood-based method in a sample with enhanced $t\bar{t}$ events [56].

3.4 Upgrade for HL-LHC

As mentioned in Fig. 3.6, the current LHC will be upgraded to a high luminosity version after the long shutdown 3 in 2029. In order to achieve the target integrated luminosity of 3000 fb^{-1} which is twenty times as the current recorded one of Run 2, the main parameters foreseen for the HL-LHC [58] are listed in Tab. 3.7, respectively for different bunch filling schemes. As compared to the design of the current LHC, the HL-LHC benefits from a doubled number of protons per bunch N_b, which brings a nearly doubled beam current, reduction on the β function and normalized emittance ϵ_n. In addition, the crab-cavity modules used to compensate for the bunch crossing angle can further improve the luminosity. All these upgrades contribute to the improvement of luminosity at the HL-LHC.

Parameter	**Nominal LHC (design report)**	**HL-LHC 25 ns (standard)**	**HL-LHC 25 ns (BCMS)**	**HL-LHC (8b4e)**
Beam energy in collision [TeV]	7	7	7	7
N_b $[10^{11}]$	1.15	2.2	2.2	2.3
n_b	2808	2748	2604	1968
Beam current $[A]$	0.58	1.09	1.03	0.82
Minimum β^* [m]	0.55	0.2	0.2	0.2
ϵ_n [μm]	3.75	2.50	2.50	2.20
ϵ_L [eVs]	2.50	2.50	2.50	2.50
Total reduction factor R_0 without crab cavities at min. β^*	0.836	0.369	0.369	0.369
Total reduction factor R_0 without crab cavities at min. β^*	(0.981)	0.715	0.715	0.740
Peak luminosity with crab cavities $L_{\text{peak}} \times R_1/R_0$ $[10^{34}\ \text{cm}^{-2}\text{s}^{-1}]$	(1.18)	12.6	11.9	11.6
Levelled luminosity for $\mu = 140$ $[10^{34}\ \text{cm}^{-2}\text{s}^{-1}]$	-	5.32	5.02	5.03
Events/crossing μ (with levelling and crab cavities)	27	140	140	140
Maximum line density of pile-up events during fill [events/mm]	0.21	1.3	1.3	1.3

Table 3.7: High Luminosity LHC main parameters for proton collisions and comparison with respect to the nominal LHC design [58].

Apart from the upgrade on collider, the experiments also need to be upgraded to suit the new high luminosity environment.

For the project of the ATLAS detector upgrade [59, 60], all the pixels and strips in the inner detector are going to be replaced by an all-silicon inner Tracker (ITK) [61], in order to satisfy the largely increased signal intensity and device occupancy, as well as the hardness to the much higher radiations. With the new ITK, the coverage on η is extended from 2.5 (current) to 4. In order to separate vertices from different pp collisions in a very high pileup environment (~ 140), a High Granularity Timing Detector (HGTD) [62] will be used to track the Z_0 information of vertices, which will be installed in the forward region ($2.4 < |\eta| < 4.0$). Other upgrades include the new sub-detectors in the muon chamber, improved electronics, trigger and data acquisition system.

For the upgrade project of the CMS detector [63], the tracker [64] will consist of about 200 m^2 silicon modules, with increased granularity and extended η acceptance up to 3.8. A MIP Timing Detector (MTD) [65] will be installed to give timing information for MIPs with 30-40 ps resolution, which helps to assign charged tracker to the correct interaction vertices. The readout electronics of the calorimeter will be replaced in order to cope with increased pileup events and to provide the needed timing resolution. The muon systematics and the triggers will be also upgraded.

3.5 Conclusion

In this chapter, an overview of the large hadron collider and the ATLAS detector has been presented. In particular, the structure and functions of the ATLAS ECAL are presented, as well as the relevant reconstruction and identification of electrons and photons. The upgrade project for HL-LHC and the ATLAS and CMS detectors are also introduced.

4 - Search for Higgs pair production in the $b\bar{b}\gamma\gamma$ final state

4.1 Double Higgs Production

As described in Eq. 1.31, the Higgs mechanism predicts the existence of the Higgs boson which has self-coupling interactions:

$$\mathcal{L} = \frac{1}{2}\partial_\mu h \partial^\mu h - \frac{1}{2} m_H^2 h^2 - g_{hhh} h^3 - g_{hhhh} h^4 \tag{4.1}$$

In case of the SM:

$$m_H^2 = -2\mu^2,\ g_{hhh} = \lambda v,\ g_{hhhh} = \frac{\lambda}{4} \tag{4.2}$$

The quartic coupling is nearly out of reach with the current data recorded in LHC. Nevertheless, the direct measurement of trilinear coupling is possible by probing the Higgs pair production. At leading order (LO), the Higgs pair production is mainly produced via gluon-gluon fusion (ggF), with two representative Feynman diagrams (Fig. 4.1). The so-called triangle diagram includes the trilinear Higgs coupling and produces two on-shell Higgs bosons, with an intermediate off-shell Higgs originating from a triangle quark loop dominated by top quark. The second diagram, the so-called box, involves a quark loop and produces also two on-shell Higgs bosons. The theory predicts a destructive interference between the triangle and the box diagrams, resulting in a total cross section of 31.02 fb computed at next-to-next-to-leading-order (NNLO) for 13 TeV center of mass energy and for a Higgs boson mass of around 125 GeV.

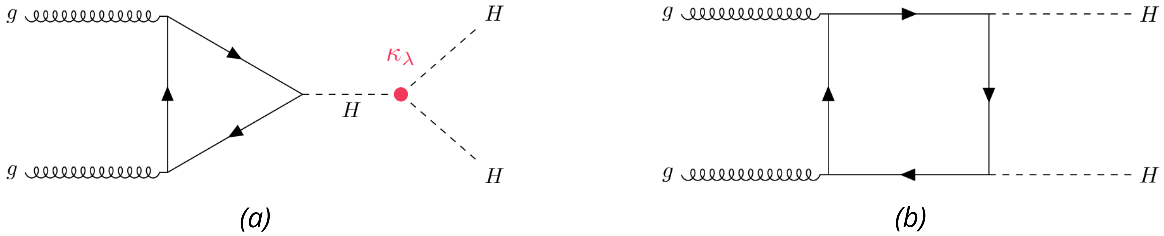

Figure 4.1: Feynman diagrams for the dominant Higgs pair production via gluon-gluon fusion, with (a) trilinear coupling, (b) box diagram. κ_λ is the Higgs self-coupling modifier [57].

A secondary contribution to Higgs pair production is the vector boson fusion (VBF) process with three main diagrams (Fig. 4.2). Under the assumption of the SM, the diagrams (a) and (c) compensate at the tree level, eventually, the production is dominated by the tri-linear diagram (b). The total cross section predicted by the SM is 1.73 fb calculated at next-to-next-to-next-to-leading order (N3LO).

The Higgs self-coupling modifier κ_λ is defined as the ratio between the measured trilinear coupling and the SM prediction.

$$\kappa_\lambda = g_{hhh}/g_{hhh}^{SM} \tag{4.3}$$

The VBF production includes also a diagram with the $VVHH$ coupling, from which one can define the relevant coupling modifier $\kappa_{2\mathrm{V}}$. In this analysis, $\kappa_{2\mathrm{V}}$ is fixed to 1, as the SM model prediction. Some on-going study is currently preceding in the group in order to study the $\kappa_{2\mathrm{V}}$ coupling, and will be published soon.

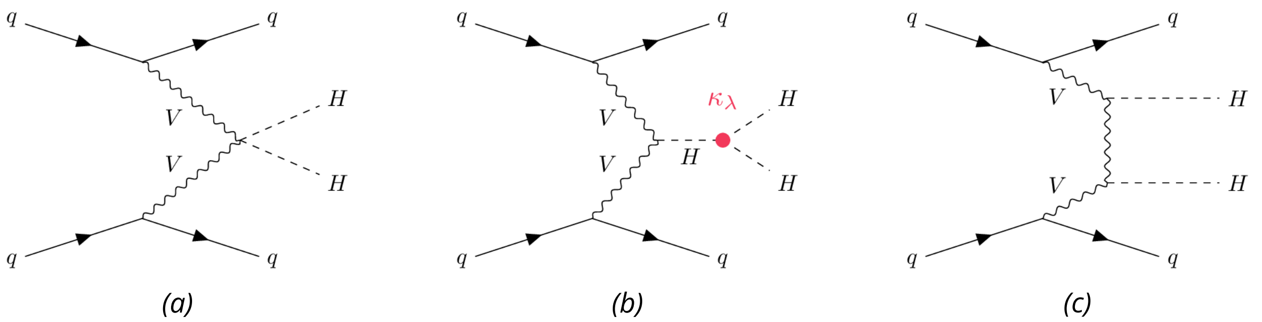

Figure 4.2: Feynman diagrams for the vector boson fusion production processes: (a) $VVHH$ vertex, (b) trilinear coupling, and (c) VVH vertex [57].

Although the cross section of the SM di-Higgs production is small (32.75 fb) which is almost one thousand times smaller than the single Higgs production, significant growth in the production rate can appear with anomalous Higg self-coupling κ_λ (Fig. 4.3), and increases the sensitivity to search for such kind of di-Higgs signal.

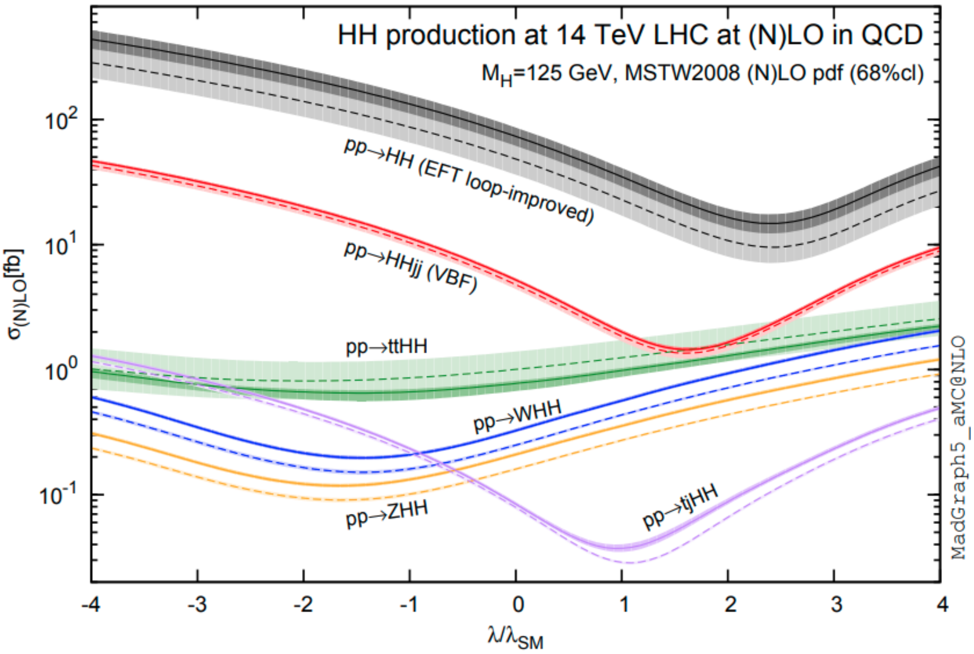

Figure 4.3: Evolution of di-Higgs production cross section with κ_λ [66].

Among the various Feynman diagrams, the triangle one prefers a softer di-Higgs mass (Fig. 4.4) due to the intermediate off-shell Higgs boson, while the ggF box one as well as the $VVHH$ and VVH ones via VBF production are more enhanced at high mass. This indicates a possibility to maximize the sensitivity of the Higgs self-coupling by exploring the low di-Higgs mass region.

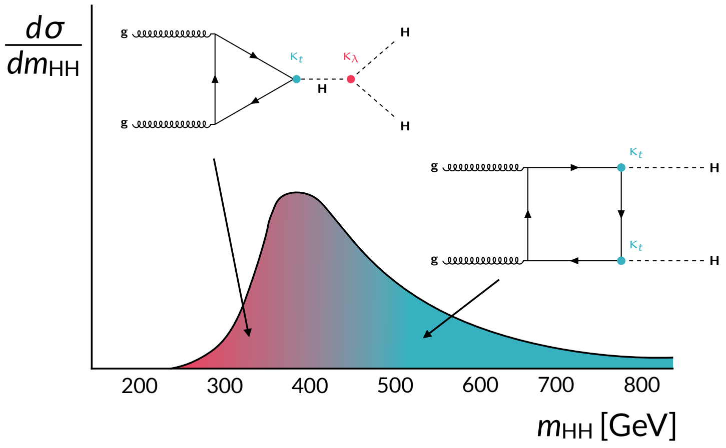

Figure 4.4: Sketch of the variant di-Higgs mass spectrum for gluon-gluon fusion process in SM [67].

Such kind of signal leaves no steep peak in the di-Higgs invariant mass spectrum, hence is called non-resonant production or signal in the context of this analysis.

In addition to the non-resonant HH signal, the analysis has also an interest in exploring new resonant particles, which are indeed predicted by the many BSM theories. In this analysis, a new CP-even scalar heavy particle similar to the Higgs is explored, which decays into two on-shell SM Higgs, as shown in Fig. 4.5. Such kind of new heavy scalar is predicted by several BSM theories, for instance, the two Higgs Doublet Model (2HDM) which extends the Higgs sector by a CP-even scalar heavy Higgs, two charged Higgs, and a CP-odd pseudoscalar [68]. In some theories, di-Higgs production can be enhanced through the presence of a graviton or radion, however current experimental limits [69] exclude these models for low-mass resonances.

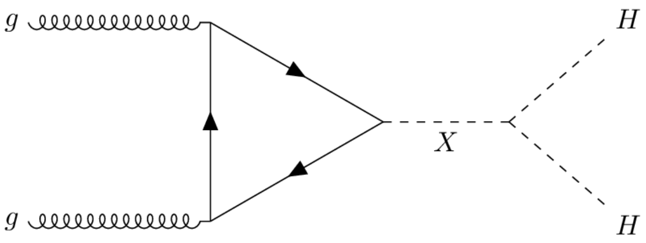

Figure 4.5: Feynman diagram of resonant HH production with a new scalar as intermediate particle [57].

4.2 Overview of Channels

The Higgs pair production can be explored with various channels according to the decays of the Higgs pair (Fig. 4.6). Reviews of status and perspectives can be found in Ref. [70, 71] . The following channels have been probed using the full Run 2 data:

- **ATLAS**: $b\bar{b}\gamma\gamma$ [57], $b\bar{b}\tau\bar{\tau}$ [72][73], $b\bar{b}b\bar{b}$ [74][75][76], $b\bar{b}l\nu l\nu$ $(WW, ZZ, \tau\tau)$ [77].
- **CMS**: $b\bar{b}\gamma\gamma$ [78], $b\bar{b}\tau\bar{\tau}$ [79][80], $b\bar{b}b\bar{b}$ [81][82], $b\bar{b}$+leptons $(WW, \tau\tau, ZZ)$ [83][84], multi-leptons [85].

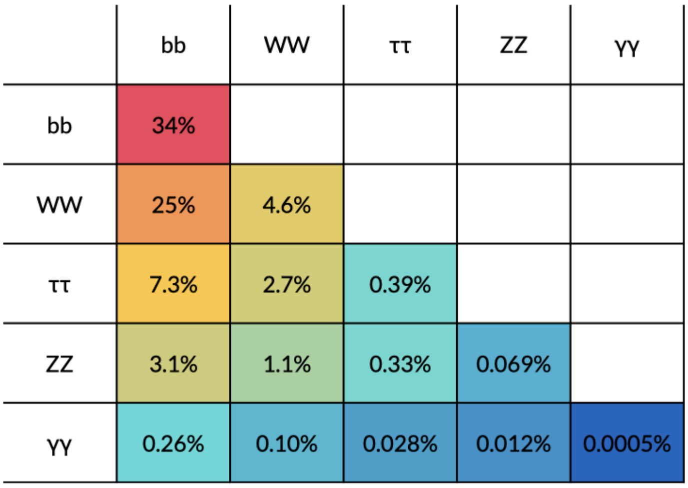

	bb	WW	ττ	ZZ	γγ
bb	34%				
WW	25%	4.6%			
ττ	7.3%	2.7%	0.39%		
ZZ	3.1%	1.1%	0.33%	0.069%	
γγ	0.26%	0.10%	0.028%	0.012%	0.0005%

Figure 4.6: HH production channels and branching ratios.

This analysis studies both the non-resonant and resonant HH production via the $b\bar{b}\gamma\gamma$ channel which benefits from both the largest branching ratio of $H \to b\bar{b}$ and the good resolution from the $H \to \gamma\gamma$ mass peak. For the non-resonant signal, the production rate and the Higgs self-coupling modifier κ_λ are studied, while for the resonant signal, the production rate as a function of the resonant mass hypotheses are also studied. Some update of the non-resonant $b\bar{b}\gamma\gamma$ channel is foreseen with further analysis (Ref. [86]), with emphasis n measurement/limit on $\kappa_{2\mathrm{V}}$. A limit on $\kappa_{2\mathrm{V}}$ deduced by the ATLAS $b\bar{b}b\bar{b}$ group can be found in Ref. [75]. CMS has explored $\kappa_{2\mathrm{V}}$ and excluded $\kappa_{2\mathrm{V}} = 0$ [87].

4.3 Data and Simulation Samples

The analysis [57] uses the full Run 2 pp collision data collected by the ATLAS experiment from 2015 to 2018 at a center of mass energy of $\sqrt{s} = 13$ TeV. After data quality requirements, the full dataset represents an integrated luminosity of 139 ± 2.4 fb^{-1}, with an averaged number of inelastic pp collisions per bunch crossing of 34.2.

The Monte Carlo samples (Tab. 4.1) are simulated for both signal and background. The background is mainly made of the continuum diphoton and single Higgs processes, where the continuum diphoton background includes $\gamma\gamma$, γj and jj components with jet misidentified as a photon. The fractions of components are estimated using a data-driven technique [88].

Process	Generator	PDF set	Showering	Tune
non-resonant ggF HH	Powheg Box v2 +FT	PDFLHC	Pythia 8.2	A14
non-resonant VBF HH	MadGraph5_aMC@NLO	NNPDF3.0nlo	Pythia 8.2	A14
Resonant ggF HH	MadGraph5_aMC@NLO	NNPDF2.3lo	Herwig 7.1.3	H7.1 - Default
ggF H	NNLOPS	PDFLHC	Pythia 8.2	AZNLO
VBF H	Powheg Box v2	PDFLHC	Pythia 8.2	AZNLO
WH	Powheg Box v2	PDFLHC	Pythia 8.2	AZNLO
$qq \rightarrow ZH$	Powheg Box v2	PDFLHC	Pythia 8.2	AZNLO
$gg \rightarrow ZH$	Powheg Box v2	PDFLHC	Pythia 8.2	AZNLO
$t\bar{t}H$	Powheg Box v2	NNPDF3.0nlo	Pythia 8.2	A14
$b\bar{b}H$	Powheg Box v2	NNPDF3.0nlo	Pythia 8.2	A14
tHq	MadGraph5_aMC@NLO	NNPDF3.0nlo	Pythia 8.2	A14
tHW	MadGraph5_aMC@NLO	NNPDF3.0nlo	Pythia 8.2	A14
$\gamma\gamma$+jets	Sherpa 2.2.4 [57]	NNPDF3.0nnlo	Sherpa 2.2.4	–
$t\bar{t}\gamma\gamma$	MadGraph5_aMC@NLO	NNPDF2.3lo	Pythia 8.2	–

Table 4.1: Summary of samples used for nominal Higgs boson pair signal and single-Higgs-boson background, split by production mode, and continuum background. The generator used in the simulation, the PDF set, and the set of tuned parameters (tune) are also provided [57].

The ggF non-resonant HH signal is generated at next-to-leading-order accuracy in QCD with finite top-quark mass in both the real and virtual corrections (NLO FT) [89], using the Powheg generator with the PDF4LHC15 parton distribution function (PDF) set.

The Pythia 8 generator is used for parton showering, hadronization and underlying-event simulation. Herwig 7 is used as an alternative generator to estimate the theory uncertainty from the parton shower generator. Samples are generated for coupling modifier values $\kappa_\lambda = 1$ and 10. A reweighting technique [90], which will be described in the next section, is used to generate any κ_λ signal sample by a linear combination of a basis of samples with $\kappa_\lambda = 0, 1, 20.$

For events from VBF HH production, MadGraph5_aMC@NLO is used to generate events at leading order (LO), interfaced with Pythia 8 for parton showering. Samples are generated at LO for four values of the coupling modifier $\kappa_\lambda = 0, 1, 2 \text{ and } 10$ and with all the other couplings equal to the SM predictions, such as κ_{2V} and κ_V, the $VVHH$ and VVH coupling modifiers. The cross section of the VBF HH process is evaluated at N3LO in QCD, and the N3LO-to-LO cross-section ratio at the SM value is calculated and this factor is applied to the VBF HH cross section.

The cross sections used for the HH signal generations are parameterized as a function of κ_λ with a second order polynomial, as shown in Fig. 4.7 where the values are taken from the LHC HH cross section working group [91]. GeV [16].

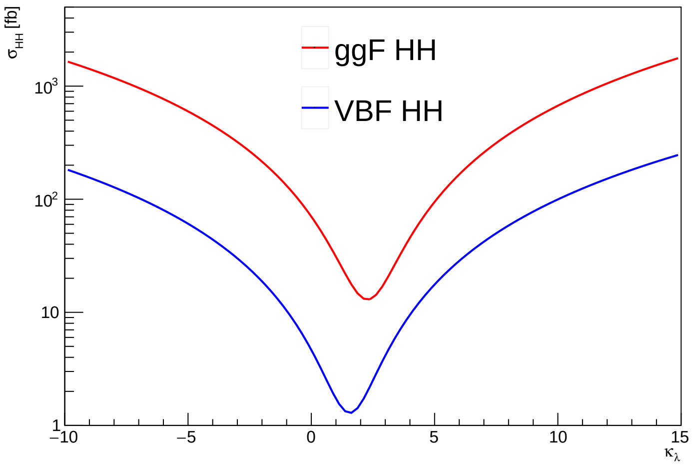

Figure 4.7: Cross section in the function of κ_λ for HH production via ggF and VBF.

The dominant background is the continuum, including $\gamma\gamma$, $\gamma\mathrm{jet}$ and dijets with additional jets. The two last correspond to the final states with jets misidentified as photons. The fractions of these components are estimated using a data-driven technique [88] based on photon identification and isolation. The $\gamma\gamma + \mathrm{jets}$ background is simulated with the Sherpa generator. QCD NLO-accurate matrix elements for up to one parton, and LO-accurate matrix elements for up to three partons, are calculated. These are calculated in the five-flavour scheme including b-quarks in the massless approximation and merged with the Sherpa parton shower. Within the parton shower, b-quarks were then treated as being massive. Events from $t\bar{t}\gamma\gamma$ processes are produced with MadGraph5_aMC@NLO in the four-flavor scheme.

Production of single Higgs bosons via ggF, VBF, WH, ZH ($qq \to ZH$ and $gg \to ZH$), $t\bar{t}H$, bbH, and tH (tHq and tHW) is modelled using the set of MC generation configurations in Tab. 4.1.

For both single Higgs boson production and di-Higgs signal, a Higgs boson mass of 125.09 GeV is assumed. The analysis assumes a branching ratio of 0.227% for the Higgs boson decay into two photons and a branching ratio of 58.2% for the Higgs boson decay into two b-quarks. The inclusive cross sections of these processes are normalized to the most precise available theoretical values.

The pileup effect is simulated in the MC, and the differences between the simulated and observed distributions of the number of interactions per bunch crossing are corrected for by applying pileup scale factors to simulated events. A full simulation of the ATLAS detector based on Geant4 is used to reproduce the detector response to single-Higgs-boson processes. The continuum background and signal samples are processed by AtlFastII [92], a fast simulation of the ATLAS detector response which is shown to be able to accurately simulate diphoton events.

4.4 κ_λ-reweighting Technique for Signal Sample Generations

In order to avoid generating numerous MC samples for various κ_λ, a reweighting technique is used to produce signal samples with a different hypothesis of κ_λ. The sample is obtained by applying correction weights to the SM variation of the ggHH production, as a function of the truth di-Higgs invariant mass m_{hh}. As shown in Fig. 4.1, at LO, the total amplitude $A(\kappa_\lambda)$ for a given value of κ_λ is the sum of the triangle (T) and the box (B) diagrams, which can be simply expressed as:

$$A(\kappa_\lambda) = B + \kappa_\lambda T \tag{4.4}$$

Hence the total cross section is expressed in the function of κ_λ:

$$\sigma(pp \to HH) \sim |B|^2 + \kappa_\lambda(B^*T + TB^*) + \kappa_\lambda^2|T|^2 \tag{4.5}$$

The basis of three generated samples $\kappa_\lambda = 0, 1, 20$ is used to derive the coefficients:

$$\begin{aligned} A(\kappa_\lambda = 0) = A(0) &= B \\ A(\kappa_\lambda = 1) = A(1) &= B + T \\ A(\kappa_\lambda = 20) = A(20) &= B + 20T \end{aligned} \tag{4.6}$$

Therefore the total cross section for a given κ_λ signal can be calculated through a linear combination of the three samples:

$$|A(\kappa_\lambda)|^2 = \left(1 + \frac{\kappa_\lambda^2}{20} - \frac{399}{380}\kappa_\lambda\right)|A(0)|^2 + \left(\frac{40}{38}\kappa_\lambda - \frac{2}{38}\kappa_\lambda^2\right)|A(1)|^2 + \frac{\kappa_\lambda^2 - \kappa_\lambda}{380}|A(20)|^2 \tag{4.7}$$

The method is also applied on the differential cross section, by deriving weights in the function of truth m_{hh} for each κ_λ value. It is validated by comparing the event yields and diphoton mass $m_{\gamma\gamma}$ distributions between the generated sample at $\kappa_\lambda = 10$ and the reweighted sample from $\kappa_\lambda = 1$ to $\kappa_\lambda = 10$. A systematic uncertainty of 3%-4% is assigned to the reweighting technique, by taking the maximum difference observed in this validation. More details will be introduced in the section on systematic uncertainties. The reweighting technique can be easily generated with additive degrees of κ modifiers, such as κ_t [90].

4.5 Event selection

4.5.1 Selection

Events are required to satisfy several photon-relevant selection:

- Events are required to pass triggers, requiring two reconstructed photon candidates with a minimum transverse energy of 35 GeV and 25 GeV respectively for the leading and subleading photons. The trigger also requires photon candidates to pass a loose quality photon identification criteria for 2015 and 2016, while for 2017-2018, due to the increased luminosity, a medium criteria is used.
- Events should contain at least two photons satisfying both the tight identification criteria and the Loose isolation criteria.
- The transverse momentum of the (sub)leading photon is required to be above 35% (25%) of $m_{\gamma\gamma}$.

- A neural network (NN) is trained to identify the diphoton vertex, and the one with the best NN score among the reconstructed vertices is selected. This NN gathers information about the longitudinal shower in the LAr calorimeter of the two photons, the scalar quadratic sum of the track transverse momentum associated with a vertex, and the azimuthal angle distance $\Delta\phi$ between tracks of this vertex and the diphoton system. Two NNs are trained respectively for the case with two unconverted photons, and the case with at least one converted photon. This specific diphoton vertex chosen algorithm leads to a better diphoton mass resolution as compared to the usual algorithm of ATLAS.
- The diphoton mass $m_{\gamma\gamma}$ reconstructed by the two leading photons is required to belong to the range [105, 160] GeV.

Another selection for jets and leptons is summarized below:

- Events should have exactly two b-tagged jets passing the 77% efficient working point. Jets are firstly ranked by their b-tagging scores then ranked by their transverse momentum. Any event with more than two such b-tagged jets is vetoed in order to be statistically orthogonal to the $HH \to b\bar{b}b\bar{b}$ channel.
- No electrons or muons are present, in order to suppress the top background.
- At most six jets should be present in the central region ($|\eta| < 2.5$) of the detector, which reduces mainly the $t\bar{t}H$ background, with hadronically decayed top quarks.

Events satisfying the above selection are plotted in $m_{\gamma\gamma}$ range from 105 GeV to 160 GeV in Fig. 4.9.

The background is dominated by the $\gamma\gamma$, γjet and dijets events, where the first corresponds to the genuine diphoton process, while the rest corresponds to events with either one or two jets misidentified as photons. The fractions of this component are estimated with a data-driven method called $2 \times 2D$ sideband method, which counts the number of photons and jets passing or failing the photon tight ID and loose isolation criteria. The phase space is divided into regions of leading/sub-leading photon, tight/non-tight ID and isolated/non-isolated, which gives one signal region (both photons are isolated and passing tight ID) and 15 control regions (Fig. 4.8). A loose identification is pre-requested for photons in all the 16 categories. The method solves the equations for the 16 categories, to obtained variables such as jet fakes tight ID photon, or isolated photon, etc. Of these variables, the efficiencies for the real photons are based on Monte Carlo simulation. Eventually the method extrapolates the fraction of fake photons within the signal region from the composition of the various control regions.

After the selection, in the $m_{\gamma\gamma}$ sideband defined outside the signal mass region 120 GeV $< m_{\gamma\gamma} <$130 GeV, (85 ± 3)% of the events are genuine diphoton events, with the remaining (15 ± 4)% consisting of γ–jet events and a negligible number of dijet events. The total background is normalized to the data sideband, and the single Higgs background and the di-Higgs signal are scaled to the SM predictions. At this stage, no significant discrepancy is observed between the data and the MC prediction.

4.5.2 Multivariables Selection and Categorization

A modified di-Higgs invariant mass $m^*_{b\bar{b}\gamma\gamma}$ benefiting from the correlations between the four bodies invariant mass $m_{b\bar{b}\gamma\gamma}$ and the two objects invariant masses $m_{b\bar{b}}$ and $m_{\gamma\gamma}$, is used to improve the di-Higgs mass resolution:

$$m^*_{b\bar{b}\gamma\gamma} = m_{b\bar{b}\gamma\gamma} - m_{b\bar{b}} - m_{\gamma\gamma} + 250 \text{ GeV} \tag{4.8}$$

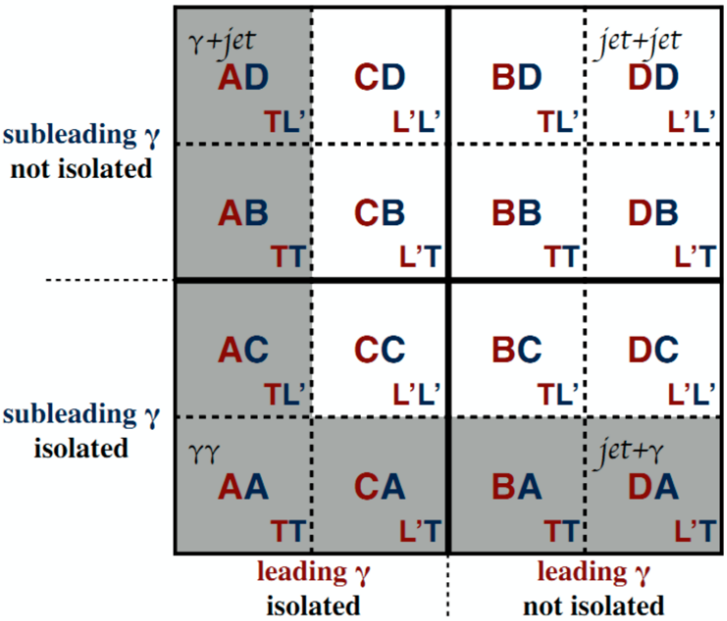

Figure 4.8: Signal region and 15 control regions in the $2 \times 2D$ sideband method based on photon identification and isolation, where A, B, C, D respectively refer to passing/failing the tight or isolation photon selection [93].

The $m^*_{b\bar{b}\gamma\gamma}$ distributions under different κ_λ hypotheses for both gluon-gluon fusion and vector boson fusion productions are shown in Fig. 4.10. For large κ_λ signals, the production is dominated by the trilinear diagram, which is enhanced more in the soft mass region due to the off-shell intermediate Higgs boson, in contrast, small κ_λ ones are more distributed at high mass.

A further selection is optimized for the non-resonant signals, using boosted decision trees (BDT). In order to prevent over-training, the MVA guideline of the analysis is to split the events into a training sample, a public test sample and a private test sample, which contain respectively 50%, 25% and 25% fractions of the events. The 50% training sample is designed to have sufficient events for the MVA model training, and the public test sample is used for the model hyperparameters optimization. Once the MVA model is frozen, its performance is evaluated with the rest 25% private test sample.

For the non-resonant signal, as seen in Fig. 4.10, there is a clear dependency of the di-Higgs mass on κ_λ. Hence two BDTs have been trained respectively in high mass ($m^*_{b\bar{b}\gamma\gamma} > 350$ GeV) and low mass ($m^*_{b\bar{b}\gamma\gamma} < 350$ GeV) regions. For high mass BDT, the SM ($\kappa_\lambda = 1$) sample is considered as the signal for training, while $\kappa_\lambda = 10$ signal is used for low mass BDT. The input training variables are listed in Tab. 4.2.

The single topness exploits the agreement of the system of jets with the W and t masses:

$$\chi_{Wt} = \min\sqrt{\left(\frac{m_{j_1 j_2} - m_W}{m_W}\right)^2 + \left(\frac{m_{j_1 j_2 j_3} - m_t}{m_t}\right)^2}, \tag{4.9}$$

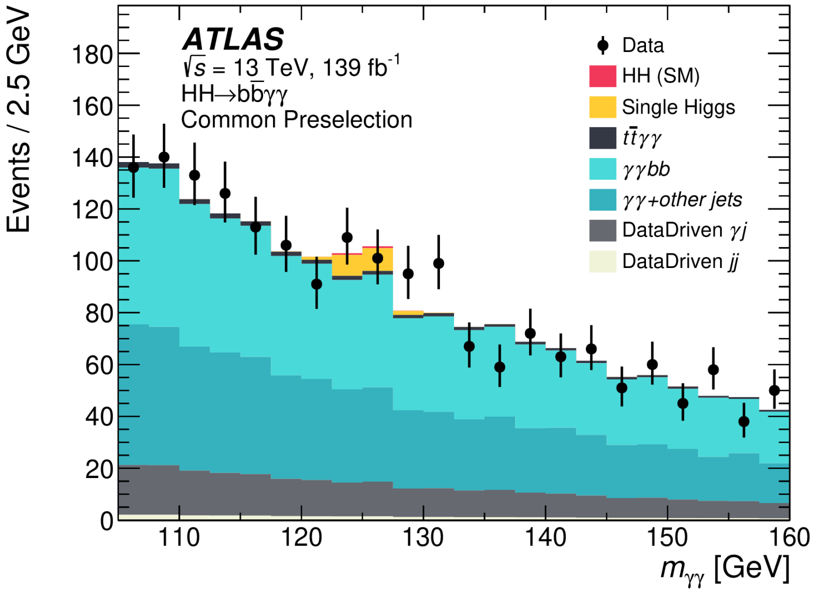

Figure 4.9: Diphoton invariant mass $m_{\gamma\gamma}$ distribution for events after the preselection. The black dots correspond to the data, the $\gamma\gamma$, γj and jj events are scaled by the data-driven scale factors and the total continuum background is normalized to the data sideband, while the single Higgs and HH signal are scaled to the SM prediction [57].

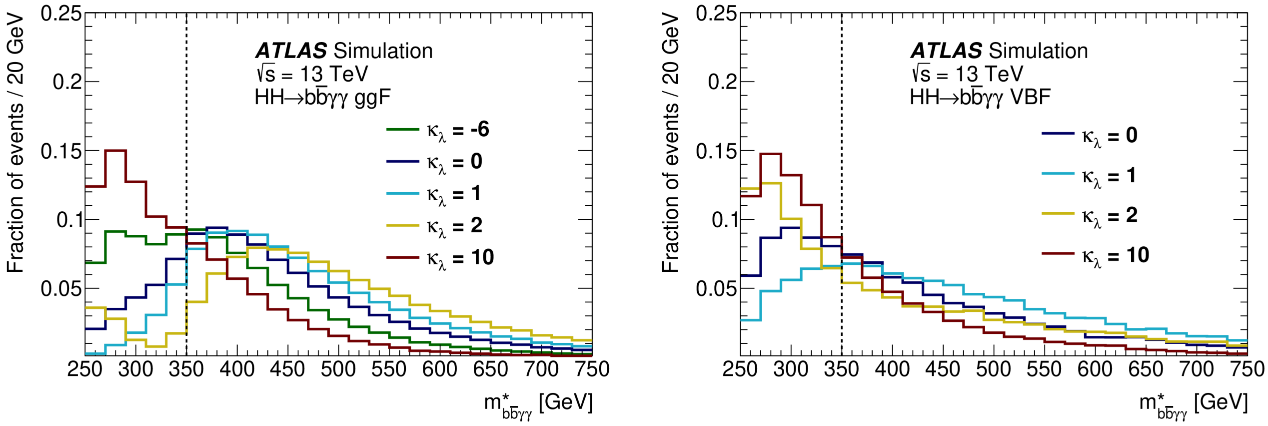

(a) *(b)*

Figure 4.10: Invariant mass distributions of two photons and two b-jets under different κ_λ hypotheses, via gluon-gluon fusion (a) and via vector boson fusion (b) [57].

Variable	Definition
Photon-related kinematic variables	
$p_T/m_{\gamma\gamma}$	Transverse momentum of each of the two photons divided by the diphoton invariant mass $m_{\gamma\gamma}$
η and ϕ	Pseudorapidity and azimuthal angle of the leading and subleading photon
Jet-related kinematic variables	
b-tag status	Tightest fixed b-tag working point (60%, 70%, or 77%) that the jet passes
p_T, η and ϕ	Transverse momentum, pseudorapidity and azimuthal angle of the two jets with the highest b-tagging score
$p_T^{b\bar{b}}$, $\eta_{b\bar{b}}$ and $\phi_{b\bar{b}}$	Transverse momentum, pseudorapidity and azimuthal angle of the b-tagged jets system
$m_{b\bar{b}}$	Invariant mass of the two jets with the highest b-tagging score
H_{T}	Scalar sum of the p_T of the jets in the event
Single topness	Variable to identify top quark as defined in Eq. (4.9)
Missing transverse momentum variables	
E_T^{miss} and ϕ^{miss}	Missing transverse momentum and its azimuthal angle

Table 4.2: Variables used in the BDT for the non-resonant analysis. All vectors in the event are rotated so that the leading photon ϕ is equal to zero, while their relative azimuthal angular differences are kept unchanged [57].

which is a useful variable to suppress the top background events.

The output BDT score is shown in Fig. 4.11 for different κ_λ signals, backgrounds and observed data. Signal-enhanced regions are considered for the final results, by cutting the BDT scores above certain thresholds. A simultaneous 2D scan is performed to locate the thresholds giving the best sensitivity. The two dashed vertical lines referring to the thresholds divide the spectrum into a tight score and a loose score category, while the low score events are discarded. With both high mass and low mass BDT, four categories are obtained for non-resonant signals. The thresholds for BDT categorization are shown in Tab. 4.3.

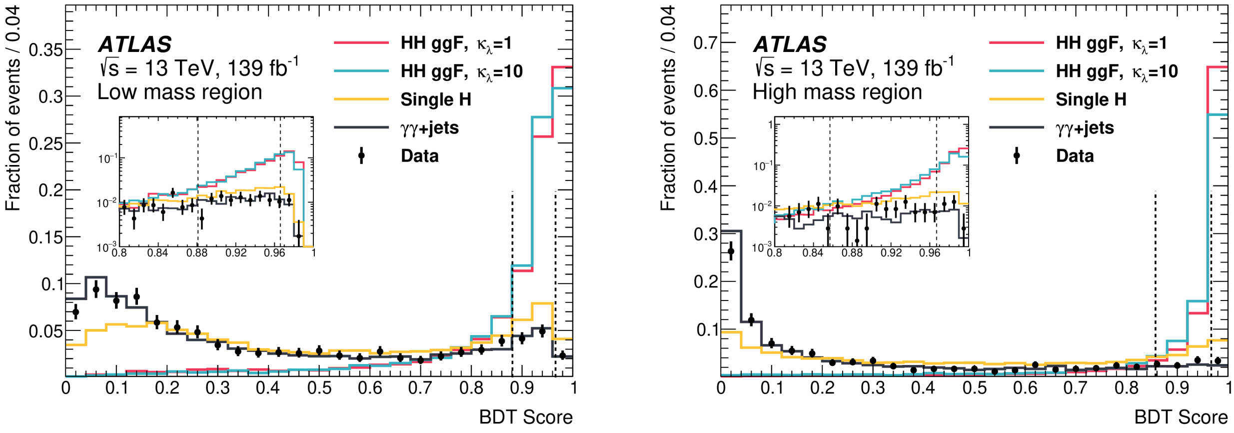

(a) Low mass BDT

(b) High mass BDT

Figure 4.11: Distributions of non-resonant BDT output, for (a) low mass region, and (b) high mass region [57].

The $m_{\gamma\gamma}$ distributions in the four signal categories are shown in Fig. 4.12. The data-derived fractions of

Category	Selection criteria
High mass BDT tight	$m^*_{b\bar{b}\gamma\gamma} > 350$ GeV, BDT score $\in [0.967, 1]$
High mass BDT loose	$m^*_{b\bar{b}\gamma\gamma} > 350$ GeV, BDT score $\in [[0.857, 0.967]$
Low mass BDT tight	$m^*_{b\bar{b}\gamma\gamma} < 350$ GeV, BDT score $\in [0.966, 1]$
Low mass BDT loose	$m^*_{b\bar{b}\gamma\gamma} < 350$ GeV, BDT score $\in [0.881, 0.966]$

Table 4.3: Definition of the four non-resonant categories defined by the $m^*_{b\bar{b}\gamma\gamma}$ regions and the BDT score thresholds [57].

non-resonant $\gamma\gamma$, γjet and dijet background are applied and the total background is normalized to the data sideband. Most probably due to statistical fluctuations, only two events have been observed in the mass window $120 \text{ GeV} \leq m_{\gamma\gamma} \leq 130 \text{ GeV}$ in the most sensitive high mass BDT tight category.

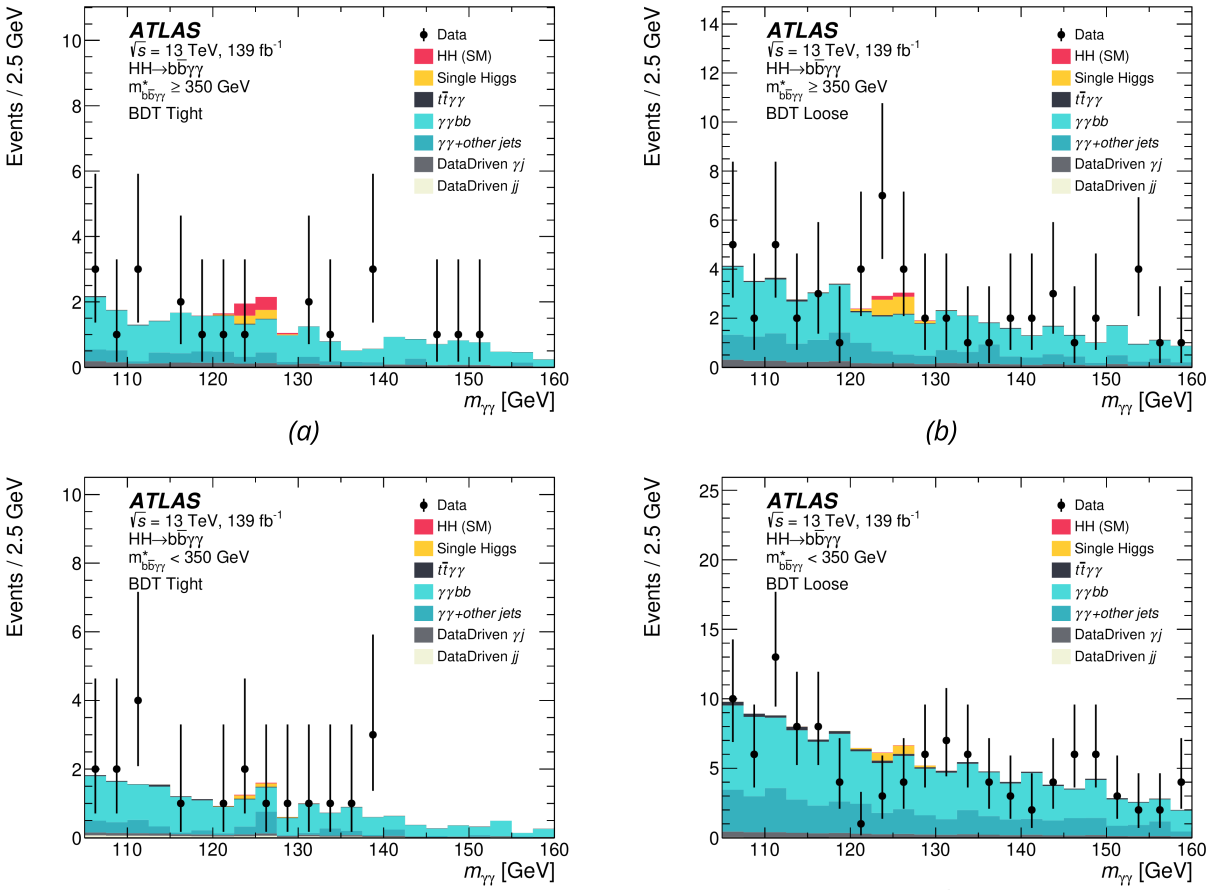

(a)

(b)

(c)

(d)

Figure 4.12: Distributions of $m_{\gamma\gamma}$ in various categories for the non-resonant HH analysis: (a) high mass BDT tight, (b) high mass BDT loose, (c) low mass BDT tight, (d) low mass BDT loose. [57].

4.6 Signal and Background Modelling

The single Higgs yields are fixed to the SM predictions, which are given by the MC simulation. The sum of yields for all the single Higgs processes is listed in Tab. 4.4, as well as the HH signal for both ggF and VBF productions at $\kappa_\lambda = 1$. In the high mass BDT tight category, the single Higgs production has a comparable yield with respect to the one of the di-Higgs process, while its contamination on signal is significantly increased in the three other categories, under the hypothesis of $\kappa_\lambda = 1$.

Yields	High Mass BDT tight	High Mass BDT loose	Low Mass BDT tight	Low Mass BDT loose
ggF HH ($\kappa_\lambda = 1$)	0.8733	0.3585	0.0471	0.0735
VBF HH ($\kappa_\lambda = 1$)	0.0128	0.0165	0.0033	0.0071
Sum of single Higgs	0.6668	1.6140	0.2348	1.5247

Table 4.4: Table of the di-Higgs ($\kappa_\lambda = 1$) and the single Higgs yields in the non-resonant BDT categories.

In order to interpolate between different κ_λ, a second order polynomial is used to parametrize the signal yields in the function of κ_λ (Tab. 4.5), respectively for ggF HH and VBF HH in each signal category.

Category	Yields ggF HH	Yields VBF HH
High Mass BDT tight	$1.56276 - 0.80348\kappa_\lambda + 0.12113\kappa_\lambda^2$	$0.04610 - 0.04709\kappa_\lambda + 0.01376\kappa_\lambda^2$
High Mass BDT loose	$0.69522 - 0.39900\kappa_\lambda + 0.06464\kappa_\lambda^2$	$0.03877 - 0.03045\kappa_\lambda + 0.00811\kappa_\lambda^2$
Low Mass BDT tight	$0.19526 - 0.20606\kappa_\lambda + 0.05781\kappa_\lambda^2$	$0.01885 - 0.02444\kappa_\lambda + 0.00889\kappa_\lambda^2$
Low Mass BDT loose	$0.32765 - 0.36127\kappa_\lambda + 0.10695\kappa_\lambda^2$	$0.03575 - 0.04573\kappa_\lambda + 0.01712\kappa_\lambda^2$

Table 4.5: Yields parametrization in the function of κ_λ for ggF HH and VBF HH signal in the four non-resonant BDT categories.

After normalizing the yields with respect to the luminosity and the theoretical cross sections as shown in Fig. 4.7, the efficiency[1] of the ggF HH signal in each category is shown in Fig. 4.13 for the various κ_λ hypotheses. The blue curves are the efficiencies obtained with the κ_λ-reweighted samples, where the statistical errors are plotted. The red points correspond to the generated $\kappa_\lambda = 10$ sample, with a generally good agreement with respect to the reweighted $\kappa_\lambda = 10$ sample. The largest discrepancy of around 6% is observed in the high mass tight category, which is considered as systematic uncertainty from the reweighting technique.

The striking evolution of efficiencies in the function of κ_λ is mainly due to the 350 GeV $m^*_{b\bar{b}\gamma\gamma}$ splitting and the signal hypothesis used for the BDT training. First of all, the events from $\kappa_\lambda = 1 \text{ and } 10$ are respectively used as signals for the training of the high mass and the low mass BDTs, therefore one expects them to have high efficiencies of the BDT cuts. As well as the kinematic dependency of $m^*_{b\bar{b}\gamma\gamma}$ in function

---

[1] It is actually acceptance times efficiency, for simplicity, the word efficiency will be used in all the following text.

of κ_λ, that for large absolute value of κ_λ, the di-Higgs production is dominated by the trilinear diagram which is softer in the $m^*_{b\bar{b}\gamma\gamma}$ spectrum. This leads to the decrease of efficiency in the high mass categories when κ_λ is far from zero, as well as the increase in efficiency in the low mass categories.

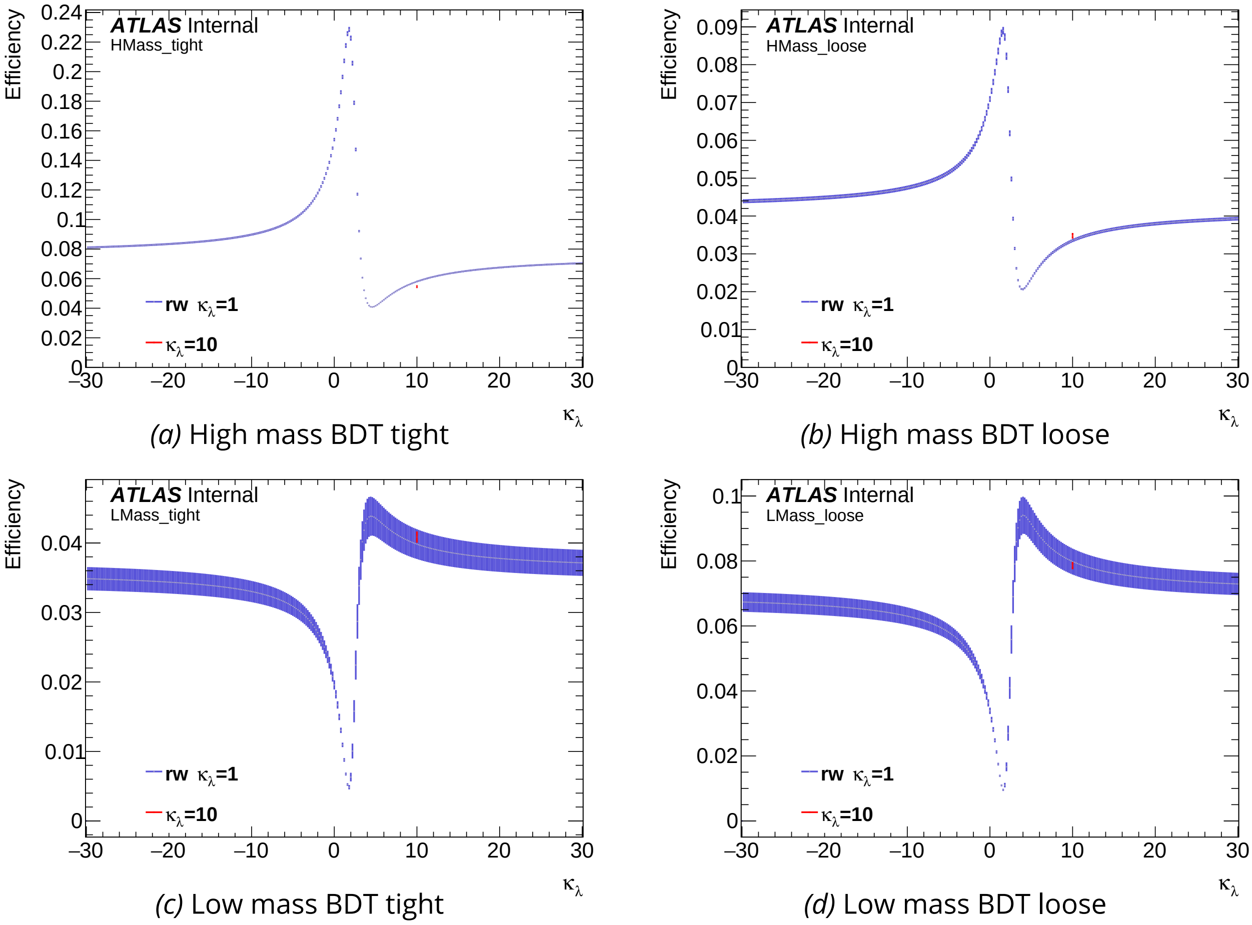

(a) High mass BDT tight *(b)* High mass BDT loose

(c) Low mass BDT tight *(d)* Low mass BDT loose

Figure 4.13: Efficiencies of the ggF HH signal in the four non-resonant BDT categories. Using the SM (κ_λ) reweighted to any κ_λ, with overlap of the generated $\kappa_\lambda = 10$ sample [93].

The analysis uses the diphoton invariant mass $m_{\gamma\gamma}$ as a final discriminate variable. The shape modelling is derived from simulation, in particular, for $\gamma\gamma$ continuum background, a dedicated spurious signal criteria is used to choose its shape.

4.6.1 HH signal and single H modelling

The HH signal and single Higgs $m_{\gamma\gamma}$ distributions are modelled with a double-sided crystal ball function (DSCB) following the definition:

$$f_{DSCB}(t) = N \cdot \begin{cases} A_{\text{Low}} \cdot \left[\frac{\alpha_{\text{Low}}}{n_{\text{Low}}}(b_{\text{Low}} - t)\right]^{-n_{\text{Low}}}, & t < -\alpha_{\text{Low}} \\ \exp\left(-\frac{t^2}{2\sigma_{CB}}\right), & t \in [-\alpha_{\text{Low}}, \alpha_{\text{High}}] \\ A^{\text{High}} \cdot \left[\frac{\alpha_{\text{High}}}{n_{\text{High}}}(b_{\text{High}} - t)\right]^{-n_{\text{High}}}, & t > \alpha_{\text{High}} \end{cases} \quad (4.10)$$

where

- $t = \frac{m_{\gamma\gamma}-\mu_{CB}}{\sigma_{CB}}$, with m_h and σ_{CB} the center and the width of the Gaussian.
- $A_{\text{Low}} = \exp\left(-\frac{\alpha^2_{\text{Low}}}{2}\right)$, with $-\alpha_{\text{Low}}$ the lower intersection of the point-wise function.
- $A_{\text{High}} = \exp\left(-\frac{\alpha^2_{\text{High}}}{2}\right)$, with α_{High} the higher intersection of the point-wise function.
- $b_{\text{Low}} = \frac{n_{\text{Low}}}{\alpha_{\text{Low}}} - \alpha_{\text{Low}}$, with n_{Low} the order of power law on the left tail.
- $b_{\text{High}} = \frac{n_{\text{High}}}{\alpha_{\text{High}}} - \alpha_{\text{High}}$, with n_{High} the order of power law on the right tail.
- N is a normalization factor of the distribution.

The parameters of the function are derived by fitting to the MC of both ggF HH and VBF HH processes with $\kappa_\lambda = 1$. Since there is no significant dependency of the function form on κ_λ for the non yet excluded values, the shape modelling obtained with $\kappa_\lambda = 1$ signal samples is used for all the κ_λ hypotheses. The fit results of the signal modelling are shown in Fig. 4.14 respectively in each of the four categories defined by the non-resonant BDTs. After the DSCB fit, the m_h parameter is further shifted by +0.09 GeV to account for the fact that the MC samples were generated with kinematics assuming a Higgs boson mass of 125 GeV, while the best ATLAS measurement of the Higgs boson mass is 125.09 GeV [3].

It is also proved that applying the HH signal modelling to the single Higgs process will not bias the final result, therefore, a common modelling is used for both HH and single Higgs production.

4.6.2 Diphoton Continuum Background Modelling

The $\gamma\gamma$ continuum background is modelled by an analytical function, with a fixed form of a fixed number of degrees of freedom. The improper choice of the function may lead to potential bias in the results, for instance, functions with high degrees of freedom have the risk to absorb the real signal, while those with low degrees of freedom may result in poor fits and create artificial signals with the residual unfitted background. The function form and its associated bias are determined using the so-called spurious signal test. The spurious signal refers to the potential signal bias, obtained by fitting the smooth background distribution to a function describing both signal and background.

The first step is to prepare a statistically enhanced background template, which represents the background shape. In this analysis, the template is constructed by the $\gamma\gamma$+jets MC. The shape modification due to the presence of the γ+jet and the dijets events was approximately estimated using a linear reweighting. The $m_{\gamma\gamma}$ distribution of the templates and the data sideband are plotted in Fig. 4.15. The impact of shape correction from the γ+jet and the dijets events was checked to be negligible, therefore for the spurious signal test, the MC templates with only the $\gamma\gamma$+jets events are used. The templates are further normalized to the data sideband.

Then a signal plus background model is fitted to the background template, where the background model is the function to be evaluated, and the double-sided crystal ball function (Eq. 4.10) is taken for the signal modelling. In order to evaluate the bias in the full mass range where the signal appears, the parameter μ_{CB} representing the mass peak position is varying in intervals of 1 GeV in a range from 121 GeV to 129 GeV. During the test for a given background functional form, the signal modelling is fixed, and for each value of

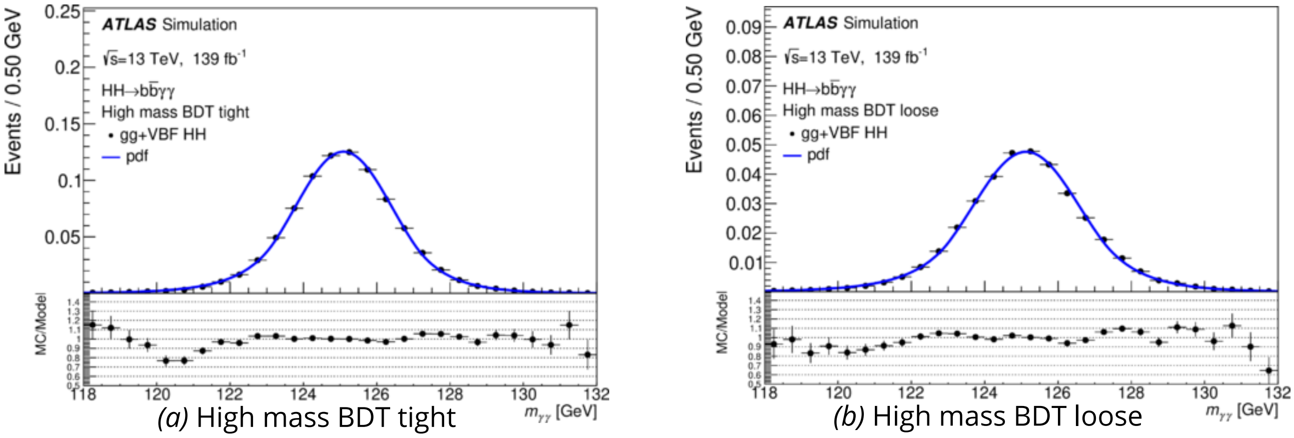

(a) High mass BDT tight *(b)* High mass BDT loose

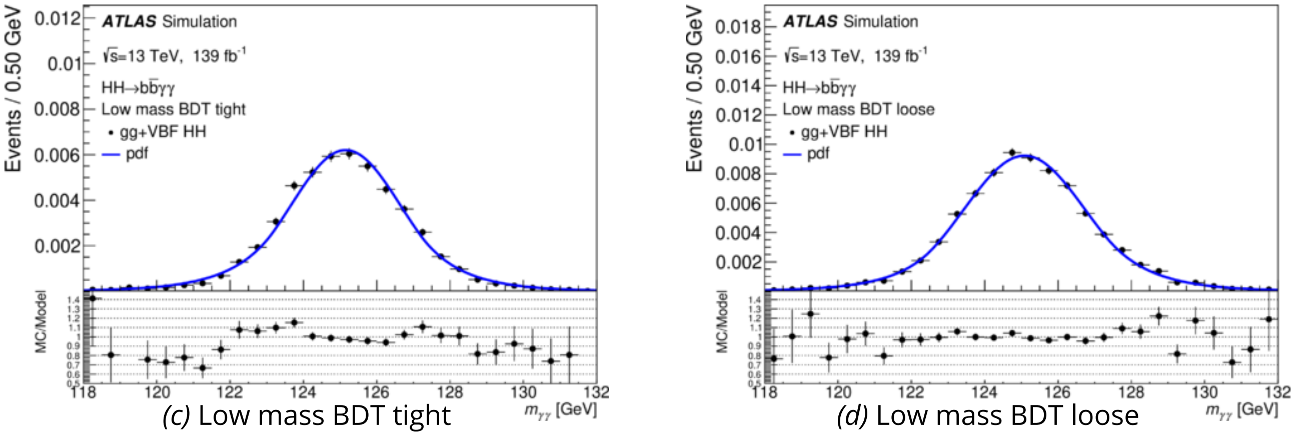

(c) Low mass BDT tight *(d)* Low mass BDT loose

Figure 4.14: $m_{\gamma\gamma}$ signal modelling, by fitting double-sided crystal ball function to the ggF+VBF HH signal MC at $\kappa_\lambda = 1$ respectively in each of the four signal categories. The black dots are the MC events, and the fitted double-sided crystal ball functions are shown by the blue curve, with the fitted parameters displayed on the top right of each plot [57].

μ_{CB}, the signal events, the background events and background function parameters are fitted. The largest fitted signal among the different μ_{CB} values is defined as the spurious signal N_{sp} for this functional form.

The typical spurious signal test requires the background function to satisfy at least one of the following criteria:

- $|\max(N_{sp}/N_{S,\text{exp}})| < 10\%$, where $N_{S,\text{exp}}$ represents the expected signal events predicted by the SM in the current category, which corresponds to the sum of ggF HH and VBF HH yields shown in Tab. 4.4.
- $|\max(N_{sp}/\sigma_S)| < 20\%$, where σ_S is the statistical uncertainty of the fitted number of signal events obtained from the spurious signal test.

However, due to the low number of expected signal, the typical criteria is not satisfied in all the categories. In this case, a relaxed criteria is used by accommodating the spurious signal N_{sp} with 2σ local statistical fluctuation of the background template. A new variable ξ_{sp} is defined to replace the role of N_{sp} to pass the

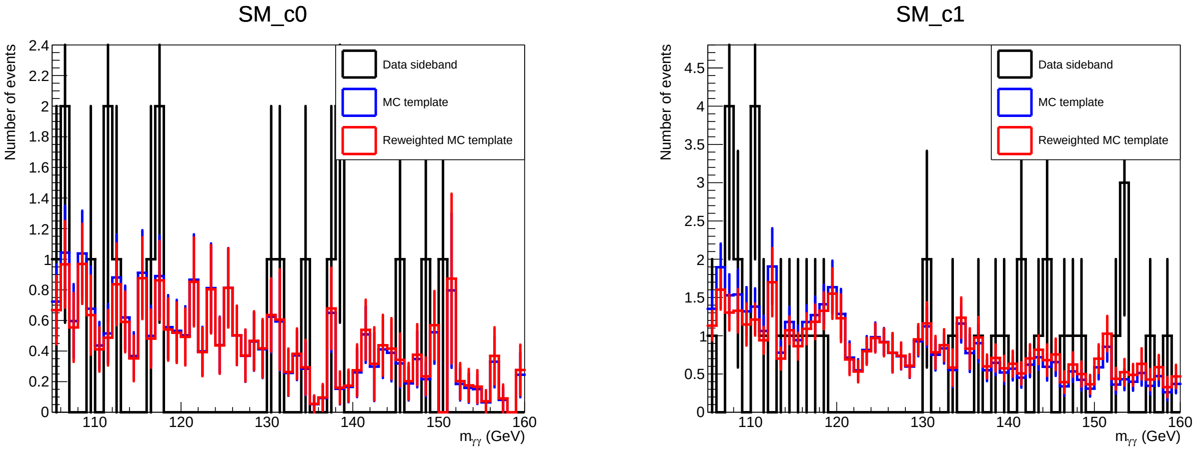

(a) High mass BDT tight

(b) High mass BDT loose

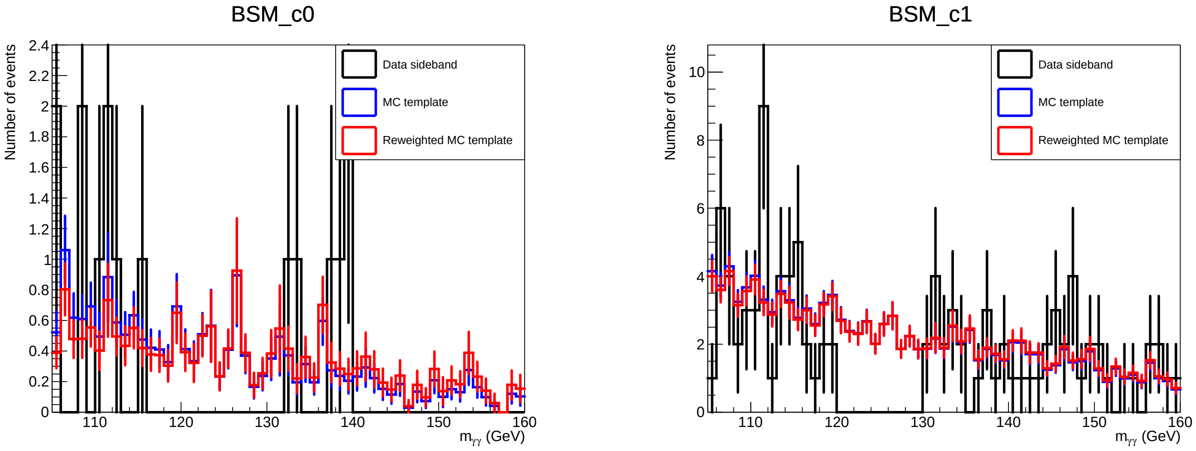

(c) Low mass BDT tight

(d) Low mass BDT loose

Figure 4.15: $m_{\gamma\gamma}$ distributions of the data sideband (black), the $\gamma\gamma$+jets MC templates (blue) and the reweighted MC templates (red) in the non-resonant categories. The MC templates are normalized to the data sideband [93].

typical spurious signal criteria:

$$\xi_{sp} = \begin{cases} N_{sp} + 2\sigma_{\mathrm{MC}}, & N_{sp} + 2\sigma_{\mathrm{MC}} < 0 \\ N_{sp} - 2\sigma_{\mathrm{MC}}, & N_{sp} - 2\sigma_{\mathrm{MC}} < 0 \\ 0, & \text{otherwise} \end{cases} \tag{4.11}$$

where σ_{MC} is the local statistical fluctuation of the background template calculated in the signal modelling window. Finally, the function passing the criteria with the smallest spurious signal N_{sp} and the lowest degrees of freedom is selected for the background modelling. The corresponding value of N_{sp} is taken to be the systematics that represents this spurious signal.

In fact, due to the poor statistics of the MC templates, the spurious test has no clear preference for the evaluated function forms, including exponential function, polynomials, power law, and other more sophisticated functions. In consequence, the exponential function is chosen for simplicity. The detailed spurious signal test scanned over the signal mass range is shown in Fig. 4.16. The black curves show the fitted signal events as a function of the Higgs mass parameter m_h used in the signal modelling for fit. The blue bands stand for the statistical uncertainty of signal yields σ_s. The typical criteria fail in all four categories due to the poor statistics, so the relaxed one is applied. The envelopes of the fitted signal are taken as the final spurious signal, as shown in Tab. 4.6. With respect to the HH signal yields shown in Tab. 4.4, the spurious signal is obviously a remarkable systematics of the background modelling, the striking values are induced by the statistical fluctuations due to the limited statistics in the MC template.

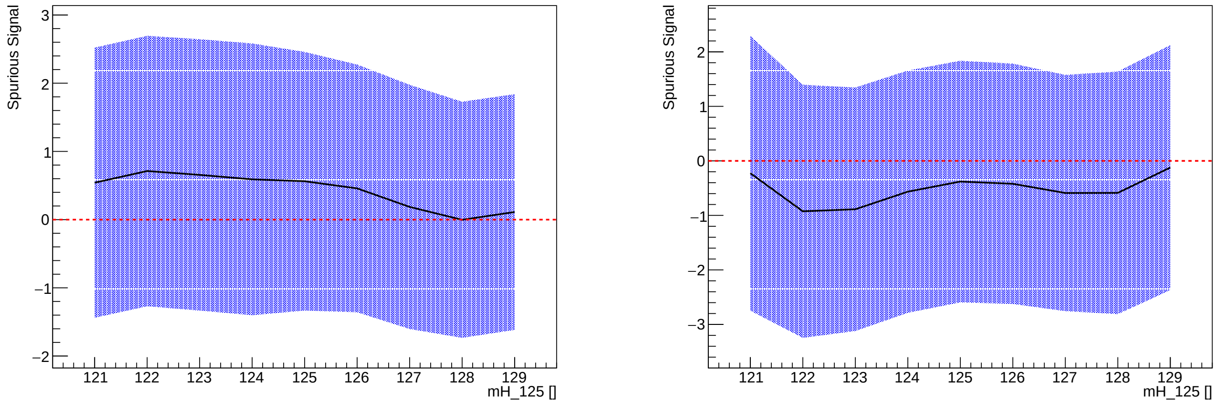

(a) High mass BDT tight

(b) High mass BDT loose

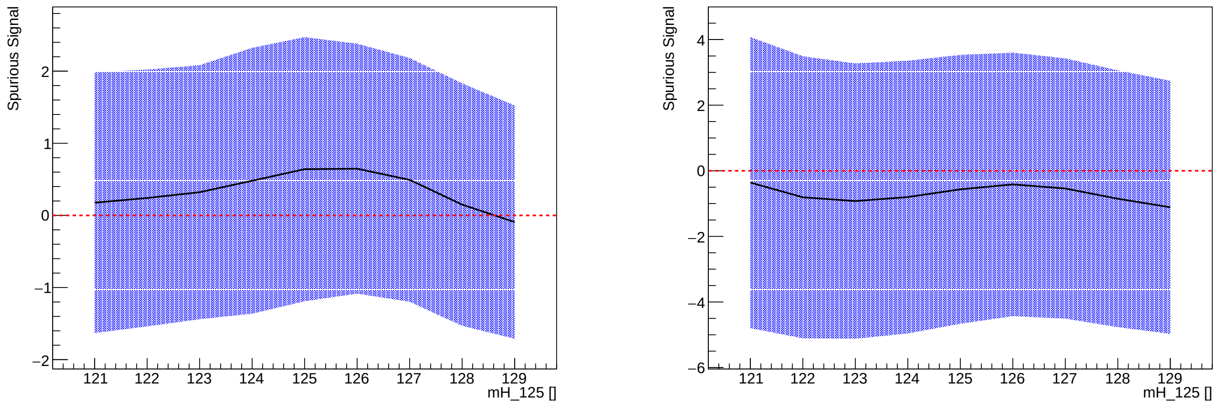

(c) Low mass BDT tight

(d) Low mass BDT loose

Figure 4.16: The spurious signal (black) in function of m_H in the non-resonant categories [93].

On the other hand, since the background modelling was arbitrarily chosen without following exactly the criteria, a Wald test on the blinded data was proposed and confirmed there was no preference for higher degree functions with respect to the chosen exponential function. The test is done with a likelihood ratio by comparing the hypothesis of exponential function and the one of function with an additional one degree

Category	High Mass BDT tight	High Mass BDT loose	Low Mass BDT tight	Low Mass BDT loose
N_{sp}	0.688	0.990	0.594	1.088
$N_{\text{sp}}/N_{s,\text{exp}}$	0.78	2.64	11.79	13.50
N_{sp}/σ_s	0.394	0.384	0.378	0.272

Table 4.6: Spurious signal test results for the exponential function in the various non-resonant categories.

of freedom. The likelihood ratio is written in the form

$$q_0 = -2\ln\frac{\mathcal{L}(\text{exp})}{\mathcal{L}(\text{exp+1dof})} \tag{4.12}$$

where $\mathcal{L}(\text{exp})$ is the likelihood computed with the exponential functions obtained from the spurious signal test, $\mathcal{L}(\text{exp+1dof})$ is the one computed with the same exponential family of $\mathcal{L}(\text{exp})$ but with one more degree of freedom. In order to check whether the background can be properly described by the simple exponential function, one considers it as the null hypothesis H_0, under which q_0 follows asymptotically a chi-square law of one degree of freedom. The p-value is computed with the observed q_0 using the data sideband, which shows that data doesn't prefer a higher order exponential function. The study was also repeated with toys generated from the exponential hypothesis, which was used to obtain the pdf of q_0 and gave the same conclusion as the asymptotic case.

4.7 Systematic Uncertainties

Although the current analysis for this rare signal is highly statistically dominated, the systematic uncertainties are carefully taken into account. In the following, the theoretical and experimental systematics will be introduced, especially, for their effects on the yields and shape modelling.

4.7.1 Theoretical Uncertainties

For HH signal and dominant samples of single Higgs ($t\bar{t}H$ and ZH) processes[2], the effect of the QCD theoretical scale uncertainties due to missing higher-order corrections to the cross section are estimated by varying the factorization (μ_F) and renormalization (μ_R) scales up and down with respect to their nominal values by a factor of 2. Six relative variations of (μ_R, μ_F) are used to evaluate the effect on cross section, specifically $(0.5, 0.5), (0.5, 1), (2, 1), (1, 2), (1, 0.5), (2, 2)$, where the nominal case is $(1, 1)$. The enveloping effect is taken as the final scale uncertainty. The uncertainties are both evaluated for the inclusive cross section and the efficiencies (eff) in each category. In particular, for ggF HH, the scale uncertainty was investigated for various κ_λ signal samples in the range between -10 and 10, and the maximum effect was taken as the final uncertainty. The uncertainties on cross section due to the PDF+α_s systematic and the missing NNLO finite top quark effect within the FTapprox are also taken into account. For the PDF+α_s systematic of the ggF HH signal, similarly to the QCD scale uncertainty, the maximum values over different κ_λ scenarios are considered. The uncertainty related to the parton showering model is evaluated by comparing the predictions by two generators, Pythia 8 and Herwig 7, respectively for the different processes.

---

[2] For the single Higgs ggH process, the heavy-flavour systematic, described later in the paragraph, already takes into account the QCD theoretical scale uncertainty.

For ggF HH signal, the difference between the two generators is evaluated respectively with the $\kappa_\lambda = 1$ and 10 signal, of which the maximum is taken as the final uncertainty.

In addition, specifically for the ggF HH signal, since the MC samples are generated using the κ_λ reweighting technique, a systematic uncertainty is assigned to this approach. The uncertainty is evaluated by comparing the yields predictions between the generated sample at $\kappa_\lambda = 10$ and the reweighted sample from $\kappa_\lambda = 1$ to $\kappa_\lambda = 10$. Finally, a $^{-2.90}_{+2.84}\%$ uncertainty for the Higgs decay branching ratio of $H \to \gamma\gamma$ is assigned to the HH signal and all the single Higgs processes, and a $^{+1.70}_{-1.73}\%$ uncertainty for the Higgs decay branching ratio of $H \to b\bar{b}$ is assigned to the HH signals.

For the single Higgs process via ggF, VBF, and the production associated with a W boson, an additional 100% uncertainty is assigned in order to take into account the heavy-flavor modelling, as motivated by the studies of heavy-flavor production in association with top-quark pairs and of W boson production in association with b-jets. This heavy-flavor uncertainty is not presented for the $t\bar{t}H$ and ZH productions, which already contain two b quarks at LO. For other unmentioned single Higgs processes, the theoretical systematic is negligible.

The theoretical uncertainties of the ggF HH signal, $t\bar{t}H$ and ZH are listed in Tab. 4.7, where the uncertainties are evaluated respectively for cross section and efficiency (eff) for the HH signal, while simply on yields for the single Higgs. The reason to assign uncertainties respectively on the HH cross section and efficiency is that depending on the parameter of interest, different uncertainties are used. For instance, when exploring the signal strength μ, both uncertainties on cross section and efficiency are taken into account, while for the purpose of measuring HH cross section, the uncertainty on cross section is no longer needed. In case of single Higgs, since only the yields are of interest, one doesn't need to distinguish uncertainty between cross section and efficiency.

4.7.2 Experimental Uncertainties

The uncertainty in the integrated luminosity of the full Run 2 data set is 1.7%, obtained using the LUCID-2 detector for the primary luminosity measurements, which is applied to the production rates of the HH and all the single Higgs processes.

The uncertainty of di-photon trigger efficiency was evaluated to have an effect of around 1% on the expected production rates in the non-resonant categories. The pileup modelling systematic is also presented for the expected yields. The systematics raised from the photon identification and isolation efficiency, and from jet flavour tagging efficiencies are also evaluated on the yields. Besides, uncertainties from the jet energy scale and the jet energy resolution affect the m_{bb} distribution, consequently affecting the efficiency of b-jet relevant selection. Other systematics relevant to the jet vertex tagging efficiency and the b-jet momentum correction accounting for the presence of muons and neutrinos are found to be negligible.

For the $m_{\gamma\gamma}$ shape modelling of HH and single Higgs, it is established that the photon energy scale systematic shifts the mass peak of Higgs, and the effect from photon energy resolution systematic smears the distribution. Hence a clean treatment of the shape systematics is made by accounting for only the photon energy scale and resolution effect, of which the effects are respectively estimated for different processes in different categories. However, different to the $H \to \gamma\gamma$ mass analysis (Sec. 6.2.5) where the shape uncertainty is evaluated using the mean and inter-quartile of the $m_{\gamma\gamma}$ distribution, this analysis directly computes

Uncertainty (%)	QCD	PDF+α_s	m_{top}	PS	κ_λ-RW
Cross section	$^{+4.78}_{-8.46}$	±3.00	±2.6	-	-
(eff)$_{\text{High Mass BDT tight}}$	±4.91	±1.26	-	±7.27	±2.71
(eff)$_{\text{High Mass BDT loose}}$	±3.40	±1.00	-	±0.93	±4.61
(eff)$_{\text{Low Mass BDT tight}}$	±4.17	±2.08	-	±6.62	±3.87
(eff)$_{\text{Low Mass BDT loose}}$	±5.43	±1.89	-	±3.95	±3.13

ggF HH

Uncertainty (%)	QCD	PDF+α_s	PS
Cross section	$^{+0.03}_{-0.04}$	±2.10	-
(eff)$_{\text{High Mass BDT tight}}$	-	-	±7.81
(eff)$_{\text{High Mass BDT loose}}$	-	-	±5.04
(eff)$_{\text{Low Mass BDT tight}}$	-	-	±8.27
(eff)$_{\text{Low Mass BDT loose}}$	-	-	±5.63

VBF HH

Uncertainty (%)	QCD	PDF+α_s	PS
(yields)$_{\text{High Mass BDT tight}}$	±7.28	±9.96	±3.54
(yields)$_{\text{High Mass BDT loose}}$	±7.60	±9.90	±6.62
(yields)$_{\text{Low Mass BDT tight}}$	±8.68	±10.91	±1.05
(yields)$_{\text{Low Mass BDT loose}}$	±8.78	±10.55	±4.40

$t\bar{t}H$

Uncertainty (%)	QCD	PDF+α_s	PS
(yields)$_{\text{High Mass BDT tight}}$	±10.37	±2.55	±10.16
(yields)$_{\text{High Mass BDT loose}}$	±10.38	±2.23	±5.84
(yields)$_{\text{Low Mass BDT tight}}$	±4.76	±2.95	±43.93
(yields)$_{\text{Low Mass BDT loose}}$	±5.28	±4.66	±7.83

ZH

Table 4.7: Theoretical uncertainties for the ggF HH and VBF HH signals, including effects from the QCD scale, PDF+α_s, top mass (m_{top}), parton showering generators (PS) and κ_λ-reweighting technique (κ_λ-RW). The theoretical uncertainties of $t\bar{t}H$, ZH single Higgs background are shown as well. The unfilled cells represent the in-applicability or negligible values.

the uncertainty variation on the shape modelling parameter μ_{CB} and σ_{CB}.

In particular, for ggF HH signal, the uncertainties are chosen to be the maximum evaluations among the $\kappa_\lambda = 1$ and 10 samples. The table of the dominant experimental systematics on the expected yields of the ggF HH signal is shown in Tab. 4.8. For the shape modelling, there is 0.19% uncertainty coming from the LHC Higgs mass measurement and the photon energy scale systematics which affect the Higgs mass peak parameter m_h, and the resolution parameter σ is driven by the photon energy resolution systematics. The uncertainties of the ggF HH signal modelling are summarized in Tab. 4.9.

Systematic uncertainty (%)		High Mass BDT tight	High Mass BDT loose	Low Mass BDT tight	Low Mass BDT loose
Event-based	`PRW`	±1.18	±1.25	±1.87	±2.14
	`Trigger`	±0.97	±0.98	±0.95	±0.95
Photon	`PH_PES`	±0.38	±0.50	±0.95	±1.03
	`PH_PER`	±0.17	±0.31	±0.73	±0.16
	`PH_EFF_ID`	±1.38	±1.55	±1.63	±1.75
	`PH_EFF_Isol`	±1.37	±1.52	±1.53	±1.63
Jet	`JET_JES`	±2.05	±2.68	±3.04	±2.61
	`JET_JER`	±2.82	±3.64	±4.42	±1.92
Flavour tagging	`FT_EFF_B`	±2.47	±2.82	±2.83	±3.25
	`FT_EFF_C`	< 0.1	< 0.1	< 0.1	< 0.1
	`FT_EFF_Light`	±0.29	±0.39	±0.31	±0.39

Table 4.8: Summary of the dominant systematic uncertainties affecting ggF HH expected normalization in the four BDT categories.

Systematic uncertainty (%)		High Mass BDT tight	High Mass BDT loose	Low Mass BDT tight	Low Mass BDT loose
m_h	`PH_PES`	$^{+0.53}_{-0.53}$	$^{+0.52}_{-0.52}$	$^{+0.45}_{-0.44}$	$^{+0.44}_{-0.45}$
σ	`PH_PER`	$^{+16.00}_{-10.76}$	$^{+12.65}_{-10.90}$	$^{+12.86}_{-9.45}$	$^{+10.92}_{-7.61}$

Table 4.9: Summary of systematic uncertainties affecting ggF HH shape modelling in the four BDT categories.

For the continuum background, which is fitted directly on the data, there is only the spurious signal systematic. The spurious signal described in Tab. 4.6, represents the systematic uncertainty of the modelling of the $\gamma\gamma$ continuum background. It is implemented as special additive systematics on the signal events, which are uncorrelated between the categories. The exact implementation will be described in the Sec. 4.8.

4.8 Statistical Model and Interpretation

The statistical results are obtained with an unbinned maximum profile likelihood fit. The likelihood is the product of the extended likelihood of the four categories, and prefit constraint terms for systematic uncertainties. The extended likelihood contains the part of the diphoton mass $m_{\gamma\gamma}$ pdf and the extended Poisson term of the yields. The parameter of interest in this analysis is either the signal strength μ or the Higgs self-coupling modifier κ_λ.

$$\mathcal{L} = \prod_{c=1}^{4} \left(\mathrm{Pois}\left(n_c | N_c\left(\mu, \kappa_\lambda, \boldsymbol{\theta}\right)\right) \cdot \prod_{i}^{n_c} f_c\left(m^i_{\gamma\gamma} | \mu, \kappa_\lambda, \boldsymbol{\theta}\right) \right) \cdot \mathcal{G}(\boldsymbol{\theta_0} | \boldsymbol{\theta}) \tag{4.13}$$

where

- $\mathrm{Pois}\left(n_c | N_c\left(\mu, \kappa_\lambda, \boldsymbol{\theta}\right)\right)$ is an extended term describing the Poisson probability to observe n_c events in a given category c, with an expectation value of $N_c\left(\mu, \kappa_\lambda, \boldsymbol{\theta}\right)$ depending on $\mu, \kappa_\lambda, \text{and } \boldsymbol{\theta}$.

$$N_c\left(\mu, \kappa_\lambda, \boldsymbol{\theta}\right) = \mu \cdot N_c^{HH}(\kappa_\lambda, \boldsymbol{\theta}) + N_c^{H}(\boldsymbol{\theta}) + N_c^{\gamma\gamma} + N_c^{ss}\theta_c^{ss} \tag{4.14}$$

$$N_c^{HH}(\kappa_\lambda, \boldsymbol{\theta}) = N_c^{HH}(\kappa_\lambda) \cdot \prod_{k}^{N_{sys}} \cdot \left(1 + \sigma_{c,k}^{HH}\theta_k\right) \tag{4.15}$$

$$N_c^{H}(\boldsymbol{\theta}) = \sum_{j}^{N_H} N_{c,j}^{H} \cdot \prod_{k}^{N_{sys}} \cdot \left(1 + \sigma_{c,j,k}^{H}\theta_k\right) \tag{4.16}$$

with $N_c^{HH}(\kappa_\lambda, \boldsymbol{\theta})$ and $N_c^{H}(\boldsymbol{\theta})$ respectively the expected number of events for HH signal and single Higgs background in a given category c, including the dependency on κ_λ for the HH signal and the relevant systematic uncertainties, as represented by the nuisance parameters $\boldsymbol{\theta}$. $N_c^{HH}(\kappa_\lambda)$ is the constant HH signal yields of a given κ_λ hypothesis in the category c, $\sigma_{c,k}^{HH}$ is the corresponding relative uncertainty from the systematic source k. $N_{c,j}^{H}$ is the expected yields of the single Higgs process j in the category c as predicted by the SM, $\sigma_{c,j,k}^{H}$ is the relevant systematic uncertainty.
$N_c^{\gamma\gamma}$ is the event number of $\gamma\gamma$ continuum background, which is going to be fitted with data. N_{ss}^{c} is the spurious signal of a given category c as shown in Tab. 4.6, with θ_{ss}^{c} the corresponding nuisance parameter, which is uncorrelated to the ones of spurious signal in the other categories.

- $f_c\left(m^i_{\gamma\gamma}|\mu,\kappa_\lambda,\boldsymbol{\theta}\right)$ represents the joint probability density function of $m_{\gamma\gamma}$ for all the physics processes in a given category c, which is evaluated on the discrete data points. The $m_{\gamma\gamma}$ pdf depends on the parameters $\mu,\kappa_\lambda,\boldsymbol{\theta}$.

  $$\begin{aligned} f\left(m^i_{\gamma\gamma}|\mu,\kappa_\lambda,\boldsymbol{\theta}\right) =& \big[\left(\mu\cdot N_c^{HH}(\kappa_\lambda,\boldsymbol{\theta}) + N_c^{ss}\cdot\theta_c^{ss}\right)\cdot f_c^{HH}\left(m^i_{\gamma\gamma}|m_h^{HH}(\boldsymbol{\theta}),\sigma^{HH}(\boldsymbol{\theta})\right) \\ & + N_c^{H}(\boldsymbol{\theta})\cdot f_c^{H}\left(m^i_{\gamma\gamma}|m_h^{H}(\boldsymbol{\theta}),\sigma^{H}(\boldsymbol{\theta})\right) \\ & + N_c^{\gamma\gamma}\cdot f_c^{\gamma\gamma}(m^i_{\gamma\gamma})\big]\cdot\frac{1}{N_c\left(\mu,\kappa_\lambda,\boldsymbol{\theta}\right)} \end{aligned} \tag{4.17}$$

  $$m_h^{HH}(\boldsymbol{\theta}) = m_h^{HH}\cdot\prod_k^{N_{sys}}(1+\sigma_k^{HH}\theta_k),\ \sigma^{HH}(\boldsymbol{\theta}) = \sigma^{HH}\cdot\prod_k^{N_{sys}}(1+\sigma_k^{HH}\theta_k) \tag{4.18}$$

  $$m_h^{H}(\boldsymbol{\theta}) = m_h^{H}\cdot\prod_k^{N_{sys}}(1+\sigma_k^{H}\theta_k),\ \sigma^{H}(\boldsymbol{\theta}) = \sigma^{H}\cdot\prod_k^{N_{sys}}(1+\sigma_k^{y}\theta_k) \tag{4.19}$$

  where $f_c^{HH}\left(m^i_{\gamma\gamma}|m_h^{HH}(\boldsymbol{\theta}),\sigma^{HH}(\boldsymbol{\theta})\right)$, $f_c^{H}\left(m^i_{\gamma\gamma}|m_h^{H}(\boldsymbol{\theta}),\sigma^{H}(\boldsymbol{\theta})\right)$ are the $m_{\gamma\gamma}$ pdf of the HH and single Higgs production, which are described by a double-sided crystal function, as shown in Fig. 4.14. The same $m_{\gamma\gamma}$ pdf is taken for the HH and single Higgs production. Similarly to the yields, the systematic uncertainties on the shape modelling are applied as well to the parameters of the peak position m_h and the width σ. $f_c^{\gamma\gamma}(m^i_{\gamma\gamma})$ is the exponential function used to model the $\gamma\gamma$ continuum background, where the slope parameter will be fitted by data. The joint pdf is eventually normalized by the total yields of all the processes.

- $\mathcal{G}(\boldsymbol{\theta_0}|\boldsymbol{\theta})$ stands for the constraints of nuisance parameters $\boldsymbol{\theta}$ with auxiliary measurement (or global observables) $\boldsymbol{\theta_0}$. The constraint is usually a normal or log-normal distribution. And $\boldsymbol{\theta_0}$ are conventionally set to 0 by assuming all the theoretical computations, MC simulation and detector calibrations are perfect. For nuisance parameter θ_k associated with a given systematic k, it can have an impact on several quantities, for instance, the yields and shape modelling of various physics processes, which actually assumes a 100% correlation of its systematic effects, which will later be pulled or constrained by data. One technical remark is that in case that a negative quantity is forbidden, e.g. yields, resolution, a log-normal constrain is favored rather than a Gaussian. This is technically implemented by replacing $(1+\sigma_k\cdot\theta_k)$ by $\exp\left(\sqrt{\ln(1+\sigma_k^2)}\cdot\theta_k\right)$, where the later exponential follows a log-normal law if θ follows $\mathcal{G}(0;1)$.

Eventually, a simultaneous profile maximum likelihood fit to data in all the four categories is performed, where the parameter of interest, either signal strength μ or κ_λ, and the nuisance parameters including the background events $N_c^{\gamma\gamma}$, the slope of the exponential λ and all the systematic NPs $\boldsymbol{\theta}$ are fitted.
Unfortunately as shown in Fig. 4.12, only two events are observed in the high mass BDT tight category which is supposed to be the most sensitive one to the SM HH signal. Such a deficit in data leads to a negative fitted signal strength μ when assuming κ_λ equals 1.

4.9 Results

A free fit is performed with the signal strength μ and all the nuisance parameters as free parameters, meanwhile assuming the SM Higgs self-coupling $\kappa_\lambda = 1$. In addition, taking into account the observed deficit in data, a background-only fit is done by fixing the signal strength to 0. The profile likelihood scans are also studied, respectively for μ when setting $\kappa_\lambda = 1$, and for κ_λ with μ fixed to 1. No evident signal was observed, hence the limits on HH signal strength and on κ_λ are derived. The NP ranking which shows the pulls and constraints of the systematic uncertainties is also presented below.

4.9.1 Signal+background Fit

Assuming the SM Higgs self-coupling $\kappa_\lambda = 1$, a signal plus background fit is performed with the observed data simultaneously in the four categories. Due to the deficit in the high mass BDT tight category, the best-fit of μ is equal to -2.1. The maximum profile likelihood scan on μ is shown in Fig. 4.17.
The black curve is the likelihood scan when fitting all the collected data. The other curves are the ones when fitting with part of the data, where the sensitivity is highly dominated by the contribution from the high mass BDT tight category.

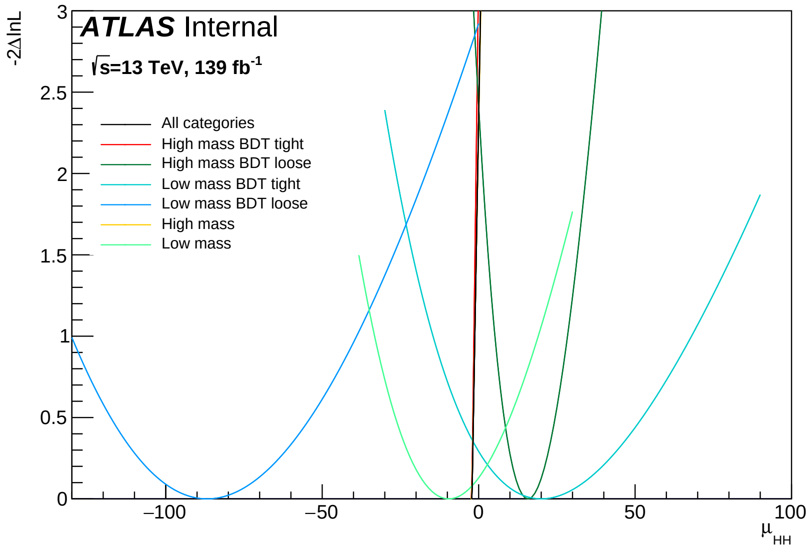

Figure 4.17: Maximum profile likelihood scan on the HH signal strength μ assuming $\kappa_\lambda = 1$ when fitting to the inclusive data and to data collected in different categories. The High mass curve represents the fit with both tight and loose categories defined by the high mass BDT, and the Low mass curve is the one defined by the low mass BDT [93].

The likelihood scans fitting with all the categories, high mass BDT tight only and high mass only, behave almost as a straight line, which is mainly driven by the deficit in data. For the inclusive fit, the fitted $m_{\gamma\gamma}$ distributions are shown in Fig. 4.18, where the one in the high mass BDT tight category reaches zero near 125 GeV, due to the absence of events in data
This phenomenon can be explained by a local Poisson behavior around the signal peak. For the mass region around the Higgs peak of the high mass BDT tight category, considering the expected signal yields S_{loc} and the total background B_{loc}, then its contribution to the full statistic test can be approximated by a likelihood function defined by a Poisson distribution with expected yields of $\mu(S_{loc} + B_{loc})$:

$$\mathcal{L}(\mu; N_{loc}) = \frac{\exp\left(-(\mu S_{loc} + B_{loc})\right) \cdot (\mu S_{loc} + B_{loc})^{N_{loc}}}{N_{loc}!} \tag{4.20}$$

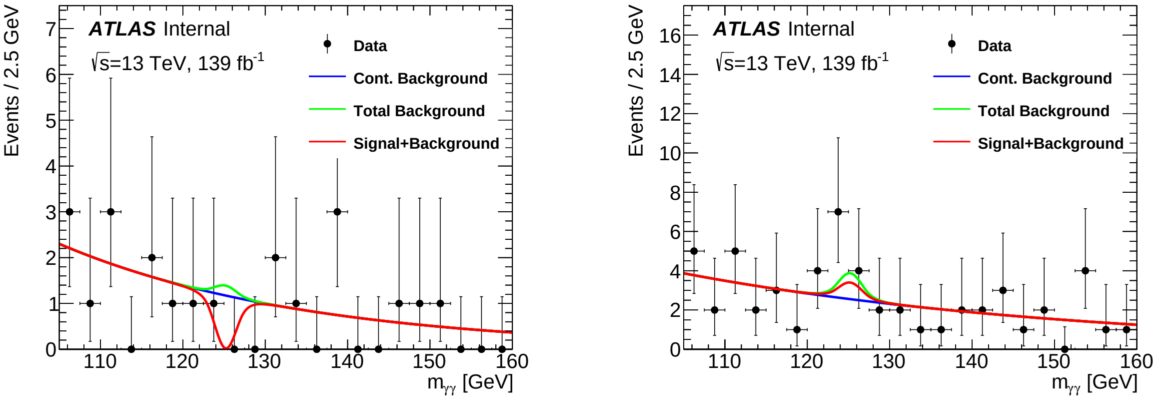

(a) High mass BDT tight

(b) High mass BDT loose

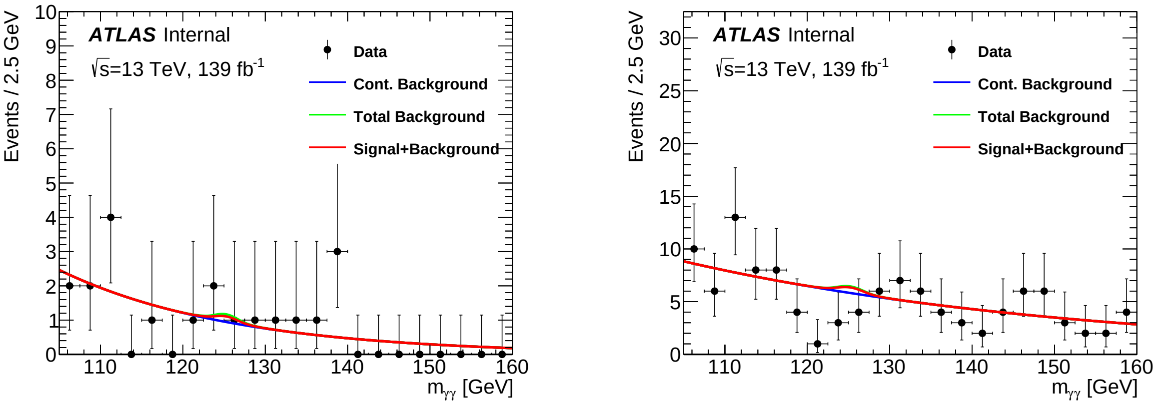

(c) Low mass BDT tight

(d) Low mass BDT loose

Figure 4.18: Signal+background fit in four categories of non-resonant analysis. The little bumps that appeared in the total background curves represent the single Higgs background [93].

where N_{loc} is the observed data near the Higgs peak in the high mass BDT tight category.

In case no event is observed $(N_{loc} = 0)$, the likelihood is reduced to

$$\mathcal{L}(\mu; N_{loc}) = \exp\left(-(\mu S_{loc} + B_{loc})\right) \tag{4.21}$$

Consequently the log-likelihood becomes linear in function of μ, and the MLE $\hat{\mu}$ is set to $-\frac{B_{loc}}{S_{loc}}$ so that the inclusive events remain positive. It explains the negative value of $\hat{\mu}$ and the fact that the $m_{\gamma\gamma}$ distribution of the high mass BDT tight category touches the bottom as shown in Fig. 4.18.

The detailed fit results are shown in Tab. 4.10. For the signal+background fit, since the log-likelihood is almost linear, the Fisher information is difficult to be calculated, therefore only the post-fit central values are presented. Since the signal strength μ is an unconstrained free parameter, the fit preferred to pull μ to match the deficit in the high mass BDT tight category rather than the systematic nuisance parameters, then the effects in the other categories due to change of μ were balanced by the spurious signal.

4.9.2 Background-only Fit

A background-only fit (Fig. 4.19) is also performed by fixing signal strength μ to zero. The little resonant bumps in the total background curves represent the single Higgs background. No clear discrepancy has been observed against the background-only hypothesis.

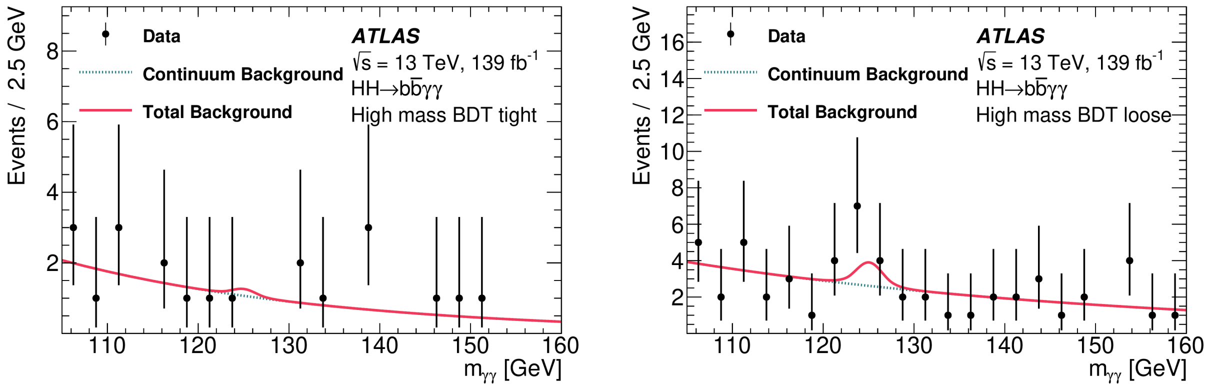

(a) High mass BDT tight

(b) High mass BDT loose

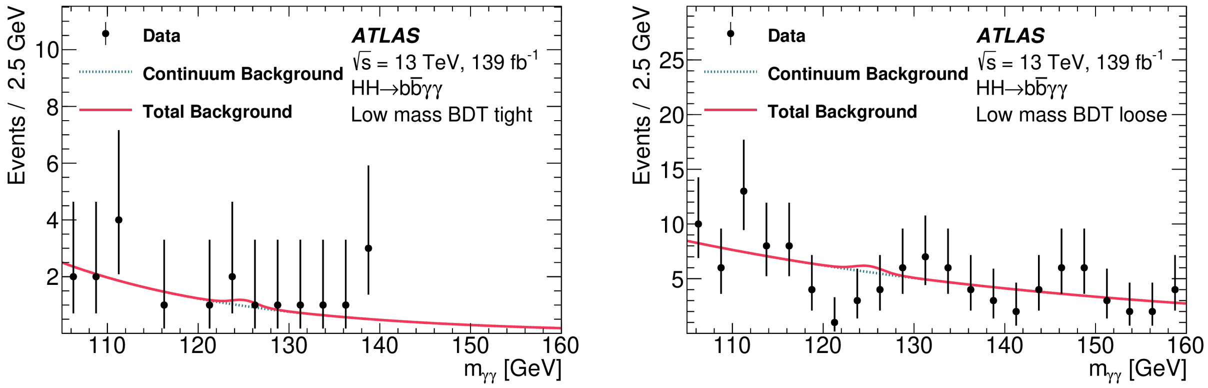

(c) Low mass BDT tight

(d) Low mass BDT loose

Figure 4.19: Background-only fit in four categories of non-resonant analysis [57].

The detailed fit results are shown in Tab. 4.10. In this case, since μ is forced to be 0, the observed deficit in the high mass BDT tight categories is covered by a negative pull of the spurious signal, and the fitted continuum background remains similar to the signal plus background. In absence of the HH signal, the photon energy scale systematic ($\theta_{\mathrm{PH\_PES}}$) is still present on the single Higgs background, and it is shifted due to more data observed in the signal region with diphoton mass between 120 and 125 GeV.

4.9.3 Likelihood Scan on κ_λ

A maximum profile likelihood scan (Fig. 4.20) is performed on κ_λ by considering it as a free parameter in the fit while setting μ to 1. The observed and expected scans are respectively done with the observed and the Asimov data, that the latter is generated with signal hypothesis ($\kappa_\lambda = 1, \mu = 1$) and nuisance parameters profiled from the background-only fit as shown in the B-only fit column of Tab. 4.10.

Parameter name	S+B fit	B-only fit
$N^{\gamma\gamma}_{\text{high mass BDT tight}}$	21.63	20.96 ± 4.59
$N^{\gamma\gamma}_{\text{high mass BDT loose}}$	53.09	52.03 ± 7.48
$N^{\gamma\gamma}_{\text{low mass BDT tight}}$	19.67	19.55 ± 4.51
$N^{\gamma\gamma}_{\text{low mass BDT loose}}$	111.41	111.41 ± 10.60
$\text{slope}_{\text{high mass BDT tight}}$	-3.33×10^{-2}	$(-3.32 \pm 1.49) \times 10^{-2}$
$\text{slope}_{\text{high mass BDT loose}}$	-2.06×10^{-2}	$(-2.03 \pm 0.90) \times 10^{-2}$
$\text{slope}_{\text{low mass BDT tight}}$	-4.72×10^{-2}	$(-4.73 \pm 1.66) \times 10^{-2}$
$\text{slope}_{\text{low mass BDT loose}}$	-2.06×10^{-2}	$(-2.06 \pm 0.62) \times 10^{-2}$
$\theta^{ss}_{\text{high mass BDT tight}}$	-	-0.57 ± 0.99
$\theta^{ss}_{\text{high mass BDT loose}}$	0.54	0.45 ± 0.94
$\theta^{ss}_{\text{low mass BDT tight}}$	0.22	0.19 ± 0.91
$\theta^{ss}_{\text{low mass BDT loose}}$	-0.39	-0.42 ± 0.98
$\theta_{\text{PH\_PES}}$	-	-0.22 ± 0.99

Table 4.10: Summary of the post-fit nuisance parameters of the signal+background fit and background-only fit. The background parameters and the systematic nuisance parameters with the largest pull are shown. The unfilled cells correspond to systematic nuisance parameters with a pull less than 10%.

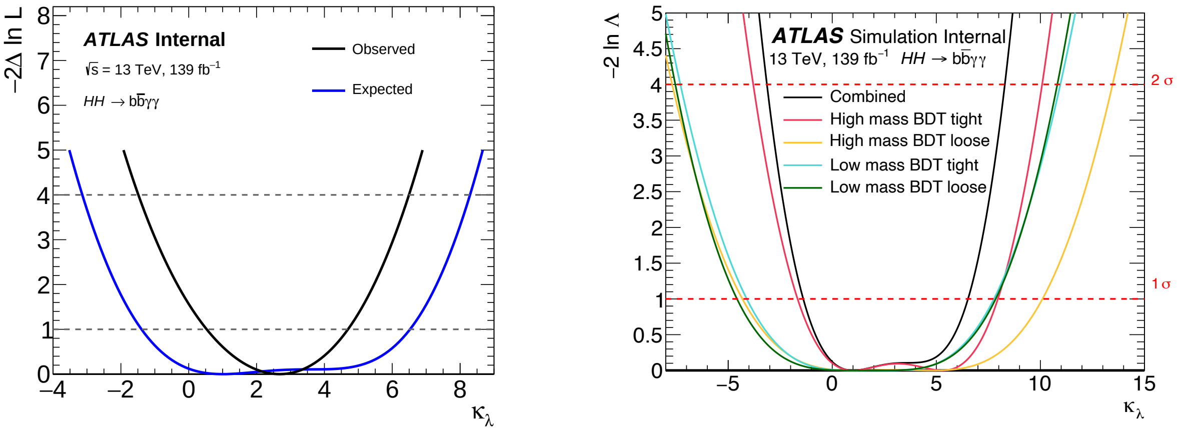

(a)

(b)

Figure 4.20: (a) Maximum profile likelihood scan κ_λ assuming $\mu = 1$. The best fit κ_λ is 2.7 with the observed data. The 68% CL range is [0.53, 4.70] for observed, and [-1.41, 6.42] for expected. (b) The sensitivity on κ_λ of each category estimated with the Asimov dataset generated at $\kappa_\lambda = 1$, a double minimum occurs when fitting with only the high mass BDT tight category, and fitting with categories optimized with different κ_λ values helps to mitigate the ambiguity [93].

The expected likelihood scan gives a measurement of $\kappa_\lambda = 1^{+5.4}_{-2.4}$. Since it is derived with an Asimov dataset generated at $\kappa_\lambda = 1$, the sensitivity is dominated by the high mass BDT tight category, where the double minimums of the likelihood are due to the same expected yields between $\kappa_\lambda = 1$ and $\kappa_\lambda \approx 5.3$, according to Tab. 4.5. Eventually after combining with all the four categories, a local minimum emerges near $\kappa_\lambda = 4$. However, for the observed result, the measured κ_λ is $2.7^{+2.1}_{-2.2}$. That is because around $\kappa_\lambda = 2.7$ the HH signal has the smallest cross section as shown in Fig. 4.7, which is more compatible with respect to the deficit in data.

4.9.4 Systematic Ranking

Although the current sensitivity is mainly driven by limited statistics, it is still useful to know the impact on the final results from systematic uncertainties.

For each systematic nuisance parameter θ_k, its pull is computed as the difference between the post-fit value $\hat{\theta}_k$ and the corresponding global observable θ_k^0, the impact on the POI is the change on POI when fixing θ_k to $\hat{\theta}_k \pm \sigma_k$, where σ_k can be the pre-fit or post-fit uncertainty of θ_k. Due to the observed deficit signal under the assumption of the SM, the fit of the signal strength μ is obtained by preventing negative yields in the signal region, which makes it hard to estimate uncertainties of parameters in the statistical model, hence the systematics pulls and impacts are studied with only Asimov data generated at $\mu = 1$ and nuisance parameters profiled from the background-only fit. The ranking of systematics is shown in Fig. 4.21.

According to the definition of Asimov data, the post-fit parameters are equal to the values used for the generation, hence the same as the global observables. Therefore all the systematics nuisance parameters are not pulled. The error bar of the pull stands for the post-fit uncertainty, where the spurious signals (named with "BIAS") and the photon energy scale (EG_SCALE_ALL) systematics are slightly constrained. The largest impacts are carried by the spurious signal from the high mass BDT tight category, heavy flavour of ggH and the spurious signal from the high mass BDT loose category. The nuisance parameters having a positive (negative) impact when varied by $+\sigma$ $(-\sigma)$ is shown in blue, on the contrary in green. Since the events in Asimov data are preserved, when the spurious signals or the single Higgs are increased, a negative impact is foreseen on the signal. While the photon energy scale is applied to the peak position, both up and down variations will shift the peak in a similar way, bringing a negative impact on μ to cover the induced gap between the shifted peak and the Asimov data.

On the other hand, the pull is defined as the relative NP shift normalized to its uncertainty, the shift is defined as $\hat{\theta} - \theta^0$, with its uncertainty equal to $\sqrt{\sigma_{\mathrm{pre}}^2 - \sigma_{\mathrm{post}}^2}$, where $\sigma_{\mathrm{pre}} = 1$ is the pre-fit uncertainty, σ_{post} is the post-fit uncertainty obtained from the fit. The advantage of such a definition is that the pull follows a normal distribution, such that if the pull is much larger than 1, it implies a larger significance of the NP pulls fitted with data. However, when the NP is not constrained, the computation of pull often suffers from the fit accuracy and could give an expected large pull, hence this definition is not used here.

4.9.5 Limits

Since no obvious signal was observed, the 95% CL upper limits on SM HH signal strength and on κ_λ are derived using the asymptotic formula and the CL_s method using the $\tilde{q}_\mu$ statistic as described in Sec. 2. The limits are obtained by excluding signal hypotheses when CL_s is lower than 5%, assuming no observation of signal. Hence the null hypothesis H_0 is the case with background and signal of a given μ, the alternative is background-only.

A background-only Asimov data was generated at $\mu = 0$ with all the nuisance parameters profiled at

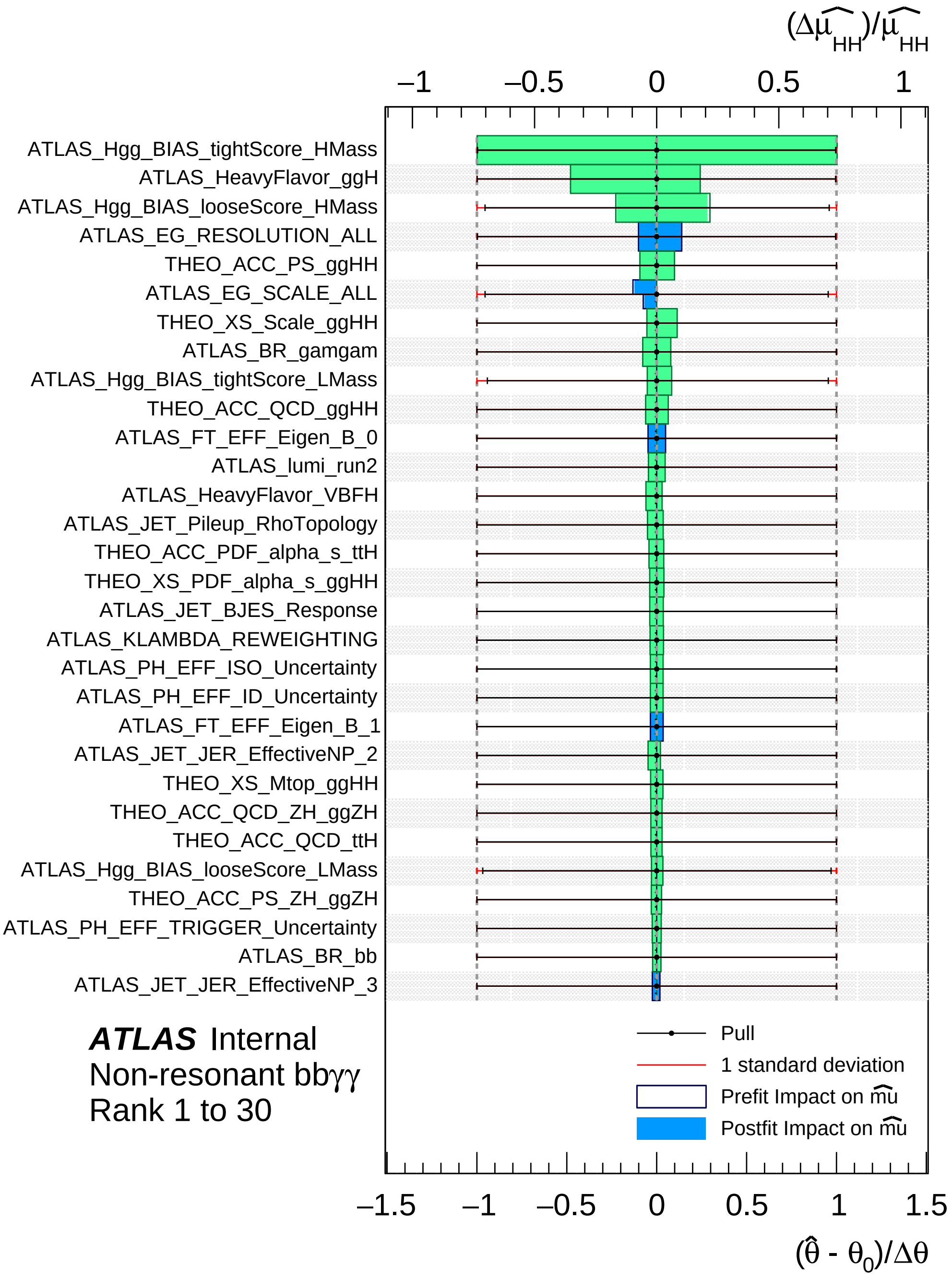

Figure 4.21: Pulls of the systematic uncertainties and their impacts on μ made on Asimov dataset. The impact is calculated as the change in the POI after varying the systematic NP by $\pm 1\sigma$ from its post-fit value. Parameters increasing the POI value when varied by $+1\sigma$ are shown in blue, while others is shown in green [93].

$\mu = \hat{\mu}$, which is used to estimate the variance of $\hat{\mu}$ and the pdf of the test statistic $\tilde{q}_\mu$, according to Eq. 2.50

and Eq. 2.35. A maximum unconditional profile likelihood fit is then performed with this Asimov data, where $\hat{\mu}$ is fitted to 0 by definition.

A CL_s scan is performed by looping over different null hypotheses, that for each hypothetical value μ, the following steps are proceeded:

- Maximum conditional profile likelihood fit to the b-only Asimov data and to the observed data, where μ is fixed to a given value, and all the nuisance parameters are profiled.
- Compute the test statistic $\tilde{q}_{\mu,\mathrm{exp}}$ and $\tilde{q}_{\mu,\mathrm{obs}}$ with both Asimov and observed data.
- Estimate the variance σ^2 with the Asimov profile likelihood ratio, and construct the asymptotic pdfs $f(\tilde{q}_\mu|\mu)$ and $f(\tilde{q}_\mu|0)$.
- Compute the median, $\pm 1\sigma$ and $\pm 2\sigma$ quantile of the alternative pdf $f(\tilde{q}_\mu|0)$ according to Eq. 2.36.
- Compute the CL_s values corresponding to the observed $\tilde{q}_{\mu,\mathrm{obs}}$ and the expected quantile estimated with the Asimov data.

The fact that the variance of $\hat{\mu}$ is estimated at different fixed values of μ is in order to take into account any potential non-parabolic likelihood shape. The σ estimated with the b-only Asimov data is also used to establish the null hypothesis pdf $f(\tilde{q}_\mu|\mu)$. As shown in Eq. 2.38, at low $\tilde{q}_\mu$ values the pdf is described by the sum of a Dirac function and a chi-square distribution which is independent of σ. The relevant part of $\tilde{q}_\mu > \mu^2/\sigma^2$ corresponds exactly to the case when $\hat{\mu} < 0$, hence using the b-only Asimov data for estimation is approximately valid.

The asymptotic-based CL_s scan on the signal strength μ is shown in Fig. 4.22. The observed curve is drawn with the CL_s computed with the observed data, the expected curves correspond respectively to the median, as well as the $\pm 1\sigma$ and $\pm 2\sigma$ bands of the μ limits. The 95% CL limits are defined as the intersections at 1-CL_s=0.95. These results are obtained corresponds to the first version of publication, in the latest results [57] after using a more conservative top mass theoretical uncertainty, the observed (expected) limit becomes 4.2 (5.7) times the SM prediction.

The stat-only results are also derived by fixing all the systematic nuisance parameters to the ones profiled at $\hat{\mu}$, the full model and stat-only limits are shown in Tab. 4.11. The sensitivity is currently driven by the limited statistics, the impact of systematic is around 12% (5%) on the observed (expected) limit.

μ_{limit}	obs	-2σ	-1σ	med	$+1\sigma$	$+2\sigma$
stat+sys	4.1	2.5	3.6	5.5	8.6	13.5
stat-only	3.6	2.5	3.5	5.2	8.1	12

Table 4.11: Summary of limit on HH signal strength assuming $\kappa_\lambda = 1$, the sensitivity is mostly statistically dominated, the impact of systematic uncertainties is around 10% in maximum.

The impact from different sources of systematics on the sensitivity is studied by fixing the relevant nuisance

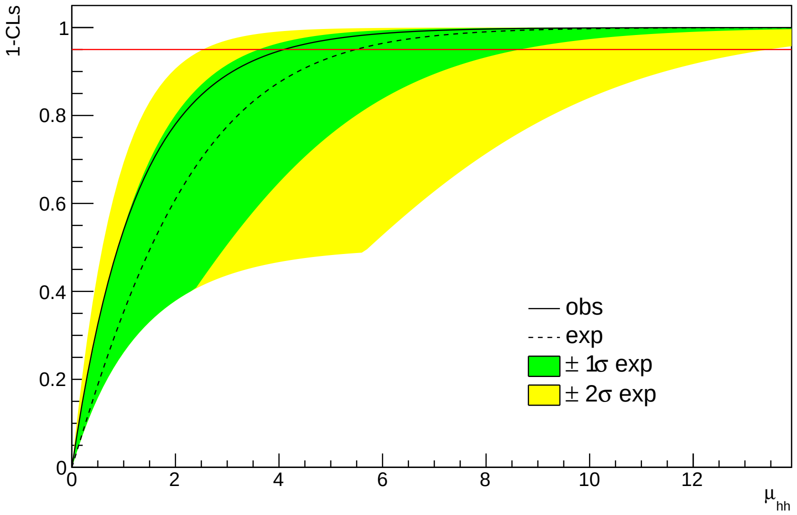

Figure 4.22: The CL_s scan on the HH signal strength μ using the asymptotic formula with the assumption of $\kappa_\lambda = 1$. The shrinkage of the $+1\sigma$ and $+2\sigma$ bands at low μ is because the -1 and -2 quantile of $f(\tilde{q}_\mu|0)$ overlap at $\tilde{q}_\mu = 0$.

parameters to their best-fit values to data, with all the remaining nuisance parameters floated, re-evaluating the likelihood-based test, and computing the change on the expected upper limit. The breakdown of systematic impact is shown in Tab. 4.12. The largest impact comes from the spurious signal, which affects the sensitivity by around 3%.

Source	Type	Relative impact of the systematic uncertainties [%] non-resonant analysis HH
Experimental		
Photon energy resolution	Norm. + Shape	0.4
Jet energy scale and resolution	Normalization	< 0.2
Flavor tagging	Normalization	< 0.2
Theoretical		
Factorization and renormalization scale	Normalization	0.3
Parton showering model	Norm. + Shape	0.6
Heavy-flavor content	Normalization	0.3
$\mathcal{B}(H \to \gamma\gamma, b\bar{b})$	Normalization	0.2
Spurious signal	Normalization	3.0

Table 4.12: Breakdown of the dominant systematic uncertainties. The impact of the uncertainties corresponds to the relative variation of the expected upper limit on the cross section when re-evaluating the profile likelihood ratio after fixing the nuisance parameter in question to its best-fit value, while all remaining nuisance parameters remain free to float.

For the Higgs self-coupling κ_λ, the limit interval is obtained by computing the upper limits of the HH production cross section under difference κ_λ assumptions, using the same approach described above for the upper limit of signal strength μ. Fig. 4.23 shows the $pp \to HH$ cross section upper limits in the function of κ_λ including both the ggF and VBF productions. The observed (expected) κ_λ limit interval is [-1.5, 6.7] ([-2.4, 7.7]) defined as the range with cross section upper limit lower than the theoretical prediction. Since the POI is now the cross section, the theoretical systematic on the cross section of the HH signal as described in Tab. 4.7 was removed, but included in the theory prediction values.

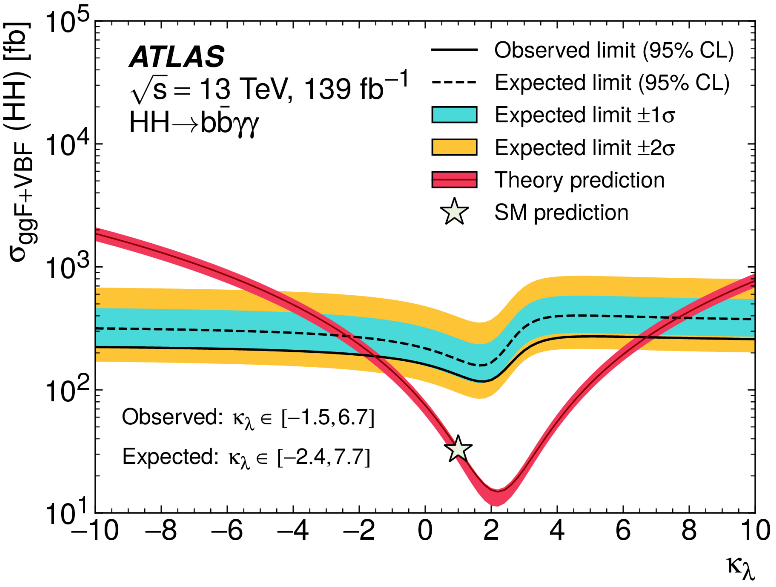

Figure 4.23: Cross section upper limits of non-resonant di-Higgs production in function of κ_λ. The range of κ_λ with upper limits below the theory is defined as the 95% CL limit interval [57].

4.9.6 Limits Estimated With Pseudo Experiments (Toys)

Clearly, the asymptotic approach relies on the sufficient sample size such that the Wald approximation and the Gaussian assumption still hold, while it starts to fail when data is small. For this analysis, since only two events are observed in the signal area of the most sensitive high mass BDT tight category, checking the statistical results with pseudo-experiments is important.

In alternative to the analytical asymptotic approach, the distributions of the test statistic $f(\tilde{q}_\mu|\mu)$ and $f(\tilde{q}_\mu|0)$ are obtained with a large number of toys, where each toy is randomized from the pdf of the studied observables and used to compute the value of the test statistic.

In order to obtain the distribution $f(\tilde{q}_\mu|\mu')$ with μ' equal to μ or 0, the detailed procedure is summarized below:

- Maximum conditional likelihood fit by fixing POI μ to the hypothetical value μ' with the observed data, the profiled nuisance parameters are denoted as $\hat{\hat{\boldsymbol{\theta}}}_{\mathrm{obs}}(\mu)$ in which the subset for systematic NPs are $\hat{\hat{\boldsymbol{\theta}}}_{\mathrm{sys,obs}}(\mu)$.

- Generate a large amount of toys, each including a set of the $m_{\gamma\gamma}$ data randomized according to the pdf $f(m_{\gamma\gamma}|\mu', 1, \hat{\hat{\boldsymbol{\theta}}}_{\text{obs}}(\mu))$ in Eq. 4.17, and the auxiliary measurements randomized from a Gaussian distribution centered around the conditional best-fit value of systematic nuisance parameters and with width of 1, i.e. $\mathcal{G}(\hat{\hat{\boldsymbol{\theta}}}_{\text{sys,obs}}(\mu), 1)$.
- Compute the test statistic $\tilde{q}_\mu$ for each toy and consider the obtained sampling distribution as the toy-based estimation of $f(\tilde{q}_\mu|\mu')$.

The generation flow is repeated for different hypotheses μ ranging from 2 to 13 with a step size of 0.1, 100k toys generated for $\mu \in [3.5, 6.5]$ as they are close to the asymptotic limits, 35k toys for the rest.

Toys example generated under the hypothesis of $\mu' = 5.5$ is taken for further illustration. As described above, the first step is to compute the profiled values of NPs at $\mu = \mu'$ with the observed data, the values are summarised in Tab. 4.13. Then these values are considered as the truth value for generation, one hundred thousands toy are generated, and each toy is performed with an unconditional maximum likelihood fit. The best-fit values of the main parameters pulled by the observed data are plotted in Fig. 4.24. The top plots show the distribution of the global observables which follows well the normal distribution centered at the truth value. The best-fit values of the systematic nuisance parameters are consistently randomized around the truth values as shown in the bottom plots.

Systematic NP	profiled at $\mu = 5.5$
$\theta^{ss}_{\text{high mass BDT tight}}$	-0.570
$\theta^{ss}_{\text{high mass BDT loose}}$	0.298
$\theta^{ss}_{\text{low mass BDT tight}}$	0.110
$\theta^{ss}_{\text{low mass BDT loose}}$	-0.472
θ_{LHCmass}	-0.281
$\theta_{\text{PH\_PES}}$	-0.817
$\theta_{\text{QCD HH}}$	-0.279
$\theta_{\text{PS ggFHH}}$	-0.292

Table 4.13: Systematic nuisance parameters profiled at $\mu = 5.5$ with the observed data. Only the one with the largest pulls is shown.

The obtained sampling distributions of the $\tilde{q}_\mu$ statistic in the specific cases of $\mu = 4.1$ and $\mu = 5.5$ are shown in Fig. 4.25. For comparison, the analytical pdf estimated with the asymptotic approach is drawn as the continuous curve. Some discrepancies between the asymptotic and pseudo-experiments approaches are observed, but remain at an acceptable level.

The CL_s scan on μ assuming $\kappa_\lambda = 1$ based on pseudo-experiments approach is shown in Fig. 4.26.

The 95% CL limits are shown in Tab. 4.14. The discrepancy between the asymptotic and pseudo-experiment approaches is around 7% for the median expected limit and 2% for the observed limit, which shows the asymptotic approach is still validated with sufficiently good accuracy in this analysis. The extension of the

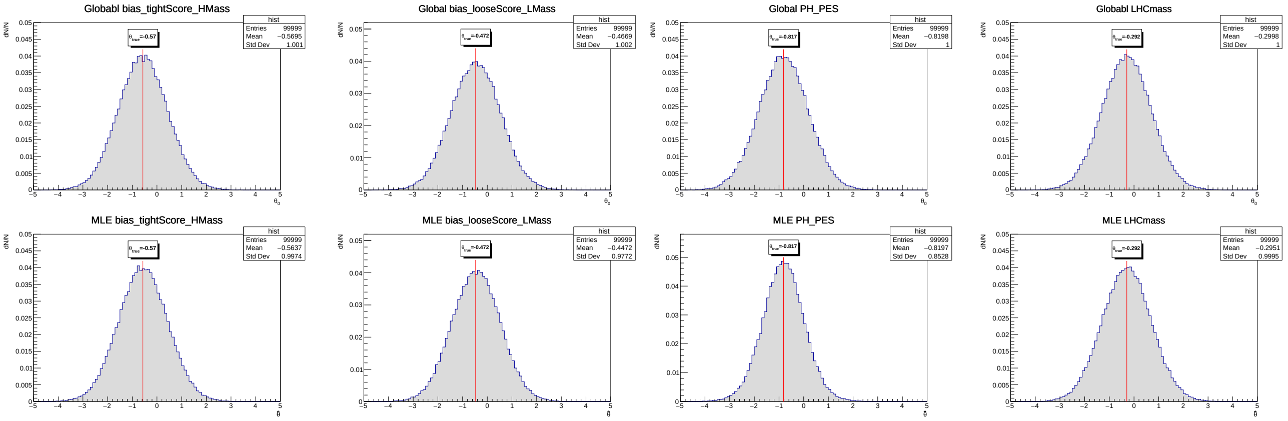

Figure 4.24: Distribution of the global observables (top) and the unconditional maximum likelihood fit results (bottom) and for the systematic nuisance parameters. The truth values used for generation are shown by the vertical red lines and pave text in the middle. The mean value and standard deviation of the plotted parameter are shown in the top right statistic box. The toys which failed to converge for the unconditional maximum likelihood fit are discarded (one toy).

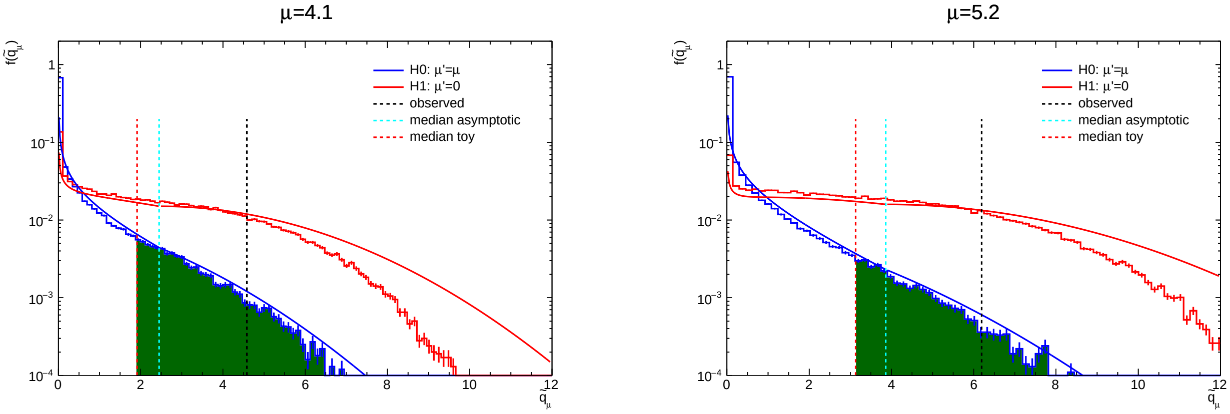

Figure 4.25: Comparison of the $\tilde{q}_\mu$ distributions obtained with pseudo-experiments (histograms) and the asymptotic formula (continuous functions). The blue (red) curves represent the null (alternative) hypothesis. The green area is the p-value defined with $\tilde{q}_\mu$ higher than the median of alternative toy distribution.

toy-based limit intervals is due to the higher coverage probability of Poisson distribution than the one of Gaussian.

μ_{limit}	obs	-2σ	-1σ	med	$+1\sigma$	$+2\sigma$
Toys	4.2	3.4	4.2	5.9	8.6	12.7

Table 4.14: Summary of toy-based limits on HH signal strength assuming $\kappa_\lambda = 1$.

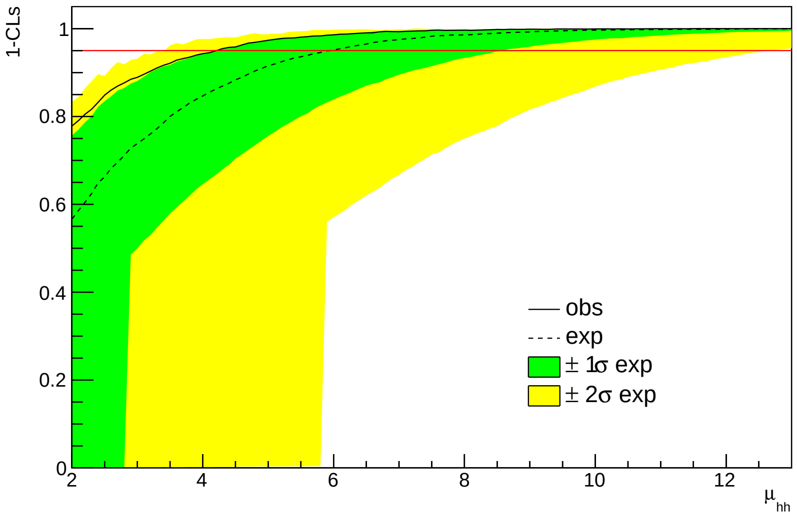

Figure 4.26: CL_s scan on the HH signal strength μ obtained with pseudo experiments, assuming $\kappa_\lambda = 1$ [93].

4.10 Resonant Analysis

The resonant analysis has been performed by searching for new spin-0 particles with mass in the range between 251 GeV and 1 TeV, under a narrow width approximation. The signal is denoted as resonant.

The resonant analysis uses the same pre-selection as the non-resonant one, with further selection optimized with a dedicated BDT algorithm. BDTs are trained simultaneously for all the signals with different mass hypotheses. Different resonant signals are merged and reweighted to have the same $m^*_{b\bar{b}\gamma\gamma}$ profile as the background events. This specific reweighting approach is used to eliminate the discriminant power of the $m^*_{b\bar{b}\gamma\gamma}$ variable, hence preventing conflicts between different m_X signals in the training. Two BDTS are optimized respectively against the $\gamma\gamma$ continuum and the single Higgs background, which are subsequently combined in quadrature to define the final BDT output. The combined BDT score distribution is shown in Fig. 4.27 for the mass hypothesis of 300 GeV and 500 GeV. The signal region is defined for each m_X scenario by the cut threshold on the combined BDT score and a m_X-dependent mass window cut on $m^*_{b\bar{b}\gamma\gamma}$ optimized to have the maximum sensitivity.

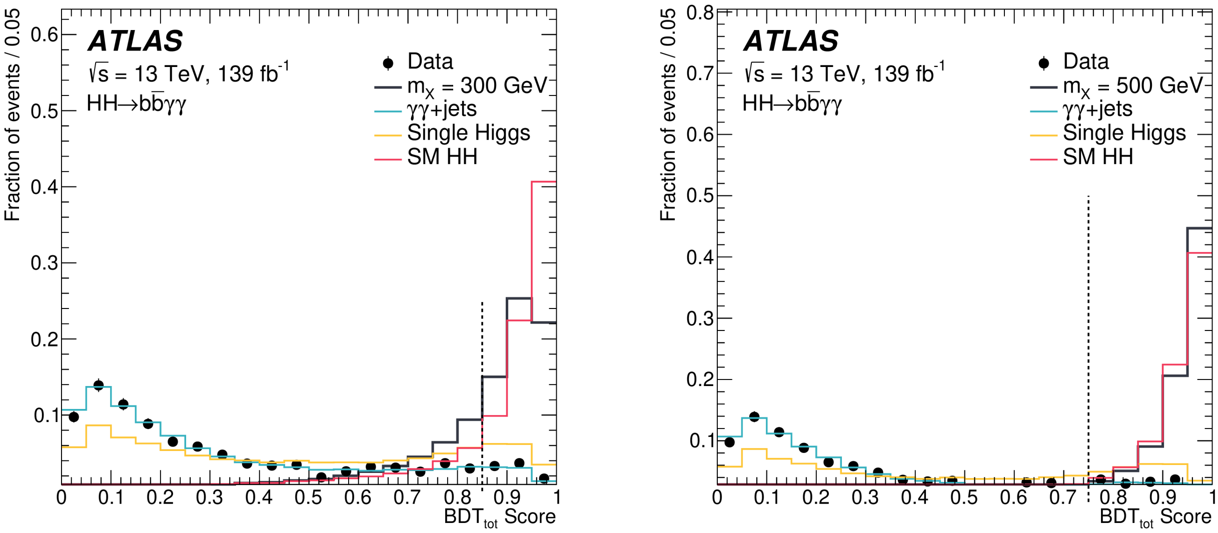

(a) $m_X = 300$ GeV *(b)* $m_X = 500$ GeV

Figure 4.27: BDT outputs for resonant signals with $m_X = 300$ GeV an $m_X = 500$ GeV [57].

The upper limits of the cross section for resonant signals are presented in Fig. 4.28. The observed (expected) upper limits are in the range 640-47 fb (390-43 fb) for $251 \leq m_X \leq 1000$ GeV.

4.11 Conclusion of $b\bar{b}\gamma\gamma$ Analysis

Searches for non-resonant and resonant Higgs boson pair production are performed in the $b\bar{b}\gamma\gamma$ final state using 139 fb^{-1} of 13 TeV pp collision data collected with the ATLAS detector at the LHC. No significant excess above the Standard Model background expectation is observed. A 95% CL upper limit of

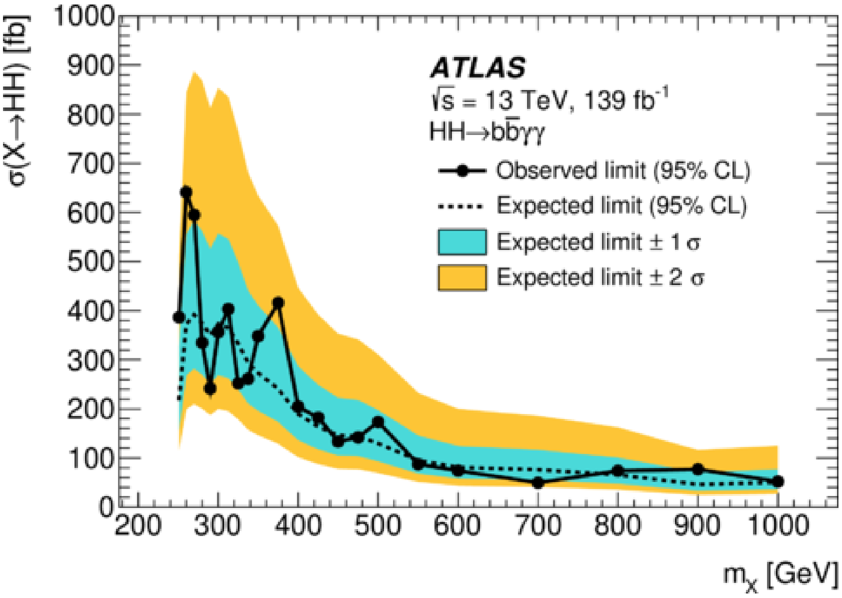

Figure 4.28: Resonant HH cross section upper limits in function of m_X [57].

130 fb is set on the non-resonant production cross section, where the expected limit is 180 fb. The observed (expected) limit corresponds to 4.2 (5.7) times the cross section predicted by the Standard Model. Constraints on the Higgs boson self-coupling are also derived and limits of $-1.5 < \kappa_\lambda < 6.7$ are obtained, where $-2.4 < \kappa_\lambda < 7.7$ is expected. For resonant production of a scalar particle $X \to HH \to b\bar{b}\gamma\gamma$, upper limits on the production cross section are obtained for the narrow-width hypothesis as a function of m_X. The observed (expected) upper limits are in the range 640-47 fb (390-43 fb) for $251 \leq m_X \leq 1000$ GeV. Compared to the previous ATLAS result based on 36 fb^{-1} of 13 TeV pp collisions [94], a general factor of 5 times improvements has been seen, which benefits from the increase of luminosity, the improvement on flavour tagging and the selection optimization.

Similar searches in the $b\bar{b}\gamma\gamma$ final state [78] are performed by the CMS experiment at the LHC using 137 fb^{-1} of 13 TeV pp collision data. The results are similar between the two experiments. For CMS, the observed (expected) upper limit of the non-resonant production cross section with the $HH \to b\bar{b}\gamma\gamma$ branching ratio is determined to be 0.67 (0.45) fb, which corresponds to 7.7 (5.2) times the standard model prediction. Assuming all other Higgs boson couplings are equal to their values in the standard model, the observed (expected) coupling modifiers of the trilinear Higgs boson self-coupling κ_λ is constrained within the ranges $-3.3 < \kappa_\lambda < 8.5$ ($-2.5 < \kappa_\lambda < 8.2$) at 95% confidence level, as shown in Fig. 4.29.

4.12 Di-Higgs Combination of $b\bar{b}\gamma\gamma$, $b\bar{b}b\bar{b}$ and $b\bar{b}\tau\bar{\tau}$ Channels in ATLAS

As illustrated in Fig. 4.6, apart from HH decay final state in $b\bar{b}\gamma\gamma$, there are other important channels. The current ATLAS Run2 publication includes the $b\bar{b}b\bar{b}$ [74][76], $b\bar{b}\tau\bar{\tau}$ [72] channel for both non-resonant

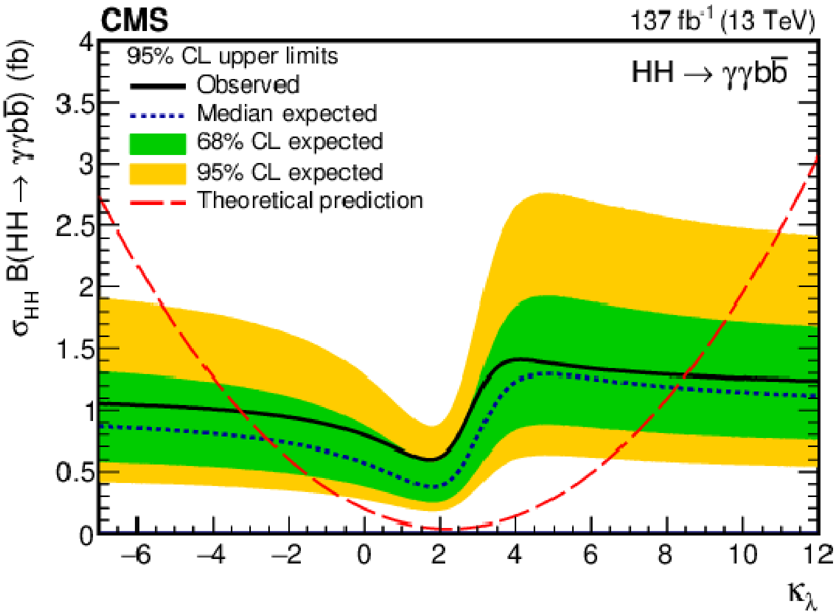

Figure 4.29: 95% CL upper limits on the product of the HH production cross section and BR($HH \to b\bar{b}\gamma\gamma$) obtained for different values of κ_λ with all other couplings fixed to SM predictions. [78]

and resonant searches.

$b\bar{b}\tau\bar{\tau}$ channel: at least one τ decaying into hadrons and the other with either hadronic or leptonic decays with dedicate $\tau_{\text{had}}\tau_{\text{had}}$ and $\tau_{\text{had}}\tau_{\text{lep}}$ triggers. A RNN-based τ identification criteria are used.

- Non-resonant: the observed (expected) upper limits are set at the 95% confidence level on the non-resonant Higgs boson pair production cross-section of 4.7 (3.9) times the Standard Model prediction, assuming Standard Model kinematics. The observed (expected) Higgs self-coupling κ_λ is constrained to be between -2.4 and 9.2 (-2 and 9).

- Resonant: the observed (expected) upper limits on cross-section are set between 23 and 920 fb (12 and 840 fb), depending on the heavy resonance mass.

$b\bar{b}b\bar{b}$ channel: with four b-jets in the final state which are paired using dedicated criteria in order to reconstruct the two Higgs boson candidates. The main background is from the QCD multi-jets and top processes.

- Non-resonant: the signal is produced by both ggF and VBF modes. The 95% CL observed (expected) upper limit on the cross section for non-resonant Higgs boson pair production is determined to be 5.4 (8.1) times the Standard Model prediction. The observed (expected) Higgs coupling modifier κ_λ is determined to be [-3.9, 11.1] ([-4.6, 10.8]) at 95% CL.

- Resonant: It targets heavy resonance of spin-0 with mass ranging from 251 GeV to 3000 GeV produced by VBF production. In the resolved case when $m_X < 1500$ GeV, the standard jet reconstruction with $\Delta R = 0.4$ is used, while for very high resonances with 900 GeV $< m_X <$ 3000 GeV, the decay products

> will be highly boosted and lead to the merging of two jets, hence a large radius jet reconstruction algorithm with $\Delta R = 1$ is applied to reconstruct the two b-jets in the same time. The signal region is defined in the 2D map of the invariant mass of the two reconstructed Higgs candidates from the four b-tagged jets using the 77% working points.

The ATLAS combination [95, 96] of different channels has been performed using a likelihood-based approach by taking into account the proper correlations of systematic uncertainties. The combined limits of the non-resonant analysis are shown in Fig. 4.30, and Fig. 4.31 for the resonant.

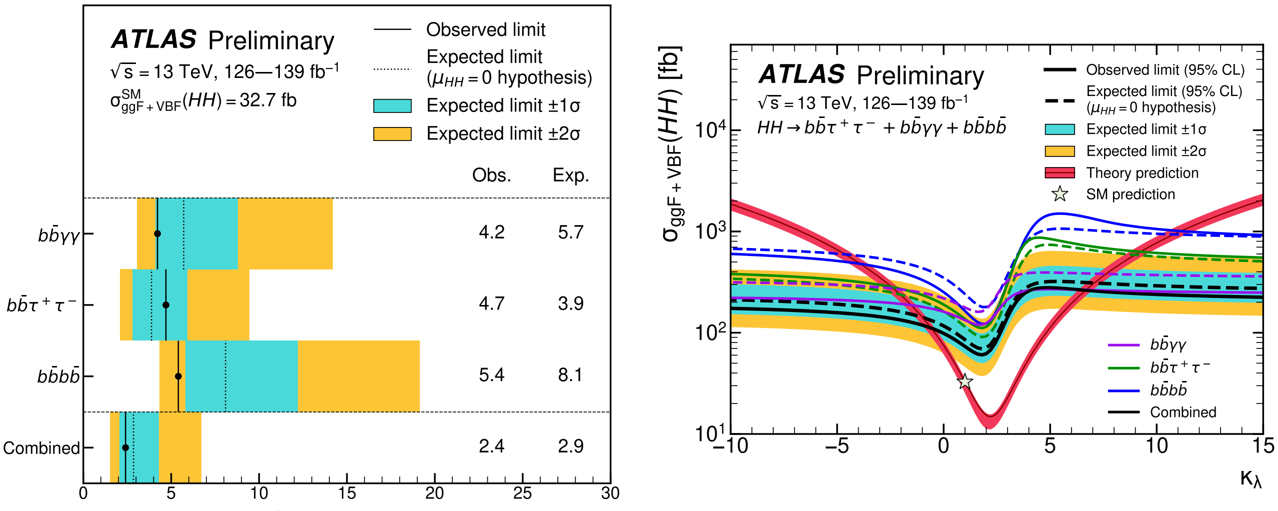

(a)

(b)

Figure 4.30: Observed and expected 95% CL upper limits on the signal strength for SM HH production (a) and the limit interval on the Higgs self-coupling modifier κ_λ (b) in the $b\bar{b}\gamma\gamma$, $b\bar{b}\tau\bar{\tau}$ and $b\bar{b}b\bar{b}$ searches, and their combination. The expected limits assume no HH production. [96].

For the non-resonant SM di-Higgs production, the combination of the $b\bar{b}\gamma\gamma$, $b\bar{b}b\bar{b}$ and $b\bar{b}\tau\bar{\tau}$ channels gives an observed (expected) 95% CL limit on the HH production cross section equal to 2.4 (2.9) times the SM prediction. For the Higgs self-coupling κ_λ, the combination further constrains its value to be within an observed (expected) limit interval of $[-0.6, 6.6]$ ($[-2.1, 7.8]$) at 95% CL.

For the resonant part, the combined result benefits from the sensitivities of the three channels in different m_X ranges, and arrive to further constrain the upper limit of the resonant production cross section. The largest excess between the observed and expected results is found at $m_X = 1.1$ TeV and it corresponds to a local (global) significance of 3.1σ (2.1σ).

The CMS Di-Higgs combination can be found in Ref. [87].

4.13 Combination of Di-Higgs and Single Higgs for κ_λ constraint

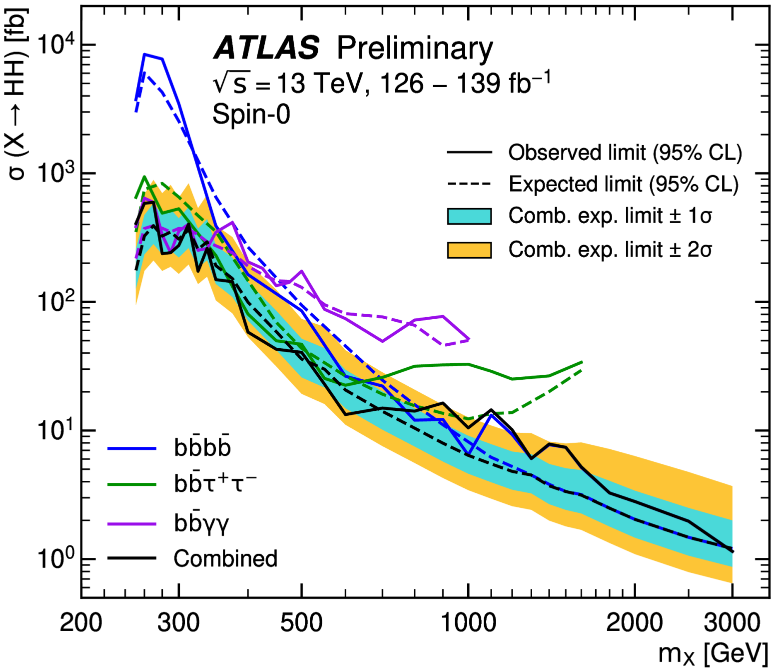

Figure 4.31: Expected and observed 95% CL upper limits on $\sigma(X \to HH)$ for a spin-0 resonance as a function of its mass m_X in the $b\bar{b}\gamma\gamma$, $b\bar{b}\tau\bar{\tau}$ and $b\bar{b}b\bar{b}$ searches, and their statistical combination. The discontinuities in the limit visible in the range $m_X < 400$ GeV are caused by the partial availability of the different analysis limits on a point-by-point basis, which are provided only for the $b\bar{b}\gamma\gamma$ search at the weakest limit points [95].

The Higgs self-coupling can emerge not only in the double Higgs production but also in the single Higgs production through additional loops. The examples of diagrams with one additional loop are shown in Fig. 4.32 respectively for the single Higgs production via ggF, VBF, VH and $t\bar{t}H$ modes. These Higgs self-coupling loops can modify the production cross section as well as the Higgs decay branching ratios. Hence both the double and single Higgs production can be parameterized with κ_λ, hence contributing to its constraint.

The individual and combined constraint on κ_λ of the di-Higgs and single Higgs channels are presented in Fig. 4.33, that the combination constrains the Higgs self-coupling to be in the range $[-0.4, 6.3]$ for the observed and $[-1.9, 7.5]$ for the expected at 95% CL. It brings a slight improvement on the HH combination constraint as shown in Fig. 4.30.

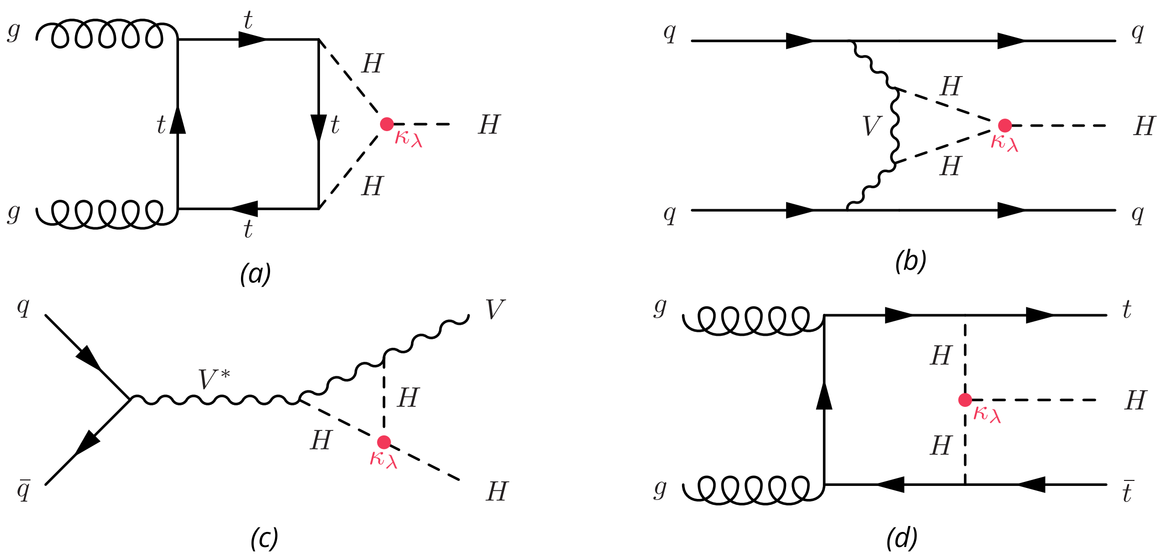

(a) (b) (c) (d)

Figure 4.32: Examples of one loop λ_{hhh}-dependent diagrams for the ggF (a), VBF (b), VH (c), and $t\bar{t}H$ (d) modes. The self-coupling vertex is indicated by the filled circle. [96].

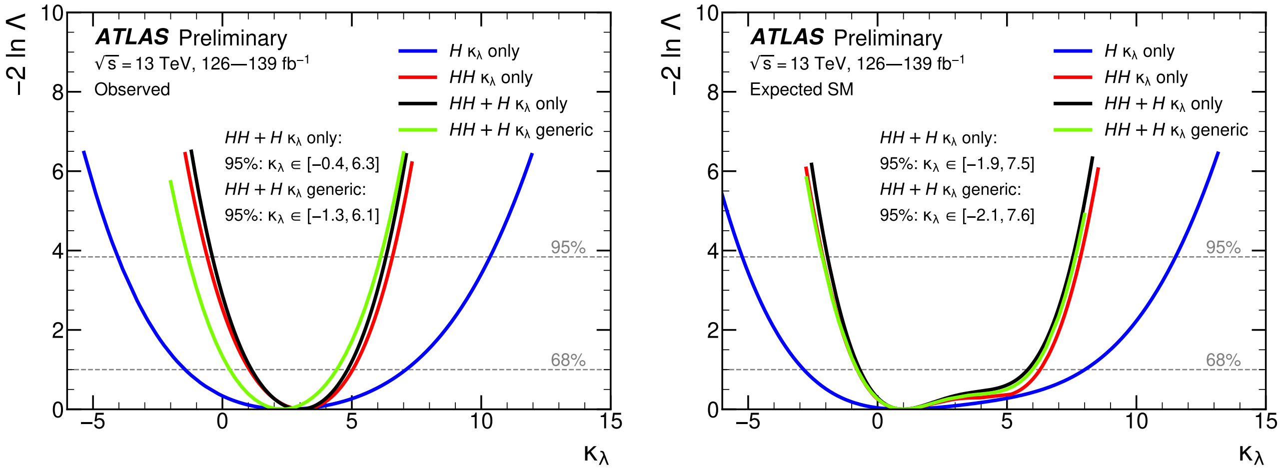

(a) (b)

Figure 4.33: : Observed (a) and expected (b) value of the profile likelihood ratio, as a function of the κ_λ parameter for the single-Higgs (blue) double-Higgs analyses (red), and their combination (black) derived from the combined single-Higgs and double-Higgs analyses with all other coupling modifiers fixed to unity. The combined result for the generic model (free floating $\kappa_t, \kappa_b, \kappa_V, \kappa_\tau$) is also superimposed (green curve). [96].

4.14 HL-LHC and Future Colliders Prospects

For the future upgraded high luminosity LHC, a total of 3000 fb^{-1} is designed which is around twenty times larger than the currently available data. On the other hand, the center of mass energy of the pp collision will increase from 13 to 14 TeV, which enhances the di-Higgs production by around 18%.

The current 139 fb^{-1} [95] ATLAS Run 2 non-resonant analysis after combining the $b\bar{b}\gamma\gamma$ and the $b\bar{b}\tau\bar{\tau}$ channels is extrapolated to the 3000 fb^{-1} HL-LHC [97], taking into account the change on cross section of the various signal and background processes, and the potential improvements on the systematic uncertainties. The revisions of the systematic uncertainties are performed by applying scale factors as shown in Tab. 4.15, according to the recommendations of the ATLAS conventions for HL-LHC projections [98]. In particular, for the most important systematics of the current $b\bar{b}\gamma\gamma$ analysis, the spurious signal, a scale factor of zero is applied since a sufficient MC simulation is expected to perform the $\gamma\gamma$ continuum background modelling. In the same principle, the MC statistical uncertainties of the $b\bar{b}\tau\bar{\tau}$ channel are expected to be null when extrapolating to HL-LHC.

Source	**Scale factor**	$b\bar{b}\gamma\gamma$	$b\bar{b}\tau\bar{\tau}$
Experimental Uncertainties			
Luminosity	0.6	*	*
b-jet tagging efficiency	0.5	*	*
c-jet tagging efficiency	0.5	*	*
Light-jet tagging efficiency	1.0	*	*
Jet energy scale and resolution, E_T^{miss}	1.0	*	*
κ_λ reweighting	0.0	*	*
Photon efficiency (ID, trigger, isolation efficiency)	0.8	*	
Photon energy scale and resolution	1.0	*	
Spurious signal	0.0	*	
Value of m_H	0.08	*	
τ_{had} efficiency (statistical)	0.0		*
τ_{had} efficiency (systematic)	1.0		*
τ_{had} energy scale	1.0		*
Fake-τ_{had} estimation	1.0		*
MC statistical uncertainties	0.0		*
Theoretical Uncertainties	0.5	*	*

Table 4.15: Summary of HL-LHC scale factors for relevant systematic uncertainties. A "*" indicates that the uncertainty is considered by the corresponding analysis [99].

In order to predict the sensitivity for the discovery of the double Higgs production, the expected HH significance and precision of signal strength (Tab. 4.16) are estimated with a signal and background Asimov data, under the SM hypothesis ($\mu = 1$ and $\kappa_\lambda = 1$). In the case with only the statistical uncertainty, a 4.6 σ combined significance and $\pm 23\%$ signal strength precision are expected. The baseline corresponding to the revised systematic recommendation described in Tab. 4.15, gives an expected significance of 3.2 σ and precision of $^{+34\%}_{-31\%}$, while a lower sensitivity is expected if extrapolating with the current Run 2 systematics. This more than 3 σ expected sensitivity lightens the possibility to probe the double Higgs production with HL-LHC.

Uncertainty scenario	Significance [σ] $b\bar{b}\gamma\gamma$	$b\bar{b}\tau\bar{\tau}$	Combination	Combined signal strength precision [%]
No syst. unc.	2.3	4.0	4.6	-23/+23
Baseline	2.2	2.8	3.2	-21/+34
Theoretical unc. halved	1.1	1.7	2.0	-49/+51
Run 2 syst. unc.	1.1	1.5	1.7	-57/+68

Table 4.16: HL-LHC prospects of the expected sensitivity for SM HH production, under different assumptions of the systematic uncertainties [99].

The likelihood scan is also performed with the signal and background Asimov data, by considering κ_λ as a free parameter while fixing the signal strength μ. The likelihood-based 1 σ confidence interval of κ_λ is $[0.5, 1.6]$ for the baseline setup and $[0.6, 1.5]$ for the case with only statistical uncertainty. It implies an expected accuracy of around 50% of the κ_λ measurement.

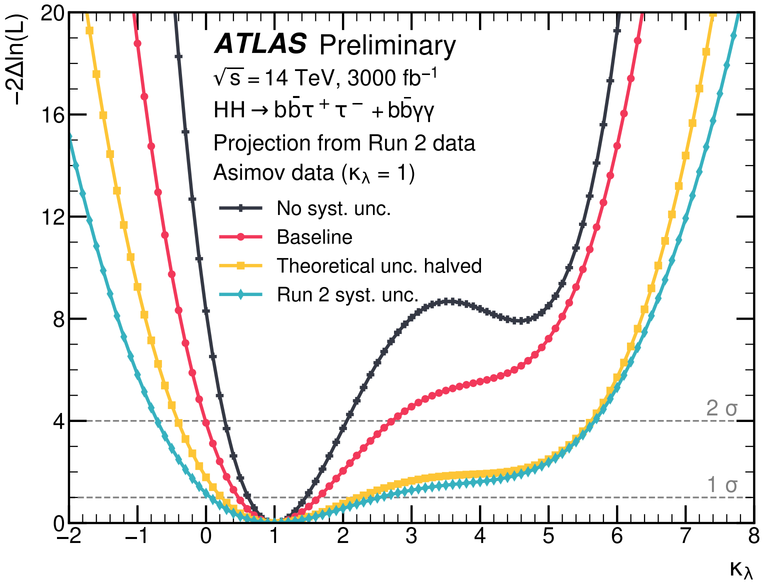

Figure 4.34: HL-LHC prospects of the expected negative log-likelihood scan on the Higgs self-coupling modifier under different assumptions of the systematic uncertainties. The dashed gray horizontal lines correspond to the 1 σ and 2 σ confidence intervals [99].

On the other hand, the projection to HL-LHC is also studied for limits of HH cross section and κ_λ, assuming no observation of HH signal. A background-only Asimov data is generated for this study. As shown in Fig. 4.35, for the baseline case, the expected upper limit of the HH signal strength is 0.56, and the expected limit interval of κ_λ is $[2.0, 4.1]$ at 95% confidence level. The expected results exclude the SM HH production with $\mu = 1$ and $\kappa_\lambda = 1$ under an assumption of no HH signal, hence if the SM HH signal exists, a large excess between the observed and expected results is expected. CMS has similar results [97].

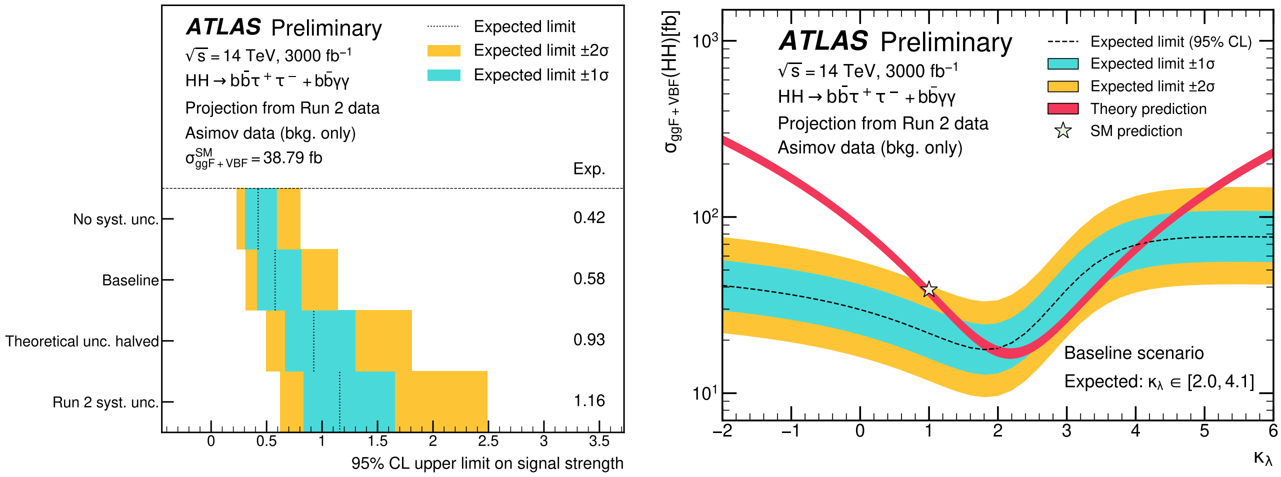

(a) *(b)*

Figure 4.35: HL-LHC projections of the 95% expected upper limit of HH signal strength assuming SM Higgs self-coupling (a) and the 95% expected limit interval of κ_λ [99].

Contrary to the hadron colliders, where the double Higgs production is dominated by gluon-gluon fusion ($gg \to HH$), at lepton colliders, it proceeds via double Higgs-strahlung ($e^+e^- \to ZHH$) particularly relevant at low energy, or via vector boson fusion ($e^+e^- \to HH\nu_e\bar{\nu}_e$), more important at center-of-mass energy of 1 TeV or above. For instance, CLIC at $\sqrt{s} = 3$ TeV or ILC at $\sqrt{s} = 1$ TeV can get κ_λ with a precision of about 10%, while FCC-hh is expected to reach 5% [100]. Information on potential of HE-LHC can be found in Ref. [101].

4.15 Conclusion

In this chapter, the latest ATLAS result of the double Higgs production using Run 2 data in the $b\bar{b}\gamma\gamma$ channels is presented, including searches for both non-resonant and resonant signals. The obtained results are very similar to the one in the same channel from CMS. Results of ATLAS from other channels are also presented, involving $b\bar{b}b\bar{b}$ and $b\bar{b}\tau\bar{\tau}$, a combination is performed for the three decay channels where a significant improvement on the sensitivity is obtained. The combination between double and single Higgs production, as well as the prospects for HL-LHC, are introduced.

5 - Calibration of the LAr electromagnetic Calorimeter

ATLAS made an electromagnetic calorimeter calibration paper with the Run-1 data [102] and another one [103] with the first 36 fb^{-1} Run 2 data (2015 and 2016). Then new algorithms for electron and photon reconstruction were used, including the change of clustering algorithm (from fixed-size cluster to super-cluster) [48], the calibration done with the changes is described in Ref. [49], with an integrated luminosity of about 81 fb^{-1} (2015-2017). The calibration to be presented in the following corresponds to the final recommendation of calibration using the full Run 2 139 fb^{-1}) data (2015-2018), which will be published soon.

5.1 Overview of ECAL Calibration

Electrons and photons, whose energy is measured from the electromagnetic calorimeter, are important signatures for many analyses, in particular for the Higgs mass measurement in the two photons channel. Early Higgs mass measurement with LHC Run 1 data using both the $H \to \gamma\gamma$ and $H \to ZZ^* \to 4l$ channels achieves an impressive result of 125.09 ± 0.24 GeV [3], where the $H \to \gamma\gamma$ channel experimental uncertainty is dominated by the photon energy scale systematics. In this sense, accurate calibration of the calorimeter is important for precise measurements.

The complete procedure of ATLAS ECAL calibrations is illustrated in Fig. 5.1.
Starting from the reconstructed cluster energy in the LAr calorimeter, a multivariate (MVA) regression based on simulation is performed in order to recover energy loss outside the LAr calorimeter. In parallel, the relative energy response of the LAr longitudinal layers is calibrated before applying the MVA regression to the data. Additional corrections are applied in order to improve the uniformity of the energy response in data, including the uniformity in azimuthal angle as well as residual electronic non-linearity from an analogue-to-digital converter (ADC) and layer 2 electronic gains (L2Gain). Afterwards, the so-called in-situ calibration which corrects both the energy scale and resolution using the Z boson mass peak is performed. Specific correction for photons is applied for the purpose of recovering the lateral energy leakage outside the cluster [105]. Eventually, validation of the whole calibration is done with the $J/\psi \to ee$ and $Z \to ll\gamma$ events, which check the energy response respectively for electrons at very low energy and for photons which have different signals in the LAr calorimeter.

5.2 MVA Calibration

The energy of electrons and photons are reconstructed mainly based on the LAr calorimeter cluster, which does not include energy lost due to the upstream material, leakage outside the cluster to the neighbour cells and longitudinal downstream leakage. All these effects are calibrated using a multivariate regression from reconstructed to truth energy, which is called the MVA calibration. Boosted decision trees (BDT) are trained with full simulated single particle samples without pileup, optimized respectively for electron, converted photon and unconverted photon in regions of $|\eta|$ and $|E_T|$ of the particle. The input variables for training include η and ϕ of the cluster, total energy deposited in the accordion (strips, middle, back), and longitudinal shape variables including the ratio of energy between the presampler and the accordion, and the one between the first and second layer (E1/E2). For the converted photon, additional variables are

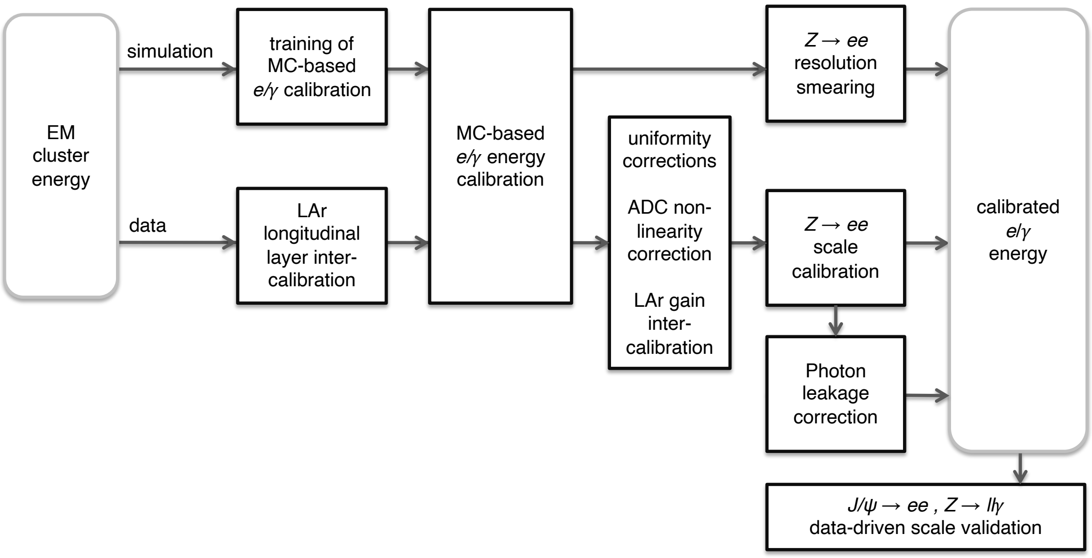

Figure 5.1: Calibration flow of the ATLAS electromagnetic calorimeter [104].

included, such as conversion radius and conversion track variables. In the transition region between barrel and endcap, the information stored in the E4 scintillator is used to mitigate the degradation of resolution due to the increased amount of upstream material in this region. A shift in energy is also applied to keep E_{reco}/E_{truth} centered at one.

The performance of the MVA calibration is shown in Fig. 5.2. The energy resolution is better at high energy due to the reduced stochastic uncertainty and noise. The response is similar between electron and converted photon due to a similar shower from the electron in the LAr calorimeter. The performance is slightly better for the unconverted photon.
The MVA regression is trained on the MC simulation, hence any mis-modelling in MC can lead to different energy responses when applying it to data. In order to correct for these effects, additional calibrations are needed.

5.3 Layer Calibrations

The longitudinal shower development is taken as an input variable for the MVA calibration, including the ratio of energy between PS and accordion and the one between the first and second layers. Therefore if the layer energy response is different between data and MC, the energy response after MVA calibration will be also different. Hence a calibration of PS using muons and an inter-calibration of layer 1 and layer 2 using both muons and electrons are used to adjust the relative layers' energy responses between data and

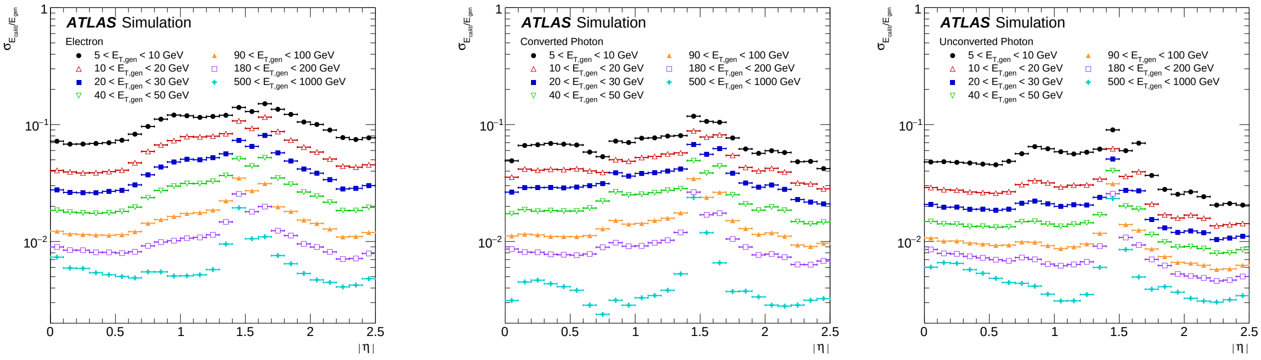

(a) (b) (c)

Figure 5.2: Calibrated relative energy resolution in function of η and truth E_T for electron (a), converted photon (b) and unconverted photon (c) [103].

MC.

5.3.1 Presampler Energy Scale

The presampler is used to measure the early longitudinal shower segmentation induced by the material before the accordion. The presampler energy is calibrated with muons from Z and W bosons decay using the low pileup data at a center-of-mass energy of 13 TeV, with a total luminosity of 0.33 fb^{-1} collected in 2017 and 2018 [106]. Benefiting from the blindness of muon to the upstream material, the energy scale factor is simply calculated as the ratio of the PS energy between data and MC:

$$\alpha_{\text{PS}} = \frac{E_0^{data}}{E_0^{MC}} \tag{5.1}$$

The scale factor is calculated with the mean values of the PS energy distributions in bins of η, where the PS energy is calculated as the energy deposit in the cells closest to the one matched to the muon track. Since the low-mu data is used for calibration, the pileup noise effect for muon is neglected.

5.3.2 E1/E2 Energy Scale

The layer 1 and layer 2 inter-calibration allows the adjustment of the differences in the relative layer energy response, due to mis-modelling of the upstream material before layer 1, electronic miscalibration, cross-talk effect and misalignment between layers. This difference is absorbed by the E1/E2 scale factor defined as the double ratio of energy measured in the two layers between data and MC:

$$\alpha_{1/2} = \frac{E_1^{data}/E_2^{data}}{E_1^{MC}/E_2^{MC}} \tag{5.2}$$

This scale factor is derived independently with $Z \to \mu\mu$ and $Z \to ee$ events, and respectively with two different methods for each.

Muon, the so-called minimum ionized particle, induces a compact shower of very low energy (hundreds of MeV) in the LAr calorimeter and is insensitive to the upstream material. Two methods are used to extract the E1/E2 scale factor with muons [107]. One is a fit method, which fits respectively the energy

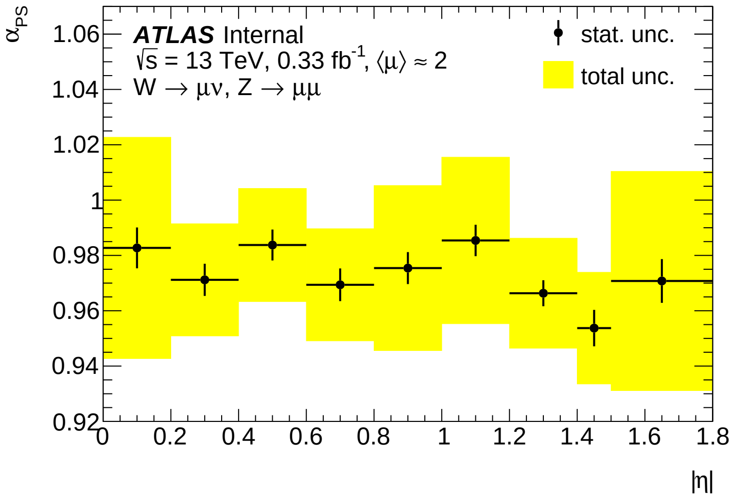

Figure 5.3: Presampler scale factor deduced with low pileup data using muons from Z and W decay [104].

profiles in the two layers by a convolution of Landau function and noise template, where the noise template is obtained from zero-bias events in order to describe the noise due to pileup and electronics effect. Afterwards, the most probable value (MPV) of the fitted function is used to calculate the scale factor. The other method is called truncated mean (TM), which calculates the mean values of E1 and E2 in a truncated window, hence is much less sensitive to noise and no noise template is needed. For both methods, the MPV and the TM of the layer energy are computed in intervals of η and pileup, and further extrapolated to zero pileup in order to get rid of the pileup noise, before computing the final E1/E2 scale factor for muons.

As opposite to muon, electron produces a real electromagnetic shower in the LAr calorimeter and is much less affected by the pileup noise, although it is more sensitive to the material in front of the calorimeter. The scale factor is determined by respectively exploiting the dielectron mass m_{ee} and the ratio of energy and momentum E/p in intervals of $E1/E2$ [108]. The scale factor which eliminates the dependency on E1/E2 of the ratio of data and MC is taken as the value for electrons. The electron results was used only for cross check in early calibration recommendation [49], now it is used to reduce the extrapolation systematic uncertainty of E1/E2 calibration from muon to electron.

A combination using the best linear unbiased estimator (BLUE) method is performed [109] to firstly combine results obtained with different methods for a given particle channel, followed by a combination of the muon and electron channels. The combination is shown in Fig. 5.4. Subsequently the combined E1/E2 scale factor is applied to correct the layer 2 energy in data, and the combined uncertainty is considered as the final systematic uncertainty of E1/E2 calibration.

5.4 Uniformity Corrections

The signal in the front-end readout boards is amplified and shaped by three linear electronic gains, depending on the ADC counts, in order to accommodate the same required dynamic range. High gain (HG),

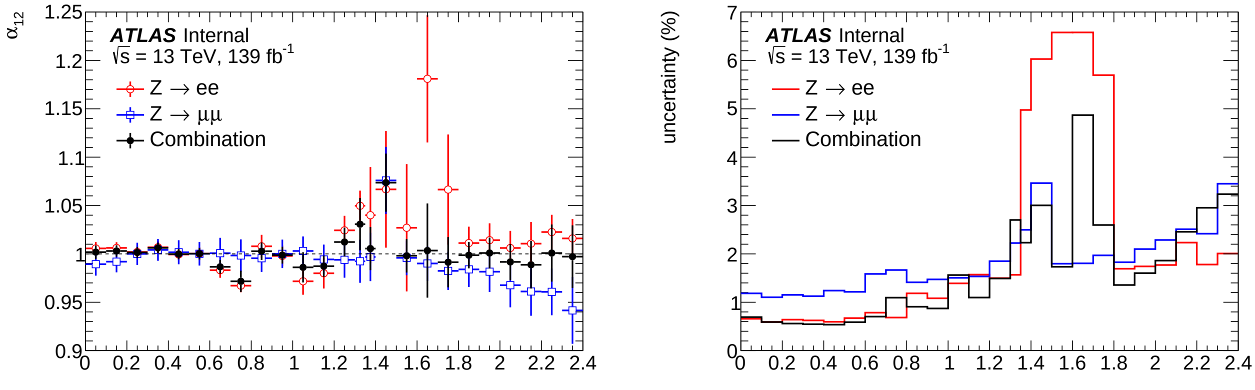

(a) *(b)*

Figure 5.4: Combined E1/E2 scale factors (a) and uncertainties (b) for electron, muon and electron+muon channels[104].

medium gain (HG), and low gain (LG) are used respectively for ADC counts lower than 1300, between 1300 and 3900 and very high ADC.

For each electronic gain, a linear function is used to convert the ADC counts to input ionization current (DAC) for the standard reconstruction, which is determined from dedicated electronics calibration ramp runs. However residual difference between the injected current and the linear ramp has been observed in particular at low ADC values, as shown in Fig. 5.5a. A fifth order polynomial function is used to parametrize the residual after the linear ramp, respectively for the MG and HG, in different η regions. The impact of the fitted residual is then estimated in the cluster energy level, and defined as the ADC non-linearity correction as a function of η and E_T as shown in Fig. 5.5b. This correction is applied to data.

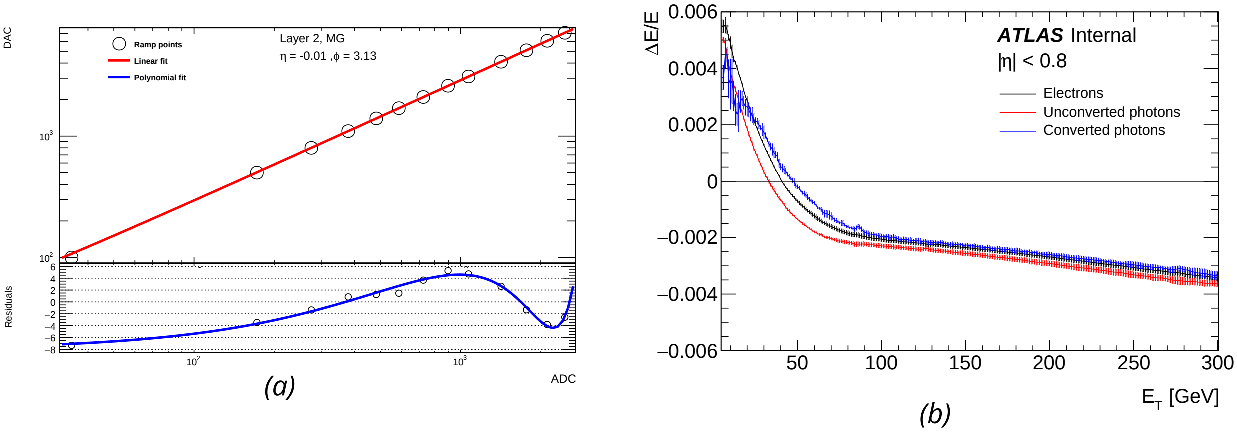

(a) *(b)*

Figure 5.5: (a) Example of electronic ramp runs. The discrete points represent the injected current (DAC) as a function of the ADC counts. The red curve is a linear ramp fit. The blue curve corresponds to the fifth order polynomial for parametrization of the residual. (b) Relative cluster energy correction from the residual ramp as a function of the E_T for electrons and photons[104].

Apart from the ADC non-linearity, the three electronic gains are required to be properly intercalibrated, in order to avoid possible non-linearity energy response when switching from one to another. For example, the in-situ calibration (described in Sec. 5.5) studies the electrons from Z boson decay, where most of them have HG cells, while a large fraction of the photons from Higgs decay is in MG. Hence miscalibration between MG and HG will lead to a non-linearity effect when extrapolating the in-situ calibration to the Higgs decay photons. A relative inter-calibration of the MG and HG in layer 2 of the LAr calorimeter is performed, using the special runs recorded in 2017 and 2018, where a much lower ADC threshold is used to move from HG to MG [**?**, 110]. The MG/HG scale factor is extracted between the MG-dominant special runs and the HG-dominant standard runs, by exploiting the dielectron mass of the $Z \to ee$ events in bins of η. The ADC non-linearity correction is applied before scale factor extraction. As shown in Fig. 5.6, the MG and HG responses are different by an order of $O(10^{-3})$, but since the fractions of MG and HG cells evolve with the particle energy, this difference can lead to a large non-linearity of the energy response. Hence the MG/HG scale factor is used to derive a correction as a function of η and E_T applied on data to suppress this non-linearity effect.

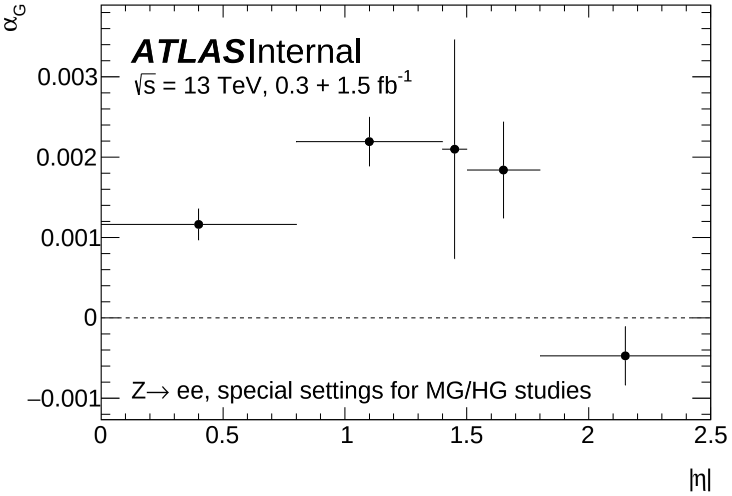

Figure 5.6: MG/HG scale factor derived between the standard and special runs using $Z \to ee$ events[104].

In the previous recommendation [49], there are already the uniformity corrections as a function of ϕ, in order to recover the energy loss near barrel calorimeter modules and the effect of high voltage inhomogeneity [103]. A new uniformity correction is applied to correct the so-called sagging effect that the calorimeter is deformed by its gravity and gives different energy response in the ϕ direction. The correction is derived by comparing the mean value of the electron energy profile between data and MC. The improvement of the azimuthal uniformity is shown in Fig. 5.7, where the performance in function of the azimuthal angle is drawn. Before the correction, there is a non-uniformity effect varying as a function of the azimuthal angle, with a magnitude up to 0.3%, and the correction is able to achieve a nearly flat response. This correction does not modify the inclusive average mass and improves the resolution of data.

5.5 In-situ calibration with $Z \to ee$ Events

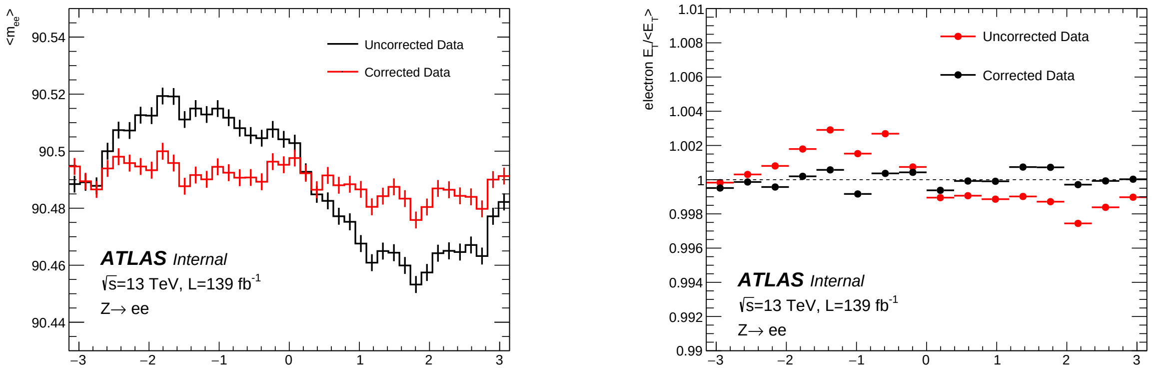

(a) *(b)*

Figure 5.7: Improvement on Φ uniformity of the data dielectron mass from $Z \to ee$ events. (a) Dielectron mass is plotted in function of the Z boson ϕ angle. (b) Electron energy response is shown in function of its ϕ angle[104].

Finally, the in-situ calibration, using the Z boson mass peak as a well-measured reference, calibrates all the residual energy response differences, with an energy scale factor α and a resolution constant term c [111]. The energy scale factor shifts data to the correct Z mass peak position. The resolution constant term smears the MC mass distribution to match the same spread as in data.

5.5.1 Data, Simulation and Event Selection

The 13 TeV pp collision data corresponding to an integrated luminosity of 139 fb^{-1} is used for calibration. The data events are required to be of good quality, that is to be belonging to the list of good lumi-block numbers (GRL) and pass the LAr quality cut. The individual luminosities of data are 3.2 fb^{-1}, 33.0 fb^{-1}, 44.4 fb^{-1}, 58.5 fb^{-1} respectively for 2015, 2016, 2017 and 2018.

The $Z \to ee$ Monte Carlo samples are simulated at NLO in QCD using POWHEG-BOX interfaced to the PYTHIA8 parton shower model. The background processes, such as $t\bar{t}$, $Z \to \tau\tau$, W and the di-boson production, represent less than 1% of the $Z \to ee$ events after selection. The background effect on the in-situ calibration and mass lineshape between 80 and 100 GeV is negligible, hence only the $Z \to ee$ is used for the calibration.

Events are first required to pass the high-level dielectron trigger for each year:

- 2015: `HLT_2e12_lhloose_L12EM10VH`
- 2016: `HLT_2e17_lhvloose_nod0`
- 2017: `HLT_2e24_lhvloose_nod0`
- 2018: `HLT_2e24_lhvloose_nod0 or HLT_2e17_lhvloose_nod0_L12EM15VHI`

Events should have a primary vertex (PV) which should further satisfy the cut on its z position: $|z_{vertex}| < 150$ mm, in order to suppress the non-collision background (cosmics, etc.).
Events are finally kept if they contain exactly two reconstructed electrons passing the following selection:

- with opposite charges.

- in the center region of detector: $|\eta_{\text{track}}| < 2.47$.
- transverse momentum above 27 GeV.
- not falling in the bad clusters of the calorimeter (GoodOQ).
- passing medium likelihood ID.
- d0 (the transverse impact parameter with respect to the beam line) significance smaller than 5.
- $|z_0 \sin\theta|$ (distance between the track and the PV) smaller than 0.5 mm.
- passing Loose isolation cut.
- invariant mass falling in $[80, 100]$ GeV window.

5.5.2 Principle of Calibration

After applying the MVA, layer calibrations and the uniformity corrections, a quick comparison of Z mass distributions (Fig. 5.8) shows around 50 MeV difference between data and MC on the peak position and a few hundred MeV difference on resolution. The remaining differences are supposed to be absorbed by the energy scale factor α and constant term c.

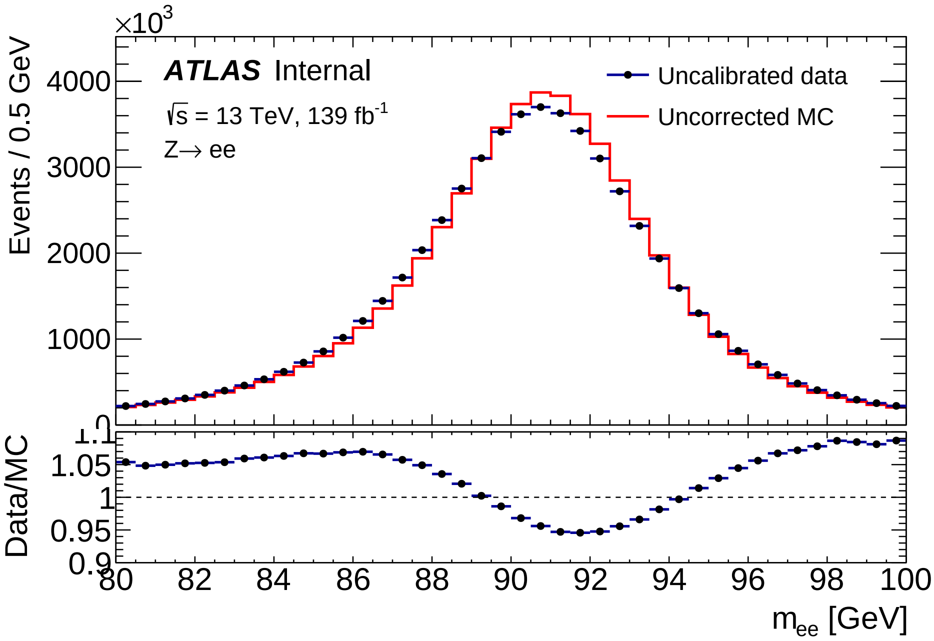

Figure 5.8: Di-electron invariant mass distribution of the full Run 2 data and the $Z \to ee$ MC simulation before applying the in-situ calibration. A shifted peak and different spread have been observed.

The scale factor α is defined as the relative difference of energy scale between data and MC depending on the pseudorapidity of the calorimeter cluster[1]:

$$E^{data} = E^{MC}(1 + \alpha(\eta)) \tag{5.3}$$

---

[1] In the following, the cluster pseudorapidity will be simply denoted as η.

where the energy scale of MC is assumed to be perfectly calibrated.

The constant term c is an additional term used to smear the width of MC mass distribution to the one of data

$$\left(\frac{\sigma(E)}{E}\right)^{data} = \left(\frac{\sigma(E)}{E}\right)^{MC} \oplus c(\eta) \tag{5.4}$$

$$E^{data} = E^{MC}\left(1 + c\left(\eta\right) \times x\right) \tag{5.5}$$

where the constant term c is smeared with a random variable x following a Normal distribution $\mathcal{N}(0,1)$.

The α and c parameters are then propagated to the invariant mass m_{ee}. Before the Zee in-situ calibration, the di-electron mass m_{ee} expresses as

$$m_{ee} \approx \sqrt{2E_1E_2(1-\cos\theta_{12})} \tag{5.6}$$

where E_1 and E_2 are electron (positron)[2] energies, and θ_{12} is their opening angle.
After applying α and c, the new mass expresses as

$$\begin{aligned} m_{ee}^{data} &= m_{ee}^{MC}\sqrt{\left(1+\alpha(\eta_i)\right)\left(1+\alpha(\eta_j)\right)} \\ m_{ee}^{data} &= m_{ee}^{MC}\left(1+\frac{\alpha(\eta_i)+\alpha(\eta_j)}{2}+O(\alpha^2)\right) \\ m_{ee}^{data} &\approx m_{ee}^{MC}(1+\alpha_{ij}) \end{aligned} \tag{5.7}$$

with

$$\alpha_{ij} = \frac{\alpha(\eta_i)+\alpha(\eta_j)}{2} \tag{5.8}$$

where i and j are the indices of η bins of the two electrons. Assuming that scale factors are much smaller than 1, the second order term could be neglected.

From the same principle, the effect of the constant term on the mass is

$$m_{ee}^{data} = m_{ee}^{MC}\sqrt{\left(1+c\left(\eta_i\right)\times x_i\right)\left(1+c\left(\eta_j\right)\times x_j\right)} \tag{5.9}$$

where x_i and x_j are two independent Normal random variables. The relative mass resolution is deduced as

$$\left(\frac{\sigma(m)}{m}\right)^2_{data} = \left(\frac{\sigma(m)}{m}\right)^2_{MC} + \frac{c_{ij}^2}{2} \tag{5.10}$$

with

$$c_{ij}^2 = \frac{c^2(\eta_i)+c^2(\eta_j)^2}{2} \tag{5.11}$$

---

[2] The positron will be also labelled as the electron in the following document, and the calibration is done regardless of the charge.

5.5.3 Template Method

The α_{ij} and c_{ij} parameters in couples of bin (i, j) of η are simultaneously fitted using the so-called template method, followed by a χ^2 inversion in order to extract the individual α_i and c_i. For each pair of η_i and η_j of the calorimeter, a 2D scan is repeated for possible values of α_{ij} and c_{ij}, which distorts the di-electron mass in MC to produce the m_{ee} templates. The generated template mass is in the following form

$$m_{ee}^{template} = m_{ee}^{MC}\sqrt{(1+\alpha_i)(1+\alpha_j)(1+c(\eta_i)\times x_i)(1+c(\eta_j)\times x_j)} \tag{5.12}$$

For each template, the χ^2 value of mass distributions between templates and data is calculated

$$\chi^2 = \sum_{k=1}^{N} \frac{\left(P(m_{ee,k}^{data}) - P(m_{ee,k}^{template})\right)^2}{\left(\sigma_k^{data}\right)^2 + \left(\sigma_k^{template}\right)^2} \tag{5.13}$$

where $1 \leq k \leq N$ is the bin index of the invariant mass distribution of di-electron, $P(m_{ee,k}^{data})$ and $P(m_{ee,k}^{template})$ are respectively the probabilities to have the mass in bin k for data and MC template, and σ_k^{data} and $\sigma_k^{template}$ are respectively the statistical uncertainties in this bin. The typical choice of mass bin size is 1 GeV. An example of the 2D χ^2 scan matrix is shown in Fig. 5.9.

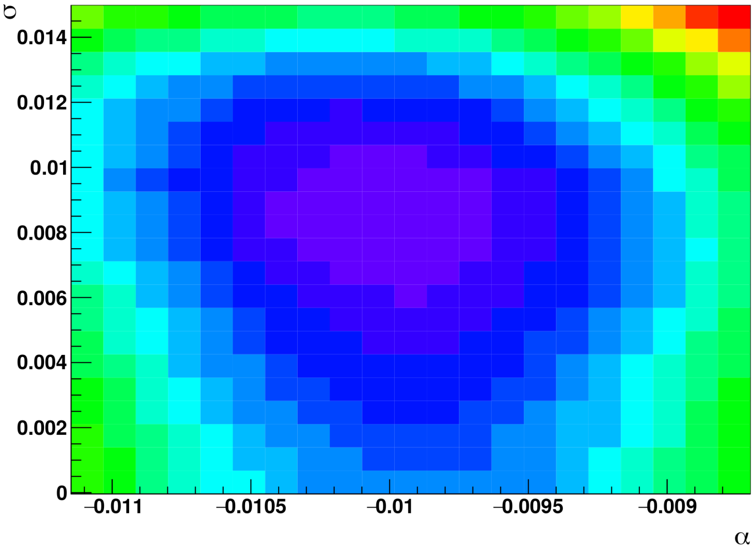

Figure 5.9: Distribution of χ^2 between data m_{ee} distribution and MC template, as a function of tested values of energy scale factor α_{ij} and resolution additional constant term c_{ij} [112].

The best α_{ij} and c_{ij} correspond to the minimum of the χ^2 scan. However, due to the non-trivial correlation between α_{ij} and c_{ij} as well as the non-parabolic behavior at low c_{ij}, a direct 2D fit is poorly converging. Instead 1D fits are performed to improve the stability of the fit. Firstly the value $\alpha_i j$ is profiled at fixed value of c_{ij} as shown in the left plot of Fig. 5.10, the minimum is derived with a parabolic fit to the χ^2 function:

$$\chi^2(\alpha_{ij}; c_{ij}) = a_0(c_{ij}) + \frac{(\alpha_{ij} - \hat{\alpha}_{ij}(c_{ij}))^2}{\delta\alpha_{ij}^2(c_{ij})} \tag{5.14}$$

where a_0 is the minimum χ^2 value, $\hat{\alpha}_{ij}$ and $\delta\alpha_{ij}$ are respectively the profiled value and the corresponding uncertainty of α_{ij}. The three parameters are calculated in function of different smearing c_{ij}, as shown in the right plot of Fig. 5.10.

Subsequently the χ^2 is plotted in function of c_{ij} and the associated profiled α_{ij}. The behavior of χ^2 is much less symmetric with respect to c_{ij}, that is the reason why α_{ij} is profiled while c_{ij} is only fitted once in the end. A third order polynomial function is used to fit the χ^2 curve in function of c_{ij}, and the uncertainty is obtained with the intersection $\Delta\chi^2 = \chi^2(\hat{c}_{ij} \pm \delta c_{ij}) - \chi^2(\hat{c}_{ij}) = 1$, with $\hat{c}_{ij}$ the best fit value of c_{ij}.

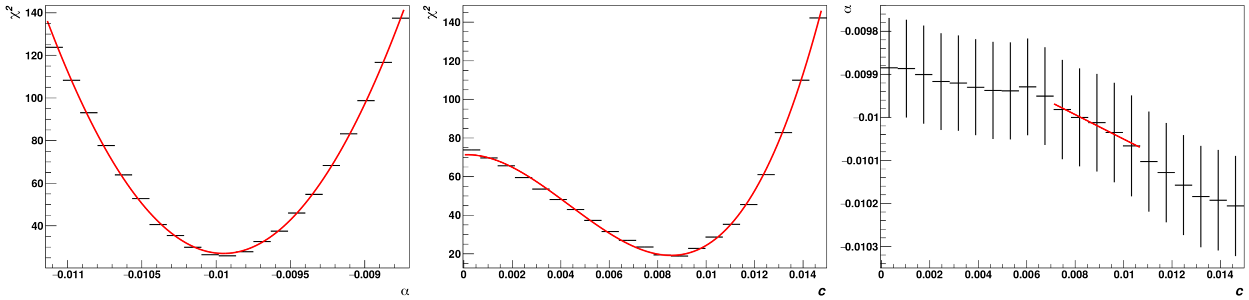

Figure 5.10: Illustration of fit procedures in the template method. Left: χ^2 as a function of $\alpha_i j$, at a fixed $c_i j$. Central: χ^2 as a function of c_{ij}, at the profiled best-fit $\alpha_i j$. Right: profiled best-fit $\alpha_i j$ in function of c_{ij}. [112].

With the measured value of α_{ij}, c_{ij} and their uncertainties $\delta\alpha_{ij}$, δc_{ij}, the individual values of α_i and c_i are obtained with a χ^2-based inversion, assuming α_{ij} and c_{ij} behave as Gaussian random variables:

$$\chi^2_\alpha = \sum_{i,j \le i} \frac{\left(\frac{\alpha_i + \alpha_j}{2} - \alpha_{ij}\right)^2}{(\delta\alpha_{ij})^2}, \quad \chi^2_c = \sum_{i,j \le i} \frac{\left(\sqrt{\frac{c_i^2 + c_j^2}{2}} - c_{ij}\right)^2}{(\delta c_{ij})^2} \tag{5.15}$$

Because the inversion weights each configuration (i, j) by its uncertainty, for configurations with few events in the fit range or with bad fit quality, an arbitrary large uncertainty is imposed to have an effective removal of their impact on the inversion. The correlations between different η bins are accessible by computing the Fisher information of the χ^2, which might be useful for additional checks and extensive studies.
More details of the method and technical implementation are described in the thesis of Christophe Goudet [112] and the one of Hicham Atmani [113].

The official in-situ calibration of Run 2 is done with different η binning for α and c, as shown in Tab. 5.1. The scale factor α is measured in 68 bins of η in order to improve the mass lineshape agreement between data and MC, while 24 bins are used for c. The wider η bin width for constant term measurement aims to increase the fit stability with a larger number of events because the non-parabolic behavior of the χ^2 curve at a small value of constant term will lead to a potential bias of the method.
In detail, the extraction is implemented within two steps of the 2D scan, the first done in 68 η bins, followed by the other in 24 η bins for which the α measured in the first step is applied on data.

$\lvert\eta\rvert$	0, 0.1, 0.2, 0.3, 0.4, 0.5, 0.6, 0.7, 0.8, 0.9, 1, 1.1, 1.2, 1.285, 1.37, 1.42, 1.47, 1.51, 1.55, 1.59, 1.63, 1.6775, 1.725, 1.7625, 1.8, 1.9, 2, 2.05, 2.1, 2.2, 2.3, 2.35, 2.4, 2.435, 2.47

Table 5.1: Absolute values of η bin frontiers for energy scale factors (black and brown) and resolution additional constant terms (brown). The extractions is done with both positive and negative values.

5.5.4 Results of Scale Factor and Constant Term

The scale factors and constant terms for each year of Run 2 are shown in Fig. 5.11, with the statistical uncertainties shown by the color bands.

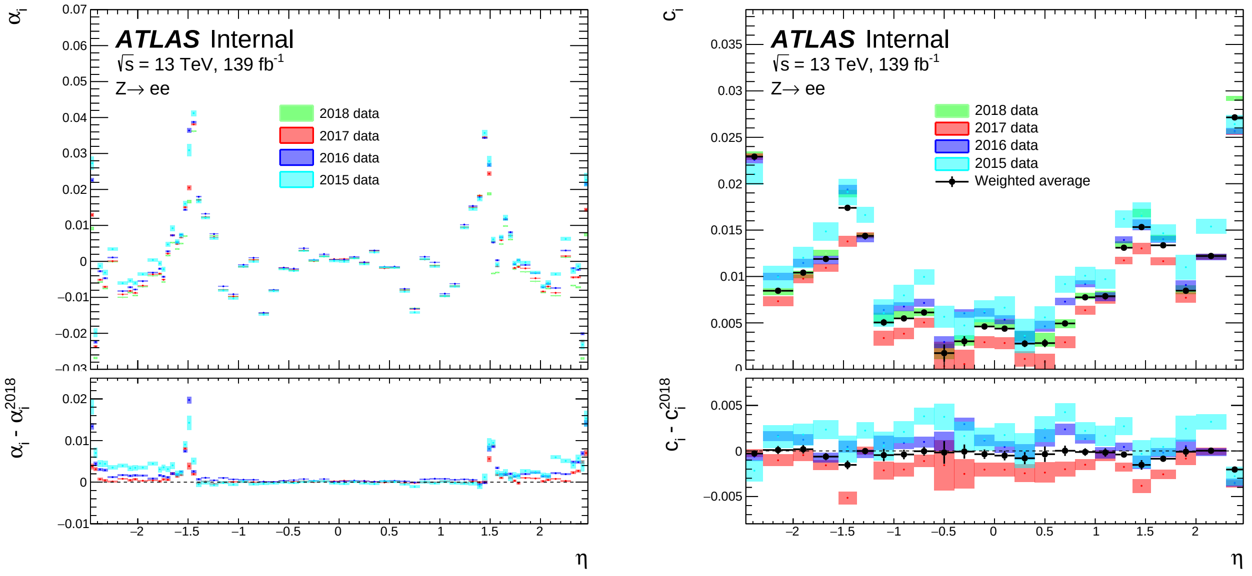

(a) (b)

Figure 5.11: Scale factor (a) and constant term (b) obtained with different years of Run 2 data. The constant terms are weighted by luminosity per year.

The α of each year differs significantly in the endcap region, with a maximum discrepancy of around 2%. The scale factor is decreasing by year, with the lowest in 2018. The main causes of such dependency are the increase of liquid Argon temperature and high voltage drop between the gaps during data recording, while it is stable in simulation. Due to the energy deposit in the calorimeter, the liquid Argon starts to be warmed up and creates a drop of energy of about $-2\%/K$. Such effect is increasing with the instantaneous luminosity. On the other hand, the ionization current produced in the shower decreases the high voltage between the gaps and leads to a smaller drift velocity of the ionized electrons hence a smaller energy response. These effects were estimated in the past with 2015 and 2016 data [103], as shown in Fig. 5.12 the prediction from the high voltage and LAr temperature changes is consistent with the observed difference of scale factors between the two years.

For the constant term c, there is almost a 0.5% maximum discrepancy among the years. If the electronic calibration is perfect, the constant term, which expresses the resolution difference between data and MC, is

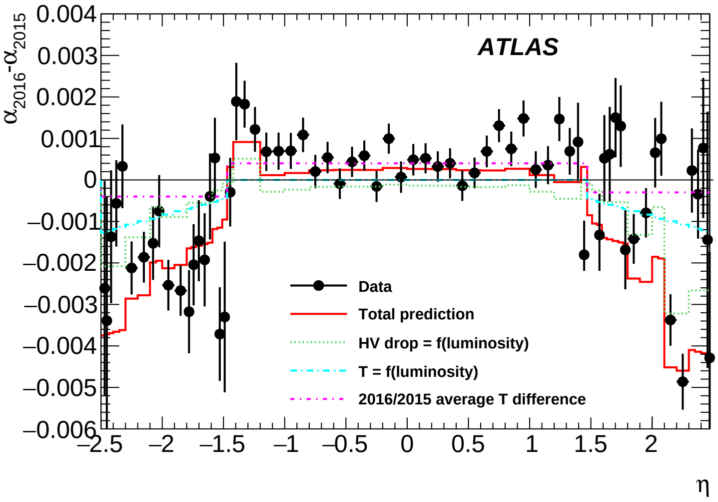

Figure 5.12: Comparison between the energy scale corrections derived from $Z \to ee$ events in 2015 and 2016 as a function of η. The difference in the energy scales measured in the data is compared with predictions taking into account the luminosity-induced high-voltage reduction and LAr temperature changes, as well as the small overall difference in LAr temperature between 2015 and 2016 [103].

expected to be independent of the data-taking periods which have different pileup conditions.
This dependency is caused by the larger pileup noise prediction in the MC, which leads to a worse energy resolution depending on the pileup and appears differently in the constant term of different years. In particular, for 2017, the constant term c is found to be globally below the other years. This is because the alternative 8b4e bunch filling scheme installed in the second period is not simulated in the MC, so the pileup noise modelling is even worse. The study of dependency of constant term on pileup will be introduced in Sec. 5.5.7. In this case, the luminosity-weighted average value of all the years is taken as the final constant term, assuming the statistical uncertainty of the constant term of each year is inversely proportional to the square root of the corresponding luminosity. The combined constant term and its statistical uncertainty are calculated with Eq. 5.16. Meanwhile, a dedicated systematic pileup noise mis-modelling is estimated for the energy resolution.

$$c_{\text{comb}} = \frac{\sum_i (L_i \cdot c_i)}{\sum_i L_i}, \quad \sigma_{\text{comb}} = \frac{\sqrt{L_i^2 \cdot \sigma_i^2}}{\sum_i L_i} \tag{5.16}$$

where $c_i \pm \sigma_i$ is the constant term with its statistical error measured with a given year i, L_i is the relevant luminosity.

The systematic uncertainties of the scale factor and the constant term had been produced in the previous EGamma recommendation. A similar exercise is repeated in this analysis: the systematic impact is estimated by computing the deviations from the nominal results after switching on the systematic variation. It is done for the systematics of the mass window, electron ID, isolation and bremsstrahlung radiation cut[3].

- Mass window: restricted cut of m_{ee} in $[87, 94.5]$ GeV instead of $[80, 100]$ GeV.
- Electron ID: tight likelihood ID quality instead of medium.

---

[3] For the official systematics, they include more sources, such as method bias, electroweak background.

- Isolation: no isolation cut instead of Loose.
- Bremsstrahlung: cutting on the so-called f_{Brem} variable to be smaller than 0.5.

$$f_{Brem} = 1 - \frac{(q/p)^{\text{1st measured}}}{(q/p)^{\text{out of Inner Dect.}}} < 0.5 \tag{5.17}$$

where q/p is the ratio of particle charge and track momentum, f_{Brem} represents the relative ratio of q/p of the last and first measurements in the inner detector, quantifying the momentum loss before entering the electromagnetic calorimeter. Ideally, if there is low bremsstrahlung radiation, f_{Brem} is close to 0.

The breakdown of systematics described above is shown in Fig. 5.13, where the shaded band is the total systematic uncertainty as a quadratic sum. For both scale factor and constant term, the systematic uncertainty is dominated by the mass window and electron ID. In the crack and the endcap region with $|\eta| > 1.37$, more material is present upstream of the ECAL and the trajectory of the particle is extended, hence it induces more bremsstrahlung radiations and gives a non-negligible systematic effect. Other systematics relevant to the selection efficiencies, electroweak background and method bias were studied in Ref. [114].

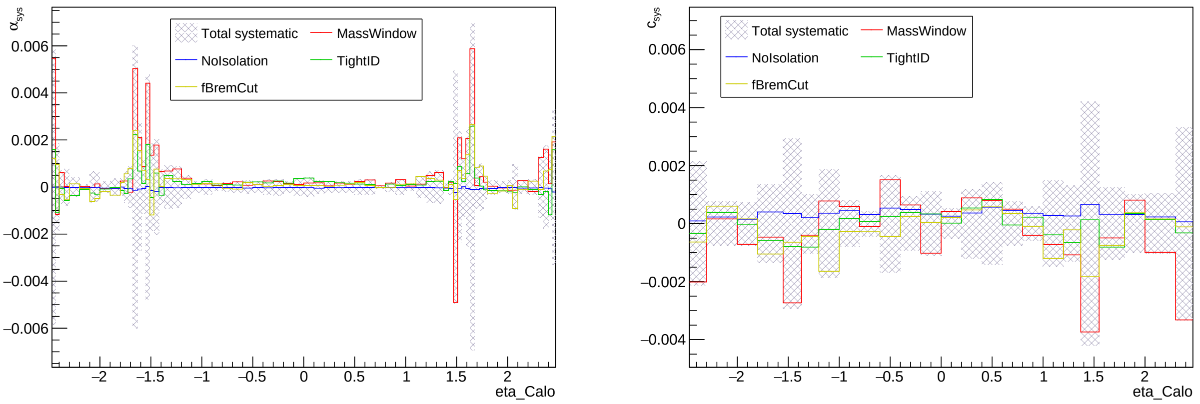

(a) *(b)*

Figure 5.13: Systematic uncertainties on scale factor (a) and constant term (b), estimated with data 2018 and MC16e. The shaded band is the total uncertainty.

5.5.5 Performance of Calibration

The performance of the calibration is validated by comparing the data and MC m_{ee} lineshape. The scale factors are applied accordingly to each period of data, and the weighted constant term is taken as a common smearing factor for MC. The calibrated mass distributions are shown in Fig. 5.14. The green band represents the uncertainty band mass lineshape originating from the scale factor systematics, which covers nicely the residual discrepancies between data and MC, except at a very low mass around 80 GeV.

The mean and standard deviation of m_{ee} distribution after the calibration are shown in Tab. 5.2. In general, the calibration is able to adjust the relative energy scale difference at the order of $O(10^{-4})$, and the relative resolution difference at the order of $O(10^{-3})$. When looking at electrons both in the barrel ($|\eta| < 1.2$) or endcap ($1.8 < |\eta| < 2.47$) region, a better mass agreement is observed in the barrel (Fig. 5.14b) with better matched peak position, better calibrated resolution, and up to 2% difference of lineshape, while the performance is slightly worse in the endcap region (Fig. 5.14c).

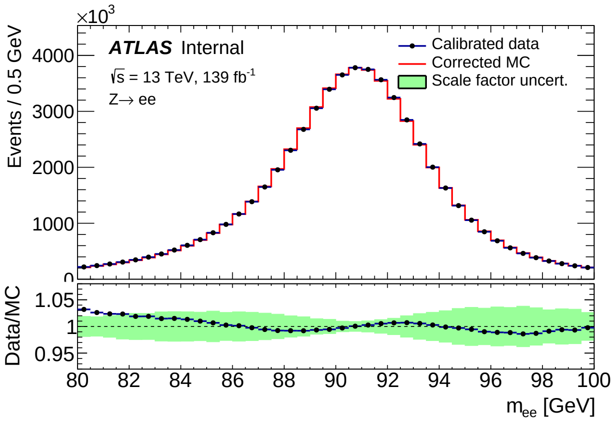

(a) inclusive

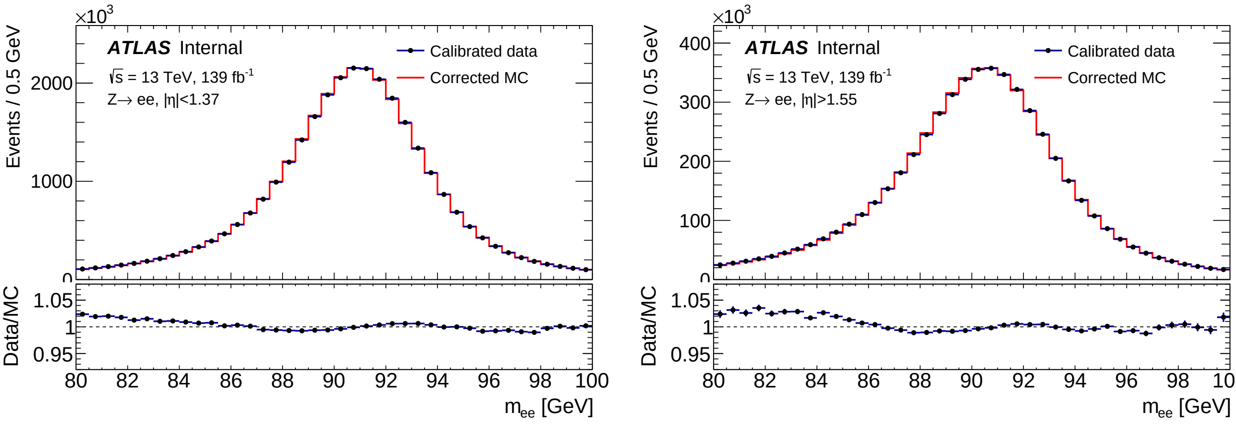

(b) barrel *(c)* endcap

Figure 5.14: Corrected mass for two electrons in a full range of calorimeter (a), both in barrel (b) and endcap (c) for the full Run 2 data and MC simulation.

The calibrated mass of the individual year is also presented. As shown in Fig. 5.15, similar lineshape is observed for 2015, 2016 and 2018, while for 2017 the mass lineshape is improved at low mass, but degrades at the peak and high mass. This implies a better resolution in data 2017 as shown with the column of Data RMS in Tab. 5.2, that mass resolution of 2017 is better than 2018, while the average pileup goes in the opposite direction.

It is mostly due to the 8b4e bunch filling scheme used in the fall of 2017, which reduced the pileup noise in the pulse signal because of the four empty spacing. Consequently, it brings a non-trivial resolution effect that can not be perfectly absorbed with a Gaussian smearing. A previous study by Saskia Falke [49] and a recent one by Antony Wendels which calibrates separately the BCMS and 8b4e periods of 2017 have achieved a better understanding of the resolution effect and the mass lineshape.

year	$< \mu >$	Data mean [GeV]	MC mean [GeV]	Data RMS [GeV]	MC RMS [GeV]	Δmean [MeV]	ΔRMS [GeV]	χ^2/ndf
full Run 2	33.7	90.490	90.499	3.525	3.518	-9.4	0.217	2500/39
full Run 2 barrel	33.7	90.574	90.578	3.392	3.386	-4.3	0.206	852/39
full Run 2 endcap	33.7	90.110	90.124	3.541	3.526	-14.4	0.326	3995/39
2015	13.4	90.442	90.453	3.455	3.433	-11.0	0.391	171/39
2016	25.1	90.479	90.493	3.499	3.485	-13.4	0.312	710/39
2017	37.8	90.498	90.503	3.523	3.529	-5.1	0.194	1198/39
2018	33.7	90.492	90.503	3.545	3.535	-10.4	0.270	1281/39

Table 5.2: Summary of statistic characteristics of the mass distribution of different years of Run 2. The mean and RMS are calculated in the mass range between 80 and 100 GeV, Δmean is the mean value difference between data and MC, ΔRMS is the quadratic difference of their RMS. The χ^2 test is bad due to the current discrepancies of lineshape as well as the tiny statistical uncertainty. The mean numbers of interactions per bunch crossing are shown [27].

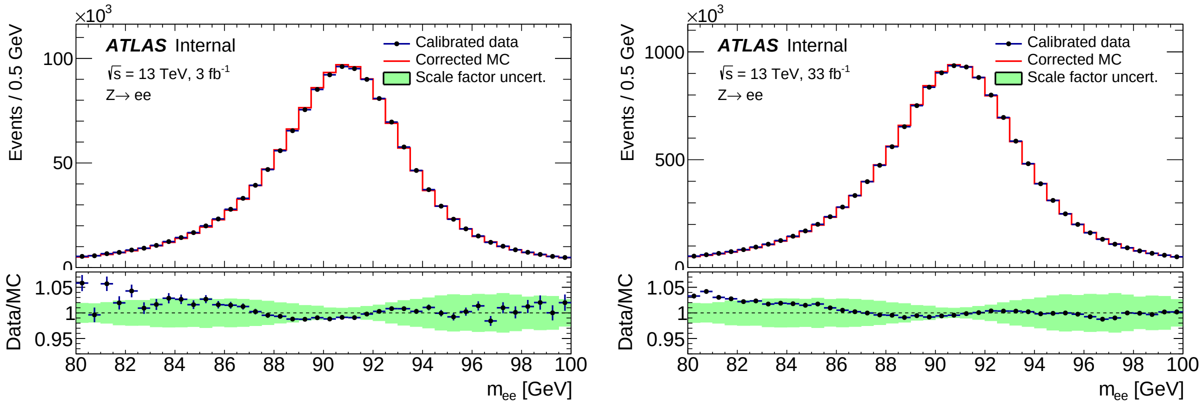

2015 2016

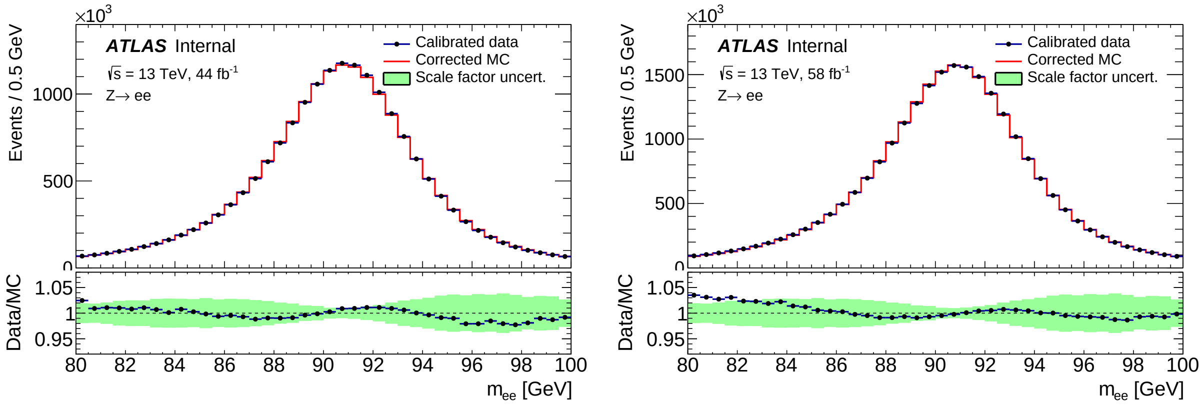

2017 2018

Figure 5.15: Mass distributions of 2015, 2016, 2017 and 2018 after Zee in-situ calibration. The green band, taking the same for all the years, represents the scale systematics effect on the mass lineshape.

The performance of the calibrated mass is also plotted in function of the azimuthal angle of the Z boson, the number of reconstructed vertices, time stamp and pileup, as shown in Fig. 5.16. The average values of m_{ee} profile in intervals of the exploited variable which are normalized to the full range average are computed respectively for data and MC using the full Run 2 dataset. The calibration achieves to have a flat distribution of m_{ee} as a function of the Z boson Φ angle because of the azimuthal uniformity correction described in Sec. 5.4. The energy response performance remains uniform with the detector running time, with a maximum deviation with respect to 1 around 0.16% and mostly smaller than 0.1%. A small dependency on the number of vertices and pileup is observed, the main reason is that the new super-cluster algorithm used to improve the resolution is however more sensitive to pileup. A sliding window clustering was used for the 36.1 fb^{-1} release, which gives a more stable performance relevant to pileup [103]. Differences between data and MC at a big number of vertices and pileup correspond to the high pileup period 8b4e of 2017, which is calibrated together with the BCMS period and appears to have some non-optimal residual.

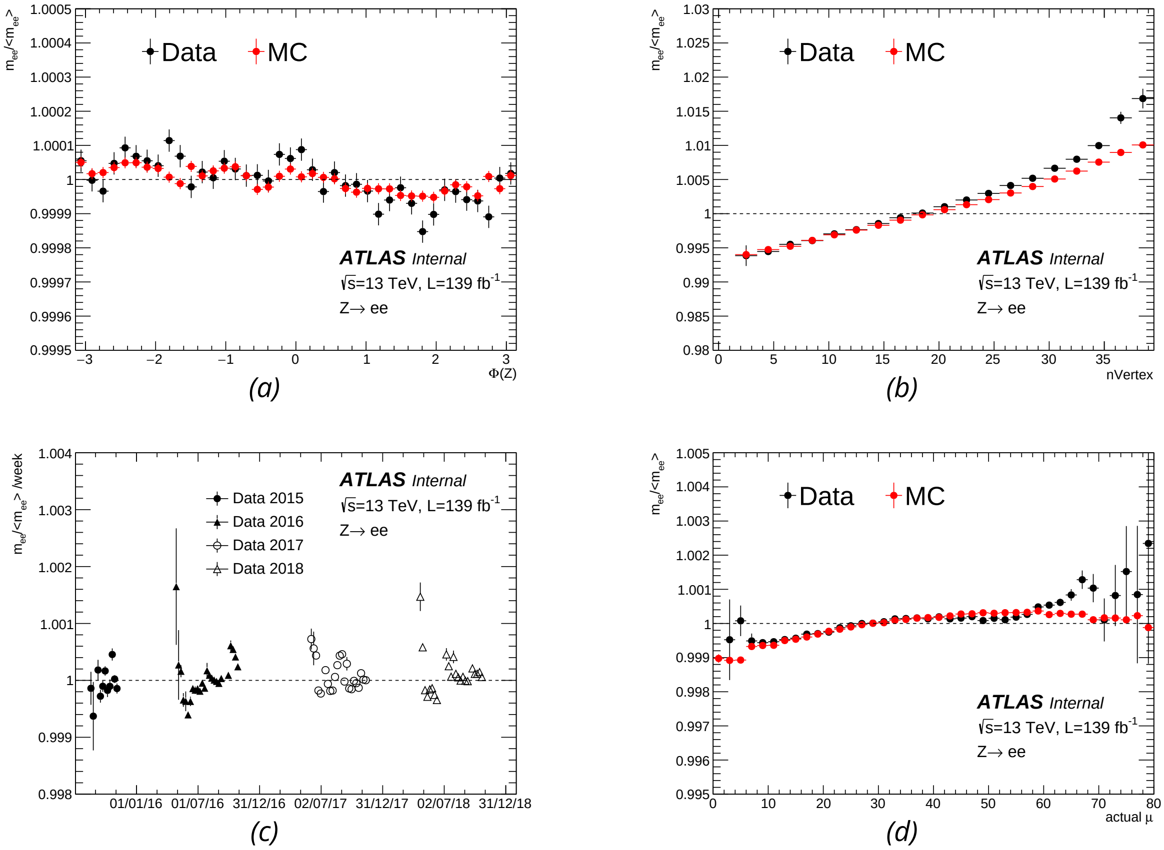

Figure 5.16: Calibrated di-electron mass performance in function of azimuthal angle of the reconstructed Z boson (a), number of primary vertices (b), LHC running time (c), and pileup up (d). The error bars represent the statistical uncertainties.

The mean and standard deviation of dielectron mass inside the [80, 100] GeV mass window are calculated in function of η of the leading and sub-leading electrons, as shown in Fig. 5.17. Three η ranges are exploited, barrel ($|\eta|$<1.37), extended crack ($1.37 < |\eta| < 1.82$) and the rest endcap ($1.82 < |\eta| < 2.47$), that m_{ee} is filled in both positive and negative η regions. The best performance is in the barrel, with around 10 MeV residual difference for mean and near 100 MeV for standard deviation, if the two electrons are both in the barrel. The energy measurement is also good in the endcap region, although less precise than the barrel. The extended crack region is less well calibrated, carrying often 50 MeV residual mass difference and 200 MeV tension on resolution.

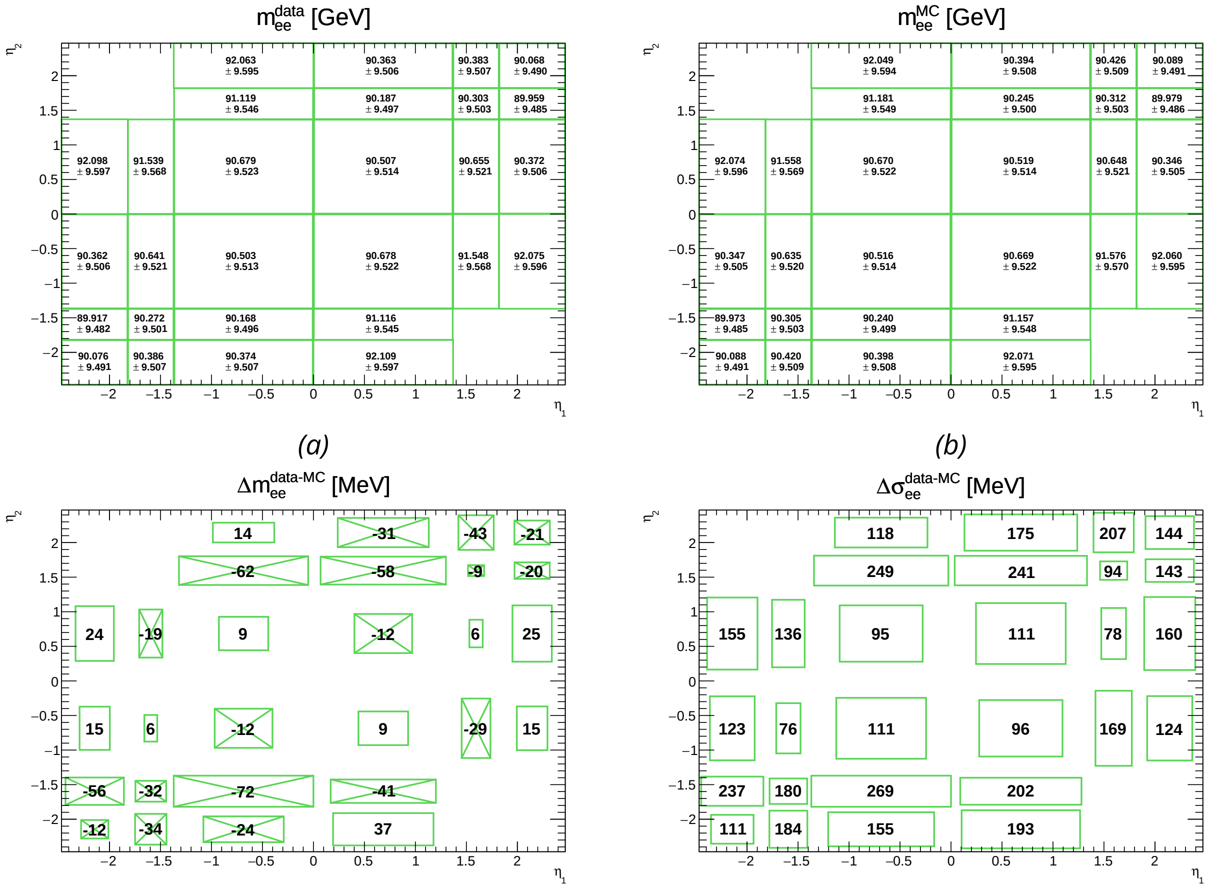

(a)

(b)

(c)

(d)

Figure 5.17: Mean and standard deviation of m_{ee} in function of pseudorapidity of leading (η_1) and subleading (η_2) electrons for full Run 2 data (a) and MC (b). The absolute difference of the mean (c) and the quadratic difference of the standard deviation (d) are shown. The empty bins contain no selected events.

The differences in the mass shape between data and MC are not perfectly absorbed by the current η-dependent scaling and smearing. To further improve the calibration, one possibility is to use an energy-dependent scale factor for more flexible calibration, named linearity, which is introduced in Sec. 5.6. Another solution is to implement a non-Gaussian smearing, assuming the residual discrepancies are due to some tails in the mass distribution, which cannot be absorbed by a symmetrical Gaussian smearing. It was initially studied in the forward ECAL ($|\eta| > 2.47$) calibration by the USTC group and then in IJCLab by Juan Tafoya [115] in the central ECAL region ($|\eta| < 2.47$). The idea is to have a resolution correction based on the difference between the reconstructed and the truth energies, which will affect the mass resolution asymmetrically.

5.5.6 Impact of ADC, L2Gain and Azimuthal Uniformity corrections

As described in Sec. 5.4, new corrections are applied for the purpose to improve the uniformity of energy response of the calorimeter. In order to check their individual influence, the three corrections are eliminated one by one starting from the baseline where all of them are applied before doing the in-situ calibration. The example of results using 2018 data and MC are used for illustration, which is shown in Fig. 5.18.

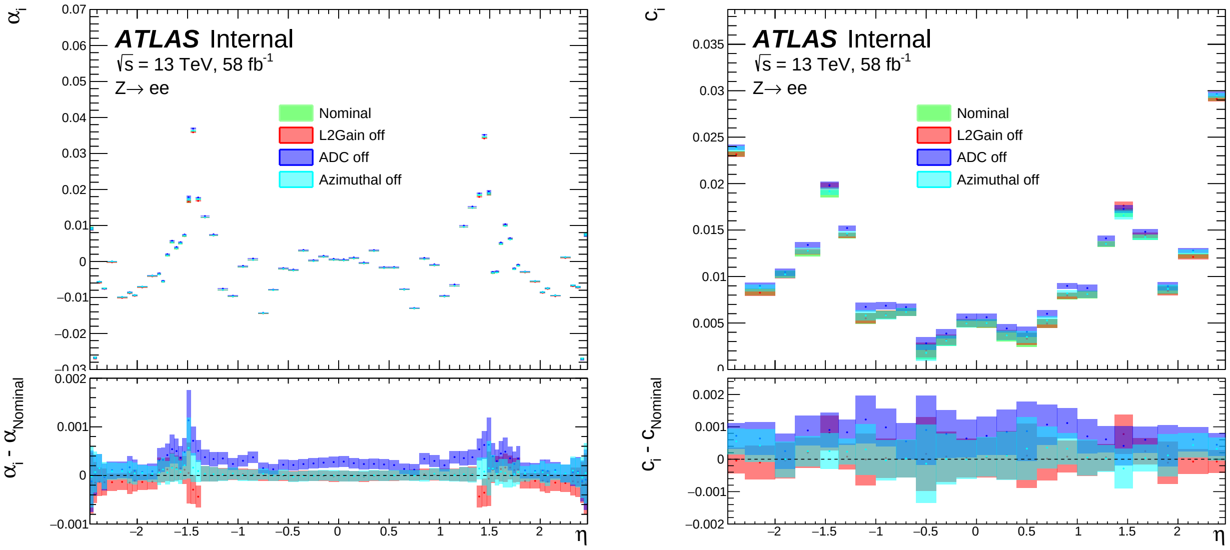

(a)

(b)

Figure 5.18: Scale factor (a) and constant term (b) obtained with 2018 data respectively for the nominal pre-stage calibration, and case without the ADC non-linearity, or L2Gain or azimuthal uniformity correction.

The ADC non-linearity has the largest impact on the calibration, it changes the energy scale by around 0.02% in both barrel and endcap regions, while a maximum effect of around 0.1% is observed in the crack. This is mainly because the correction itself is simply set to 0 for $E_T = 40$ GeV rather than the exact mean value of $Z \to ee$ electron E_T, therefore it relies on the in-situ calibration to adjust the energy scale.

The L2Gain correction has very little impact on both α and c, except at $|\eta|$ around 1.5, it increases the energy scale by around 0.02% and improves the resolution by around 0.08%. The reason is that the L2Gain correction is used to recover miscalibration of the medium gain, while the electrons from Z decay are dominated by cells at high gain, hence no significant effect is expected on the in-situ calibration. However, the impact of this correction can be enormous for electrons with transverse energy much higher than the $Z \to ee$ averaged E_T around 40 GeV, which will be discussed in Sec. 5.6.2 of the linearity for the LAr calorimeter energy response.

After switching off the azimuthal uniformity correction, the scale factor α is almost not changed, and an up to 0.06% effect on the constant term c is observed, which implies the improvement of resolution from this correction.

5.5.7 Impact of Pileup Modelling, Additional Material and Shower Shape Variable Selection

Some additional checks for the purpose of a better understanding of the calibration results were performed. They include the potential mis-modelling of the pileup noise, upstream material and selection of the shower shape variables, of which the impact on the in-situ calibration is respectively tested. The studies are based on the previous recommendation of calibrations.

Pileup noise mismodelling

As shown in Fig. 5.11b, the constant term appears to be different from 2015 to 2018 which have different pileup. Such effect is relevant to the mis-modelling of pileup noise in MC. Fig. 5.19 shows one example of the noise distribution in the second layer of the LAr calorimeter as a function of the averaged pileup, for both MC prediction and measurement in data. The noise has two main contributions, pileup and electronics. The pileup noise is almost linear as a function of $\sqrt{< \mu >}$, while the electronic noise is constant. The electronics noise can be obtained with the extrapolation of noise curve at $< \mu >= 0$, which is nearly consistent between data and MC. The different slopes imply around 10% [49] larger pileup noise simulated in MC with respect to data, such difference is proportional to $\sqrt{< \mu >}$, hence in Fig. 5.11b, the pileup noise is more over-simulated for 2018 than 2016 (2016 than 2015), so that only a smaller constant term is needed for smearing MC to data. For 2017, due to the presence of the 8b4e filling scheme, the pileup noise in data is consequently better controlled, accordingly the improved data resolution requires a much smaller constant term, also it is because this filling scheme was not simulated in MC.

A pileup reweighting approach is used to emulate a correction of the pileup noise mis-modelling, by scaling $< \mu >$ with a pileup reweighting scale factor. The standard choice is 1.03 derived from tracking observables, with which the MC pileup profile is reweighted to one of the data scaled by 1/1.03. However, this is not sufficient to correct the pileup noise mismodelling in the calorimeter. In order to compensate the observed 10% over-simulation, the pileup needs to be reduced by 20%, since the corresponding noise is linear with $\sqrt{(}\mu)$. Hence a reweighting scale factor of 1.2 is considered for the BCMS filling scheme, and 1.3 for 8b4e. For 2015, 2016 and 2018, the reweighting scale factor of 1.2 is used, and for 2017, the two sub-parts with different filling schemes are scaled by the corresponding factor. The pileup profile plotted with 2017 events are shown in Fig. 5.20, as well as the MC reweighted using the standard and alternative scale factors.

The in-situ calibration has been repeated after reweighting the MC with the alternative pileup reweighting scale factors, the α and c are re-derived for each year as shown in Fig. 5.21. As compared to Fig. 5.11b, the dependency of the constant term is significantly suppressed, and the difference as a function of η is mostly covered by the statistical error except for a few discrete bins. Given the improved consistency between different years, the weighted average constant term is now representative to describe the resolution smearing of all the years. In general, the obtained α and c are obviously different between Fig. 5.21 and Fig. 5.11, which is not only because of the application of alternative pileup reweighting scale factor but also more importantly due to different pre-stage calibrations.

Additional material before the calorimeter

The upstream material in front of the calorimeter is simulated in MC, however if it is not well modelled, the presence of any additional material in front of the calorimeter will have potential impact on the in-situ calibration. The impact of additional material is studied with material distorted samples, of which the additional material is presented in different regions of the detector. The various configurations are described in Tab. 5.3.

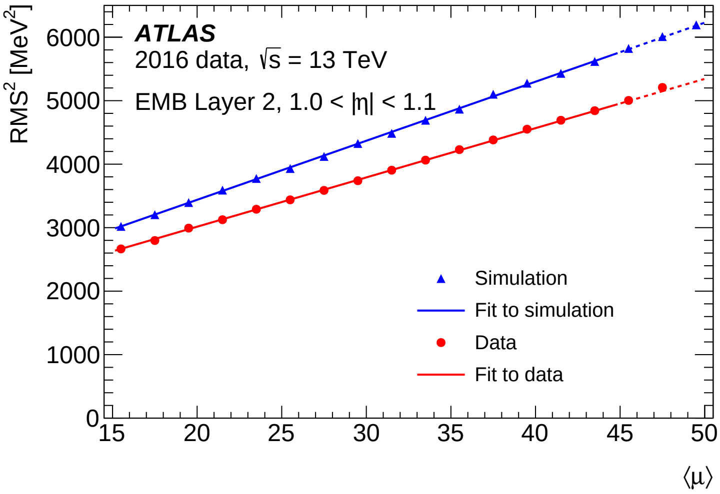

Figure 5.19: Evolution of the squared noise as a function of $< \mu >$ in data (red points) and simulation (blue triangles), for one particular η bin in the second layer of the EM calorimeter. The lines show the result of linear fits to the points for $< \mu >$ in [15,45] and the dotted lines show the extrapolation to higher $< \mu >$ [49].

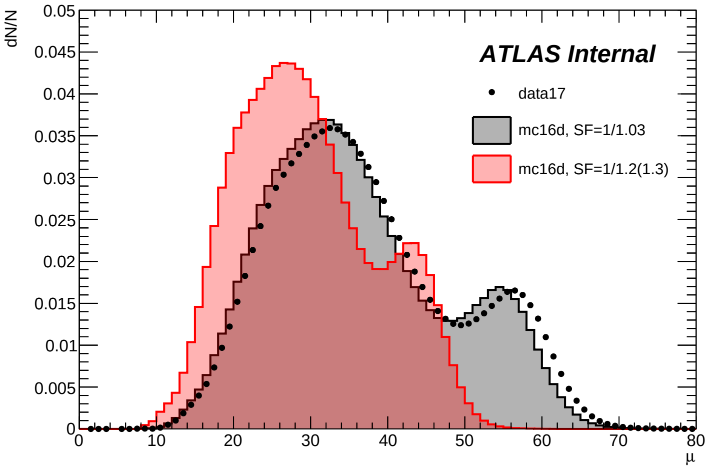

Figure 5.20: Pileup distribution of data 2017, MC reweighted with 1/1.03 and alternative factors using 1/1.2 for BCMS and 1/1.3 for 8b4e. The alternative reweighting is supposed to correct the pileup noise mismodelling in MC.

In total, six material distorted samples labelled as configA, configIBL, configPP0, configN, configEL and configFMX, defined with combinations of the additional material configurations, are used to study the impact on the in-situ calibration. The added material for part of the samples is displayed in Fig. 5.22.

The object is not only to check the influence of possible material mis-modelling on the scale factor and

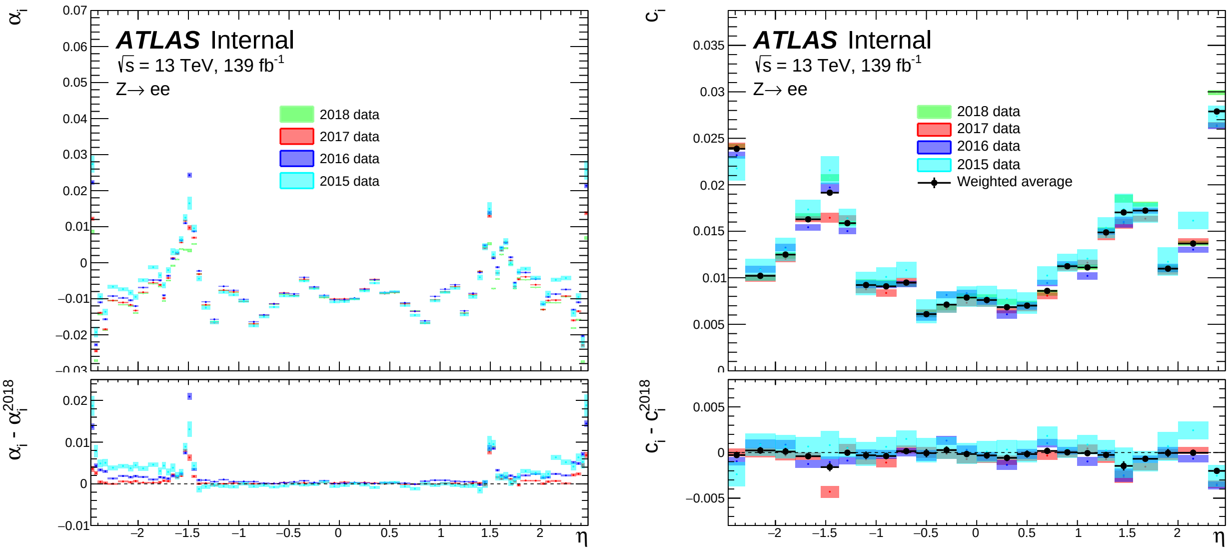

(a) *(b)*

Figure 5.21: Scale factor (a) and constant term (b) obtained with different years of Run 2 data after applying the alternative 1.2 or 1.3 pileup reweighting scale factor for the purpose of correcting the pileup noise mis-modelling. The constant terms are weighted by luminosity per year.

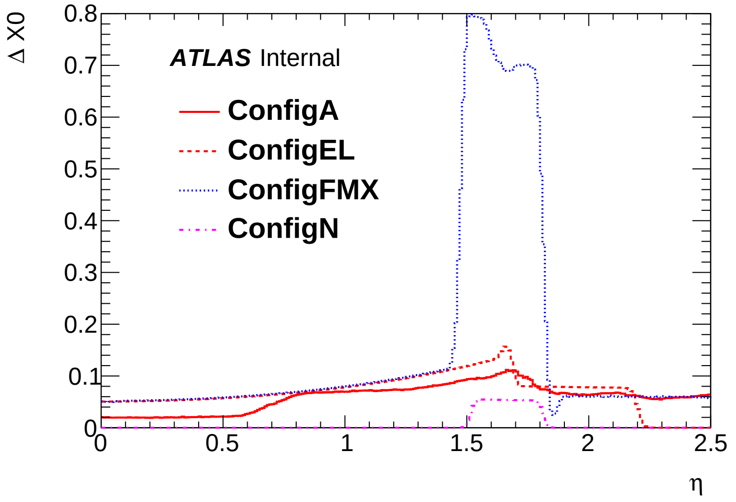

Figure 5.22: Amount of added material before the calorimeter for different distorted geometries used to compute the sensitivities to uncertainties in the material before the calorimeter [114].

constant term, but also to verify whether the material effect can be corrected using a simple scaling and a Gaussian smearing.

Name	Description
ConfigA	5% ID material scaling
ConfigL	5% X_0 of cryostat in barrel
ConfigE	7.5% X_0 in SCT/TRT endcap
ConfigF	7.5% X_0 in ID endplate
ConfigM	5% X_0 between presampler and calorimeter in barrel
ConfigX	30% X_0 in barrel-endcap transition region
ConfigN	5% X_0 between presampler and calorimeter in endcap
IBL	10% IBL material scaling
PP0	25% PP0 services scaling

Table 5.3: List of descriptions of different material distorted samples.

Due to the low number of events (10M events $\approx$ 1% of nominal MC) in the material distorted sample, the calibration is performed in 12 absolute η bins using the orange frontiers in Tab.5.1 for both α and c extractions. The material distorted samples are taken as pseudo-data to extract the scale factor and constant term with respect to the nominal MC:

$$E^{\text{pseudo-data}} = E^{MC}(1+\alpha(\eta)) \tag{5.18}$$

$$\left(\frac{\sigma(E)}{E}\right)^{\text{pseudo-data}} = \left(\frac{\sigma(E)}{E}\right)^{MC} \oplus c(\eta) \tag{5.19}$$

In practice, except in the η regions with a large amount of additional material, the resolution in material distorted samples is quite similar to the one in nominal MC. A potential problem is when the true value of the constant term is too small, since it is positively defined, the χ^2 curve will lose its parabolic behavior, and gives the biased fit result. In order to prevent such potential bias, the electron energy in material distorted samples is firstly smeared by a sufficiently large constant term of 1%, which is afterwards subtracted from the measurement as shown in Eq. 5.20.

$$C_{\text{distorted}} = \sqrt{max\,(0,\, c(|\eta|)^2 - 0.01^2)} \tag{5.20}$$

where $C(|\eta|)$ is the constant term measured between nominal MC and material distorted sample where the electron energy is relatively smeared by 1%.
The impact of additional material on the calibration is shown in Fig. 5.23. Since the distorted samples always have more simulated material, the energy scale is hence always reduced and the resolution is worse than the one of nominal MC.

As shown in Fig. 5.23a, the impact on α is significant and consistent with the amount of added material shown in Fig. 5.22. For instance, configFMX has additional material at η up to 2.5 with the maximum amount at $1.5 < |\eta| < 1.8$, hence the energy scale is changed proportionally to material bias in the full range. As for configN, it introduces more material only near the crack, so the effect on the scale factor is null elsewhere.

The measurement of the constant term is more affected by the statistical fluctuation due to its peculiar fit behavior. For most of the bins, the effect is tiny or not far away from the statistical error, the most visible effect occurs at $1.5 < |\eta| < 1.8$ in particular for configFMX, configA, configEL. The sample configN has a null impact on constant term near the crack region where additional material is actually presented is mainly due to the fact the material is added in the last stage between PS and accordion, therefore the influence is smaller than the ones with material added further from the calorimeter. Another reason is the fit stability of the constant term.

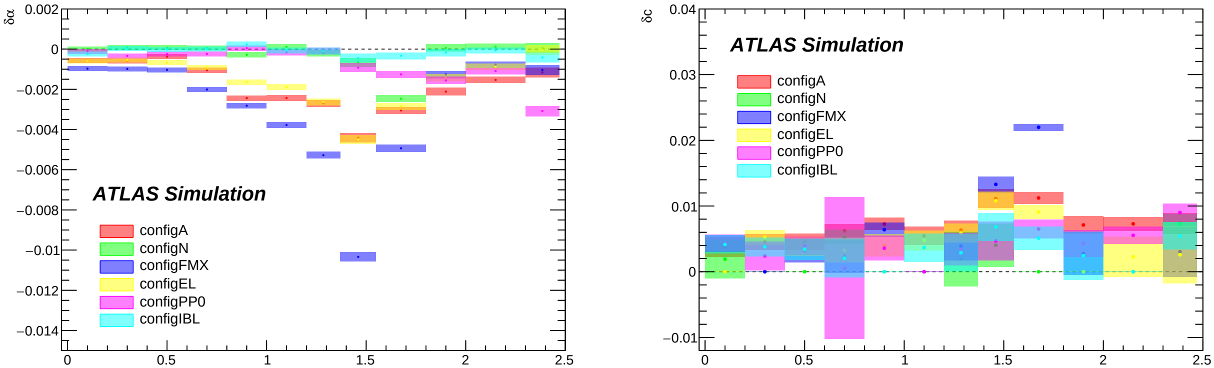

(a) *(b)*

Figure 5.23: Changes in energy scale factor (a) and constant term (b) due to the presence of additional material in different regions of the detector in front of the calorimeter. The colored bands represent the statistical uncertainty.

The original mass lineshape between the nominal and material distorted MC is shown by the black curve in Fig. 5.24, where configA. configFMX and configEL change obviously the m_{ee} shape. The additional material induces more bremsstrahlung radiation hence the dielectron mass is often smaller than the nominal one. After the in-situ calibration, the distortion on mass due to additional material is significantly absorbed, the mass lineshape is almost flat, and no similar trend is found as compared to the residual difference between standard data and MC as shown in Fig. 5.14 and Fig. 5.15.

Shower shape variable study

The shower shape variables, as characteristics of the electromagnetic shower properties in the LAr calorimeter, are important discriminating variables to identify electrons and photons. These intrinsic variables are not used as inputs of the MVA energy regression for electrons (Sec. 5.2), while they may be helpful to reduce the non-Gaussian dielectron mass behavior and improve the mass lineshape. Two lateral shower shape variables have been studied:

- R_ϕ: ratio of 3×3 to 3×7 $\eta \times \phi$ cluster energies at layer 2
- w_{stot}: total lateral shower width at layer 1

The R_ϕ and w_{stot} variables are sensitive to bremsstrahlung radiation, for electrons with no radiated photons, with less energy deposit in the nearby cells of the most energetic one, R_ϕ closer to 1 and smaller w_{stot} are expected. Hence an η-dependent cut with an efficiency of 85% has been deduced, in order to reduce large bremsstrahlung radiation.

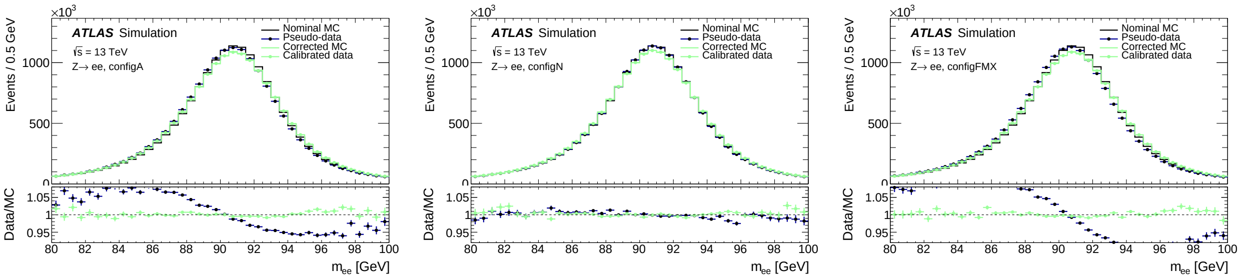

(a) configA *(b)* configN *(c)* configFMX

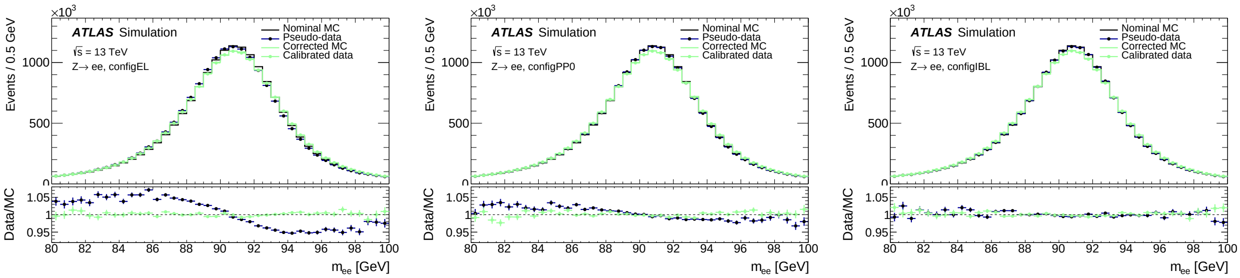

(d) configEL *(e)* configPP0 *(f)* configIBL

Figure 5.24: Mass lineshape between the nominal and material distorted MC before (black) and after (green) the in-situ calibration. The pseudo-data corresponds to the material distorted sample, which is calibrated by α and gives the green dot as calibrated data. The corrected MC is defined as the nominal MC corrected by c. The worse resolution of the green curves with respect to the black ones is mainly due to the introduced 1% smearing for mitigation of bias of c extraction.

The shower shape variables are not well modelled in the Geant4 detector simulation. In order to correct this effect, a cell level energy correction has been applied to produce re-weighted clusters with similar shower shapes as data, which is called shower shape fudging. The fudging preserves the total energy in the 7×11 cluster. However, because there is the cell-based medium ID selection, the efficiency of identification will be affected after modifying the cluster cells.

The distributions of the two shower shape variables as a function of η plotted with 2018 datasets are shown in Fig. 5.25: the shower shape fudging gives relatively good agreement between data and MC. Near the crack region $1.37 < |\eta| < 1.55$, the increased material and extended track trajectory lead to larger lateral shower dispersion, hence smaller R_{ϕ} and worse w_{stot} are observed. While there is less upstream material in the barrel therefore less bremsstrahlung radiation is produced, and in the endcap region, the radius is smaller hence the radiated electrons are less affected by the electromagnetic field. In consequence, the lateral shower shape is more compact for the barrel and endcap.
The 85% η-dependent cutting points obtained with data distributions are listed in Tab. 5.4, where R_{ϕ} is required to be larger than the cutting points, and w_{stot} and are selected to be smaller than the values.
The in-situ calibration is re-implemented after applying selection respectively on the two shower shape variables. The effect on scale factor and constant term is demonstrated in Fig. 5.26, which is negligible in most of the η regions, except in the crack with η around 1.5 where the upstream material is large and the trajectory of the electron is long.

The impact of the additional shower shape variable selection is shown in Fig. 5.27 plotted with 2018 data

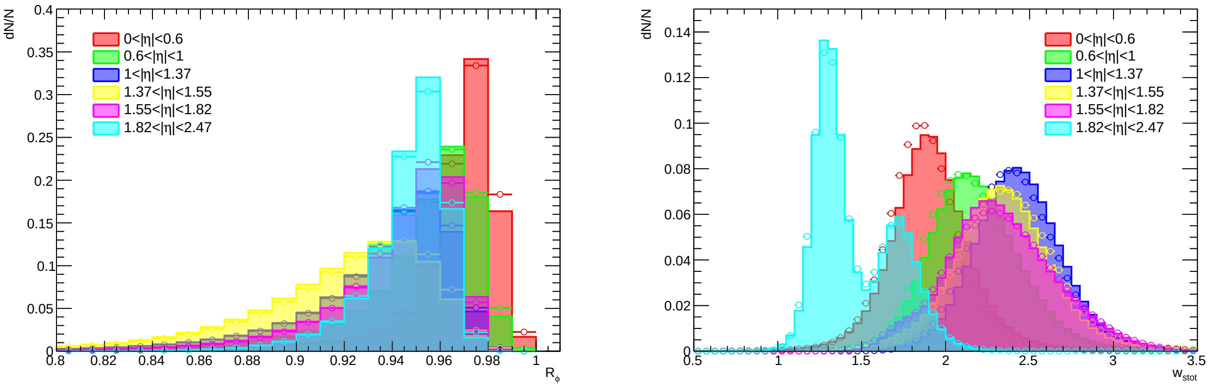

(a) *(b)*

Figure 5.25: Distributions of the shower shape variables R_ϕ (a) and w_{stot} (b) in function of $|\eta|$. The empty circles represent 2018 data, the colored histograms are the corresponding MC simulation. The distributions are normalized in each bins of $|\eta|$.

η^{calo}	[0, 0.6]	[0.6, 1]	[1, 1.38]	[1.38, 1.55]	[1.55, 1.82]	[1.82, 2.47]
R_ϕ	0.951	0.925	0.904	0.880	0.917	0.930
w_{stot}	2.096	2.432	2.672	2.674	2.685	1.756

Table 5.4: Cutting thresholds on shower variable variables R_ϕ and w_{stot} with an 85% efficiency respectively in each bin of η.

and MC, where the corresponding calibrations are respectively applied for cases with a different selection. The shower shape cut helps to reduce the discrepancies near the Z peak, while degrading the agreement in the left and right tails. The impact from w_{stot} cut is more significant with respect to R_ϕ.

5.6 Linearity Measurement with $Z \to ee$ Events

The linearity measurement is not part of the calibrations which is going to be applied on neither data nor MC, however, it gives an estimation of the residual non-linearity of the LAr calorimeter energy response, and can be useful for further study of the energy scale systematics.

5.6.1 Overview

Since the in-situ calibration is done with electrons from Z decay, with an average energy of around 40 GeV, electrons with this energy can be considered as successfully calibrated. However, it is not guaranteed that the energy response of the calorimeter is still accurate at different energy. For instance, residual non-uniformity of electronic gains, layer miscalibration and mis-modelling of upstream material can lead to the potential nonlinear performance of the calorimeter. Such kind of effect could be a challenge for precise measurement and search of new physics when applying the Z-based calibration on a high energy scale. Specifically for the Higgs mass measurement in the two photon channel, the non-linearity of the LAr calorimeter is the dominant systematic uncertainty.

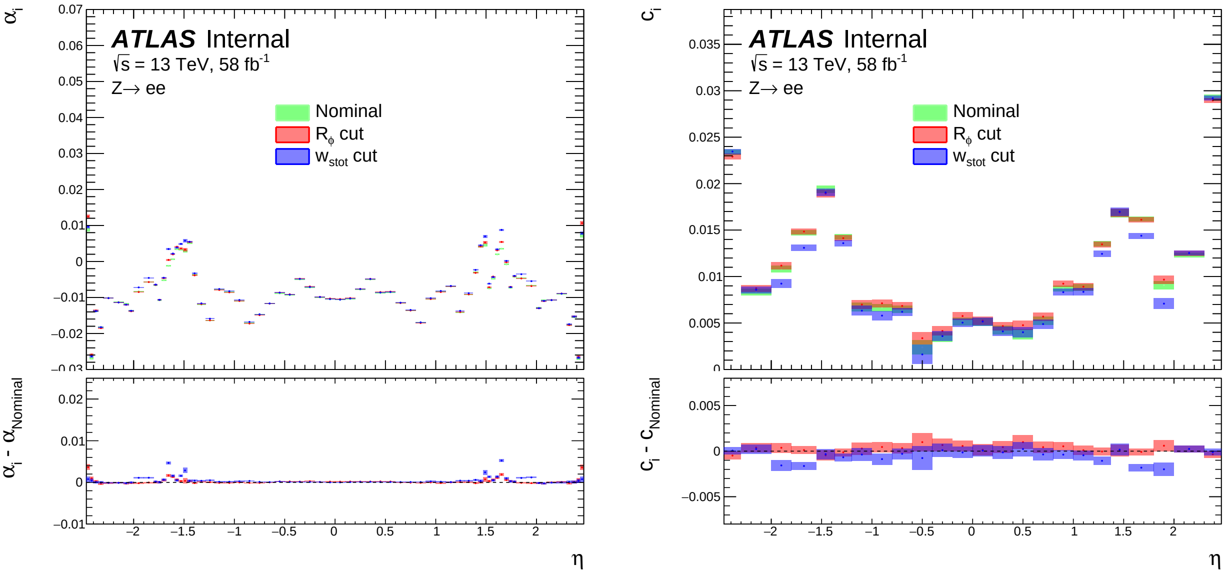

(a) (b)

Figure 5.26: Scale factor (a) and constant term (b) obtained with 2018 data using nominal selection, and additional cut on shower shape variables R_ϕ and w_{stot}.

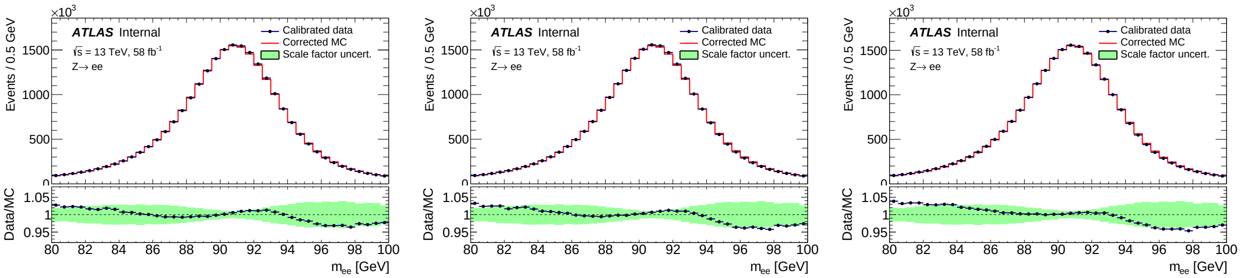

(a) Nominal *(b)* Cut on R_ϕ *(c)* Cut on w_{stot}

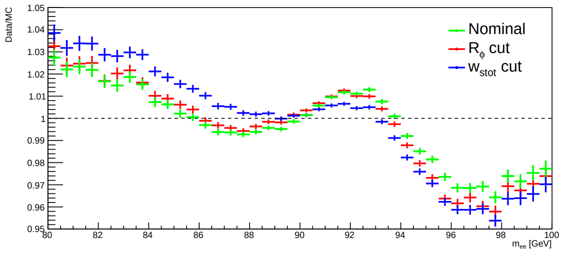

(d) Overlay of m_{ee} lineshape of the three variations.

Figure 5.27: Calibrated mass of data 2018 and MC with the nominal selection, and additional cut on shower shape variables R_ϕ and w_{stot}. The mass lineshape is overlapped in the bottom plot. The previous Rel. 21 calibrations are applied.

Therefore the measurement of energy linearity using the $Z \to ee$ events is performed in order to estimate the nonlinear response of the calorimeter as a function of the particle energy which indicates a potential miscalibration effect. The $Z \to ee$ linearity is defined as the energy-dependent scale factor between data and MC, that represents their residual scale difference after applying the η-only dependent calibrations. Similar to Eq. 5.3, the linearity can be expressed as

$$E^{data} = E^{MC}(1 + \alpha(\eta))(1 + \alpha'(|\eta|, E_T)) \tag{5.21}$$

If the global effect has been perfectly absorbed by the inclusive η-dependent scale factor, the average linearity in the range of E_T is expected to be zero.

The binning of η and E_T used to measure the linearity is summarized in Tab. 5.5. The η bins are now defined with the absolute value and are much coarser than the ones of the inclusive scale factor. The choice is made to mitigate the statistical fluctuations and to maintain a symmetric mass distribution in particular when the two electrons have really different kinematics.

	Borders of bins
$\|\eta\|$	0, 0.6, 1, 1.37, 1.55, 1.82, 2.47
E_T [GeV]	27, 33, 38, 44, 50, 62, 100, ∞

Table 5.5: η and E_T binning for linearity measurement.

5.6.2 Method

The linearity is extracted with the template method, after correcting the scale factor $\alpha(\eta)$ on data and the constant term c on MC. However, the typical approach which firstly measures α_{ij} in pair of η bins i and j then makes the inversion is not working properly for linearity. The kinematics of electrons from Z decay prevents the electrons to be located in very different η regions, or both having too large or too small energy. For these cases, the mass distribution is often shaped, sometimes even does not form the Z peak. An example of the mass distribution when requiring both electrons at very low transverse momentum is shown by the red curves in Fig. 5.28. In this special phase space, the electrons' transverse momentum is too low to reconstruct the Z mass peak which leads to visible asymmetric mass distribution. Since the peak is often lost within the current mass window between 80 and 100 GeV, the template fit is not always as good as the normal case.

A trick of event splitting is used to avoid such an issue, which is called the summing criteria. Such criteria select events with at least one electron belonging to a given $\eta \times E_T$ bin, when measuring the linearity at this region. This means that the other electron is not necessary to be in the current bin under investigation, but filling the full space of η and E_T. The mass distributions obtained with the summing criteria are plotted in black in Fig. 5.28, which fixes the shaping of the distribution and forms a nice Z mass peak in the center.

For events collected with this summing criteria, the di-electron mass is written as

$$m_{ee}^{data} = m_{ee}^{MC}\sqrt{(1 + \alpha'(|\eta|, E_T))(1 + \alpha'(|\eta|', E'_T))} \tag{5.22}$$

$$m_{ee}^{data} \approx m_{ee}^{MC}(1 + \frac{1}{2}\alpha'(|\eta|, E_T) + \frac{1}{2}\alpha'(|\eta|', E'_T)) \tag{5.23}$$

where $\alpha'(|\eta|, E_T)$ is the linearity from the electron in the common studied bin, while $\alpha'(|\eta'|, E'_T)$ is different for each event.

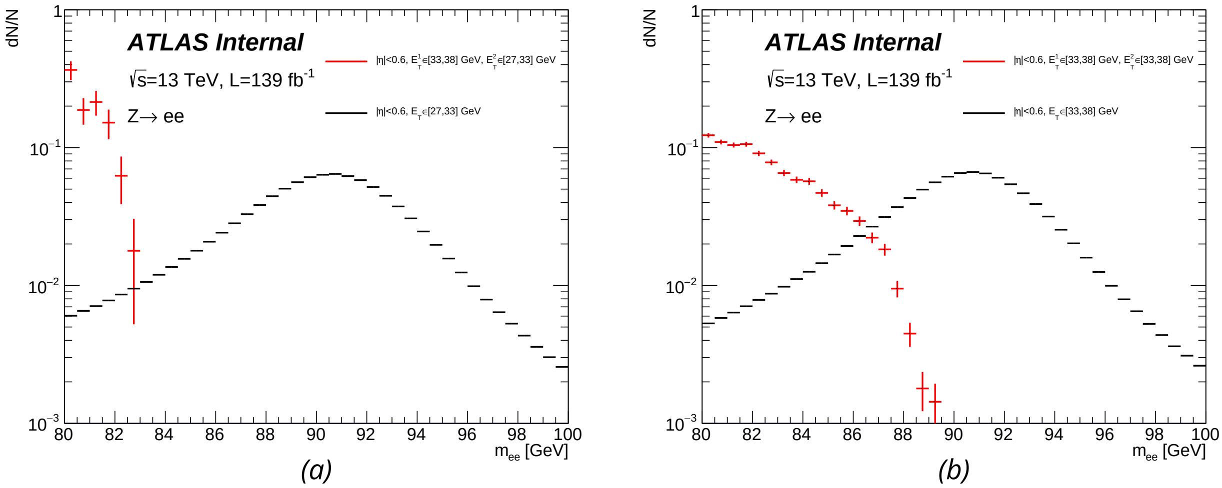

(a) *(b)*

Figure 5.28: (a) Distribution of m_{ee} when leading electron $E_T \in [33, 38]$ GeV, sub-leading electron $E_T \in [27, 33]$ GeV (red) and both with $|\eta| < 0.6$, the black curve is plotted with the summing criteria with at least one electron having $|\eta| < 0.6$ and $E_T \in [27, 33]$ GeV. (b) Distribution of m_{ee} when both electrons having $|\eta| < 0.6$ and $E_T \in [33, 38]$ GeV (red), and the black one is with at least one electron satisfying this selection.

Under assumption that after correcting the inclusive $\alpha'(\eta)$, the linearity integrated over the full η and E_T space is assumed to be 0, that $< \alpha'(|\eta'|, E'_T) > \approx 0$. Eq. 5.22 can thus be approximated as:

$$m_{ee}^{data} \approx m_{ee}^{MC}(1 + \frac{1}{2}\alpha'(|\eta|, E_T)) \tag{5.24}$$

Templates are generated by introducing a boost factor x, for a candidate linearity value $\beta(|\eta|, E_T)$:

$$m_{ee}^{template} = m_{ee}^{MC}\,(1 + x\beta(|\eta|, E_T)) \tag{5.25}$$

Since each event is used twice respectively in the according $\eta \times E_T$ bins of the two electrons, in order to preserve the statistical uncertainty, a half-weight is assigned to all the events, when filling them to plot the mass distribution.

The template method is essentially minimizing difference between m_{ee}^{data} and $m_{ee}^{template}$, thus the best-fit $\hat{\beta}(|\eta|, E_T)$ is an estimator of the truth linearity with a factor $\frac{1}{2x}$

$$\hat{\beta}(|\eta|, E_T) = \frac{1}{2x}\alpha'(|\eta|, E_T) \tag{5.26}$$

Hence $\hat{\beta}(|\eta|, E_T)$ extracts a fraction of the exact linearity characterised by the factor $\frac{1}{2x}$, which is a kind of boost factor of the fit convergence. Different boost factors were investigated by David Delgove, who proved with a closure test that the method is converging with $x \geq \frac{1}{2}$. Regarding the convergence rate, $x = 1$ is chosen as baseline.

The best-fit value $\hat{\beta}(|\eta|, E_T)$ is then applied to data, where the energy of electron and mass of di-electron are corrected.

$$E_e^{corr} = \frac{E_e}{1 + \hat{\beta}(|\eta|, E_T)} \tag{5.27}$$

$$m_{ee}^{data,corr} = \frac{m_{ee}^{data}}{\sqrt{(1 + \hat{\beta}(|\eta_1|, E_{T,1}))(1 + \hat{\beta}(|\eta_2|, E_{T,2}))}} \tag{5.28}$$

Then the whole procedure above is iterated until the template fit has converged. The final measurement of linearity is defined as the sum of all the iterations. Given the unclear correlations between the best-fit $\hat{\beta}$ obtained in different iterations, the statistical uncertainty of the final combined α' is not trivial to be calculated in an analytical way, hence a bootstrap method is used to evaluate the statistical uncertainty, which will be described in Sec. 5.6.9.

$$\alpha'(|\eta|, E_T) = \prod_{i=1}^{N} \Big(1 + \hat{\beta}^i(|\eta|, E_T)\Big) - 1 \tag{5.29}$$

5.6.3 Closure Test

The linearity extraction is based on several assumptions. It is assumed that after requiring one electron in a given $\eta \times E_T$ bin, the averaged linearity of the other one is zero. However, any residual inclusive scale factor $\alpha(\eta)$ would violate this assumption. In addition, due to the kinematics correlation between the two electrons, once selecting one electron in dedicated phase space, the averaged linearity of the other electron is not always null. All the ambiguities are supposed to be solved by doing several iterations, and a dedicated closure test is implemented to estimate the bias of the method. On the other hand, electron migration between E_T bins occurs due to non-zero linearity, and the use of iterations smoothly corrects the electron E_T and resolves the migration effect.

The closure test starts with the generation of pseudo-data. It is produced by injecting certain well-known linearity effects in MC. The MC sample mapped to 2018 is used for pseudo-data generation, with linear functions chosen as truth values of linearity. The linear functions are shown in Tab. 5.6, of which the slopes are chosen similarly as observation with data and the first term vanishes at 45 GeV ($m_Z/2$ chosen rather than the average E_T around 40 GeV). Pedestals are introduced in order to test the robustness of the method in presence of a residual inclusive scale.

The injected values are averaged in each $\eta \times E_T$ bins using Zee electron kinematics and then are compared to the measurements obtained between the pseudo-data and the raw MC. In total, 8 iterations are made, and for each of them, the cumulative linearity as a function of η and E_T is shown in Fig. 5.29. The truth linearity described in Tab. 5.6 is displayed by the continuous black curve where the discrete dots represent the evaluation at the average electron E_T in each bin of $\eta \times E_T$. The measured linearity by iterations and the residual bias with respect to the truth are shown in form of histograms. The residual bias is calculated as the difference between the measured linearity and the expectation of truth linearity. Since the truth is linear in E_T, the average effect is exactly equal to truth linearity evaluated in the average E_T.

The final results of the closure test are shown in Fig. 5.30a, with bias up to 2.10^{-4}. The largest effect appears in the last bin with $100 < E_T < +\infty$ GeV. It is worthwhile to clarify the importance of correcting electron E_T after each iteration, which reverses the migration of electrons due to non-zero linearity. Otherwise, the residual bias is increased to $2.5 \cdot 10^{-4}$ around 45 GeV where more electrons are present

η bins	Truth linearity
$\|\eta\| < 0.6$	$\alpha' = 3.10^{-5} \cdot (E_T - 45) + 5.10^{-4}$
$0.6 < \|\eta\| < 1$	$\alpha' = 3.10^{-5} \cdot (E_T - 45) + 5.10^{-4}$
$1 < \|\eta\| < 1.37$	$\alpha' = 3.10^{-5} \cdot (E_T - 45) + 5.10^{-4}$
$1.37 < \|\eta\| < 1.55$	$\alpha' = 8.10^{-5} \cdot (E_T - 45) + 1.10^{-3}$
$1.55 < \|\eta\| < 1.82$	$\alpha' = 8.10^{-5} \cdot (E_T - 45) + 1.10^{-3}$
$1.82 < \|\eta\| < 2.47$	$\alpha' = 3.10^{-5} \cdot (E_T - 45) + 5.10^{-4}$

Table 5.6: Injection linearity values used for pseudo-data generation. For simplicity, the same linear functions are respectively chosen for 1.37<$|\eta|$<1.82 and other regions. E_T is in the unit of GeV.

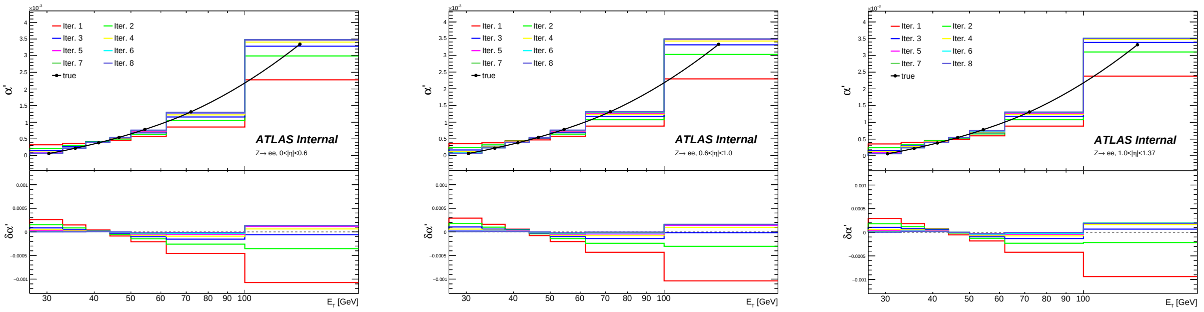

$0 < |\eta| < 0.6$ $0.6 < |\eta| < 1$ $1 < |\eta| < 1.37$

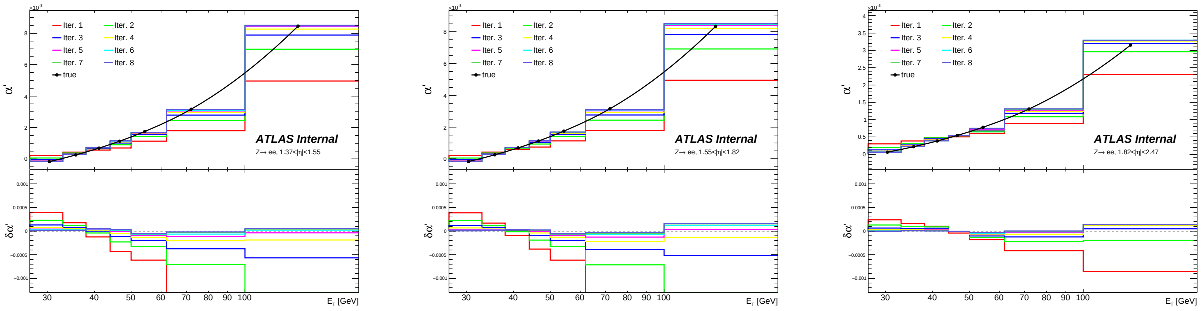

$1.37 < |\eta| < 1.55$ $1.55 < |\eta| < 1.82$ $1.82 < |\eta| < 2.47$

Figure 5.29: Closure test results of linearity. The truth injected values are shown by the black curve which are linear functions, the black dots correspond to the values at average E_T in each bin. The cumulative linearity up to a given iteration is shown by the colored histogram in the top pad, with residual linearity after subtracting the truth value plotted in the bottom pad.

and the migration effect is, therefore, more obvious.

A perfect closure on the m_{ee} distribution is observed when applying the measured linearity to pseudo-data and compared with the original MC. As shown in Fig. 5.30b, after linearity correction, the ratio of data and MC is flat, the residual difference on the average mass is only a few tens of keV, and 5 MeV for the standard deviation.

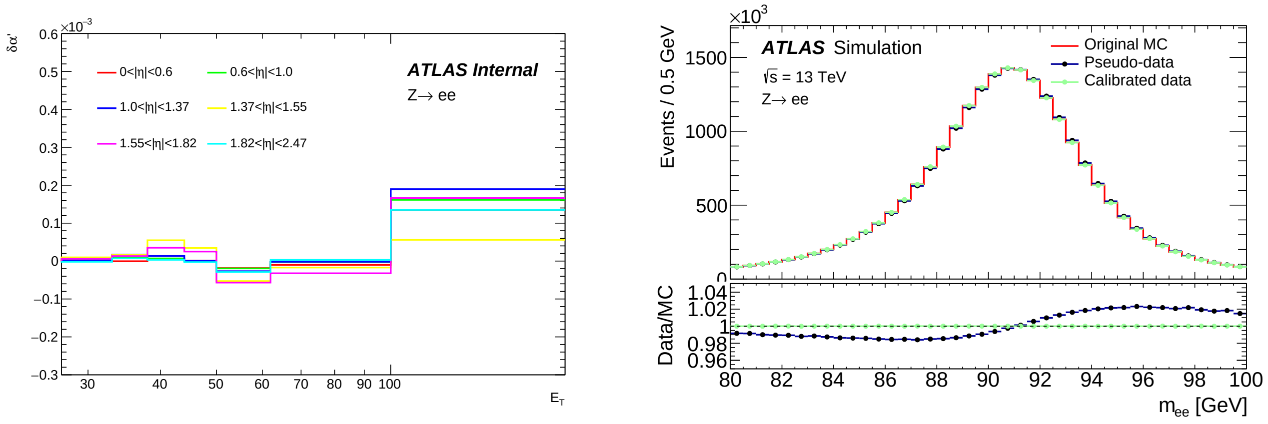

(a) *(b)*

Figure 5.30: (a) Summary of method bias of linearity in function of η and E_T after proceeding 8 iterations. (b) Mass distributions of original MC, pseudo-data bias by the injected linearity, calibrated data after applying the measured linearity. The linearity measurement shows a perfect closure on the mass.

5.6.4 Correction on Mis-modelling of Z Boson Transverse Momentum

The transverse momentum of Z boson is known to be not perfectly simulated in the Powheg samples. As shown by Fig. 5.31a, near the peak position around 5 GeV, the discrepancy between data and MC is more than 2%, and between 10 and 30 GeV, a good agreement is observed, however it starts to explode at larger p_T. The mis-modelling grows up with the rapidity for y bigger than 1.82, and around 10% disagreement appears at low p_T.

Such mis-modelling of Z boson p_T is corrected by reweighting the MC events with the data over MC ratio in Fig. 5.31a depending on p_Z and y of the Z boson. As a consequence of correcting the Z boson p_T, it also has significant improvement in electron transverse momentum modelling. As shown in Fig. 5.31b, the electron E_T is still quite different between data and MC after the inclusive Zee calibration. The difference is around 1% in the range below 50 GeV, while a significantly increased discrepancy occurs at larger E_T, which is compatible with the enhancement of data at large Z boson p_T. After performing the Z boson p_T reweighting, the difference on electron E_T is remarkably reduced that in most of the range the residual is smaller than 1%.

The modelling of the electron transverse momentum has an unignorable impact on the $Z \to ee$ linearity measurement. Because of the summing criteria described in Sec. 5.6.2 which is particularly used to avoid asymmetric mass shape, when exploiting a specific $\eta \times E_T$ bin, only one of the two electrons is forced to be in this bin, and the other one can be in the full phase space. Consequently, the effect of Z boson p_T reweighting is not uniform for different events selected by the summing criteria and depends on the kinematics of the electron distributed outside the current bin. The impact of such reweighting on linearity is estimated by doing the measurement with and without the reweighting, which will be introduced in Sec. 5.6.5.

5.6.5 Results

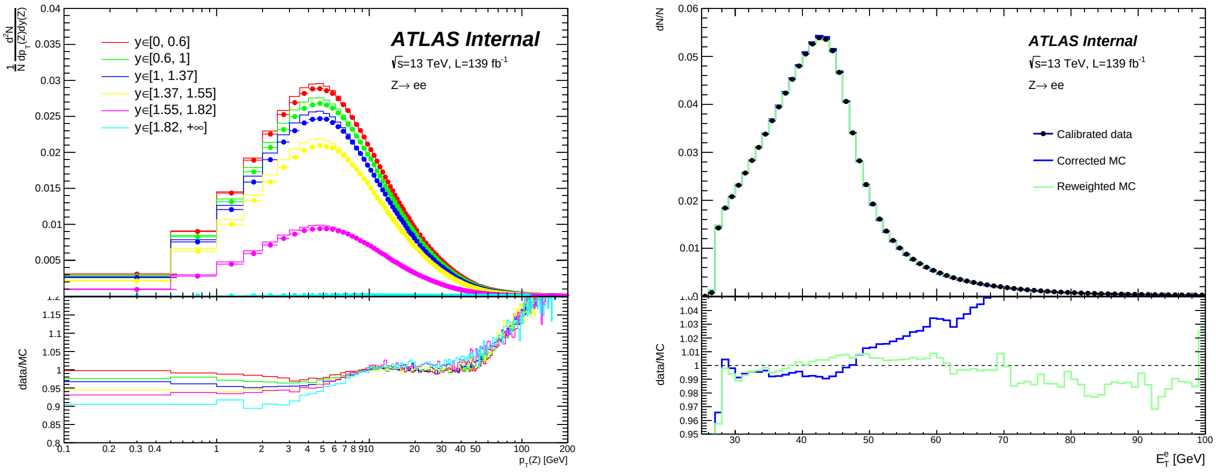

(a) *(b)*

Figure 5.31: (a) Mismodelling of the Z boson transverse momentum. Density distributions of Z boson p_T are plotted in function of its rapidity y, the inclusive $p_T \times y$ phase space is normalized to 1. The histograms correspond to the MC simulation, and the discrete dots are from the data. (b) Electron p_T distribution comparison between calibrated data and MC. The green curve represents the MC after applying the Z boson p_T reweighting.

The linearity is extracted with the full Run 2 datasets, as well the subset measurements with respectively 2015+2016, 2017 and 2018 are produced for additional checks. The transverse momentum of the Z boson is not well simulated in MC and corrected using the reweighting approach described in Sec. 5.6.4. The final results are shown in Fig. 5.32, where the linearity has a similar shape in different data. The error bars represent the statistical uncertainty estimated with the bootstrap method described in Sec. 5.6.9. The bootstrap study is performed using the full Run 2 datasets, the obtained uncertainty is extrapolated to the subset years' luminosity, which is used as the statistical error of the subset measurement.

The observed non-linearity of electron energy is in order of $O(10^{-3})$, in particular for the center of barrel ($|\eta| < 0.6$) and end-plate of endcap regions ($1.82 < |\eta| < 2.47$) where the effect is almost null except at $E_T > 100$ GeV. For the other η region, the measured non-linearity response on the energy scale is smaller than 5.10^{-3} in the E_T range of 27 and 150 GeV, the effect is around 1.10^{-3} at low E_T and around $3{-}4.10^{-3}$ at high E_T.

Since the linearity is extracted after calibrating the inclusive η-dependent energy scale, the linearity is expected to be null for electrons with E_T around 40 GeV[4]. The observation agrees with the expectation in most of the η region, except $1.37 < |\eta| < 1.55$, where a residual effect near 1.10^{-3} appears at 40 GeV. Such residual inclusive energy scale is also demonstrated by the residual mass difference near the crack region as shown in Fig. 5.17. One possible reason is that α and c in in-situ calibration are optimized using different η binning, and due to the large variation of energy scale and resolution in the crack region, the 68 bins

---

[4] $Z \to ee$ electrons has an average of transverse momentum around 40 GeV, while the Jacobian peak is located at $m_Z/2$.

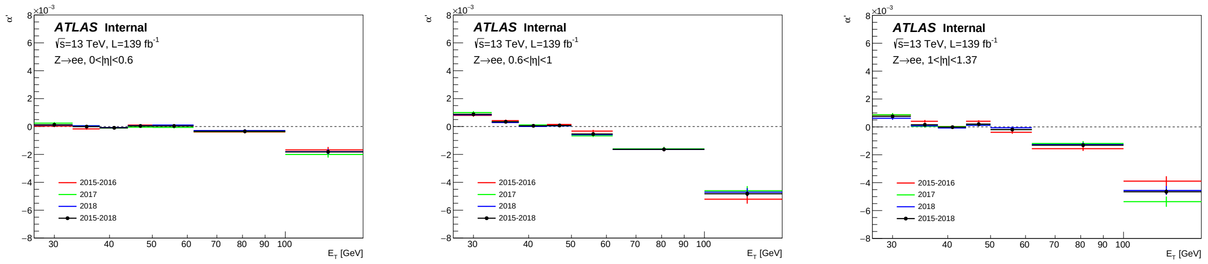

$0 < |\eta| < 0.6$ $0.6 < |\eta| < 1$ $1 < |\eta| < 1.37$

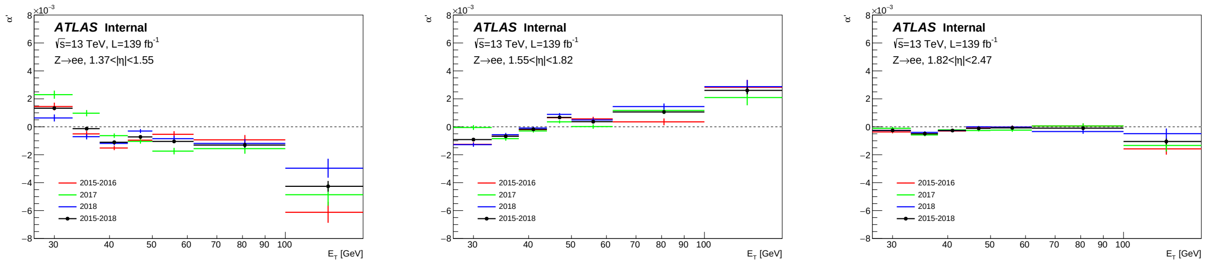

$1.37 < |\eta| < 1.55$ $1.55 < |\eta| < 1.82$ $1.82 < |\eta| < 2.47$

Figure 5.32: Measurement of linearity of LAr calorimeter with $Z \to ee$ events using 2015+2016, 2017, 2018 and full Run 2 data. The error bars correspond to the statistical errors estimated using the bootstrap method. The linearity is very similar between different years.

version of α is not optimal with the 24 bins c. Another possibility is that the higher order terms on mass are ignored when extracting α (Eq. 5.7), while as shown in Fig. 5.11a, the measured scale factor reaches 3% near $|\eta| = 1.5$ which can lead to bias of the method. Fortunately, in the crack region, the method bias uncertainty of the in-situ η-depednet scale factor [49] has the same magnitude as the observed residual of linearity.

5.6.6 Impact of Z boson p_T Reweighting on Linearity and Cross-Check with E/p Method

The linearity measured by fitting the m_{ee} distribution with the mass peak is cross-checked by looking at the E/p variable which is the ratio between the electron energy measured in the LAr calorimeter and the momentum measured by the inner tracker. The study was done by Aleksei Lukianchuk [116]. Unlike the m_{ee} method which has to deal with the kinematic correlations between the leading and sub-leading electrons and take care of the m_{ee} distribution when looking at energy-dependent measurement, the E/p method only needs to study the single electron, and no matter which cut is applied on E_T, the E/p is always nicely peaked at 1.

The E/p distribution is fitted to a Crystal ball function, which is a piece-wise function with a Gaussian defined for small and medium values, and a power law in a range of big values.

$$f_{CB}(t;\mu,\sigma,\alpha,n) = N \cdot \begin{cases} \exp\left(-\frac{t^2}{2\sigma}\right), & t \leq \alpha \\ A \cdot \left[\frac{\alpha}{n}(b-t)\right]^{-n}, & t > \alpha \end{cases} \tag{5.30}$$

where

- $t = \frac{E/p - \mu}{\sigma}$, with μ and σ the center and the width of the Gaussian.
- $A = \exp\left(-\frac{\alpha^2}{2}\right)$, with α the intersection of the point-wise function.
- $b = \frac{n}{|\alpha|} - |\alpha|$, with n the order of power law on the right tail.
- N is a normalization factor of the distribution.

The relative difference of mean values of the Gaussian between data and MC is used to estimate the linearity:

$$\alpha'_{E/p}(|\eta|, E_T) = \frac{\mu^{data}}{\mu^{MC}} - 1 \tag{5.31}$$

Another important advantage is that the E/p is much less sensitive to the Z boson p_T mis-modelling because the E/p looks at electrons satisfying the same η and E_T cut, which often drives to similar Z boson transverse momentum, hence its mis-modelling appears nearly as an inclusive normalization, which can be automatically factorized when normalizing the E/p distribution to unity.
The drawback of E/p is the worse resolution of track momentum at large p_T and high η, which broadens the distribution and degrades the fit quality and stability. Therefore in these regions, the measured statistical uncertainty is often large.

Investigating different methods and meanwhile the impact of Z boson p_T reweighting, the corresponding linearity results are shown in Fig. 5.33. The results are obtained with 2018 data, based on previous calibration recommendation where the ADC and L2Gain uniformity corrections are not applied.

The E/p method shows consistent results as compared to the ones exploring m_{ee}. The nearly constant differences between the two methods are originating from the residual momentum scale difference. Results after correcting the Z boson transverse momentum is also produced using E/p variable, which is almost identical to the one without correction, hence only one version of E/p results is presented.

One can notice that without correcting the mis-modelling of Z boson p_T, linearity with m_{ee} method has strikingly different values at the third E_T bin (38 GeV$<$ E_T $<$44 GeV), than the neighbor ones. Such effect is more evident at large η region, which makes less monotonic linearity curves. After correcting the Z boson momentum, more similar tendencies are observed between m_{ee} and E/p methods (similar slope, and the difference tends to be flat in E_T), except in the last E_T bin where the track momentum resolution is worse. It provides a cross-check of the current linearity result and the validation of the Z boson momentum reweighting since E/p is less sensitive to the modelling of Z bons p_T. And another advantage of correcting the Z boson p_T is that it brings more monotonic linearity values, which is useful to improve the goodness-of-fit in the study of global fit (Sec. 6.1.2).

5.6.7 Impact of Uniformity Corrections on Linearity

The uniformity corrections introduced in Sec. 5.4 are promoted to improve the linearity of the LAr calorimeter. The influences of the ADC and L2Gain corrections are exploited: for each configuration with different corrections, the inclusive energy scale and resolution differences are calibrated respectively with standard-alone in-situ calibration. Their impacts on linearity are shown in Fig. 5.34. Without any correction, the linearity is worse in particular for $|\eta| < 0.6$ and $1.55 < |\eta| < 1.82$, while it improves for $0.6 < |\eta| < 1.37$.

The azimuthal uniformity correction has little influence on the linearity, hence it is not shown.

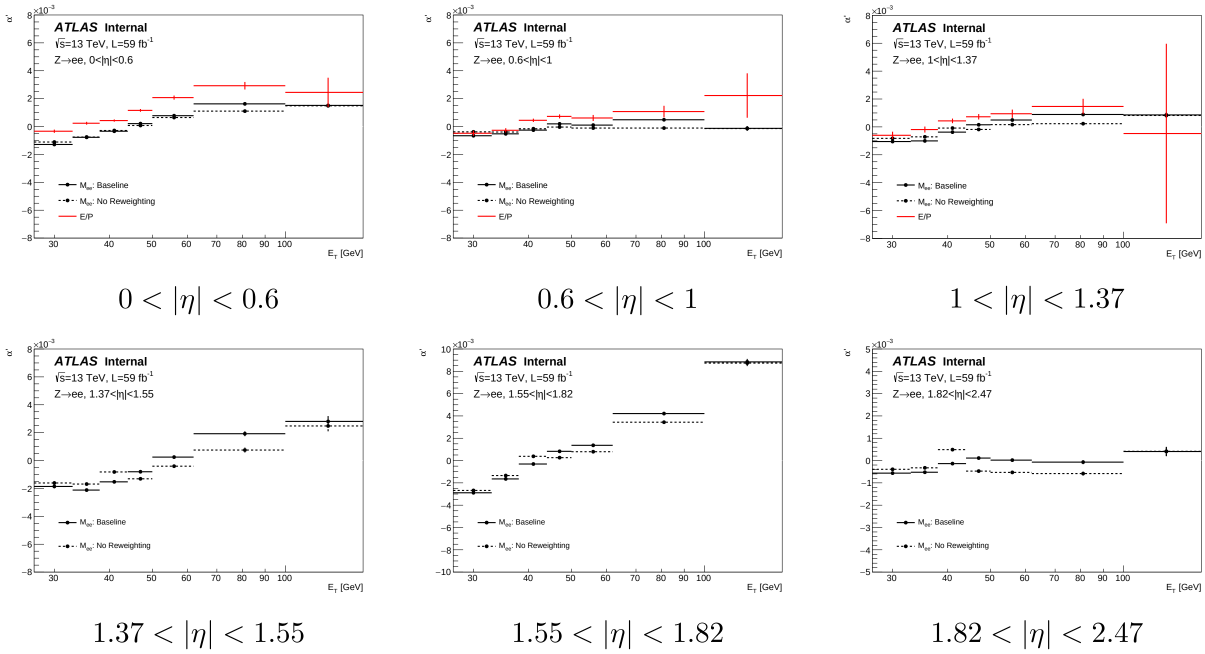

$0 < |\eta| < 0.6$ $0.6 < |\eta| < 1$ $1 < |\eta| < 1.37$

$1.37 < |\eta| < 1.55$ $1.55 < |\eta| < 1.82$ $1.82 < |\eta| < 2.47$

Figure 5.33: Measurement of linearity of LAr calorimeter with $Z \rightarrow ee$ events with and without applying the Z boson p_T reweighting. E/p results are only shown in the barrel, due to its degradation on precision at high η. Baseline is the one with reweighted Z momentum.

5.6.8 Impact of Linearity Correction on the Mass Lineshape

One remaining issue of the typical LAr calibration is the imperfect Z mass lineshape (Fig. 5.14), the linearity calibrates the energy scale with an additional degree of freedom of electron transverse momentum, which may solve this problem. Hence the linearity is applied to data, the obtained mass lineshape is shown in Fig. 5.35. No obvious effect is observed after applying the linearity as correction, which is mainly because the ADC and L2Gain non-linearity absorb part of the effect in particular at very low η, so that the remaining effect becomes negligible on the dielectron mass.

5.6.9 Uncertainty of Linearity and Study Using the Bootstrap Method

The statistical and systematic uncertainties are estimated for the $Z \rightarrow ee$ linearity measurements. A bootstrap method [117] is used to estimate the statistical uncertainties and their correlations between different bins, as well as the statistical significance of the systematic uncertainty estimations. The bootstrap study is performed using the previous recommendation of LAr calibrations, hence the central values of linearity are different to the ones shown above, but the uncertainties are assumed to be not affected.

Statistical uncertainty

As described in Eq. 5.29, as the final linearity is summed over different iterations, their non-trivial correlations make it difficult to calculate the statistical uncertainty of linearity. A stringent estimation can be provided by the bootstrap method [117]. The bootstrap method is a powerful technique to estimate the statistical uncertainty and correlation between different observables. The basic idea is to use a set of replicas to obtain a sampling of measurements, of which each replica contains events fluctuated by a random Poisson process.

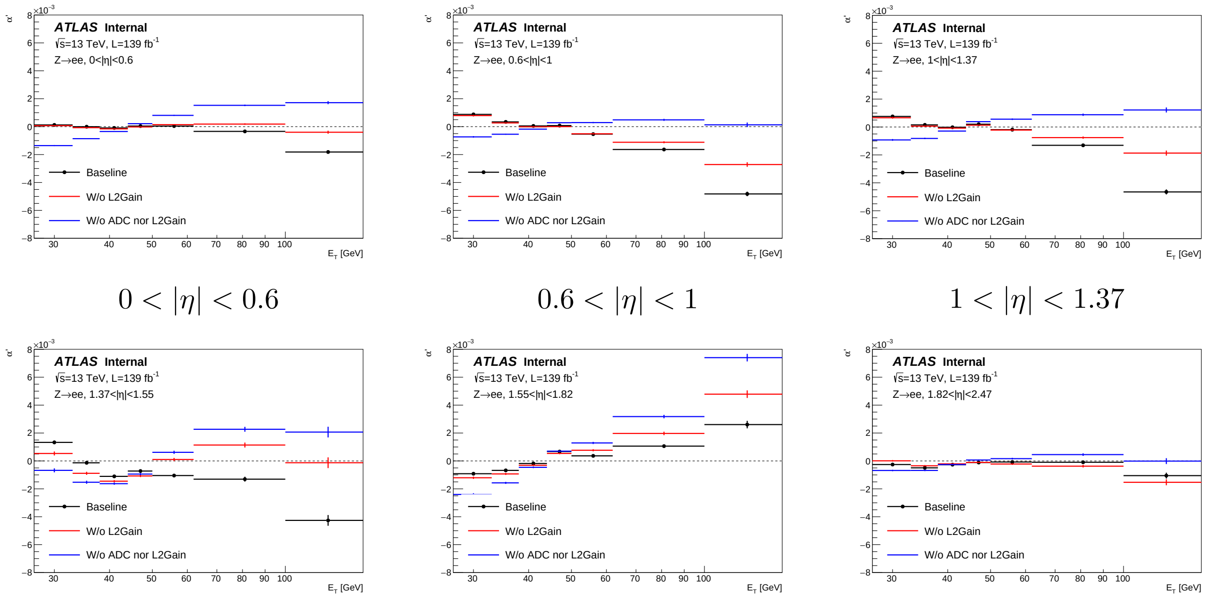

$0 < |\eta| < 0.6$ $0.6 < |\eta| < 1$ $1 < |\eta| < 1.37$

$1.37 < |\eta| < 1.55$ $1.55 < |\eta| < 1.82$ $1.82 < |\eta| < 2.47$

Figure 5.34: Influence of the ADC and L2Gain non-linearity corrections on the measurement of LAr calorimeter linearity with $Z \to ee$ events. The baseline corresponds to the case with all the uniformity corrections applied. The influence of removing L2Gain is shown by the red curve, and the removal of the summed contribution from both ADC and L2Gain is shown in blue.

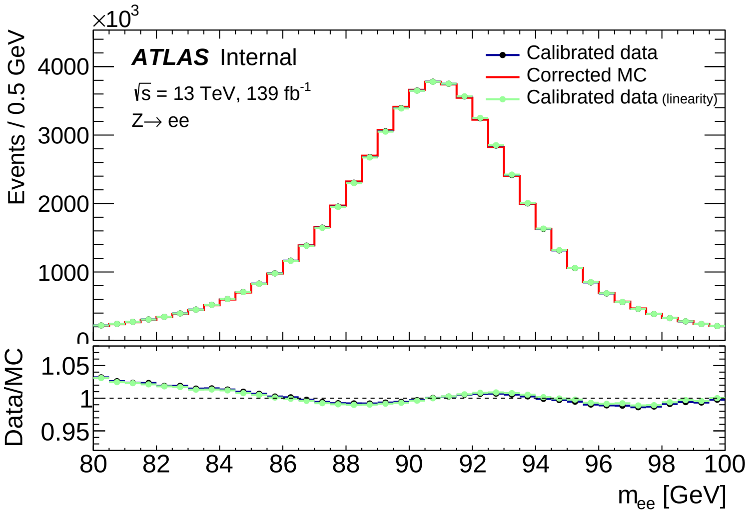

Figure 5.35: Mass lineshape after in-situ calibration (black) and additional correction of linearity (green). The change from linearity is negligible on mass.

This is done by assigning each event a weight independently generated by a Poisson law with an average of 1. Afterwards, the standard deviation for the sampling of measurements is considered as the statistical uncertainty estimated by the bootstrap method. In case of multi-dimensional observables, the correlations can be also calculated with the samplings of measurements.

Suppose a set of nominal events denoted as the raw data, gives measurements of some observables $\boldsymbol{\alpha}$, which are usually the estimators of some model parameters. A bootstrap replica is a copy of the raw data with an additional random Poisson weight respectively assigned to each event. The Poisson law has a mean of unity, which simulates the statistical fluctuation around the raw events. By repeating the independent generations, an ensemble of replicas is created and used to give the replicas measurements $\boldsymbol{\alpha}^m$, with m index of replica ranging up to the total number of replicas N. The obtained ensemble of replicas measurements allows to compute the statistical quantities, such as mean, variance, covariance, etc.

Let's denote the mean and covariance as $\bar{\alpha}_i$ and $\mathrm{cov}(\alpha_i, \alpha_j)$, which are computed with the ensemble of replicas measurements:

$$\bar{\alpha}_i = \frac{1}{N}\sum_{\beta}^{N} \alpha_i^{\beta} \tag{5.32}$$

$$\mathrm{cov}(\alpha_i, \alpha_j) = \frac{1}{N}\sum_{\beta}^{N} (\alpha_i^{\beta} - \bar{\alpha}_i)(\alpha_j^{\beta} - \bar{\alpha}_j) \tag{5.33}$$

Hence the correlation between α_i and α_j is defined as

$$\rho(\alpha_i, \alpha_j) = \frac{\mathrm{cov}(\alpha_i, \alpha_j)}{\sqrt{\mathrm{cov}(\alpha_i, \alpha_i) \cdot \mathrm{cov}(\alpha_j, \alpha_j)}} \tag{5.34}$$

For the study of linearity, 1000 bootstrap replicas have been generated to estimate its statistical uncertainties and correlations, as well as the statistical significance of systematic uncertainty. The complete full run2 data (2015-2018) is bootstrapped, while the MC events remain untouched, because of its large sample size, which gives a subdominant contribution to the overall statistical uncertainty. In the following, the bootstrap studies for estimations of the statistical errors and their correlations, as well as the significance of systematic estimations are going to be summarized.

For the 1000 generated replicas, the nominal linearity scales are measured respectively with each replica, for each $\eta \times E_T$ bin. The results are shown in Fig. 5.36, each colored curve represents the bootstrap measurements as a function of the replica seed for one bin of $\boldsymbol{\alpha}$. These bootstrap measurements correspond to raw measurements as shown by the 2015-2018 results in Fig. 5.32.

The average and the standard deviation are calculated respectively for each bin using the sets of measurements shown in Fig. 5.36 and compared with the raw measurements. Since the replicas are generated with statistical fluctuations around the raw dataset, the average of the bootstrap results converges asymptotically to the raw measurement in the large replicas number limit. A perfect agreement between the bootstrap average and the raw linearity is shown in Fig. 5.37a.

Fig. 5.37b presents the comparison of the statistical error as the standard deviation given by bootstrap and one of the last iteration of linearity measured with the raw dataset. A difference of factor near 1.75 is

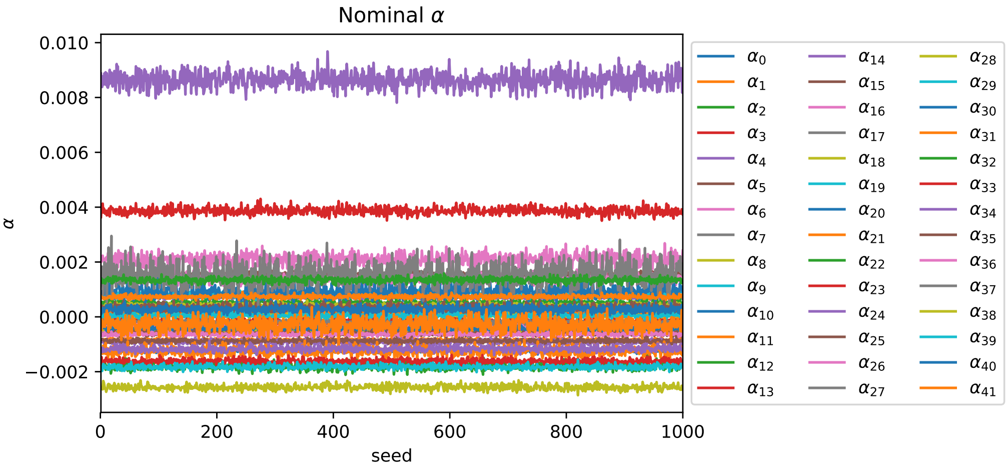

Figure 5.36: Bootstrap measurements for nominal linearity for a total number of 1000 replicas. The lower index of α in the legend on right corresponds to the unrolled $\eta \times E_T$ index, for which each period of 7 indices corresponds to the 7 E_T bins inside one η bin.

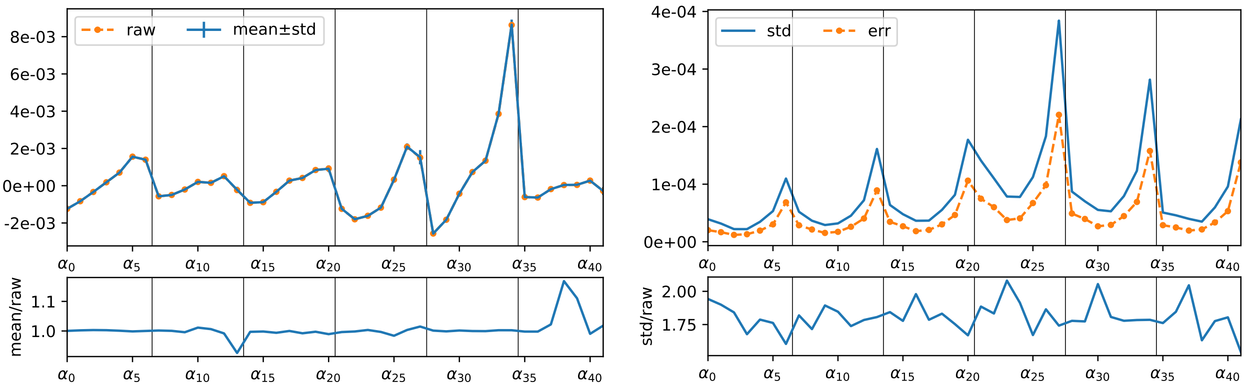

(a) *(b)*

Figure 5.37: Comparison between the raw measurements and the bootstrap measurements. (a) shows the averages of the bootstrap results (blue solid) with the error bars defined as the standard deviation of the bootstrap measurements, and the central value of linearity from the raw measurement (orange dashed). (b) stands for the comparison between the raw statistic error (orange dashed) and the standard deviation calculated from bootstrap (blue solid). The vertical bars separate the six $|\eta|$ bins, with a small value of $|\eta|$ starting from the left. Each $|\eta|$ bin contains 7 E_T bins.

observed. In principle, the bootstrap gives more reliable estimates of the statistical errors, hence, in the following, they are considered as the genuine statistical uncertainties of the linearity measurement.

Correlation of the statistical uncertainties:

In the usual case, the statistical uncertainties in different bins of the observations are uncorrelated, if no events are shared among them. Unfortunately, it is not our situation, since the pair of electron-positron from one event can enter two different bins, according to the linearity extraction. Such kind of confusion about the statistical correlations can be solved with Eq. 5.34 with bootstrap.

Starting from the ensembles of replicas measurements stored in Fig. 5.36, the statistical correlations between each pair of α are calculated. Fig. 5.38 shows relatively small correlations, with a maximum correlation or anti-correlation of around 20%. These estimates allow us to know the realistic correlations of the statistical errors. However, from the results, in particular at very large E_T where the statistical error is bigger, no significant correlation is observed, hence the estimated correlation is expected to have no evident impact for further study.

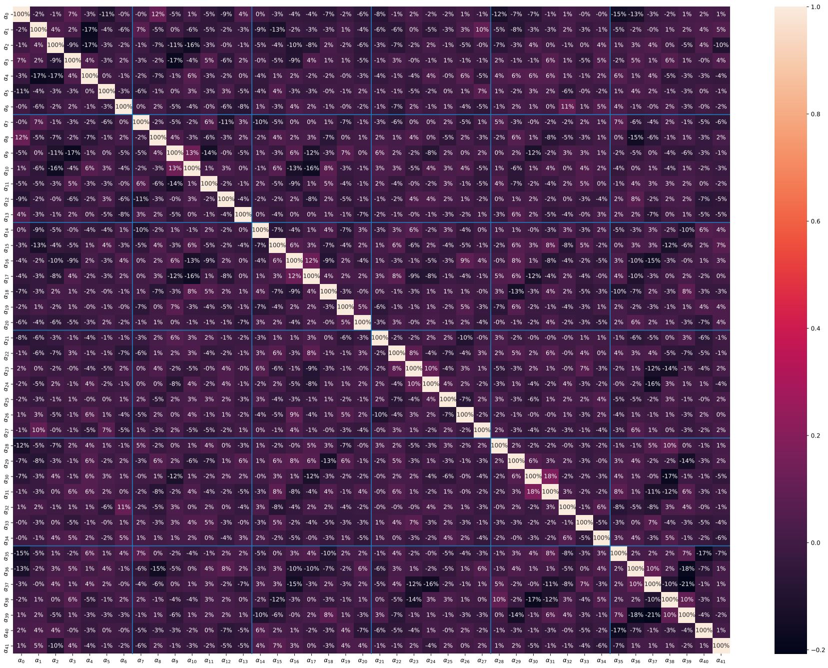

Figure 5.38: The statistical correlations between different bins of linearity estimated with 1000 bootstrap replicas. The maximum (minimum) correlation coefficient is 18% (-21%), in general, the absolute correlation is within 10%.

Systematic uncertainty and its statistical significance:

Similar systematics as the inclusive scale factor described in Fig. 5.13a are estimated for linearity. The systematic errors are calculated as a deviation to the nominal one after switching on the systematic variant, but without changing the inclusive calibration ($\alpha(\eta)$ and $c(\eta)$):

$$\sigma_i^k = \alpha_i^k - \alpha_i^{\text{nom}} \tag{5.35}$$

where σ_i^k is the systematic error of source k measured at bin i, α_i^{nom} and α_i^k are respectively the nominal linearity and the linearity after switching on the systematic effect, which is measured with the initial dataset but passing different selection.

The ideal case is that according to the same nature of systematic, the systematics errors are fully correlated between the various bins. However in practice when the statistical fluctuation is high in one bin, its correlation to the other bins can be contaminated and become less than 1. Therefore, it is useful to evaluate the level of statistical fluctuation by looking at the significance, which is defined as the ratio of the systematic error estimation and its statistical uncertainty.

The challenge is that the available measurements are α^k and α^{nom} with their associated statistical uncertainties, but given the same events are used to perform the measurements, due to non-trivial correlations, it is not easy to directly propagate the statistical uncertainties to the difference of the two measurements. In this case, the bootstrap method can still be helpful.

Considering $\sigma_i^{k,\beta} = \alpha_i^{k,\beta} - \alpha_i^{\mathrm{nom},\beta}$ is the systematic error calculated accordingly with the nominal and the systematic variant linearity with synchronized bootstrap replicas β, there using the ensemble of measurements with N bootstrap replicas (N=1000), the statistical uncertainty of $\sigma_i^{k,\beta}$ is formulated as

$$\sigma(\sigma_i^k) = \sqrt{\frac{1}{N}\sum_{\beta}^{N}\left(\sigma_i^{k,\beta} - \hat{\sigma}_i^{k,\beta}\right)^2} \tag{5.36}$$

$$\text{with } \hat{\sigma}_i^{k,\beta} = \frac{1}{N}\sum_{\beta}^{N}\sigma_i^{k,\beta}$$

After acquiring the statistical uncertainty, one can calculate the statistical significance Z of the estimated systematic error as

$$Z_i^k = \frac{\hat{\sigma}_i^{k,\beta}}{\sigma(\sigma_i^k)} \tag{5.37}$$

The detailed values are visualised in Fig. 5.39, where for all the four systematic sources, the statistical significance is drawn for each bin of the measurements.

The $\pm 1\sigma$ are thresholds to justify the significance, such that if the absolute value of Z is less than 1, the current bin is considered statistically contaminated, therefore the statistical uncertainty $\sigma(\sigma_i^{k,\beta})$ is taken as the final systematic error for linearity, rather than $\sigma_i^{k,\beta}$. For such noisy bins, since the systematic error is replaced by its statistical fluctuation, its correlation to the other bins is set to null. While for those with Z bigger than 1, a full correlation is assigned. In general, most of the bins have systematics which is statistically significant, while for the f_{Brem} systematic more than ten bins are noisy, which is because the efficiency of the fixed-threshold f_{Brem} cut decreases rapidly where there is a lot of material, and the statistical fluctuations are more obvious.

Summary of uncertainty for linearity

The final uncertainties of linearity are shown in Fig. 5.40 and summarized in Tab. 5.7. The closure systematic corresponds to Fig. 5.30a. The bootstrap method is used to evaluate the statistical uncertainty and

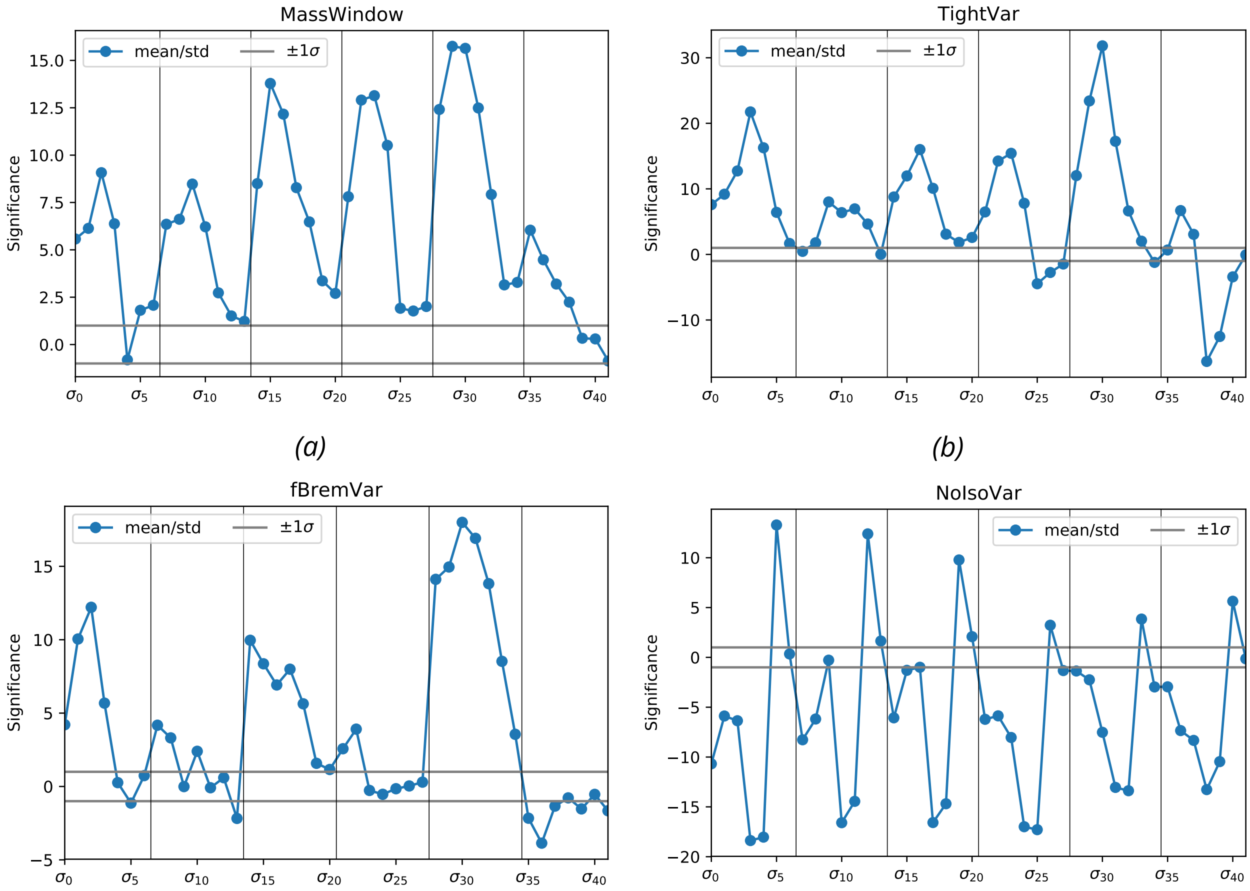

(a) (b)

(c) (d)

Figure 5.39: The statistical significance of the estimated systematic errors for the four types of systematic sources, which are obtained using the bootstrap method. In each plot, the horizontal gray bars corresponds to the $\pm 1\sigma$ thresholds.

check the statistical significance of the other systematics as described in Sec. 5.6.9.

In general, the systematics have a notable effect near 40 GeV, since the nominal in-situ calibration is always applied, therefore the systematic of the inclusive scale factor $\alpha(\eta)$ (Fig. 5.13a) is indeed propagated to the one of linearity measurement. The dominant uncertainties are systematics from MassWindow, TightVar, and fBremVar, specifically the MassWindow contributes mostly at $1.37 < |\eta| < 1.55$, and fBremVar has striking effect at $1.55 < |\eta| < 1.82$ and high E_T regions of $0.6 < |\eta| < 1$ and $1.82 < |\eta| < 2.47$. The closure and statistical uncertainties arise significantly at very large E_T which are comparable with other uncertainties, while for $E_T < 100$ GeV, their contributions are indeed minor. The NoIsoVar systematic remains tiny and hence is less important than the others.

5.7 Conclusion

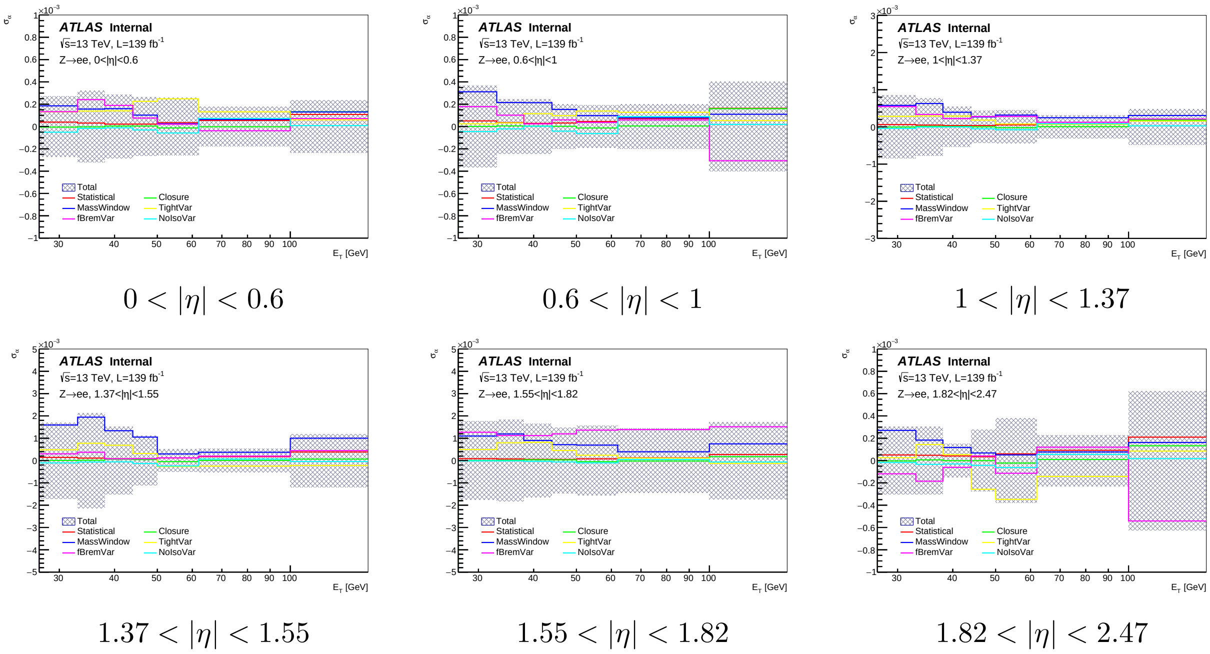

$0 < |\eta| < 0.6$ $0.6 < |\eta| < 1$ $1 < |\eta| < 1.37$

$1.37 < |\eta| < 1.55$ $1.55 < |\eta| < 1.82$ $1.82 < |\eta| < 2.47$

Figure 5.40: Uncertainties of $Z \to ee$ linearity using full Run 2 data.

In this chapter, the baseline calibration of the LAr calorimeter energy is introduced, including the MVA regression, layer inter-calibrations, uniformity corrections and a focusing description of the in-situ calibration. In addition, the energy-dependent scale factor is studied, which represents the residual non-linearity response of the calorimeter. The linearity is indeed not part of the official recommendation, but it can be used to constrain the calibration energy scale uncertainty through a global fit model, of which the output can be easily integrated in the physics analysis. The details of the global fit model will be presented in the next chapter.

$\lvert\eta\rvert$	E_T [GeV]	Statistical	Closure	MassWindow	TightVar	fBremVar	NoIsoVar	Total
$[0, 0.6]$	$[27, 33]$	3.9×10^{-5}	-5.2×10^{-6}	1.9×10^{-4}	1.3×10^{-4}	1.3×10^{-4}	-5.1×10^{-5}	2.7×10^{-4}
	$[33, 38]$	3.1×10^{-5}	-2.7×10^{-6}	1.6×10^{-4}	1.4×10^{-4}	2.4×10^{-4}	-1.7×10^{-5}	3.2×10^{-4}
	$[38, 44]$	2.2×10^{-5}	4.0×10^{-6}	1.6×10^{-4}	1.4×10^{-4}	1.9×10^{-4}	-1.2×10^{-5}	2.9×10^{-4}
	$[44, 50]$	2.2×10^{-5}	4.0×10^{-6}	1.0×10^{-4}	2.3×10^{-4}	7.6×10^{-5}	-3.0×10^{-5}	2.6×10^{-4}
	$[50, 62]$	3.4×10^{-5}	-1.2×10^{-5}	2.5×10^{-5}	2.5×10^{-4}	2.1×10^{-5}	-5.8×10^{-5}	2.6×10^{-4}
	$[62, 100]$	5.4×10^{-5}	-1.9×10^{-6}	6.4×10^{-5}	1.3×10^{-4}	-3.8×10^{-5}	7.2×10^{-5}	1.8×10^{-4}
	$[100, \infty]$	1.1×10^{-4}	1.3×10^{-4}	1.3×10^{-4}	6.0×10^{-5}	7.1×10^{-5}	8.6×10^{-6}	2.3×10^{-4}
$[0.6, 1]$	$[27, 33]$	5.1×10^{-5}	5.2×10^{-7}	3.1×10^{-4}	2.5×10^{-5}	1.8×10^{-4}	-4.5×10^{-5}	3.7×10^{-4}
	$[33, 38]$	3.5×10^{-5}	5.4×10^{-6}	2.1×10^{-4}	3.2×10^{-5}	1.0×10^{-4}	-2.1×10^{-5}	2.4×10^{-4}
	$[38, 44]$	2.9×10^{-5}	4.1×10^{-6}	2.1×10^{-4}	1.2×10^{-4}	2.4×10^{-5}	2.3×10^{-6}	2.5×10^{-4}
	$[44, 50]$	3.2×10^{-5}	1.8×10^{-6}	1.5×10^{-4}	9.7×10^{-5}	6.0×10^{-5}	-4.1×10^{-5}	2.0×10^{-4}
	$[50, 62]$	4.5×10^{-5}	-1.3×10^{-5}	9.8×10^{-5}	1.4×10^{-4}	3.7×10^{-5}	-6.3×10^{-5}	1.9×10^{-4}
	$[62, 100]$	7.1×10^{-5}	4.9×10^{-6}	7.9×10^{-5}	1.3×10^{-4}	5.9×10^{-5}	9.0×10^{-5}	2.0×10^{-4}
	$[100, \infty]$	1.6×10^{-4}	1.6×10^{-4}	1.1×10^{-4}	5.3×10^{-5}	-3.1×10^{-4}	1.9×10^{-5}	4.0×10^{-4}
$[1, 1.37]$	$[27, 33]$	6.2×10^{-5}	-3.7×10^{-6}	5.8×10^{-4}	2.8×10^{-4}	5.5×10^{-4}	-4.3×10^{-5}	8.5×10^{-4}
	$[33, 38]$	4.9×10^{-5}	1.3×10^{-5}	6.3×10^{-4}	2.9×10^{-4}	3.4×10^{-4}	-5.9×10^{-6}	7.7×10^{-4}
	$[38, 44]$	3.5×10^{-5}	1.0×10^{-5}	3.9×10^{-4}	2.9×10^{-4}	2.2×10^{-4}	-2.9×10^{-6}	5.4×10^{-4}
	$[44, 50]$	3.7×10^{-5}	1.5×10^{-6}	2.7×10^{-4}	1.8×10^{-4}	2.8×10^{-4}	-5.1×10^{-5}	4.3×10^{-4}
	$[50, 62]$	5.4×10^{-5}	-2.1×10^{-5}	3.2×10^{-4}	7.8×10^{-5}	2.8×10^{-4}	-7.6×10^{-5}	4.4×10^{-4}
	$[62, 100]$	8.2×10^{-5}	5.4×10^{-6}	2.5×10^{-4}	6.5×10^{-5}	1.2×10^{-4}	8.6×10^{-5}	3.1×10^{-4}
	$[100, \infty]$	1.8×10^{-4}	1.9×10^{-4}	3.1×10^{-4}	1.6×10^{-4}	2.1×10^{-4}	2.9×10^{-5}	4.8×10^{-4}
$[1.37, 1.55]$	$[27, 33]$	1.4×10^{-4}	3.8×10^{-6}	1.6×10^{-3}	4.8×10^{-4}	3.0×10^{-4}	-1.0×10^{-4}	1.7×10^{-3}
	$[33, 38]$	1.1×10^{-4}	1.2×10^{-5}	1.9×10^{-3}	7.7×10^{-4}	3.7×10^{-4}	-6.7×10^{-5}	2.1×10^{-3}
	$[38, 44]$	7.8×10^{-5}	5.8×10^{-5}	1.3×10^{-3}	6.9×10^{-4}	7.8×10^{-5}	-5.9×10^{-5}	1.5×10^{-3}
	$[44, 50]$	7.8×10^{-5}	4.3×10^{-5}	1.1×10^{-3}	3.2×10^{-4}	8.3×10^{-5}	-1.3×10^{-4}	1.1×10^{-3}
	$[50, 62]$	1.1×10^{-4}	-4.7×10^{-5}	3.0×10^{-4}	-2.7×10^{-4}	1.2×10^{-4}	-2.4×10^{-4}	5.0×10^{-4}
	$[62, 100]$	1.8×10^{-4}	4.6×10^{-6}	3.7×10^{-4}	-2.5×10^{-4}	2.0×10^{-4}	6.5×10^{-5}	5.2×10^{-4}
	$[100, \infty]$	3.8×10^{-4}	6.6×10^{-5}	1.0×10^{-3}	-2.2×10^{-4}	4.5×10^{-4}	-4.3×10^{-5}	1.2×10^{-3}
$[1.55, 1.82]$	$[27, 33]$	8.3×10^{-5}	1.1×10^{-6}	1.1×10^{-3}	4.9×10^{-4}	1.3×10^{-3}	-1.4×10^{-5}	1.8×10^{-3}
	$[33, 38]$	7.2×10^{-5}	9.4×10^{-6}	1.2×10^{-3}	8.0×10^{-4}	1.1×10^{-3}	-1.6×10^{-5}	1.8×10^{-3}
	$[38, 44]$	5.5×10^{-5}	3.5×10^{-5}	9.0×10^{-4}	8.1×10^{-4}	1.1×10^{-3}	-3.6×10^{-5}	1.7×10^{-3}
	$[44, 50]$	5.3×10^{-5}	3.1×10^{-5}	7.1×10^{-4}	4.5×10^{-4}	1.2×10^{-3}	-6.2×10^{-5}	1.5×10^{-3}
	$[50, 62]$	7.7×10^{-5}	-5.0×10^{-5}	6.9×10^{-4}	2.4×10^{-4}	1.4×10^{-3}	-1.0×10^{-4}	1.6×10^{-3}
	$[62, 100]$	1.2×10^{-4}	-2.1×10^{-5}	3.9×10^{-4}	1.1×10^{-4}	1.4×10^{-3}	5.0×10^{-5}	1.5×10^{-3}
	$[100, \infty]$	2.7×10^{-4}	1.7×10^{-4}	7.5×10^{-4}	-1.3×10^{-4}	1.5×10^{-3}	-6.4×10^{-5}	1.7×10^{-3}
$[1.82, 2.47]$	$[27, 33]$	5.0×10^{-5}	-3.2×10^{-6}	2.7×10^{-4}	2.6×10^{-5}	-1.2×10^{-4}	-1.8×10^{-5}	3.0×10^{-4}
	$[33, 38]$	4.7×10^{-5}	6.1×10^{-6}	1.8×10^{-4}	1.4×10^{-4}	-1.8×10^{-4}	-3.4×10^{-5}	3.0×10^{-4}
	$[38, 44]$	4.1×10^{-5}	-1.1×10^{-6}	1.2×10^{-4}	5.3×10^{-5}	-6.1×10^{-5}	-3.0×10^{-5}	1.5×10^{-4}
	$[44, 50]$	3.4×10^{-5}	-7.3×10^{-7}	6.8×10^{-5}	-2.6×10^{-4}	4.1×10^{-5}	-4.3×10^{-5}	2.8×10^{-4}
	$[50, 62]$	6.0×10^{-5}	-2.2×10^{-5}	5.1×10^{-5}	-3.5×10^{-4}	-1.1×10^{-4}	-6.3×10^{-5}	3.8×10^{-4}
	$[62, 100]$	9.2×10^{-5}	9.7×10^{-6}	7.7×10^{-5}	-1.4×10^{-4}	1.2×10^{-4}	5.5×10^{-5}	2.3×10^{-4}
	$[100, \infty]$	2.1×10^{-4}	1.3×10^{-4}	1.6×10^{-4}	8.5×10^{-5}	-5.4×10^{-4}	1.7×10^{-5}	6.2×10^{-4}

Table 5.7: Summary of $Z \rightarrow ee$ linearity uncertainties using full Run 2 data. The signed systematic uncertainties are shown, for the same source, the negative uncertainty implies a -100% correlation to those positive values. The brown values correspond to the case of noisy estimation of systematic, which has a statistical significance of less than 1 and was replaced by its statistical error, in addition, its correlation is set to 0 with respect to other bins.

6 - Improvement on the $H \to \gamma\gamma$ mass measurement by constraining the photon energy scale uncertainty

The Higgs mass was measured in the final states of two photons using ATLAS part of Run 2 data at 36.1 fb^{-1} [16]:

$$m_H = 124.93 \pm 0.40\,(0.21\,(\mathrm{stat}) \pm 0.34\,(\mathrm{syst}))\ \mathrm{GeV} \tag{6.1}$$

The main sources of the experimental systematics come from the energy scale of the photon, in particular the relative calibration between medium and high gain, layer calibration, material mis-modelling and lateral shower leakage. The need for higher precision on the Higgs mass motivates more accurate calibrations of the electromagnetic calorimeter. In the following, in addition to improving the calibration, a new approach is introduced to constrain the scale uncertainties with the $Z \to ee$ linearity measurement.

6.1 Constraining electron photon energy scale uncertainty with $Z \to ee$ linearity measurement

Given the dominating contribution from electron and photon energy scale systematics to the Higgs mass measurement in $H \to \gamma\gamma$ decay, a new approach of constraining the energy scale uncertainties with the $Z \to ee$ linearity has been implemented in order to improve the precision of the mass measurement, following various ideas (for instance, in Ref. [118]).

6.1.1 Overview of the egamma energy scale uncertainties

The uncertainties from the various calibrations introduced in Ch. 5 can be propagated to the energy scale of electrons and photons as a function of η and the energy of the particle. In addition, due to the sensitivity of energy responses to the amount of the upstream material and EM shower shape, a possible wrong description of the detector in the MC can induce uncertainties on the energy scale. The impacts on the energy scale from different systematic sources are evaluated and then used in the physics analysis.

The uncertainties of the energy scale are evaluated in function of the transverse energy and pseudorapidity, respectively for electron: and photons:

$$\frac{\Delta E^{e,\gamma}}{E^{e,\gamma}}(E_T,\eta) = \frac{\delta E^{e,\gamma}}{E^{e,\gamma}}(E_T,\eta) - \frac{\delta E^{e,\gamma}}{E^{e,\gamma}}\left(\left\langle E_T^{e(Z\to ee)}\right\rangle,\eta\right) \tag{6.2}$$

where $\frac{\delta E^{e,\gamma}}{E^{e,\gamma}}(E_T,\eta)$ is the relative impact on electron or photon energy for a given uncertainty variation, $\left\langle E_T^{e(Z\to ee)}\right\rangle \approx$ 40 GeV stands for the averaged transverse energy for electron from Z decay. The $Z \to ee$ in-situ calibration described in Sec. 5.5 absorbs all the effect for electron with $E_T = \left\langle E_T^{e(Z\to ee)}\right\rangle$ and leaves the residual uncertainty $\frac{\Delta E^{e,\gamma}}{E^{e,\gamma}}(E_T,\eta)$.

The study is based on the previous calibration recommendation [49], of which the systematic model is described by 69 independent nuisance parameters. A brief description of the various uncertainties is summarised in Tab. 6.1. Some systematics are divided into different η regions, each of them is uncorrelated by assigning an independent nuisance parameter. More detailed description of energy scale uncertainties can be found in Ref. [103].

- $Z \to ee$ calibration: uncertainty of in-situ calibration depending on η but independent of E_T.
  - EG_SCALE_ZEESTAT: statistical uncertainty of the in-situ scale factor.
  - EG_SCALE_ZEESYST: systematic uncertainty of the in-situ scale factor, including variations of the mass window, electron identification, isolation, Bremsstrahlung radiation, background processes, method, etc...
- Electronic gain calibration:
  - EG_SCALE_L2GAIN: layer 2 MG/HG relative calibration between special and standard runs.
  - EG_SCALE_L1GAIN: layer 1 MG/HG relative calibration.
- Layer calibrations: inter-calibration of the PS, Layer 1 and Layer 2 of the calorimeter.
  - EG_SCALE_PS: uncertainty associated with the spread of α_{PS}[1] inside a PS module, which has a width of $|\Delta\eta| = 0.2$ in barrel and $|\Delta\eta| = 0.3$ in endcap.
  - EG_SCALE_PS_BARREL_B12: uncertainty associated with the $b_{1/2}$ in the PS calibration, which estimates the passive material between PS and layer 1 of ECAL.
  - EG_SCALE_S12:uncertainty associated to the spread of $\alpha_{1/2}$ determined using muons[2]. In total five η regions are divided: $|\eta| < 0.6$, $0.6 < |\eta| < 1.4$, $1.4 < |\eta| < 1.5$, $1.5 < |\eta| < 2.4$ and $2.4 < |\eta| < 2.5$.
- LAr-related uncertainties: modelling of the LAr calorimeter internal geometry and layer cross-talk effect.
  - EG_SCALE_LARCALIB: uncertainty accounting for the extrapolation of E1/E2 calibration from muons to electrons. Two η regions, i.e. barrel and endcap are split.
  - EG_SCALE_LARUNCONVCALIB: LAr longitudinal shower modelling measured with unconverted photon respectively in the barrel and endcap up to $|\eta| < 1.8$.
  - EG_SCALE_LARELECUNCONV: LAr longitudinal shower modelling difference between an electron and unconverted photon at $|\eta| < 1.8$.
  - EG_SCALE_LARELECCALIB: LAr longitudinal shower modelling measured with the electron at $|\eta| > 1.8$.
- Material uncertainties: passive material determined with both data and distorted geometry simulation.
  - EG_SCALE_MATID: uncertainty from the ID material, divided into 4 decorrelated η regions, i.e. $|\eta| < 1.1$, $1.1 < |\eta| < 1.5$, $1.5 < |\eta| < 2.1$ and $|\eta| > 2.1$.
  - EG_SCALE_MATPP0: uncertainty associated to IBL and pixel service in the Patch Panel 0 (PP0), decorrelated between barrel and endcap.
  - EG_SCALE_MATCRYO: uncertainty associated to passive material between ID and PS at $|\eta| < 1.8$ (9 uniform η bins), and between ID and the accordion for the rest of endcap (3 η bins).
  - EG_SCALE_MATCALO: uncertainty associated to passive material between PS and the accordion at $|\eta| < 1.8$ (9 uniform η bins).
- Dedicated uncertainty for photons:
  - PH_SCALE_LEAKAGECONV and PH_SCALE_LEAKAGEUNCONV: uncertainty from the lateral shower leakage respectively for converted and unconverted photons.
  - PH_SCALE_CONVEFFICIENCY, PH_SCALE_CONVFAKERATE and PH_SCALE_CONVRADIUS: uncertainty associated with the converted reconstruction efficiency, fake rate and the conversion radius.
- Other uncertainties:
  - EG_SCALE_PEDESTAL: residual mis-modelling after pileup-induced energy shift correction, which is observed at about 10 MeV per cluster in Zero Bias data.
  - EG_SCALE_WTOTS1: modelling of the layer 1 lateral shower width.
  - EG_SCALE_E4SCINTILLATOR: uncertainty from the E4 scintillators calibration in the transition region $1.4 < |\eta| < 1.6$ which is split into 3 η bins.
  - EG_SCALE_TOPOCLUSTER_THRES: uncertainty associated with the noise threshold of the supercluster.
  - EG_SCALE_G4: different shower shape description in various physics modelling options in Geant4.
  - EG_SCALE_AF: uncertainty if the full simulation of the ATLAS detector is not used.

---

[1] PS was calibrated with electrons, in the new recommendation it is done with low pileup muons data.

[2] E1/E2 was calibrated with muons, in the new recommendation it is done with both muons and electrons.

Source	Label	Description	Number of $\|\eta\|$ regions
$Z \to e^+e^-$ calibration	ZEESTAT	Statistic uncertainty	1
	ZEESYST	Systematic uncertainty	1
Lar cell non-linearity	L1Gain	MG/HG layer1	1
	L2Gain	MG/HG layer2	1
	PEDESTAL	Pileup noise shift	1
Layer1/Layer2 calibration	S12	$\alpha_{1/2}$ μ measurement	5
	LARCALIB	$\alpha_{1/2}$ $\mu \to e$ extrapolation	2
Presampler calibration	PS	Module spread	9
	PS_BARREL_B12	$b_{1/2}$ correction	1
B-E gap scintillator ($1.4 < \|\eta\| < 1.6$)	E4_SCINTILLATOR	Scintillator calibration	3
ID material	MATID	Material in ID	4
	MATPP0	Inner most pixel layer description	1
	MATPP0	Pixel services description	1
Material ID to PS ($\|\eta\| < 1.8$)	MATCRYO	Measurement with electrons	9
	LARELECUNCONV	Simulation of longitudinal shower shape electron ($\|\eta\| < 1.8$)	2
Material PS to Calo ($\|\eta\| < 1.8$)	MATCALO	Material from PS to Calo	12
	LARUNCONVCALIB	Simulation of longitudinal shower shape unconv-γ ($\|\eta\| < 1.8$)	2
Material ID to Calo ($\|\eta\| > 1.8$)	MATCRYO	Measurement with electron	3
	LARELECCALIB	Simulation of longitudinal shower shape electron ($\|\eta\| > 1.8$)	1
All material ID to calorimeter	G4	Variations of GEANT4 physics list	1
Lateral shower shape	WTOTS1	Lateral shower η width (w_{stot})	1
	LEAKAGECONV	Lateral leakage for converted photon	1
	LEAKAGEUNCONV	Lateral leakage for unconverted photon	1
Photon reconstruction	CONVEFFICIENCY	Conversion efficiency	1
	CONVFAKERATE	Conversion fake rate	1
	CONVRADIUS	Conversion radius	1
Detector simulation	AF2	Fast simulation of ATLAS	1
Topo-cluster threshold	TOPOCLUSTER_THRES	Topocluster noise threshold	1

Table 6.1: Descriptions of the e/γ scale uncertainties, classified in different sources. For each class or sub-class, the number of associated nuisance parameters is given. The uncertainty relevant to the fast simulation of the ATLAS detector is null since the full simulation samples are used in all the analyses.

The evolution of energy scale uncertainties as a function of η and E_T is shown in Fig. 6.1, respectively for electrons, converted and unconverted photons.

For electrons, at $|\eta| = 0.3$, there is a large impact coming from the MG/HG non-linearity and E1/E2 inter-calibration at high E_T, while at low E_T, the energy is more sensitive to PS, E1/E2 calibrations and material in front of the calorimeter. At $E_T = 40$ GeV, since any impact on the energy scale has been absorbed by the $Z \to ee$ in-situ calibration, the only remaining effect is the uncertainty of in-situ calibration. At $|\eta| = 1$, the sensitivity is dominated by the MG/HG non-linearity at high E_T and by material effect at low E_T. While for the endcap region ($|\eta| = 2$), E1/E calibration and MG/HG non-linearity are the most important ones.

For photons, there are additional impacts from lateral shower leakage and photon reconstruction. In particular, for converted photons, the leakage uncertainty has the largest effect in the center of the barrel, since the electrons from converted photons have a larger probability to escape from the reconstructed calorimeter cluster. Specifically, the impact is calculated as the difference between photons and 40 GeV electrons (Eq. 6.2), due to the larger discrepancy in EM shower between electron and unconverted photon, therefore a generally higher impact is observed on unconverted photons with respect to converted photons.

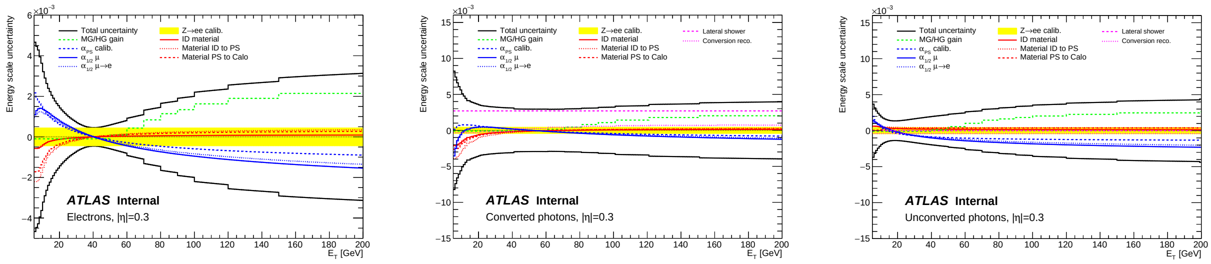

Electron, $|\eta| = 0.3$ Converted photon, $|\eta| = 0.3$ Unconverted photon, $|\eta| = 0.3$

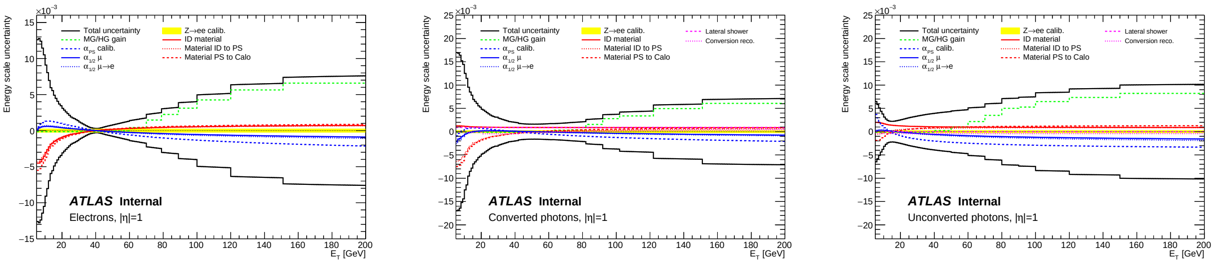

Electron, $|\eta| = 1$ Converted photon, $|\eta| = 1$ Unconverted photon, $|\eta| = 1$

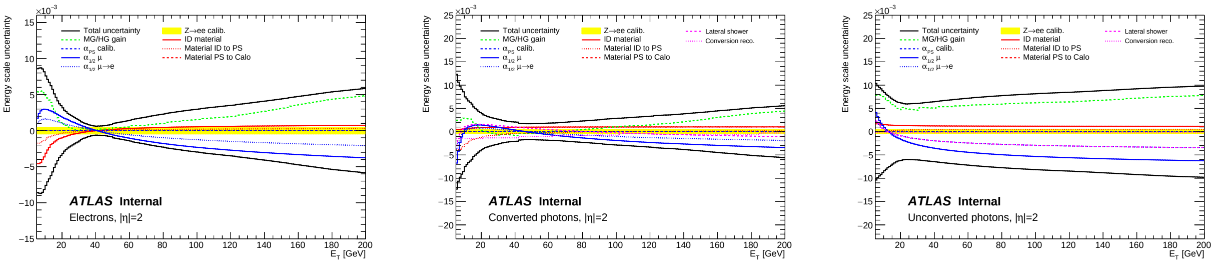

Electron, $|\eta| = 2$ Converted photon, $|\eta| = 2$ Unconverted photon, $|\eta| = 2$

Figure 6.1: Impact on electron and photon energy scale of dominant systematic uncertainties relevant to the LAr calibration and description of the detector.

The $Z \to ee$ linearity measurement based on the previous recommendation [49] is shown in Fig. 6.2. The largest effect is observed at around 1% for $|\eta| \in [1.55, 1.82]$, in the other η regions, the effects remain lower than 2×10^{-3}.

In the final Run 2 recommendation (Sec. 5.1), mainly due to the update of layer calibration and the application of new cell non-linearity corrections (ADC non-linearity, MG/HG, intercalibration), the corresponding linearity results are significantly different (2015-2018 curves in Fig. 5.32).

6.1.2 Global fit model for systematic constraint

For the purpose to constrain the $e\gamma$ energy scale uncertainties, the main idea is to consider the $Z \to ee$ linearity as an observation of all these uncertainties effects, which will indicate the pulls and constraints of different sources of uncertainty.

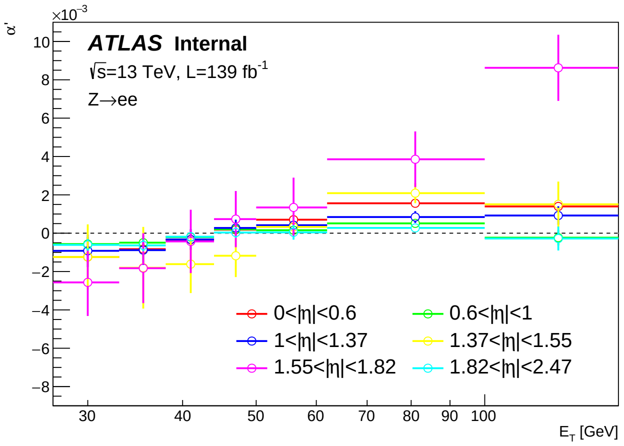

Figure 6.2: Measurement of $Z \to ee$ linearity with the previous calibration recommendation [49]. The error bars correspond to the total uncertainty shown in Fig. 5.40.

The linearity is parameterized as a linear combination of the energy scale uncertainties:

$$y\left(E_T, \eta \middle| \vec{\alpha}_g, \vec{\theta}\right) = \alpha_g(\eta) + \sum_k^{N_{sys}} \frac{\Delta E_k^e}{E_k^e}(E_T, \eta)\theta^k \tag{6.3}$$

where $y\left(E_T, \eta \middle| \vec{\alpha}_g, \vec{\theta}\right)$ describes the linearity of an electron for a given transverse energy E_T and pseudo-rapidity η, depending on parameters $\vec{\alpha}_g$ and $\vec{\theta}$. $\frac{\Delta E_k^e}{E_k^e}(E_T, \eta)$ is the electron scale uncertainty for a given systematic source k, as given in Eq. 6.2 and shown in Fig. 6.1. A nuisance parameter θ^k is defined for systematic variant k, with a prior Gaussian constraint with center of 0 and unity width, i.e. $G(\theta_0^k \middle| \theta^k, 1)$, where θ_0^k is the global observable with a value equal to 0 since all the calibrations are applied. Additional global scale parameters $\alpha_g(\eta)$ allow to absorb the residual inclusive scale in regions of η.

This parametrization is used to fit the $Z \to ee$ linearity. Each bin of linearity gives a measurement in the form $\alpha_i \pm \sigma_i$, with i the index of $\eta \times E_T$ bin. Subsequently, a multi-dimensional Gaussian likelihood fit is used to determine the best-fit values of $\vec{\alpha}_g$ and $\vec{\theta}$. In particular, any reduction on the post-fit uncertainty of $\vec{\theta}$ will reflect the constraint on the corresponding scale uncertainty.

Mathematical regularization

The $Z \to ee$ linearity is measured in 6×7 bins of $\eta \times E_T$, such that 6 global scale parameters in η are defined. Concatenation is done between $\vec{\alpha}_g$ and $\vec{\theta}$ to define the vector of parameters $\vec{x}$, in order to facilitate the mathematical description:

$$\vec{\alpha}_g = \left(\alpha_g^1, ..., \alpha_g^6\right) \tag{6.4}$$

$$\vec{\theta} = \left(\theta^1, ..., \theta^{N_{sys}}\right) \tag{6.5}$$

$$\vec{x} = (\vec{\alpha}_g, \vec{\theta}) = \left(\alpha_g^1, ..., \alpha_g^6, \theta^1, ..., \theta^{N_{sys}}\right) \tag{6.6}$$

For the same purpose, the $\eta \times E_T$ phase space is unrolled to a single dimension, such that a 42-dimensional vector of linearity is defined as the form

$$\vec{y} = \begin{pmatrix} y(E_{T,1}, |\eta_1|), & . & . & . & y(E_{T,7}, |\eta_1|), \\ y(E_{T,1}, |\eta_2|), & . & . & . & y(E_{T,7}, |\eta_2|), \\ . & & . & . & . \\ . & & . & . & . \\ . & & . & . & . \\ y(E_{T,1}, |\eta_6|), & . & . & . & y(E_{T,7}, |\eta_6|) \end{pmatrix} \tag{6.7}$$

where the lower index represents the η and E_T bins described in Tab. 5.5.

In addition, in order to give a prediction of linearity for each bin, the weighted averages of the energy scale uncertainties are calculated using $Z \to ee$ kinematics as

$$\left\langle y\left(E_T, \eta \middle| \vec{\alpha}_g, \vec{\theta}\right)\right\rangle_i = \alpha_g(\eta) + \sum_k^{N_{sys}} \left\langle \frac{\Delta E^e}{E^e}(E_T, \eta)\right\rangle_{ik} \theta_k \tag{6.8a}$$

$$\left\langle \frac{\Delta E^e}{E^e}(E_T, \eta)\right\rangle_{ik} = \frac{\int\int_{(\eta\times E_T)^i} d\eta\, dE_T\, \frac{\Delta E_k^e}{E_k^e}(E_T, \eta)\, \frac{d^2N}{d\eta dE_T}\Big|_{(\eta, E_T|Z\to ee)}}{\int\int_{(\eta\times E_T)_i} d\eta\, dE_T\, \frac{d^2N}{d\eta dE_T}\Big|_{(\eta, E_T|Z\to ee)}} \tag{6.8b}$$

with the average uncertainty $\left\langle\frac{\Delta E^e}{E^e}(E_T, \eta)\right\rangle_{ik}$ calculated at bin i of $\eta \times E_T$ for a given systematic source k, and $\frac{d^2N}{d\eta dE_T}\Big|_{(\eta, E_T|Z\to ee)}$ the differential distribution of electrons from Z boson decay. An approximation is taken to simplify the calculation, by assuming that the electron is nearly uniform in η inside a given η bin, as well as that the expectation of uncertainty is equal to its value at $E_T =< E_T >$, which is the average transverse energy in a given bin. These assumptions have been checked with the calculations using the real Zee kinematics, the obtained averaged uncertainties are very similar.

In order to reduce the number of degrees of freedom, a pruning on scale uncertainties is implemented, by selecting systematics with considerably un-negligible averaged impact (1×10^{-4}) in at least one of the 42 bins. Those systematics dedicated to photons that have no impact on electrons are discarded, such as lateral leakage, photon reconstruction, and photon conversion. Apart from these, since the systematics of the inclusive scale calibration has no degree of freedom on the transverse energy, there will be no sensitivity for linearity. In addition, due to the non-trivial correlation between the inclusive calibration and linearity, the inclusive scale calibration systematic is not involved in the parametrization. Consequently the number of systematic sources N_{sys} is decreased from 69 to 52.

The scale uncertainties averaged in bins of η and E_T are shown in Fig. 6.3, where the 8 largest sources are plotted in each η bin. These plots are the averaged versions of the electron systematic in Fig. 6.1. Hence similarly after averaging, in the barrel region, the uncertainty is clearly dominated by the L2Gain systematic, with sub-dominant contributions from the layer calibration. The crack region $1.37 < |\eta| < 1.55$ is largely affected by the PS uncertainty and the L2Gain. For the endcap electrons, the L1Gain, the layer calibration and the lateral shower shape modelling (w_{stot}) are the most important systematics. The dashed band represents the total systematic uncertainty, which is the sum of all the systematics in quadrature.

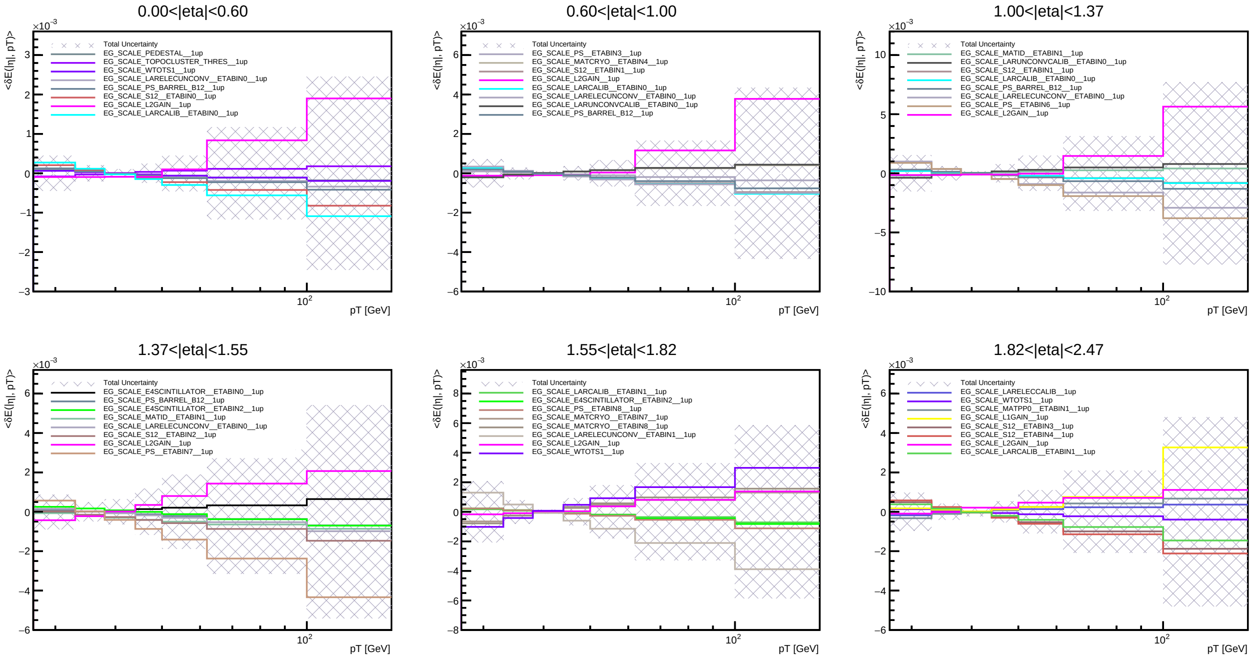

Figure 6.3: The averaged scale uncertainties $\left\langle \frac{\Delta E^e}{E^e}(E_T, \eta) \right\rangle$ in bins of η and E_T. In each η bin, the 8 dominant sources are plotted.

An impact matrix $I_{i\beta}$ is defined to as the impact of uncertainty on electron energy scale in $\eta \times E_T$ bin i for a given parameter x_β in $\vec{x}$.

$$I_{i\beta} = \begin{cases} \left\langle \frac{\Delta E^e}{E^e}(E_T, \eta) \right\rangle_{i\beta-6} & \text{if } \beta > 6 \\ 1 & \text{if } 7(\beta-1) < i \leq 7\beta \\ 0 & \text{otherwise} \end{cases} \tag{6.9}$$

where the first case stands for the average uncertainty associated with nuisance parameter $\vec{\theta}$, and the other cases imply that the impact of the global scale $\vec{\alpha_g}$ is equal to 1 at the η bin consistent with its definition, while the impact vanishes at the other η bins.
With the previous notations, the parametrization of linearity can be written as

$$y\left(\vec{\alpha_g}, \vec{\theta}\right) = I \cdot x \tag{6.10}$$

In analogy to Eq. 6.8a, the $Z \rightarrow ee$ linearity measurements can be also defined in the same format

$$\vec{y}^{Zee} = \begin{pmatrix} \alpha'(E_{T,1}, |\eta_1|), & . & . & . & \alpha'(E_{T,7}, |\eta_1|), \\ \alpha'(E_{T,1}, |\eta_2|), & . & . & . & \alpha'(E_{T,7}, |\eta_2|), \\ . & & . & . & . \\ . & & . & . & . \\ . & & . & . & . \\ \alpha'(E_{T,1}, |\eta_6|), & . & . & . & \alpha'(E_{T,7}, |\eta_6|) \end{pmatrix} \tag{6.11}$$

The covariance matrix of $\vec{y}^{Zee}$ can be constructed using the uncertainties of measurements shown in Fig. 5.40 and the correlations estimated with the bootstrap method as described in Sec. 5.6.9.

$$\Sigma(y_i^{Zee}, y_j^{Zee}) = \sum_m^M V_m(y_i^{Zee}, y_j^{Zee}) \tag{6.12}$$

where Σ represents the joint 42×42 covariance matrix defined by the sum of covariance matrices of all the uncertainty sources of the $Z \rightarrow ee$ linearity measurements, V_m is the covariance matrix corresponding to a given uncertainty source m of the measurements, including the statistical and systematic uncertainties shown in Fig. 5.40 and in Tab. 5.7. The construction of the individual and joint covariance matrices will be described in the section of the correlation model.

A multi-dimensional Gaussian distribution is postulated to describe the model.

$$\begin{aligned} \mathcal{G}(\vec{y}^{Zee}|\vec{y}, \Sigma) &= \frac{1}{\sqrt{(2\pi)^N \det(\Sigma)}} \exp\left(-\frac{1}{2}\left(y^{Zee} - y\left(\vec{\alpha}_g, \vec{\theta}\right)\right)^T \Sigma^{-1} \left(y^{Zee} - y\left(\vec{\alpha}_g, \vec{\theta}\right)\right)\right) \\ &= \frac{1}{\sqrt{(2\pi)^N \det(\Sigma)}} \exp\left(-\frac{1}{2}\left(y^{Zee} - I \cdot x\right)^T \Sigma^{-1} \left(y^{Zee} - I \cdot x\right)\right) \end{aligned} \tag{6.13}$$

with $\vec{y}$ the predicted linearity, $\vec{y}^{Zee}$ the observed linearity, and C the covariance supplied by observed linearity, $N = 42$ which is the dimension of linearity defined by the number of $\eta \times E_T$ bins.
For simplicity of the solution, a constraint matrix C is defined to describe the pre-fit constraints of the parameters $\vec{x}$:

$$C_{\beta\gamma} = \begin{cases} 1 & \text{if } \beta = \gamma > 6 \\ 0 & \text{otherwise} \end{cases} \tag{6.14}$$

The first situation corresponds to the $\mathcal{G}(\theta_0^k|\theta_k, 1)$ constraint of the systematic nuisance parameters $\vec{\theta}$. The second case is relevant to the global scale parameters $\vec{\alpha_g}$, which are artificially invented different to the nuisance parameters $\vec{\theta}$, and subsequently have no pre-fit constraint. The zero definition is barely a trick for easier mathematical implementation so that the product of all the pre-fit constraints can be represented in a brief formula:

$$\prod_k^{N_{sys}} \mathcal{G}(\theta_0^k|\theta_k, 1) = \frac{1}{\sqrt{(2\pi)^{N_{sys}}}} \exp\left(x^T C x\right) \tag{6.15}$$

where all the θ_0 are equal to 0.

Likelihood fit with a multi-dimensional Gaussian

The global fit model consists of a linear model $\vec{y}$ as a function of parameters $\vec{x}$, and its observations $\vec{y}^{Zee}$ with a covariance C, provided by the $Z \to ee$ linearity, in addition to the pre-fit constraints of the parameters $\vec{x}$. The full likelihood model is written as

$$\mathcal{L}(\vec{x}|\vec{y}^{Zee}) = \frac{1}{\sqrt{(2\pi)^N \det(\Sigma)}} \exp\left(-\frac{1}{2}\left(y^{Zee} - I \cdot x\right)^T \Sigma^{-1} \left(y^{Zee} - I \cdot x\right)\right) \times \frac{1}{\sqrt{(2\pi)^{N_{sys}}}} \exp\left(-\frac{1}{2} x^T C x\right) \tag{6.16}$$

$$-\log \mathcal{L}(\vec{x}|\vec{y}^{Zee}) = \frac{1}{2}\left(y^{Zee} - I \cdot x\right)^T \Sigma^{-1} \left(y^{Zee} - I \cdot x\right) + \frac{1}{2} x^T C x + \text{constant} \tag{6.17}$$

where

- Σ is a 42×42 matrix representing the covariance of $Z \to ee$ linearity observed in different bins.
- $N = 42$ corresponds to the 42 $\eta \times E_T$ bins of $Z \to ee$ linearity.
- $N_{sys} = 52$ corresponds to the number of systematic sources used to parametrize the linearity.
- y^{Zee} is a 42-dimensional vector of the observed $Z \to ee$ linearity.
- I is a 42×58 matrix describing the relative energy impact of parameters $\vec{x}$ in bins of linearity.
- x is a 58-dimensional vector corresponding the the systematic nuisance parameters $\vec{\theta}$ and the 6 global scale parameters $\vec{\alpha_g}$.
- C is a 58×58 matrix describing the pre-fit constraints on $\vec{x}$.

Since a Gaussian probability is assumed, the likelihood essentially coincides with the least square method.

$$\chi^2(\vec{x}) = \left(y^{Zee} - I \cdot x\right)^T \Sigma^{-1} \left(y^{Zee} - I \cdot x\right) + x^T C x \tag{6.18}$$

$$= -2 \log \mathcal{L}(\vec{x}|\vec{y}^{Zee}) + \text{constant} \tag{6.19}$$

The statistical inference is resolved analytically, by vanishing the first derivative of the χ^2 with respect to $\vec{x}$.

$$\frac{1}{2}\frac{\partial \chi^2}{\partial \vec{x}} = \left(I^T \Sigma^{-1} I + C\right) x - I^T \Sigma^{-1} y^{Zee} \tag{6.20}$$

By imposing $\frac{\partial \chi^2}{\partial x_\beta} = 0,\ \forall \beta$, the least square estimators are derived as

$$\hat{x} = \left(I^T \Sigma^{-1} I + C\right)^{-1} I^T \Sigma^{-1} y^{Zee} \tag{6.21}$$

The model $\vec{y}$ is linear in $\vec{x}$, and the Σ is independent of $\vec{x}$, therefore, the least square estimator becomes optimal, which means unbiased and asymptotically reaching the minimum variance band. Subsequently, the covariance of the estimators can be conveniently extracted by the Fisher information.

$$V^{-1}(\hat{x}_\beta, \hat{x}_\gamma) = -E\left[\frac{\partial^2 \log \mathcal{L}(\vec{x})}{\partial x_\beta \partial x_\gamma}\right] = \left(I^T \Sigma^{-1} I + C\right)_{\beta\gamma} \tag{6.22}$$

6.1.3 Correlation model of the $Z \to ee$ linearity uncertainty

The ingredients of the fit model are mostly defined, regarding the χ^2 in Eq. 6.18, the y^{Zee} corresponds to the central values of $Z \to ee$ linearity in the 42 bins, I is the impact matrix defined by the ensemble of energy scale factor systematic (and the global scale factor $\vec{\alpha}_g$), C is the prefit constraint matrix for the systematic nuisance parameters $\vec{\theta}$.

However, for the matrix Σ which describes the covariance between the 42 bins of the $Z \to ee$ linearity measurement, there can be different assumptions of the correlations, depending on the source of uncertainty contributing to the total joint covariance matrix.

As defined in Eq. 6.12, the joint covariance matrix is the sum of individual one, each of them corresponding to one source of uncertainty for the $Z \to ee$ linearity measurement. For the various sources of linearity uncertainties summarized in Tab. 5.7: for the statistical uncertainty, no correlation is assigned between any η and E_T bins; for closure systematic, a 100% correlation is assumed between E_T bins; for other systematics, given sometimes the uncertainty is replaced by its statistical fluctuation according to the bootstrap evaluation, such kinds of bins are decorrelated with the others, but for normal case, a typical 100% correlation is still assigned. In general, only for systematic uncertainties, one can correlate or decorrelate the uncertainties between different η regions, which can have a significant impact on the constraint, but also on the goodness of fit. In all the cases, the statistical uncertainty remains uncorrelated neither between E_T nor η.

The effective correlations between different η and E_T bins are demonstrated in Fig. 6.4, respectively in case when systematic uncertainties are correlated or uncorrelated between different η regions. The axis labels correspond to the $\eta \times E_T$ bin indices which are consistent with the definition of Eq. 6.8a.

In the case when η bins are uncorrelated for systematic uncertainties (Fig. 6.4b), all the off-diagonal blocks are almost null, the remaining tiny correlation around 1% at some specific positions is due to the correlation of statistical uncertainty given by the bootstrap study. According to Fig. 5.40 and Tab. 5.7: in the range of $|\eta| < 0.6$ (top left square in the plot): the first three E_T bins are dominated by MassWindow, fBremVar and TightVar, which are all quite flat[3] as a function of E_T, hence these bins are highly correlated. Similar behavior appears also for the low E_T range at $1.55 < |\eta| < 1.82$; High correlation can also occur in case that the same systematic controls several bins, for instance, all the E_T bins at $1.37 < |\eta| < 1.55$ and high E_T region at $1.55 < |\eta| < 1.82$; Another situation is that when all the systematics or the dominant systematics have the same profile versus E_T[4], the correlation of the total uncertainty is also equal to one. It happens for the two first E_T bins at $0.6 < |\eta| < 1$ when the ratio of uncertainties between these two bins is similar. One can find that the first situation with flat systematic is a special case of the last one, i.e. same E_T profile. The high correlation observed in the range of $1 < |\eta| < 1.37$, is mainly due to a mixing effect of all the three situations described above. The reduction of correlation in the bin of $E_T > 100$ GeV at $0.6 < |\eta| < 1$ is due to the fact that the most important uncertainty is fBremVar, of which the initial estimation was noisy according to the bootstrap study, hence was then replaced by a statistical uncertainty. The same argument is applied as well for the last three E_T bins of $1.37 < |\eta| < 1.55$ for the TightVar systematic. The last η bin

---

[3] Simple demonstration: $V_{ij} = \sum_k V_k = \sum_k \sigma_{ki}\rho_{ij}\sigma_{kj} = (\sum_k \sigma_k^2)J_{ij}$, if $\sigma_{ki} = \sigma_{kj}$, $\forall i, j$. J is an all-ones matrix, referring to a full correlation matrix.

[4] Simple demonstration: $\rho_{ij} = \frac{\sum_k \sigma_{ki}\sigma_{kj}}{\sqrt{\sum_k \sigma_{ki}^2 \sum_k \sigma_{kj}^2}} = 1 \to \sum_{k<l}(\sigma_{ki}\sigma_{lj} - \sigma_{li}\sigma_{kj})^2 = 0 \to \frac{\sigma_{ki}}{\sigma_{kj}} = \frac{\sigma_{li}}{\sigma_{lj}}, \forall k, l.$

between 1.82 and 2.47 contains plenty of bins with a noisy estimation of systematic as shown in Tab. 4.10, in addition, some systematics have a negative correlation, therefore small correlation or anticorrelation often appears in this η region.

As for Fig. 6.4a when systematic uncertainty is assumed to be correlated between η, the diagonal blocks remain identical to the ones of the η-decorrelated case, and then the off-diagonal parts are filled according to the corresponding correlation assumed for each source of uncertainty.

In general, the correlation assumption can have a huge impact on the fit results and the goodness of fit. Essentially, a high correlation between the two bins implies that the fit will vary them in the same direction with respect to the data, in contrast, a high anticorrelation would prefer the opposite deviation. An interesting phenomenon is that when a very high correlation is imposed, the fit will be pulled all on the same side of the data points. Roughly speaking, high correlation often leads to better constraint, but the fit quality can be very poor.

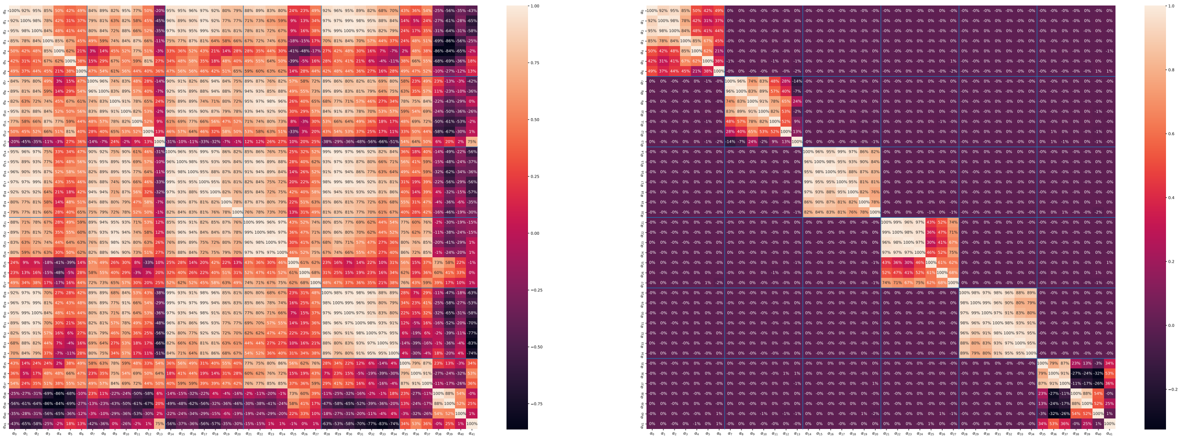

(a) η-correlated Σ

(b) η-decorrelated Σ

Figure 6.4: Effective correlation between η and E_T calculated for the joint covariance matrix Σ of the $Z \to ee$ linearity data, in case when systematic uncertainty is correlated (a) or uncorrelated (b) between the 6 coarse η bins. The X and Y axis labels correspond to the indices of $\eta \times E_T$ bins. Each square with blue border stands for the correlation between two η bins.

6.1.4 Inference results and constraint on systematic

Respectively for the η-correlated and η-decorrelated correlation models, the parameters $\vec{\alpha}_g$ and $\vec{\theta}$ are fitted to the $Z \to ee$ linearity data. In Fig. 6.5, the cyan band is the prefit uncertainty band, which is unity for the various systematic NPs $\vec{\theta}$ and zero for the six global scales $\vec{\alpha}_g$, since they have no prefit constraint. The yellow band is the postfit uncertainty band obtained from the fit. Black dots correspond to the shifts of parameters, of which the square of the error bar is equal to the quadratic difference between the prefit and postfit uncertainties (Eq. 6.23), while for $\vec{\alpha}_g$ it is equal to the postfit uncertainty.

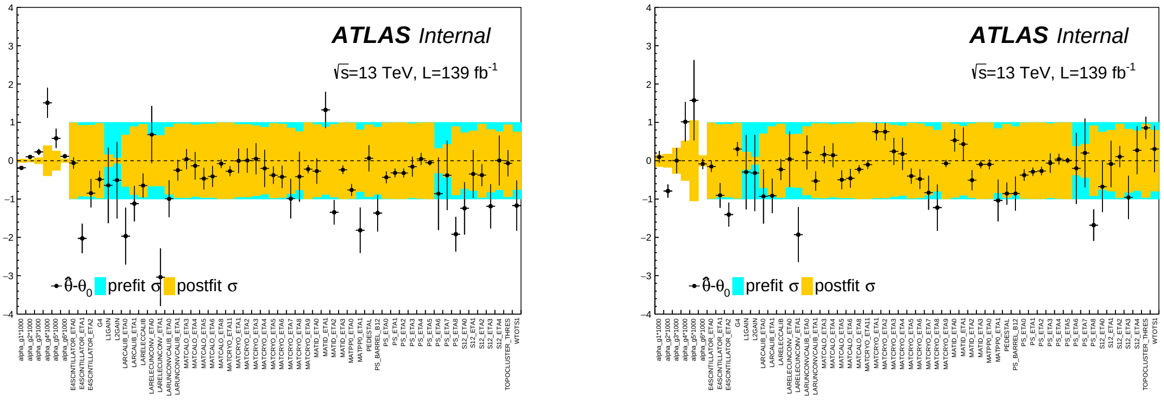

(a) η-correlated Σ

(b) η-decorrelated Σ

Figure 6.5: Pulls and constraints of the parameters in case the covariance matrix Σ is η-correlated or η-decorrelated. The cyan band is the prefit uncertainty band, the yellow band is the postfit uncertainty band. Black dots correspond to the shifts of parameters. The central value and uncertainty of $\vec{\alpha}_g$ are scaled by one thousand.

$$\sigma^2(\hat{\theta} - \theta_0) = \sigma^2(\theta_0) - \sigma^2(\hat{\theta}) \tag{6.23}$$

By comparing the prefit and postfit uncertainty bands, the MG/HG calibration (L1Gain and L2Gain), LAr modelling (LARCALIB, LARELECUNCONV) and layer calibration (PS, S12) are the most constrained, which are also the most important systematics depending on the η bins, as shown in Fig. 6.3. It implies a potential constraint on the energy scale systematic uncertainty.

The pattern in the middle corresponds to the various material systematics. They are much less constrained. The material effect remains small in most of the η region and increases when close to the crack, hence the relevant NPs in the barrel and endcap only bring small sensitivity to the fit. Apart from that, since they are split into various NPs that only part of the $Z \to ee$ linearity data in the corresponding η bins can be used to constrain them. In contrast, it explains also why L1Gain and L2Gain are so much constrained, which is not only due to their large sensitivity (large contribution to total uncertainty), but also because only one NP is defined for all the η region.

In general, the constraint on NPs is similar between the two η correlation models, and for the η-correlated case, a better constraint on the global scale parameters is observed.

The layer calibration and LAr modelling NPs are shifted with respect to 0, which are pulled to match the linearity data at both the low and high E_T range. One useful remark is that the L2Gain systematic has almost no sensitivity at low E_T, hence there is the possibility to tune only this NP to cover tension at high E_T after matching the low E_T linearity profile with the pulls on layer calibration and LAr modelling NPs. However, the limitation is that since the L2Gain has only a common NP fully correlated in η, residual tensions are still possible to occur.

Using the postfit pulls of the parameters $\hat{x}$ with $x = (\vec{\alpha}_g, \vec{\theta})$, one can calculate the postfit linearity scale as:

$$\hat{y} = I \cdot \hat{x} \tag{6.24}$$

of which the postfit uncertainty is

$$\sigma^2_{\hat{y}} = diag(I \cdot V(\hat{x}) \cdot I^T) \tag{6.25}$$

where I is the impact matrix in the $\eta \times E_T$ phase space defined for different parameters x, $V(\hat{x})$ is the postfit uncertainty of x.

For NP covariance $V(\hat{x})$, the corresponding correlation matrix is shown in Fig. 6.6. NPs having similar E_T profile in the same η bin can be correlated after fitting to the linearity data, the examples are S12_ETA0 and LARCALIB_ETA0 at $|\eta| < 0.6$, PS_ETA6 and LARELECUNCOV_ETA0 at $1 < |\eta| < 1.37$, and S12_ETA3 and S12_ETA4 at $1.82 < |\eta| < 2.47$. Between these NPs, given their similar systematic behavior, a negative correlation is observed, and similarly, if two NPs have similar E_T profile but the sign-inverted impact, for instance, WTOTS1 and LARELECUNCOV_ETA1, a positive correlation will emerge.
The η correlation imposed in the covariance matrix Σ has a significant impact on the correlations between the various global scales, as well as those NPs having an evident impact on several η bins, e.g. L2Gain and L1Gain.

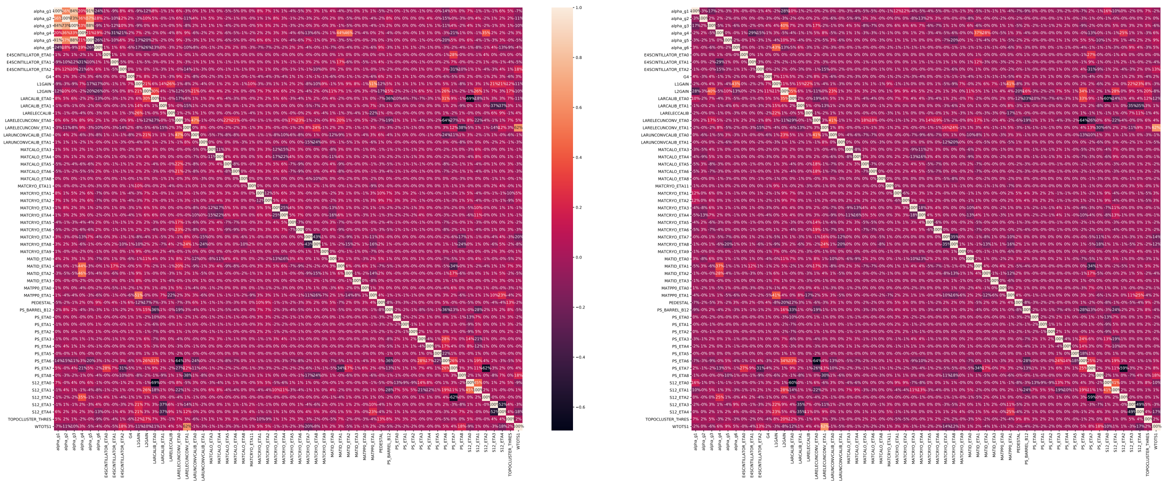

(a) η-correlated Σ

(b) η-decorrelated Σ

Figure 6.6: Postfit correlation matrix of the fitted parameters in case when input linearity systematic uncertainty η-correlated or η-decorrelated. The axis labels refer to the name of the 6 global scales and 52 systematic nuisance parameters.

While for the prefit stage, since the parameters are a priori equal to zero and the systematic nuisance parameters $\vec{\theta}$ are uncorrelated, therefore the induced linearity is also zero for all the bins, and the corresponding uncertainty is calculated by summing all the energy scale uncertainties in quadrature. The global scales are not taken into account since they have no prefit constraint. One caveat is that since the input uncertainties of linearity (MassWindow, TightID, fBremVar, etc...) are evaluated in the same way and with the same datasets as the inclusive η-dependent $Z \to ee$ calibration uncertainty (ZEE_STAT and ZEE_SYST), hence it is equivalent to say that the $Z \to ee$ calibration uncertainty is propagated to the global scale $\vec{\alpha}_g$. In order to be compatible, the $Z \to ee$ calibration uncertainty is also included in the definition of prefit uncertainty, although only the main sources of uncertainty were propagated by assuming the remaining uncertainty is negligible.

The energy scale central values and the associated uncertainties for both prefit and postfit stages are plotted in Fig. 6.7. General reduction of the uncertainty has been observed after having constraints from the $Z \to ee$ linearity data given its fine accuracy. The constraint often reaches a factor around 10 at large E_T. Such evident constraint is mainly due to the constraints on the MG/HG and layer calibration systematics, which are also the largest uncertainties in most of the η regions. At medium and low E_T, the η-correlated scheme has a much better performance than the one with η-decorrelated, however Fig. 6.5 and Fig. 6.6 had shown very similar postfit constraints and correlations for the systematic NPs. The origin of this difference is the global scale $\vec{\alpha}_g$, as it was shown in Fig. 6.5, much worse uncertainties on these parameters are obtained when there is no correlation assumed between η bins, which indeed become an important contributor to the total energy scale uncertainty after the dominant systematic sources (MG/HG and layer calibrations) have been significantly constrained. This is why the difference between the two correlation models is more obvious around 40 GeV, while it is decreased rapidly at large E_T. In particular for $1.55 < |\eta| < 1.82$, since the postfit uncertainty of α_g is in the level of $O(10^{-3})$ for η-decorrelated case, the total postfit uncertainty is mostly dominated by α_g in the full range of E_T.

Some tensions occur between the central values of the $Z \to ee$ linearity data and the postfit, which implies a possible issue for the goodness of fit. The fit quality is evaluated by a χ^2 test, according to the χ^2 formula of Eq. 6.18. Since the total χ^2 is calculated in the 6 η bins, the contributions of each η bin can be separated by decomposing this χ^2 formula into a set of terms which describe the discrepancies between fit and data only from a given η bin, as well as correlated terms between two different η bins. There is a rest term as the deviation of postfit θ from the prefit value of 0. The χ^2 decomposition is demonstrated below:

$$\begin{aligned}\chi^2(\vec{x}) &= \left(y^{Zee} - I\cdot x\right)^T \Sigma^{-1} \left(y^{Zee} - I\cdot x\right) + x^T C x \\ &= \sum_{ij} \left(y^{Zee} - I\cdot x\right)_i \times \Sigma^{-1}_{ij} \times \left(y^{Zee} - I\cdot x\right)_j + \sum_k \theta_k^2 \\ &= \sum_{\eta_i \eta_j} \left[\sum_{i\in\eta_i j\in\eta_j} \left(y^{Zee} - I\cdot x\right)_i \times \Sigma^{-1}_{ij} \times \left(y^{Zee} - I\cdot x\right)_j \right] + \sum_k \theta_k^2\end{aligned} \tag{6.26}$$

The first long term is indeed a big matrix in which each of the element stands for the χ^2 contribution between a pair of $(\eta \times E_T)_i$ and $(\eta \times E_T)_j$ bins. This χ^2 matrix is shown in Fig. 6.8, where η bins are split by the blue frontiers, then inside each separated square, the χ^2 contribution is further divided into E_T bins. For η-decorrelated scheme: since almost no correlation is introduced between η bins, the off-diagonal blocks are less important than the diagonal ones; inside the diagonal blocks, although big values are often observed for the diagonal element, because of the high correlation between E_T bins (Fig. 6.4), they are compensated by the neighboring off-diagonal elements; This is also the reason why the set of postfit energy scale points are often simultaneously 1σ always from the linearity data. For the η-correlated cases, the off-diagonal blocks have a significant negative contribution, which is due to the correlation between η bins. The characteristics

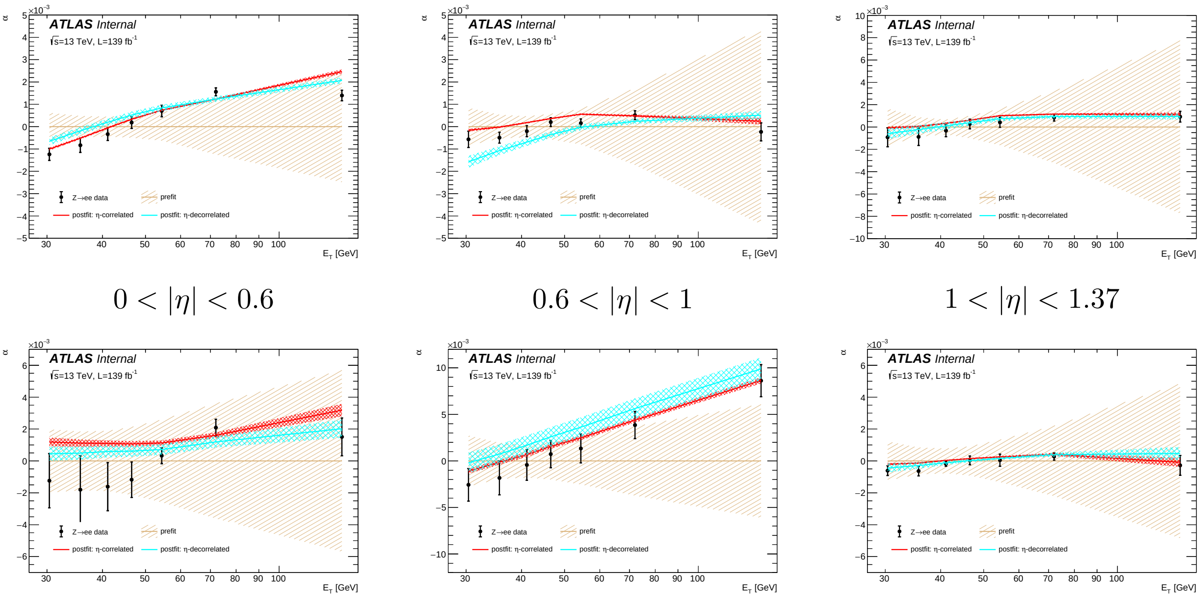

$0 < |\eta| < 0.6$ $0.6 < |\eta| < 1$ $1 < |\eta| < 1.37$

$1.37 < |\eta| < 1.55$ $1.55 < |\eta| < 1.82$ $1.82 < |\eta| < 2.47$

Figure 6.7: Comparison between the prefit and the postfit energy scale. The prefit (yellow) is centered at zero, with unconstrained energy scale uncertainty. The postfit (red and cyan) is shifted due to nonzero NP pulls fitted to the $Z \to ee$ linearity data (black dots), the color band corresponds to the constrained uncertainty. The postfit results with both the two η correlation schemes are shown.

of the goodness of fit are summarized in Tab. 6.2, which includes the total χ^2, its contribution from a single η bin by ignoring its correlation to other η regions (a diagonal block from Fig. 6.8) as well as the one from NP pulls.

The caveat is that due to the unsatisfying goodness of fit, the obtained constraint on energy scale uncertainty can be too optimistic, therefore one has to solve this χ^2 issues before applying to any physics analysis. On the other hand, for the application of the constraint, one should remove the inclusive $Z \to ee$ calibration uncertainty, since it has been already taken into account in the global scale $\vec{\alpha}_g$.

Correlation Models	χ^2/ndf	p-value	$\sum_k \theta_k^2$	$\chi^2_{\lvert\eta\rvert<0.6}$	$\chi^2_{0.6<\lvert\eta\rvert<1}$	$\chi^2_{1<\lvert\eta\rvert<1.37}$	$\chi^2_{1.37<\lvert\eta\rvert<1.55}$	$\chi^2_{1.55<\lvert\eta\rvert<1.82}$	$\chi^2_{1.82<\lvert\eta\rvert<2.47}$
η-correlated	$307/36$	$O(10^{-44})$	43	363	423	913	835	511	169
η-decorrelated	$122/36$	$O(10^{-11})$	22	25	24	10	20	15	5

Table 6.2: Goodness of fit: χ^2, degree of freedom, and the corresponding p-value. The decomposition to the sum of the square of systematic NPs and the χ^2 from a single η bin. Correlated terms between different η bins are taken into account which has important suppression on the total χ^2.

6.1.5 Performance on photon energy scale uncertainty

The global fit uses the $Z \to ee$ linearity to constrain the electron energy scale uncertainties where in total 52 NPs are constrained, then the performance of such constraint will be explored on photons, where one needs to take into account the increase of uncertainty from the difference between photon and electron,

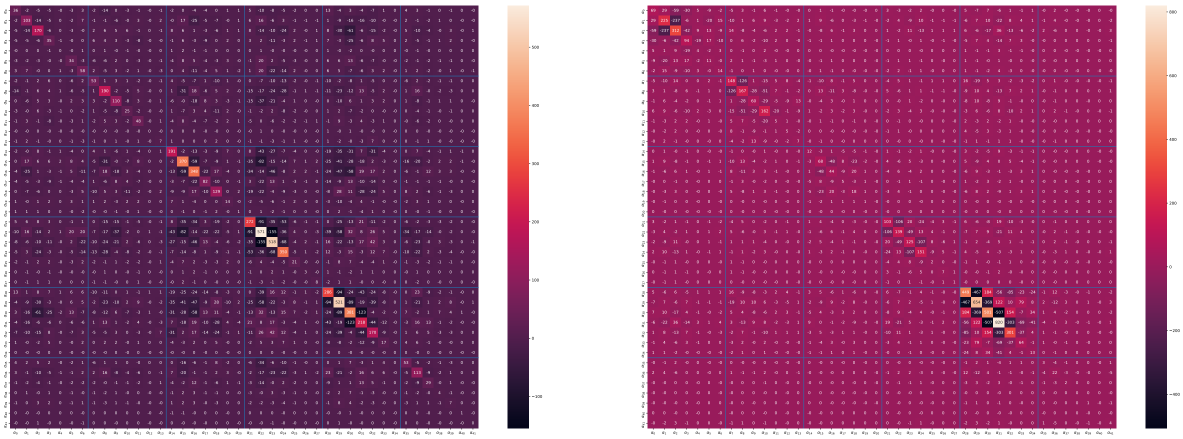

(a) η-correlated Σ *(b)* η-decorrelated Σ

Figure 6.8: Matrices showing the χ^2 contribution between different pairs of $\eta \times E_T$ bins in case the global fit is done with η-correlated or η-decorrelated correlation models. η bins are separated by the blue frontiers.

as well as the additional uncertainties from photon leakage and reconstruction.

Since one of the interesting goals is to see how the global fit will constrain the $H \to \gamma\gamma$ mass uncertainty, the photon energy scale uncertainty is evaluated at a set of $|\eta|$ and E_T values that as in Tab. 6.3 which are chosen using the HGam photon kinematics. Basically, there are more photons in the barrel than endcap, and the average transverse energy of photons from Higgs decay is around 60 GeV.

$\|\eta\|$	0.1, 0.3, 0.5, 0.7, 0.9, 1.1, 1.3, 1.5 (excluded in the HGam analysis), 1.7, 1.9, 2.1, 2.3
E_T [GeV]	40, 60, 80, 100, 120

Table 6.3: List of $|\eta|$ and E_T values used for evaluating photon energy scale uncertainty.

The prefit total uncertainties of unconverted and converted photons are shown in Fig. 6.9. The 69 NPs associated with the complete energy scale systematic model are involved. For postfit uncertainty, the constraints and correlations of the 52 NPs and 6 global scale $\vec{\alpha}_g$ used in the global fit model are included in the calculation, and the two Zee calibration NPs are removed to avoid double counting of the uncertainty.

For an unconverted photon, a general reduction factor around 2 is observed in the barrel, which is even better when moving to higher E_T. For a converted photon, the performance is much worse in particular at low η, where the dominant systematic is the photon lateral leakage, which is not constrained by $Z \to ee$ linearity. It is useful to clarify that the plots only refer to the constraint at a fixed value of η and E_T, while in principle there is also an improvement from the correlation of NPs located at different η regions that are not included at fixed η calculations. As was introduced above, the two η correlation models have similar constraints on the systematic NPs, while the difference between them is mainly due to different constraints on the global scale $\vec{\alpha}_g$. However the impact from $\vec{\alpha}_g$ becomes much less important for photons, given the increased uncertainty due to the difference between electrons and photons, and the leakage uncertainty. Indeed keeping or removing the $\vec{\alpha}_g$ only has an effect in the order of $O(10^{-3})$ on the photon energy uncertainty, which can be probably ignored in practice.

The global fit brings not the only constraint on photon energy scale uncertainty, but also a shift on the energy scale (Fig. 6.10). Given the NP pulls themselves correspond to the energy scale change on MC, a minus sign is introduced to each of the NP to have an equivalent impact on data. The change on the energy scale is often in the order of $O(10^{-3})$, similar to the associated energy scale uncertainty[5]. The pulls of the 52 NPs and 6 global scales $\vec{\alpha}_g$ are used to compute the shift on the energy scale. Due to the up to 1.5×10^{-3} relative energy scale shift from the $\vec{\alpha}_g$, these parameters are not negligible in some η and E_T regions, which can have roughly 20 MeV impact on the Higgs mass after integrating over the full phase space.

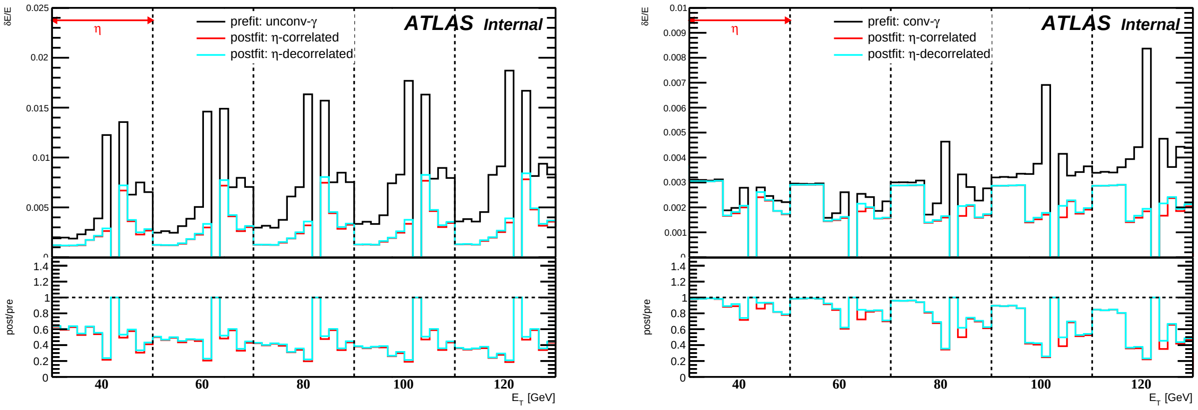

Unconverted photon

Converted photon

Figure 6.9: Constraint on photon energy scale uncertainty using global fit results from linearity. The prefit uncertainty is computed with the full 69 systematic NPs in quadrature. The postfit uncertainty is computed by applying constraints one the 52 NPs and 6 global scales used in the global fit. Each block corresponds to one E_T value, inside which the evolution of uncertainty in function of η is shown.

In conclusion, a global fit model which considers the $Z \to ee$ linearity as observation of the electron energy scale uncertainty has been studied. Doing so, one benefits from the additional constraint on these uncertainties. Such constraint can bring potential reduction of photon energy scale uncertainty, in consequence, a better precision of the $H \to \gamma\gamma$ mass measurement, which will be discussed in the next section.

---

[5] The shift on energy scale can be different with the new calibration recommendation since the non-linearity is evidently improved with the ADC and L2Gain corrections, hence smaller pulls are expected.

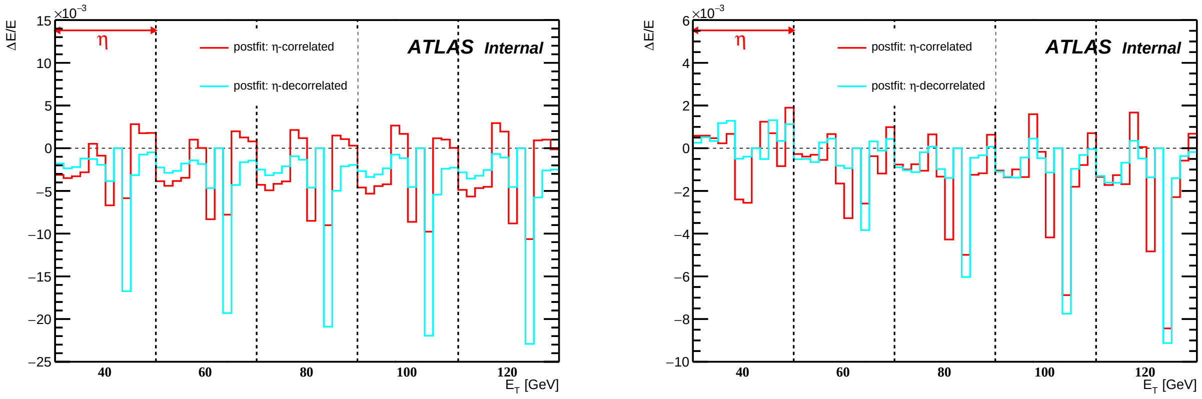

Unconverted photon Converted photon

Figure 6.10: Shift on photon energy scale using global fit results from linearity. The postfit uncertainty is computed with the pulls on the 52 NPs and 6 global scales used in the global fit. Each block corresponds to one E_T value, inside which the evolution of uncertainty as a function of η is shown.

6.2 Measurement of Higgs mass with $H \to \gamma\gamma$ decay

A measurement of the Higgs boson mass in the two photons decay channel is performed using the pp collision datasets collected by the ATLAS experiment during LHC Run 2, with a total integrated luminosity of 139 fb^{-1}.

An early study using 36.1 fb^{-1} Run 2 data [16] was performed, which gives a mass measurement of

$$m_H = 124.93 \pm 0.40\,(0.21(\text{stat}) \pm 0.34(\text{syst}))\ \text{GeV} \tag{6.27}$$

where the systematic uncertainty is dominated by the LAr cell non-linearity response, layer calibrations of ECAL and passive material effect.

In this new full Run 2 analysis, the latest ECAL calibration is applied in order to improve the uncertainty associated to the calorimeter. In addition, a global fit model is used to parametrize the linearity measured with $Z \to ee$ events with the various energy scale uncertainties, which brings potential constraint on these uncertainties and improvement on the Higgs mass precision.

The Higgs signal is exploited with several production modes, including gluon gluon fusion (ggF), vector boson fusion (VBF), association production with W or Z boson, $t\bar{t}H$, $b\bar{b}H$, and tH processes. The various signal samples are generated with the Powheg generator, except the tH production with MadGraph5_aMC@NLO. The Higgs to $\gamma\gamma$ decay is modelled by either Pythia or Herwig parton showering generator.

The irreducible background comes from the QCD $\gamma\gamma$, $V\gamma\gamma$ and $t\bar{t}\gamma\gamma$ productions, which have no resonant peak near the Higgs signal region as a continuum background. The QCD $\gamma\gamma$ and $V\gamma\gamma$ are generated with Sherpa Monte Carlo, The $t\bar{t}\gamma\gamma$ samples are generated with MadGraph5_aMC@NLO with Pythia for the parton showering.

6.2.1 Event selection

Similar selections on the two photons as in Sec. 4.5.1 are applied to enrich the signal and reduce the background:

- pass di-photon triggers, with a minimum transverse energy of 35 GeV and 25 GeV respectively for the leading and subleading photons.
- at least two photons satisfying both the tight identification criteria and the FixedCutLoose isolation criteria.
- transverse momentum of the (sub)leading photon above 35% (25%) of $m_{\gamma\gamma}$.
- Neural network (NN)-based approach to identify the diphoton vertex.
- Diphoton mass $m_{\gamma\gamma}$ required to belong to the range [105, 160] GeV.

6.2.2 Event categorization

For the measurement of the Higgs mass, the statistical uncertainty is proportional to the mass resolution, which depends on the η region of the detector and the photon conversion status. For instance, the central barrel region is better as compared to the transition region between barrel and endcap; as well the unconverted photon has a generally better resolution than the converted. Hence the relevant photon kinematics and properties are used for categorization, which include

- $|\eta_{S2}|$: absolute pseudorapidity of the reconstructed photon cluster in the second layer of the LAr calorimeter.
- Photon conversion status: converted or unconverted photons.
- $p_{Tt}^{\gamma\gamma}$: the projection of the diphoton transverse momentum in the so-called thrust-axis $\bar{t}$:

$$p_{Tt}^{\gamma\gamma} = \left|p_T^{\gamma\gamma} \times \bar{t}\right|, \quad \text{with } \bar{t} = \frac{\vec{p}_T^{\gamma 1} - \vec{p}_T^{\gamma 2}}{|\vec{p}_T^{\gamma 1} - \vec{p}_T^{\gamma 2}|} \tag{6.28}$$

A sketch of the categorization is shown in Fig. 6.11. The leading and subleading photons are classified as both unconverted or at least one converted, then split into three $|\eta_{S2}|$ regions: a central region with both photons located at $|\eta_{S2}| < 0.75$, a transition region with at least one photon satisfying $1.3 < |\eta_{S2}| < 1.75$ (the crack region $[1.37, 1.52]$ was excluded), and all the other cases labelled as rest. Apart from the division in $|\eta_{S2}|$ and photon conversion, a further splitting in the $p_{Tt}^{\gamma\gamma}$ spectrum is implemented for the central and rest regions. The cutting thresholds are 70 and 130 GeV which corresponds to the 30% and 10% quantile of the signal $p_{Tt}^{\gamma\gamma}$ distribution. Consequently there are in total 14 categories defined according to photon conversion status, $|\eta_{S2}|$ and $p_{Tt}^{\gamma\gamma}$. The thresholds on $|\eta_{S2}|$ and $p_{Tt}^{\gamma\gamma}$ are optimized to have the best expected accuracy of the Higgs mass.

The expected yields for the various signal production processes under the SM assumption are summarized in Tab. 6.4, the contribution to the total signal from each production is visualized in Fig. 6.12, which shows generally large signal fractions from the ggH and VBF modes.

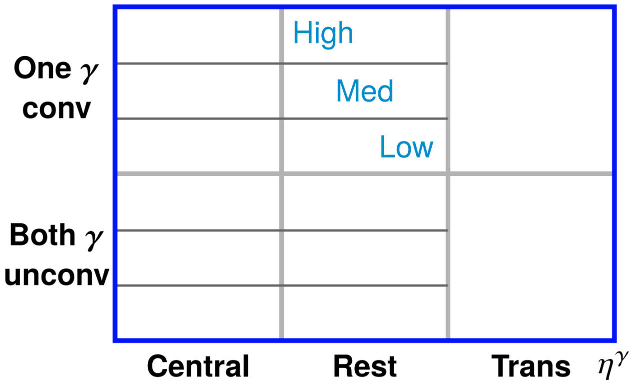

Figure 6.11: Sketch of mass categorization defined with photon conversion status, η and $p_{Tr}^{\gamma\gamma}$.

Category	ggH	VBF	WH	ZH	ggZH	ttH	bbH	tHjb	tWH
UU Cen high	24.13	9.16	2.66	1.51	0.82	2.80	0.12	0.21	0.11
UU Cen med	67.54	18.97	4.97	2.87	1.13	3.54	0.44	0.35	0.13
UU Cen low	751.50	40.40	11.55	6.54	0.88	4.75	9.02	0.44	0.14
UU Rest high	25.85	9.71	3.06	1.79	0.78	2.40	0.14	0.20	0.10
UU Rest med	114.45	31.86	8.98	5.33	1.69	4.96	0.61	0.65	0.17
UU Rest low	1260.60	66.96	21.30	11.90	1.46	7.03	14.56	1.04	0.22
UU Trans	413.74	32.32	10.57	5.94	0.97	3.63	4.42	0.60	0.10
Conv Cen high	15.41	5.98	1.68	0.91	0.52	1.78	0.06	0.18	0.06
Conv Cen med	42.80	11.95	3.18	1.84	0.67	2.27	0.28	0.24	0.09
Conv Cen low	470.75	24.97	7.17	4.18	0.53	2.98	5.60	0.29	0.10
Conv Rest high	29.40	11.21	3.80	2.11	0.84	2.66	0.15	0.36	0.12
Conv Rest med	129.32	36.28	10.69	6.30	1.82	5.40	0.72	0.71	0.17
Conv Trans	696.22	54.22	18.41	10.18	1.74	6.02	6.96	1.06	0.19
Conv Rest low	1435.81	76.33	25.39	14.15	1.52	7.58	15.73	1.26	0.19

Table 6.4: Expected SM yields at 139 fb^{-1} for the various Higgs production modes for the mass analysis categorization

6.2.3 Signal modelling

The analysis is using the diphoton invariant mass $m_{\gamma\gamma}$ as final discriminate variable. The shape of signal $m_{\gamma\gamma}$ distribution is modelled by a double sided crystal ball function (Eq. 4.10 in Sec. 4.6.1):

$$f_{DSCB}(t) = N \cdot \begin{cases} A_{\text{Low}} \cdot \left[\frac{\alpha_{\text{Low}}}{n_{\text{Low}}}(b_{\text{Low}} - t)\right]^{-n_{\text{Low}}}, & t < -\alpha_{\text{Low}} \\ \exp\left(-\frac{t^2}{2\sigma_{CB}}\right), & t \in [-\alpha_{\text{Low}}, \alpha_{\text{High}}] \\ A^{\text{High}} \cdot \left[\frac{\alpha_{\text{High}}}{n_{\text{High}}}(b_{\text{High}} - t)\right]^{-n_{\text{High}}}, & t > \alpha_{\text{High}} \end{cases} \tag{6.29}$$

In order to take into account the change on shape modelling due to different Higgs mass values, signal samples generated at $m_H = 110, 122, 123, 124, 125, 126, 127, 130, 140$ GeV are used to parametrize the

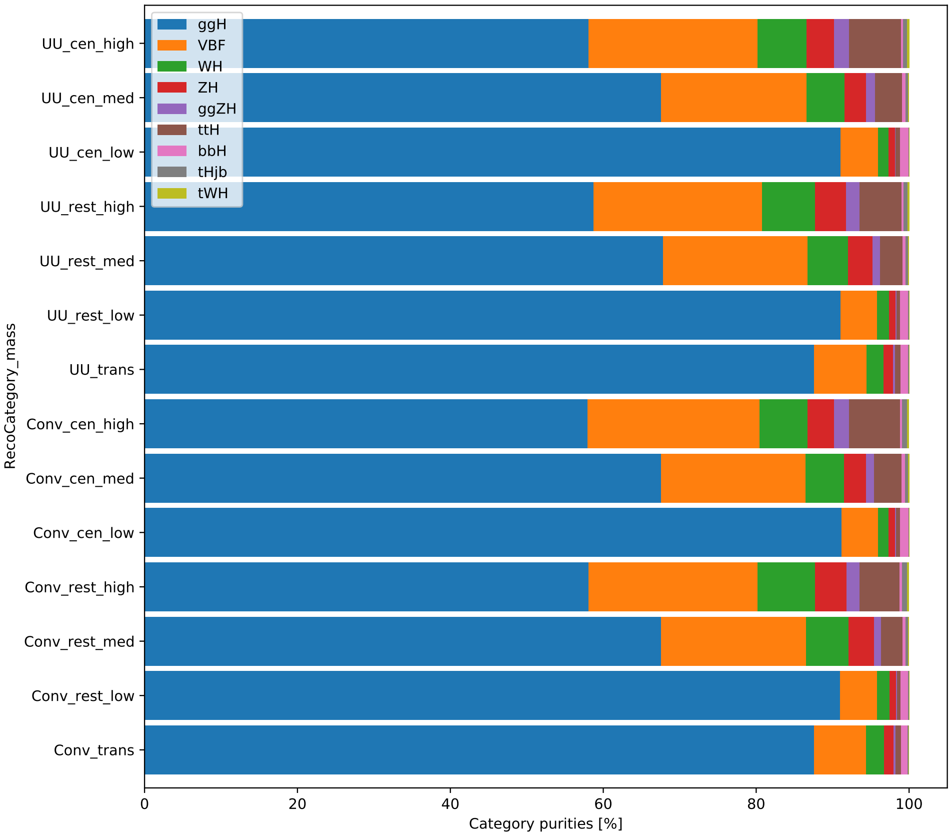

Figure 6.12: Fractions of different signal production mode with respect to the total number of signal in each Higgs mass categories.

DSCB function parameters in the following forms:

$$\begin{aligned}
\mu_{CB}(m_H) &= m_H + B_{\mu_{CB}} + A_{\mu_{CB}} \cdot (m_H - 125 \text{ GeV}) \\
\sigma_{CB}(m_H) &= B_{\sigma_{CB}} + A_{\sigma_{CB}} \cdot (m_H - 125 \text{ GeV}) \\
\alpha_{Low}(m_H) &= \alpha_{Low} \\
\alpha_{High}(m_H) &= \alpha_{High} \\
n_{Low}(m_H) &= n_{Low}|125 \text{ GeV} \\
n_{High}(m_H) &= n_{High}|125 \text{ GeV}
\end{aligned} \tag{6.30}$$

A linear parametrization is chosen for the peak position $\mu_{CB}(m_H)$ and spread $\sigma_{CB}(m_H)$. A common value for α_{Low} and α_{High} is taken to describe signal samples with different m_H. The power law orders are fixed to the one obtained with signal MC sample at $m_H = 125$ GeV. The parameters $B_{\mu_{CB}}$, $A_{\mu_{CB}}$, $B_{\sigma_{CB}}$, $A_{\sigma_{CB}}$, α_{Low} and α_{High} are simultaneously fitted to the $m_{\gamma\gamma}$ of the various signal sample at different m_H. The obtained parameters of each category are summarized in Tab. 6.5. Basically the parameter $B_{\mu_{CB}}$ represents the difference between the reconstructed Higgs peak position and the truth Higgs mass, which is several tens of MeV in the categories with both two unconverted photon, and in the level of 100 MeV in those with at least one converted photon.

Category	$B_{\mu_{\mathrm{CB}}}$ [MeV]	$A_{\mu_{\mathrm{CB}}}$	$B_{\sigma_{\mathrm{CB}}}$ [MeV]	$A_{\sigma_{\mathrm{CB}}}$	α_{Low}	$n_{\mathrm{Low}}\|_{125\mathrm{GeV}}$	α_{High}	$n_{\mathrm{High}}\|_{125\mathrm{GeV}}$
UU cen high	85.46	-0.000717	1106.20	0.006901	2.04	4.85	1.56	46.34
UU cen med	57.63	-0.001009	1282.85	0.010494	1.93	4.37	1.29	318.76
UU cen low	95.16	-0.000065	1482.59	0.006102	2.18	4.13	1.48	948.74
UU rest high	52.34	-0.001947	1227.82	0.009361	1.68	9.37	1.48	60.25
UU rest med	42.28	0.000877	1469.85	0.009664	1.87	6.70	1.45	98.09
UU rest low	17.45	-0.000023	1699.53	0.008385	1.90	5.92	1.55	967.05
UU trans	-11.16	-0.000076	1988.61	0.009320	1.69	10.91	1.50	882.07
Conv cen high	127.22	0.000588	1117.80	0.006454	1.84	4.57	1.35	110.32
Conv cen med	159.46	0.001894	1380.17	0.007712	1.99	3.19	1.34	134.75
Conv cen low	175.19	-0.002162	1624.65	0.006732	1.96	3.14	1.41	980.93
Conv rest high	143.26	0.001924	1397.29	0.011695	1.65	6.77	1.61	16.19
Conv rest med	150.21	0.000089	1660.08	0.011525	1.60	5.54	1.23	310.14
Conv rest low	136.59	0.000527	1960.41	0.007832	1.70	4.70	1.46	996.35
Conv trans	188.53	0.000087	2315.09	0.010922	1.47	7.74	1.45	963.08

Table 6.5: Parameters that describe the signal shape for each category according to the parametrization of equation 6.30.

6.2.4 Background modelling

The $\gamma\gamma$ continuum background is modelled by an analytical function, which is chosen by the spurious signal criteria described in Sec. 4.6.2. The template is constructed by the combination of $\gamma\gamma$, γj and jj processes, for which the fractions of the components are estimated using a data-driven technique as illustrate in Fig. 4.8 of Sec. 4.5.1. The template is then scaled to match the same events as data in the control regions $105 < m_{\gamma\gamma} < 120$ GeV or $130 < m_{\gamma\gamma} < 160$ GeV (data side bands). Example of the background-only MC templates are shown in Fig. 6.13.

The candidates of the background modelling functions are:

- Exponential Function: $f(m_{\gamma\gamma}) = e^{c \cdot m_{\gamma\gamma}}$.
- Exponential Function of 2nd Order Polynomial (ExpPoly2): $f(m_{\gamma\gamma}) = e^{c_1 \cdot m_{\gamma\gamma}^2 + c_2 \cdot m_{\gamma\gamma}}$.
- Exponential Function of 3rd Order Polynomial (ExpPoly3): $f(m_{\gamma\gamma}) = e^{c_1 \cdot m_{\gamma\gamma}^3 + c_2 \cdot m_{\gamma\gamma}^2 + c_3 \cdot m_{\gamma\gamma}}$.
- Bernstein polynomial of order N: $B_N(m_{\gamma\gamma}) = \sum_{i=0}^{N} c_i \cdot b_{i,N}$, with $b_{i,N} = \binom{N}{i} m_{\gamma\gamma}^i (1 - m_{\gamma\gamma})^{N-i}$.
- First-Order Power Law Function: $f(m_{\gamma\gamma}) = m_{\gamma\gamma}^c$.

Then a signal plus background model is fitted to the background template, where the background model is the function to be evaluated, and the double sided crystal ball function (Eq. 6.29) is taken for the signal modelling. The parameter μ_{CB} representing the mass peak position is varying in intervals of 0.5 GeV in a range from 123 GeV to 127 GeV. During the test for a given background functional form, the signal modelling is fixed, and for each value of μ_{CB}, the signal events, the background events and background function parameters are fitted. The largest fitted signal among the different μ_{CB} values is defined as the spurious signal N_{sp} for this functional form. The function passing the criteria with the smallest spurious signal N_{sp} and the lowest degrees of freedom is selected for the background modelling, with the corresponding spurious signal N_{sp} as the modelling systematic uncertainty.

The chosen functional forms for the various categories are shown in Tab. 6.6: the ExpPoly2 function is

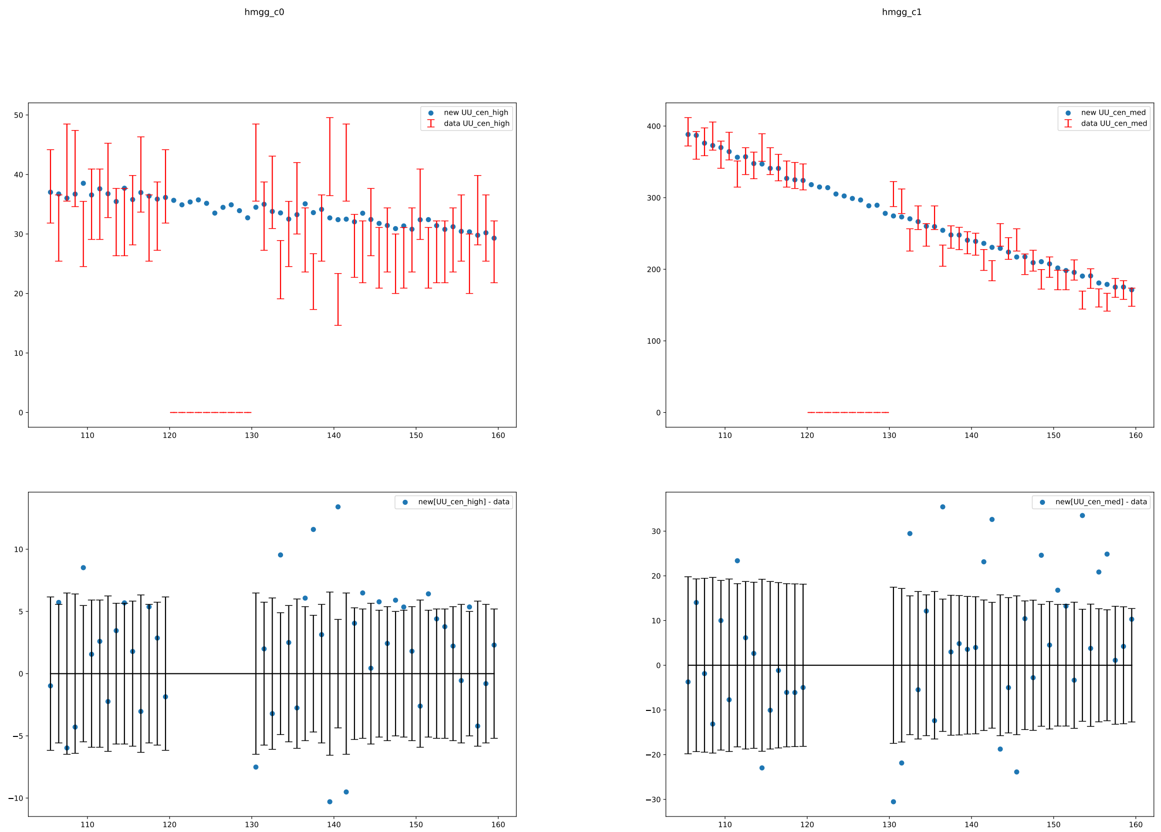

(a) UU_cen_high

(b) UU_cen_med

Figure 6.13: Examples of $m_{\gamma\gamma}$ distributions of the background template (blue) and blinded data (red) in the categories with both two central unconverted photons and with high (a) or medium (b) $p_{Tt}^{\gamma\gamma}$. The background templates are normalized to the data sideband. The bottom plots represent their differences.

preferred for categories with medium or low $p_{Tt}^{\gamma\gamma}$ which have enhanced statistics, while for high $p_{Tt}^{\gamma\gamma}$ categories, a simple power law or exponential function is chosen.

6.2.5 Systematic uncertainty

Experimental systematic uncertainties on the signal $m_{\gamma\gamma}$ shape modelling include variations of the photon energy scale (PES) and photon energy resolution (PER), which respectively affect the peak position and width of the $m_{\gamma\gamma}$ distribution. Their systematic effect is respectively incorporated in μ_{CB} and σ_{CB} parameters of the DSCB function by introducing additional response functions F_{PES} and F_{PER}:

$$\mu_{CB}' = (\mu_{CB} + m_H - 125 \text{ GeV}) \cdot F_{\mathrm{PES}}(\delta^{\pm}, \theta) \quad (6.31)$$

$$\sigma_{CB}' = \sigma_{CB} \cdot F_{PER}(\delta^{\pm}, \theta) \quad (6.32)$$

Category	m_H	N_{sp}	FF	$p(\chi^2)$ %	N_{sp}/σ_S (%)	$N_{sp}/N_{S,\text{exp}}$ (%)
UU cen high	123.0	0.953	Pow	15.5	7.28	1.5
UU cen med	126.5	2.99	ExpPoly2	9.44	6.68	1.65
UU cen low	123.0	-28.6	ExpPoly2	68.5	-13.4	-1.69
UU rest high	123.0	-1.06	Exponential	58.9	-12.3	-4.79
UU rest med	127.0	-3.81	ExpPoly2	46.2	-10.9	-4.38
UU rest low	123.0	-51.7	ExpPoly2	47.9	-29.3	-7.26
UU trans	124.5	-14.9	ExpPoly2	69.9	-13.8	-6.41
Conv cen high	127.0	1.85	Exponential	5.93	12.7	2.94
Conv cen med	125.0	-11.7	ExpPoly2	27.2	-22.1	-5.97
Conv cen low	124.0	-57	ExpPoly2	4.13	-21.8	-3.49
Conv rest high	125.5	2.37	Exponential	4.86	22.5	9.35
Conv rest med	123.0	-7.73	ExpPoly2	51.5	-18.2	-7.93
Conv rest low	125.5	-43.4	ExpPoly2	14.8	-21.5	-42
Conv trans	123.0	-28.1	ExpPoly2	28.2	-17.9	-7.24

Table 6.6: Final background modeling decision and the size of spurious signal uncertainties. m_H is the mass point of the scan at which the maximum spurious signal is fitted. χ^2 is computed for the MC template fit, which is transformed to a p-value.

The effect on the other parameters of the modelling is neglected.

- For the **scale**: the mean value of $m_{\gamma\gamma}$ is computed for the nominal $\langle m_{\gamma\gamma}^{\text{nom}} \rangle$ and $\pm 1\sigma$ variations of a given PES nuisance parameter $\langle m_{\gamma\gamma}^{\pm 1\sigma} \rangle$, then the associated uncertainty is evaluated as

  $$\delta\mu_{CB}^{\pm} = \frac{\langle m_{\gamma\gamma}^{\pm 1\sigma} \rangle}{\langle m_{\gamma\gamma}^{\text{nom}} \rangle} - 1 \tag{6.33}$$

  Fig. 6.14 shows the examples of uncertainties induced from the various sources of PES systematics in two of the categories, and the squared sum of all the PES systematic up variations for each category. In the central region, the uncertainty is dominated by the L2Gain and E1/E2 calibration, while there is a striking impact from lateral leakage for converted photons. The total effect of PES on the mass ranges from around $\pm 0.17\%$ in the Conv rest low category to around $\pm 0.58\%$ in the UU transition category. The PES uncertainty is in general larger at high $p_{Tt}^{\gamma\gamma}$, at transition or rests η regions, and larger for unconverted photon than converted one.
  Given the symmetric uncertainties between the up and down variations, the scale uncertainties are implemented with a Gaussian constraint using the $+1\sigma$ variation. Therefore the response function applied to μ_{CB} is defined as $F_{\text{PES}}(\delta^{\pm}, \theta) = \prod_i^{N_{np}} \left(1 + \delta_{\text{PES}}^{+} \cdot \theta_{\text{PES}^i}\right)$, where the 69 NPs described in Sec. 6.1.1 are included.

- For the **resolution**: the inter-quartile of $m_{\gamma\gamma}$ is computed for the nominal S^{nom} and $\pm 1\sigma$ variations of a given PER nuisance parameter $S^{\pm 1\sigma}$. The inter-quartile is defined as $S = F_{m_{\gamma\gamma}}^{-1}(75\%) - F_{m_{\gamma\gamma}}^{-1}(25\%)$, with $F_{m_{\gamma\gamma}}$ is the cumulative distribution function of the $m_{\gamma\gamma}$ distribution. The associated uncertainty is evaluated as

  $$\delta_{\text{PER}}^{\pm} = \frac{S^{\pm 1\sigma}}{S^{\text{nom}}} - 1 \tag{6.34}$$

  Fig. 6.15 shows the examples of uncertainties induced from the various sources of PER systematics in two of the categories, and the squared sum of all the PER systematic up variation for each category. The total effect of PER ranges from around $\pm 5.3\%$ in the Conv rest low category to around $\pm 20\%$

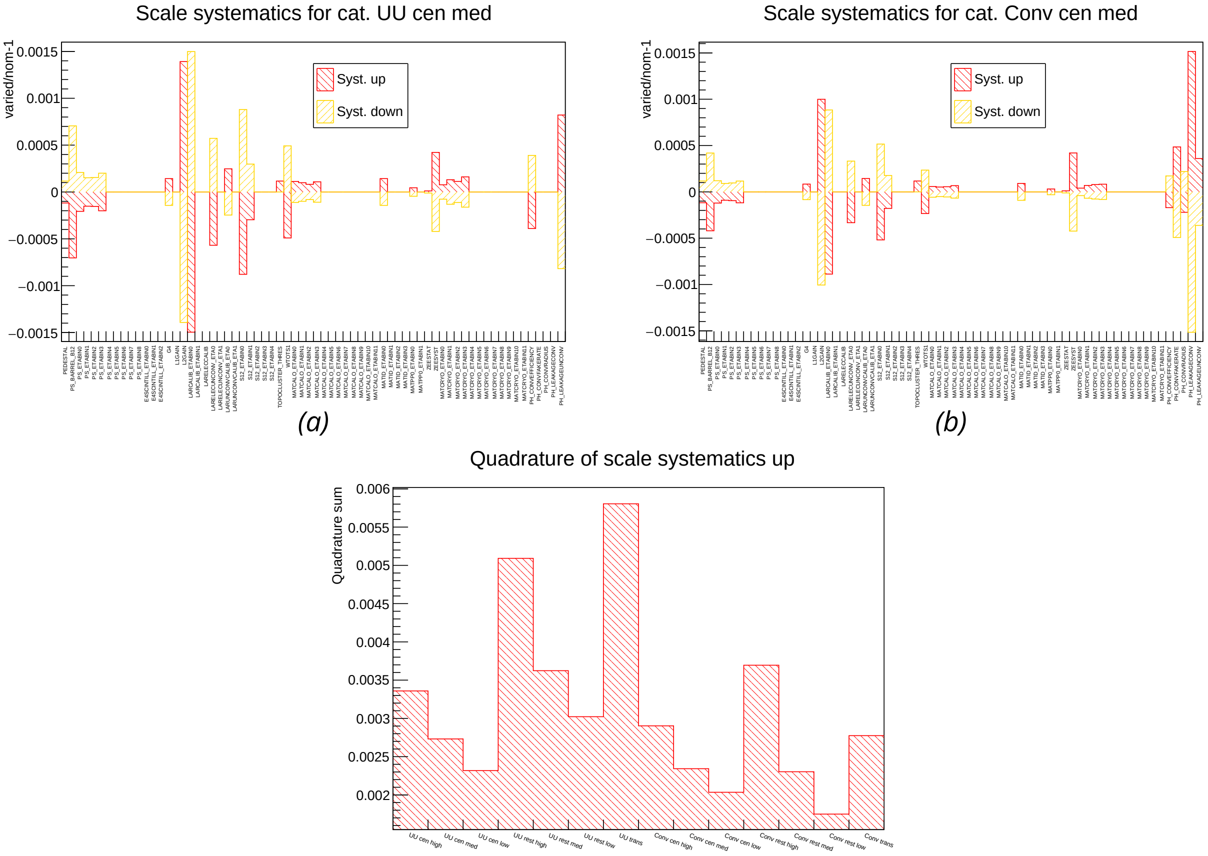

(a) (b)

(c)

Figure 6.14: Examples of $\pm 1\sigma$ PES uncertainties in the categories with two central photons at medium $p_{Tt}^{\gamma\gamma}$ that both are unconverted (a) or at least one is converted (b). (c) The squared sum of all the PES uncertainties for the various categories.

in the UU central high category. The effect is in general bigger at high $p_{Tr}^{\gamma\gamma}$. In order to take into account the difference between $+1\sigma$ and -1σ variations, an asymmetric constraint is implemented for the PER uncertainty, and a linear interpolation between $(1+\delta_{\mathrm{PER}}^{-})$ and $(1+\delta_{\mathrm{PER}}^{+})$ is considered for the calculation of the response function $F_{\mathrm{PER}}(\delta^{\pm}, \theta)$ applied on σ_{CB}.

Additional uncertainty of the signal shape modelling can arise from the mis-modelling of the signal, which affects the parameters of the signal model (Eq. 6.30) and then creates potential bias. Such kind of bias is estimated with a signal injection test, by fitting a sample composed of background Asimov data and the nominal signal MC at $m_H = 125$ GeV to the combined pdf of nominal signal and background model. The background Asimov data is generated with the background functional forms fitted to the data sideband and extrapolated to the blinded signal region ($m_{\gamma\gamma} \in [120, 130]$ GeV).

The uncertainty is then evaluated as the signal bias, defined as the relative difference between the fitted and injected ($m_H = 125$ GeV) Higgs mass (Tab. 6.7). In order to evaluate the statistical uncertainty of the signal bias, one thousand bootstrap replicas are generated for obtaining a set of replicas measurements of signal bias, which is used to calculate its mean μ and standard deviation σ. From the table, the signal bias

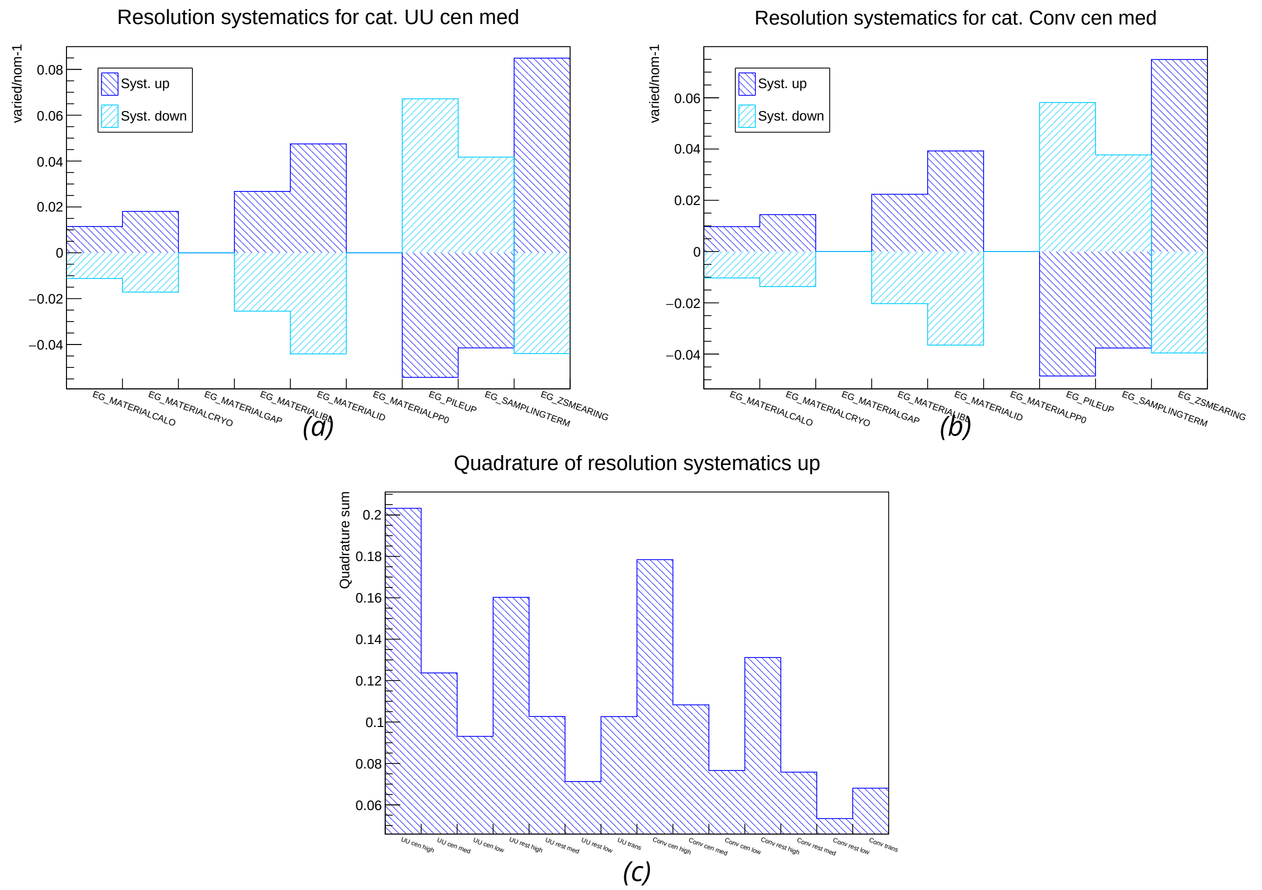

(a) (b)

(c)

Figure 6.15: Examples of $\pm 1\sigma$ PER uncertainties in the categories with two central photons at medium $p_{Tt}^{\gamma\gamma}$ that both are unconverted (a) or at least one is converted (b). (c) The squared sum of all the PER uncertainties for the various categories.

is not statistically significant (μ is comparable to σ) for around half of the categories, and the associated uncertainty is less than 10% with respect to the total PES uncertainty, consequently, the impact on total uncertainty is less than 1%.

6.2.6 Statistical model

An unbinned maximum likelihood fit using the $m_{\gamma\gamma}$ observable is performed simultaneously with the 14 categories. An extended likelihood function is constructed to describe the models of the various categories and then fitted to data:

$$\mathcal{L} = \prod_{c=1}^{N_c} \left(\text{Pois}\left(n_c | N_c\left(\mu, \boldsymbol{\theta}\right)\right) \cdot \prod_{i}^{n_c} f_c\left(m_{\gamma\gamma}^{i} | m_H, \boldsymbol{\theta}\right) \right) \cdot \mathcal{G}(\boldsymbol{\theta_0} | \boldsymbol{\theta}) \tag{6.35}$$

where

- $\text{Pois}\left(n_c | N_c\left(\mu, \boldsymbol{\theta}\right)\right)$ is an extended Poisson term constraining the observed events in a given category c, which is modelled by an expectation value:

$$N_c\left(\mu, \boldsymbol{\theta}\right) = \mu \cdot N_c^H(\boldsymbol{\theta}) + N_b + N_c^{sp} \cdot \theta_c^{sp} \tag{6.36}$$

Category	Nominal fit			Bootstrap			Comparison with PES	
	m_H^{fitted} [MeV]	bias [MeV]	bias [‰]	μ [‰]	σ [‰]	$\frac{\mu}{\sigma}$	$\sum \delta^2_{PES}$ [‰]	Bias size [%]
UU cen high	124966	-34	-0.27	-0.32	0.07	-4.26	3.36	-8.19
UU cen med	124996	-4	-0.03	-0.03	0.07	-0.39	2.73	-1.10
UU cen low	124992	-8	-0.06	-0.07	0.04	-1.80	2.32	-2.85
UU rest high	124985	-15	-0.12	-0.10	0.08	-1.23	5.09	-2.29
UU rest med	125010	10	0.08	0.08	0.06	1.31	3.62	2.25
UU rest low	124999	-1	-0.01	-0.01	0.03	-0.19	3.02	-0.27
UU trans	125009	9	0.07	0.09	0.07	1.34	5.81	1.23
Conv cen high	125006	6	0.05	0.10	0.10	0.96	2.90	1.53
Conv cen med	125002	2	0.02	0.02	0.10	0.20	2.34	0.71
Conv cen low	124996	-4	-0.03	-0.04	0.06	-0.70	2.04	-1.68
Conv rest high	125027	27	0.22	0.23	0.09	2.54	3.70	5.79
Conv rest med	124966	-34	-0.27	-0.27	0.07	-4.08	2.30	-11.73
Conv rest low	125002	2	0.02	0.01	0.03	0.28	1.75	0.84
Conv trans	124999	-1	-0.01	-0.02	0.07	-0.32	2.77	-0.32

Table 6.7: Signal bias computed as difference between the fitted and injected ($m_H = 125$ GeV) Higgs boson mass. Mean and standard deviation obtained from a bootstrap procedure with 1000 replicas are reported as well. The significance μ/σ of the bias for each category is reported. In addition, a comparison of the signal bias with the quadrature sum of the PES systematic uncertainties is reported, with "Bias size" computed as the ratio between the nominal signal bias and the quadrature sum of the scale systematics.

where $N_c^H(\boldsymbol{\theta})$ is the expected events of the Higgs signal, N_b is the continuum background and N_c^{sp} is the spurious signal with its corresponding nuisance parameter θ_c^{sp} associated for category c. Uncertainties of luminosity, branching ratio of $H \to \gamma\gamma$ and the efficiency-times-acceptance are assigned to $N_c^H(\boldsymbol{\theta})$.

- $f_c\left(m^i_{\gamma\gamma}|m_H,\boldsymbol{\theta}\right)$ is the joint probability density function of $m_{\gamma\gamma}$ for all the physics processes in a given category c, which is evaluated on the discrete data $m^i_{\gamma\gamma}$:

$$f_c\left(m^i_{\gamma\gamma}|m_H,\boldsymbol{\theta}\right) = \frac{1}{N_c\left(\mu,\boldsymbol{\theta}\right)}\left[\left(\mu \cdot N_c^H(\boldsymbol{\theta}) + N_c^{sp}\cdot\theta_c^{sp}\right)\cdot f_c^{sig}\left(m^i_{\gamma\gamma};m_H,\boldsymbol{\theta}\right) + N_b \cdot f_c^{bkg}\left(m^i_{\gamma\gamma}\right)\right] \tag{6.37}$$

where $f_c^{sig}\left(m^i_{\gamma\gamma};m_H,\boldsymbol{\theta}\right)$ and ${}_c^{bkg}\left(m^i_{\gamma\gamma}\right)$ are respectively the models of signal and background, where the corresponding uncertainties are applied. The joint pdf is normalized with the total number of events in the category.

- $\mathcal{G}(\boldsymbol{\theta_0}|\boldsymbol{\theta})$ is the term of systematic constraint for the nuisance parameters $\boldsymbol{\theta}$, which is often a normal or log-normal function. For normal function, the corresponding response function is $F(\delta,\theta) = (1+\delta\cdot\theta)$, while for log-normal, a different response function $F(\delta,\theta) = e^{\theta\sqrt{\ln(1+\delta^2)}}$ is used to emulate a log-normal variable with θ follows a normal distribution.

6.2.7 Expected results

Since the analysis is not yet unblinded, the expected results are evaluated using a signal plus background Asimov data, where the signal strength is set to one, the Higgs mass $m_H = 125.09$ GeV, background normalization and shape fitted to the data sideband, and all the systematic NP are set to zero. The best value of the Higgs mass m_H fitted to the Asimov data is:

$$m_H = 125.090^{+0.291}_{-0.290}\ \mathrm{GeV} = 125.090^{+0.125}_{-0.123}(\mathrm{stat.})^{+0.263}_{-0.263}(\mathrm{syst.})\ \mathrm{GeV} \tag{6.38}$$

where a total uncertainty of around 290 MeV is obtained, which includes a statistical component around 124 MeV, and a systematic one of 263 MeV. The statistical error is obtained by fixing all the systematic nuisance parameters, and the systematic one is calculated as the quadratic difference between the total and statistical errors. The accuracy of the measurement is dominated by systematic error, where the most important contribution is the photon energy scale uncertainty. In order to understand better the effect of different sources of uncertainties, the total uncertainty is decomposed into different groups:

- Layer calibration: inter-calibration of the PS, E1/E2 of the calorimeter; E4 scintillators calibration; uncertainty from supercluster threshold.
- Lateral shower shape: lateral leakage and lateral shower width modelling.
- LAr cell non-linearity: L1 and L2 gain calibration; pileup noise shift correction.
- Other material (not ID): material between ID and PS (or Calo), between PS and Calo and the associated LAr modelling systematics.
- $Z \to ee$ calibration: in-situ calibration.
- Conversion reconstruction: photon conversion reconstruction efficiency, fake rate and conversion radius.
- ID material: material in ID, IBL and PP0.
- Resolution: the photon energy resolution systematics.

The total Higgs mass error is decomposed using a fit on the Asimov data by floating all the systematic NPs except the ones in a particular group. The corresponding likelihood ratio scan is shown in Fig. 6.16, where for each curve the relevant group of systematics are fixed. The obtained uncertainty is subtracted from the total error in order to derive the contribution of this group (Tab. 6.7)[6]. The biggest contribution is from the layer calibration uncertainty, with significant effect from lateral shower shape and LAr cell non-linearity.

6.2.8 Improvement with constraints on photon energy scale uncertainty

The global fit (Sec. 6.1.2) introduces constrained, correlated and pulled LAr calorimeter energy scale uncertainties, which are represented in the obtained covariance matrix $V_{52\times52}(\hat{\theta})$ and the NP shift $\hat{\theta}$ for the 52 NPs included in the model. This information is directly included in the statistical model, by replacing the relevant Gaussian constraint term $\mathcal{G}(\theta,|\theta)$ by a multi-dimensional Gaussian distribution whose covariance matrix is equal to $V_{52\times52}(\hat{\boldsymbol{\theta}})$ and the auxiliary measurement $\boldsymbol{\theta_0}$ is replaced by the NP shift $\hat{\boldsymbol{\theta}}$.

$$\prod_j \mathcal{G}\left(\theta_{0,j}|\theta,1\right) \qquad \to \qquad \mathcal{G}\left(\hat{\boldsymbol{\theta}}|\boldsymbol{\theta}, V_{52\times52}(\hat{\boldsymbol{\theta}})\right) \tag{6.39}$$

---

[6] Such decomposition keeps the correlation between different groups, hence the quadratic sum of contributions is not necessarily equal to the total error, due to potential double counting of the correlated terms.

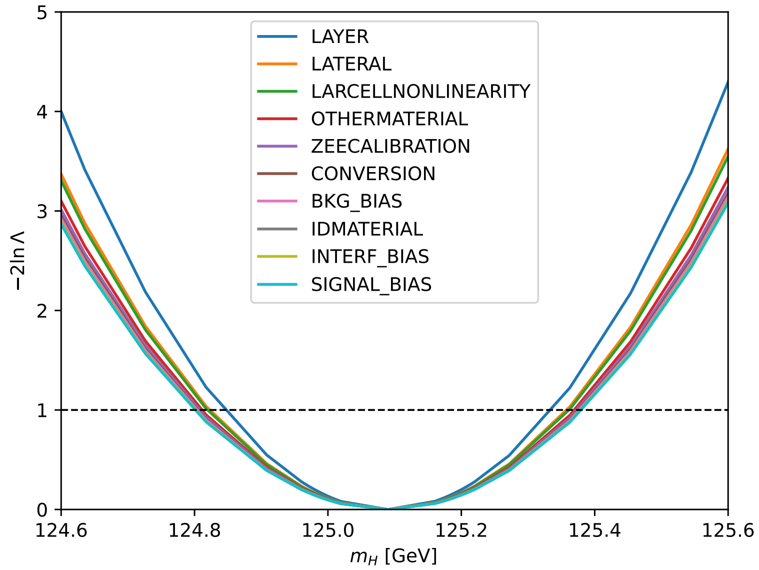

Figure 6.16: Scan of the likelihood ratio with the contribution from the various systematic groups, ordered in descending order of impact.

	Impact on m_{H}	
Systematic group	Down	Up
Layer calibration	155	155
Lateral shower shape	113	113
Lar cell non-linearity	106	106
Other material (not ID)	80	79
$Z \to ee$ calibration	64	64
Conversion reconstruction	51	50
Background model bias	40	40
ID material	24	25
Interference bias	23	23
Signal model bias	9	9
Resolution	7	3
Luminosity	0	0

Table 6.8: Systematic decomposition of the Higgs mass measurement obtained with Asimov dataset.

The global scale $\vec{\alpha}_g$ is ignored in this implementation.

Consequently, this application of global fit affects the Higgs mass measurement, with a potential constraint on the experiment uncertainty originating from the photon energy scale, and a shift on the central value due to non-zero pulls. A signal plus background Asimov data is generated to evaluate its impact on the expected results, where the signal strength is fixed to 1, Higgs mass $m_H = 125.09$ GeV, background obtained with a data sideband fit, and the systematic NPs are set to zero, except for the 52 constrained NPs, which are set to the pull from global fit. This Asimov data is fitted to the modified likelihood model with the multi-dimensional Gaussian constraint (Eq. 6.39), to evaluate the possible improvement of the mass uncertainty. Specifically, for the shift on mass central value, the auxiliary measurements $\boldsymbol{\theta_0}$ are set again to zero, hence the induced shift from NP pulls is absorbed in the Higgs mass m_H, rather than the systematic NPs.

The resulting systematic uncertainties and shift of the Higgs mass using the two correlation models of global fit are summarized in Tab. 6.9. These systematic uncertainties are calculated with total mass error after subtracting the statistical component. The shift is defined as the difference with respect to the original value of 125.09 GeV. A factor of around 1.5 reductions on the systematic error is observed after applying the global fit constraint, however, the induced shift on mass is more than 300 MeV.

m_H (MeV)	σ_{sys}	Δm_H
Prefit	263	0
Postfit: η-correlated	180	372
Postfit: η-decorrelated	182	301

Table 6.9: Prefit and postfit systematic uncertainty. The postfit one is obtained with the modified multi-dimensional Gaussian likelihood.

6.3 Preliminary results updated with the final Run 2 egamma calibration recommendation

The results described above correspond to the previous official egamma calibration recommendation. In this section, the preliminary global fit study for the final calibration recommendation will be presented.

The final Run 2 recommendation involves improvement on plenty of materials, such as the new layer calibrations, the new corrections for residual electronics calibration, layer 2 MG/HG inter-calibration and photon lateral leakage (Sec. 5.1). The relevant systematic uncertainties are shown in Fig. 6.17, for the final recommendation: the relative MG/HG response is better calibrated, hence the corresponding uncertainty is reduced by around 50%; the muon-based layer1/layer2 intercalibration uncertainty ("$\alpha_{1/2}\,\mu$" in Fig. 6.17a) and the associated uncertainty due to the extrapolation from muon to electron ("$\alpha_{1/2}\,\mu \to e$" in Fig. 6.17a) are replaced by the smaller uncertainty of the new muon-electron combination approach ("$\alpha_{1/2}\,\mu + e$" in Fig. 6.17b); At low energy range, in presence of the new ADC non-linearity correction uncertainty, the total energy systematic uncertainty is similar with respect to the previous recommendation.

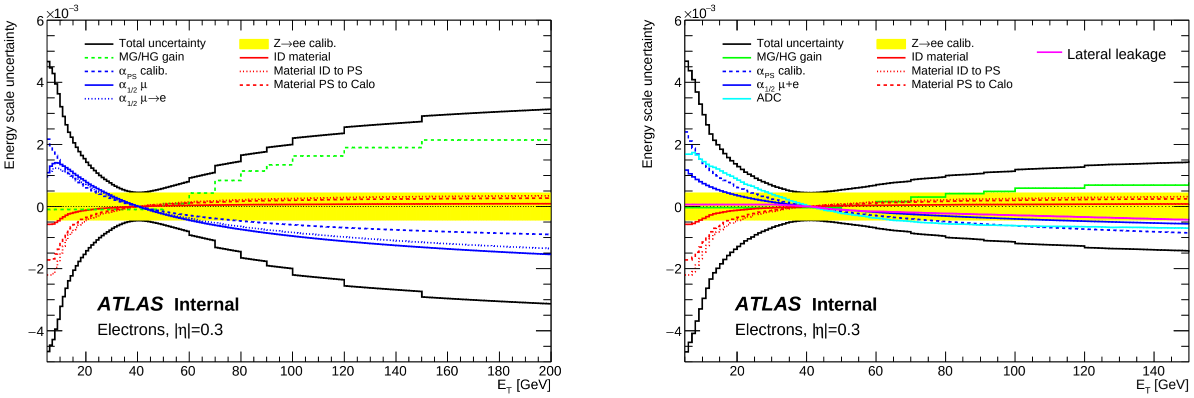

(a) Previous recommendation

(b) Final recommendation

Figure 6.17: Impact on electron and photon energy scale of dominant systematic uncertainties for the previous (a) and final (b) Run 2 calibration recommendations.

The $Z \to ee$ linearity has already been reproduced (Fig. 5.32). With recent studies, the systematic uncertainties relevant to the m_{ee} window size, electron ID, isolation, bremsstrahlung radiation level, are estimated in a different way. These uncertainties are calculated as the impact on linearity when changing a given selection:

$$\sigma_i^k = \alpha_i^k - \alpha_i^{\text{nom}} \tag{6.40}$$

where σ_i^k is the systematic error of source k measured at bin i, α_i^{nom} and α_i^k are respectively the nominal linearity and the linearity after switching on the systematic effect, which is measured with the initial dataset but passing different selection.

In the past, the systematic variant α_i^k was always calculated with the same η-dependent in-situ energy scale factor $\alpha(\eta)$ as the nominal measurement α_i^{nom}. Such estimations of systematic uncertainties involve not only an E_T dependent impact, but also a non-zero inclusive component. This inclusive component is has the same definition of the EG_SCALE_SYST systematic for the in-situ scale factor $\alpha(\eta)$ (Fig. 5.13a), which is separately taken into account and not constrained in the global fit model. On the other hand, the uncertainty of $Z \to ee$ linearity is used to fit the systematic nuisance parameters as well as the global scale factors α_g in the global fit model. In order to get the information of residual inclusive scale, it is better to fit the α_g parameters using without any highly correlated uncertainties, else, for reaching the minimum χ^2, the high correlations will give shifted post-fit scale (Fig. 6.7) with respect to the input $Z \to ee$ linearity.

The new proposal is that for the 4 systematics mentioned above, the uncertainty is always computed after re-calibrating the inclusive energy scale. Specifically, after switching on one systematic, an additional iteration of in-situ calibration os performed before getting the values of α_i^k. The new uncertainty results are shown in Fig. 6.18, the uncertainty is obviously reduced as compared to Fig. 5.40 and is close to zero at 40 GeV, since the inclusive energy scale is re-calibrated for computing systematic uncertainties.

For the new study, the η-decorrelated correlation scheme for the global fit model is taken to have more conservative constrains on systematics and better χ^2 quality.

Another improvement is on the calculation of the averaged electron energy scale uncertainty (Eq.6.8). In the past, it was based on an uniform η distribution and took the uncertainty at mean E_T as the average in the corresponding E_T bin. For the new study, the uncertainty is averaged using the real $\eta - E_T$ distribution of $Z \to ee$ events, although the difference is almost negligible as compared to the previous approximate approach.

In order to solve the χ^2 issue, the crack region $(1.37 < |\eta| < 1.55)$ is firstly discarded, which decreases the value of χ^2 by around 90. Subsequently a re-scaling of the input $Z \to ee$ linearity uncertainty in order to reach a better fit quality with more conservative input uncertainty. The increasing factors are shown in Tab. 6.10.

The re-scaling is based on the fit quality of each individual $|\eta|$ bin. In order to deduce the η-dependent rescaling factors, first of all, the global fit is respectively performed with only one $|\eta|$ bin, then the increasing factor is equal to the square root of the χ^2/ndf value. Subsequently, the re-scaling is applied on the total uncertainty of $Z \to ee$ linearity (Fig. 6.18). The bringing improvement on fit quality is shown in Tab. 6.11. The final χ^2/ndf is not necessary equal to 1, due to the fact that the re-scaling does not affect the pre-fit Gaussian constraint term of the systematics NPs in the same way as the covariance matrix term.

After discarding the crack region and making the uncertainty re-scaling, the new fit results are shown in

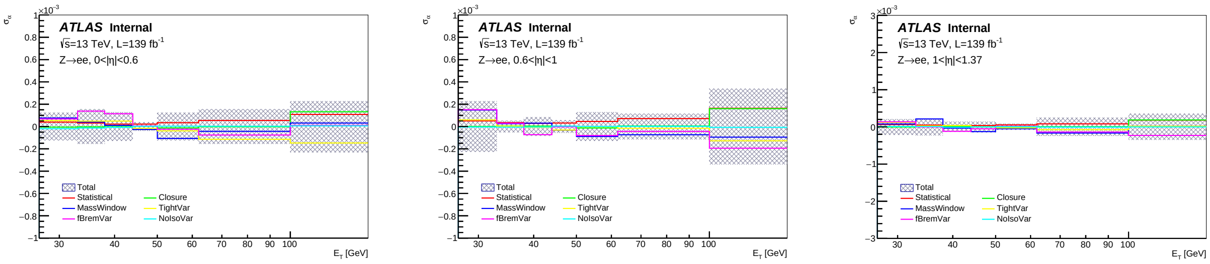

$0 < |\eta| < 0.6$ $0.6 < |\eta| < 1$ $1 < |\eta| < 1.37$

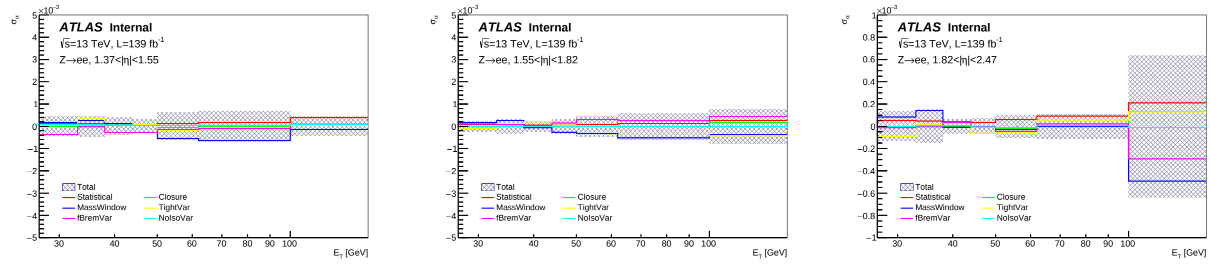

$1.37 < |\eta| < 1.55$ $1.55 < |\eta| < 1.82$ $1.82 < |\eta| < 2.47$

Figure 6.18: Uncertainties of $Z \to ee$ linearity using full Run 2 data. The MassWindow, TightVar, fBremVar and NoIsoVar systematic uncertainties are computed by re-calibrating the inclusive energy scale.

$\|\eta\|$ bin	[0, 0.6]	[0.6, 1]	[1, 1.37]	[1.55, 1.82]	[1.82, 2.47]
Single $\|\eta\|$ bin fit: χ^2/ndf	12.6/6	24.8/6	20.0/6	19.7/6	5.6/6
Increasing factor	1.4	2.0	1.8	1.8	1

Table 6.10: χ^2-test when fitting with only one $|\eta|$ bin and the factors used to increase the input $Z \to ee$ linearity uncertainty as a function of $|\eta|$. The factors are computed as the square root of χ^2/ndf of the single $|\eta|$ bin fit. For the cases with χ^2/ndf smaller than 1, no re-scaling is performed.

Fit	all the 6 $\|\eta\|$ bins	crack-veto	Re-scaled uncertainty + crack veto
χ^2/ndf	194/36	106/30	47/30
p-value	$O(10^{-23})$	$O(10^{-10})$	0.025

Table 6.11: Goodness of fit: χ^2 test for different global fit configurations. The crack-veto corresponds to the case when $1.37 < |\eta| < 1.55$ is discarded in the fit; Re-scaled uncertainty is the case when fitting with increased input $Z \to ee$ linearity uncertainty.

Fig. 6.19. A relatively good constrain is observed even the larger input uncertainties are used in the fit.

Some very preliminary results on the HGam Higgs mass measurement have been obtained (Tab. 6.12), through an analytical calculation in order to emulate an inclusive one-category mass measurement. The analytical approach propagates the photon energy scale uncertainties to the Higgs boson mass using signal MC photon kinematics.

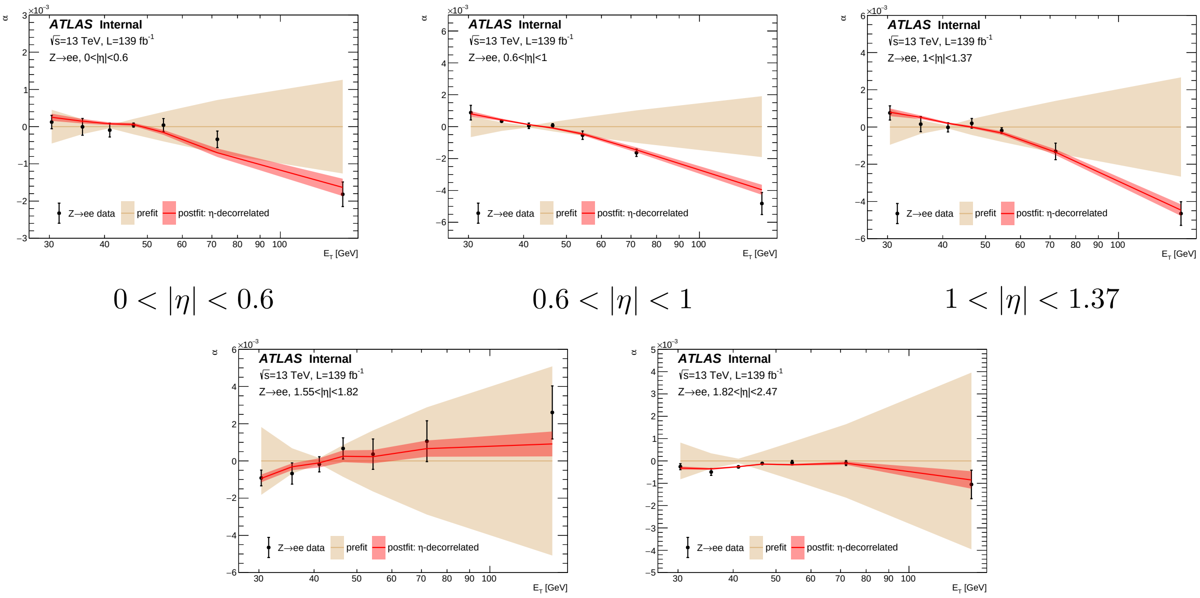

$0 < |\eta| < 0.6$ $0.6 < |\eta| < 1$ $1 < |\eta| < 1.37$

$1.55 < |\eta| < 1.82$ $1.82 < |\eta| < 2.47$

Figure 6.19: Comparison between the prefit and the postfit energy scale. The prefit (yellow) is centered at zero, with unconstrained energy scale uncertainty. The postfit (red and cyan) is shifted due to nonzero NP pulls fitted to the $Z \to ee$ linearity data (black dots), the red color band corresponds to the constrained uncertainty. The postfit results are obtained with η-decorrelated correlation scheme.

m_H (MeV)	σ_{sys}	Δm_H
Prefit	169	0
Postfit: η-decorrelated	102	130

Table 6.12: Prefit and postfit systematic uncertainty with the new egamma calibration recommendation. The postfit one is obtained with the modified multi-dimensional Gaussian likelihood.

With the new calibration recommendation, the prefit mass systematic uncertainty without applying the global fit constraints is reduced from 263 MeV to 166 MeV. The improvement is mainly because of the smaller uncertainties for the MG/HG inter-calibration, the E1/E2 inter-calibration and the photon lateral leakage.

The global fit model with the η-decorrelated correlation scheme has been tested on the Higgs mass, which brings a similar reduction on the mass uncertainty as the previous recommendation, and a shift on mass of 130 MeV. The Higgs mass uncertainty with a real analysis statistical test can be better, since this analytical one-category calculation does not benefit from any constraint brought by the categories of $H \to \gamma\gamma$ analysis. The significant change on mass shift as compared to the previous results is due to the fact that part of the linearity effect has been taken into the new corrections (ADC, L2Gain, etc.), therefore the systematic nuisance parameters θ are less pulled and the shift on mass is smaller.

6.4 Conclusion

In this chapter, a global fit model is introduced to constrain the electron and photon energy scale uncertainty, using the $Z \to ee$ linearity measurement. This model parameterizes the linearity with the sum of the sensitive energy scale uncertainties, and returns the constraints, correlations and pulls of the uncertainties. Afterwards, these outputs from the global fit are applied to the Higgs mass measurement in the diphoton decay mode. For the previous calibration recommendation, the nominal result based on Asimov data gives an expected measurement of $m_H = 125.090^{+0.291}_{-0.290}\ \mathrm{GeV} = 125.090^{+0.125}_{-0.123}(\mathrm{stat.})^{+0.263}_{-0.263}(\mathrm{syst.})\ \mathrm{GeV}$, and benefiting from the global fit constraint, a near factor two reduction on the systematic uncertainty is obtained, which is reduced from 263 MeV to around 180 MeV. The induced shift of the mass due to the systematic pulls returned by the global fit model can be larger than 300 MeV. With the new recommendation, the systematic uncertainty of Higgs mass is reduced to be around 168 MeV, and can be further reduced to be 102 MeV benefiting from the global fit constraint, which induces a shift on mass of around 130 MeV.

7 - Conclusion

A search for non-resonant double Higgs production via both ggF and VBF with one Higgs decaying into a pair of photons and the other decaying into a pair of b-quarks is presented. The non-resonant double Higgs production allows to directly explore the Higgs self-coupling κ_λ, which represents the real shape of the Higgs potential. The analysis uses the full Run 2 LHC pp collision data at $\sqrt{s} = 13$ TeV collected with the ATLAS detector, with an integrated luminosity of 139 fb^{-1}. The final states of two b-quarks and two photons give an enhanced production rate due to the large branching ratio of Higgs to two b-quarks decay, and a clean signal environment with the presence of photons. A multi-variant selection based on boosted decision trees is applied to extract the signal from the background, which is dominated by the diphoton continuum process, with a subdominant contribution from single Higgs production. The BDT is optimized respectively for signal with high and low values of the self-coupling κ_λ, which maximizes the sensitivity and constraint. The 95% confidence level observed (expected) limit on the double Higgs production cross section corresponds to 4.2 (5.7) times the prediction of the Standard Model. This result gives a factor $\sim$ 5 improvements as compared to the early Run 2 result [94], due to the near 4 times increased luminosity and the improved analysis strategy. The Higgs self-coupling κ_λ is constrained at 95% confidence level to be between $-1.5 < \kappa_\lambda < 6.7$ for the observed, where $-2.4 < \kappa_\lambda < 7.7$ is expected. This result is then combined with other decay channels including $b\bar{b}b\bar{b}$ and $b\bar{b}\tau\bar{\tau}$, and also with the single Higgs results for κ_λ where the Higgs self-coupling loops can modify the Higgs production cross section and decay. The combined result gives an observed (expected) cross section limit equal to 2.4 (2.9) times the SM prediction. With both double and single Higgs, the Higgs self-coupling is constrained to be $-0.4 < \kappa_\lambda < 6.3$ for the observed and $-1.9 < \kappa_\lambda < 7.5$ for the expected. For the high luminosity LHC with an designed luminosity of 3000 fb^{-1}, the current combined results of $b\bar{b}\gamma\gamma$ and $b\bar{b}\tau\bar{\tau}$ channels are extrapolated, which gives a possible 3σ hint for the double Higgs signal.

The in-situ calibration for energy scale and resolution of the ATLAS electromagnetic calorimeter is performed with the $Z \to ee$ Run 2 data. The calibration makes use of the precise Z boson mass distribution to calibrating the difference on energy scale and resolution between data and simulation, in function of the pseudorapidity of electrons. The linearity of the calorimeter, defined as the energy-dependent scale difference between data and MC is also measured using the $Z \to ee$ events. It is afterwards used to constrain the systematic uncertainties of the energy scale, via a global fit model, which parameterizes the linearity as a function of the various systematic uncertainties. The obtained constraint is then applied on the Higgs mass measurement in the two photon channel, of which a precision of 290 MeV is expected with the full Run 2 dataset. The 290 MeV precision includes around 125 MeV statistical uncertainty and 263 MeV systematic uncertainty, where the systematic uncertainty is dominated by the LAr cell non-linearity and ECAL layer calibration. After applying the constraint from the global fit model, the systematic uncertainty is nearly reduced by a factor 2.

A - ATLAS and CMS measurements of the Higgs boson mass

Below is presented a short review of the ATLAS and CMS results on the Higgs boson mass measurements. More detailed review can be found in the Scientific Symposium to celebrate the 10th anniversary of the Higgs boson discovery [119] on July 4th 2022 or at ICHEP 2022 [59].

Run 1 measurements:
The combined ATLAS+CMS Higgs boson Run 1 mass measurement is published in Ref. [3] and is

$$m_H = 125.09 \pm 0.24\,(0.21\,(\mathrm{stat}) \pm 0.11\,(\mathrm{syst}))\ \mathrm{GeV} \tag{A.1}$$

with the individual masses being

$$\begin{aligned} \text{ATLAS } H \to \gamma\gamma : m_H &= 126.02 \pm 0.51\,(0.43\,(\mathrm{stat}) \pm 0.27\,(\mathrm{syst}))\ \mathrm{GeV} & \text{(A.2)} \\ \text{CMS } H \to \gamma\gamma : m_H &= 124.70 \pm 0.34\,(0.31\,(\mathrm{stat}) \pm 0.15\,(\mathrm{syst}))\ \mathrm{GeV} & \text{(A.3)} \\ \text{ATLAS } H \to 4l : m_H &= 124.51 \pm 0.52\,(0.52\,(\mathrm{stat}) \pm 0.04\,(\mathrm{syst}))\ \mathrm{GeV} & \text{(A.4)} \\ \text{CMS } H \to 4l : m_H &= 125.15 \pm 0.40\,(0.37\,(\mathrm{stat}) \pm 0.15\,(\mathrm{syst}))\ \mathrm{GeV} & \text{(A.5)} \\ & & \text{(A.6)} \end{aligned}$$

Run 2 measurements ATLAS:
The ATLAS experiment has recently published a 4 leptons full Run 2 value [120] of

$$m_H = 124.99 \pm 0.18\,(\mathrm{stat}) \pm 0.04\,(\mathrm{syst})\ \mathrm{GeV} \tag{A.7}$$

This measurement is combined with the corresponding ATLAS measurement using 7 and 8 TeV pp collision data [121] which has been used in [3], resulting in a Higgs boson 4 leptons mass measurement of

$$m_H = 124.94 \pm 0.17\,(\mathrm{stat}) \pm 0.03\,(\mathrm{syst})\ \mathrm{GeV} \tag{A.8}$$

which is the current most precise ATLAS measurement.

In addition, using the 2015+2016 data (36.1 fb^{-1}) of Run 2, a value of the diphoton Higgs boson mass measurement was shown in Ref. [16]:

$$m_H = 124.93 \pm 0.40\,(0.21\,(\mathrm{stat}) \pm 0.34\,(\mathrm{syst}))\ \mathrm{GeV} \tag{A.9}$$

It is this result (see also [122]) that we want to improve using the work described in this thesis.

Run 2 measurements CMS:
CMS has published [11] a 2016 data (35.9 fb^{-1}) value of the diphoton Higgs boson mass

$$m_H = 125.78 \pm 0.26\,(0.18\,(\mathrm{stat}) \pm 0.18\,(\mathrm{syst}))\ \mathrm{GeV} \tag{A.10}$$

This value is combined with the 2016 4 leptons CMS Higgs boson mass [123] which is

$$m_H = 125.26 \pm 0.21\,(0.20\,(\mathrm{stat}) \pm 0.08\,(\mathrm{syst}))\ \mathrm{GeV} \tag{A.11}$$

and gives

$$m_H = 125.46 \pm 0.16\,(0.13\,(\mathrm{stat}) \pm 0.10\,(\mathrm{syst}))\ \mathrm{GeV} \tag{A.12}$$

This result is then combined with the full CMS Run-1 Higgs boson mass measurement [124] and gives [11]:

$$m_H = 125.38 \pm 0.14\,(0.11\,(\mathrm{stat}) \pm 0.08\,(\mathrm{syst}))\ \mathrm{GeV} \tag{A.13}$$

which is the current most precise Higgs boson mass measurement.

One should note that, the interference between the Higgs boson and the background productions induces a shift in the diphoton mass peak [125], which is about few tens of MeV [126][127][128], larger than the widh of the SM Higgs boson (4.07 MeV).

Bibliography

[1] ATLAS Collaboration. Georges Aad et al. Observation of a new particle in the search for the Standard Model Higgs boson with the ATLAS detector at the LHC. *Phys. Lett. B*, 716:1–29, 2012, 1207.7214. CERN-PH-EP-2012-218. (Cited on pages 11, 17 et 27.)

[2] CMS Collaboration. Serguei Chatrchyan et al. Observation of a New Boson at a Mass of 125 GeV with the CMS Experiment at the LHC. *Phys. Lett. B*, 716:30–61, 2012, 1207.7235. CMS-HIG-12-028, CERN-PH-EP-2012-220. (Cited on pages 11, 17 et 27.)

[3] ATLAS, CMS Collaboration. Georges Aad et al. Combined Measurement of the Higgs Boson Mass in pp Collisions at $\sqrt{s} = 7$ and 8 TeV with the ATLAS and CMS Experiments. *Phys. Rev. Lett.*, 114:191803, 2015, 1503.07589. ATLAS-HIGG-2014-14, CMS-HIG-14-042, CERN-PH-EP-2015-075. (Cited on pages 14, 23, 105, 135 et 217.)

[4] Standard Model wikipedia. `https://en.wikipedia.org/wiki/Standard_Model`. (Cited on page 20.)

[5] Steven Weinberg. The Making of the Standard Model. *Eur. Phys. J. C*, 34:5–13, 2004, hep-ph/0401010. (Cited on page 20.)

[6] Nansi Andari. *Observation of a BEH-like boson decaying into two photons with the ATLAS detector at the LHC*. PhD thesis, Orsay, LAL, 9 2012. (Cited on page 20.)

[7] John Ellis. Higgs Physics. In *2013 European School of High-Energy Physics*, pages 117–168, 2015. (Cited on pages 22 et 30.)

[8] Status of Higgs Boson Physics 2021 PDG. `https://https://pdg.lbl.gov/2022/reviews/rpp2022-rev-higgs-boson.pdf`. (Cited on page 27.)

[9] LHC Higgs working group twiki. `https://twiki.cern.ch/twiki/bin/view/LHCPhysics/LHCHWG`. (Cited on page 28.)

[10] ATLAS Collaboration. Georges Aad et al. Combined measurements of Higgs boson production and decay using up to 80 fb^{-1} of proton-proton collision data at $\sqrt{s} = 13$ TeV collected with the ATLAS experiment. *Phys. Rev. D*, 101(1):012002, 2020, 1909.02845. CERN-EP-2019-097. (Cited on page 29.)

[11] CMS Collaboration. Albert M Sirunyan et al. A measurement of the Higgs boson mass in the diphoton decay channel. *Phys. Lett. B*, 805:135425, 2020, 2002.06398. CMS-HIG-19-004, CERN-EP-2020-004. (Cited on pages 29, 217 et 218.)

[12] Giuseppe Degrassi, Stefano Di Vita, Joan Elias-Miro, Jose R. Espinosa, Gian F. Giudice, Gino Isidori, and Alessandro Strumia. Higgs mass and vacuum stability in the Standard Model at NNLO. *JHEP*, 08:098, 2012, 1205.6497. CERN-PH-TH-2012-134, RM3-TH-12-9. (Cited on pages 28 et 30.)

[13] The Nobel Prize in Physics 2004. `https://www.nobelprize.org/prizes/physics/2004/popular-information/`. (Cited on page 31.)

[14] G. Cowan. *Statistical Data Analysis*. Oxford science publications. Clarendon Press, 1998. (Cited on page 33.)

[15] Glen Cowan, Kyle Cranmer, Eilam Gross, and Ofer Vitells. Asymptotic formulae for likelihood-based tests of new physics. *Eur. Phys. J. C*, 71:1554, 2011, 1007.1727. [Erratum: Eur.Phys.J.C 73, 2501 (2013)]. (Cited on pages 33, 39, 40 et 43.)

[16] ATLAS Collaboration. Morad Aaboud et al. Measurement of the Higgs boson mass in the $H \to ZZ^* \to 4\ell$ and $H \to \gamma\gamma$ channels with $\sqrt{s} = 13$ TeV pp collisions using the ATLAS detector. *Phys. Lett. B*, 784:345–366, 2018, 1806.00242. CERN-EP-2018-085. (Cited on pages 36, 95, 179, 196 et 217.)

[17] A L Read. Presentation of search results: the CLs technique. *Journal of Physics G: Nuclear and Particle Physics*, 28(10):2693–2704, sep 2002. (Cited on pages 37 et 38.)

[18] Andrea Valassi and Roberto Chierici. Information and treatment of unknown correlations in the combination of measurements using the BLUE method. *Eur. Phys. J. C*, 74:2717, 2014, 1307.4003. CERN-IT-NOTE-2013-003. (Cited on pages 44 et 45.)

[19] Lyndon Evans and Philip Bryant. LHC machine. *Journal of Instrumentation*, 3(08):S08001–S08001, 08 2008. (Cited on page 49.)

[20] Thomas Taylor and Daniel Treille. The Large Electron Positron Collider (LEP): Probing the Standard Model. *Adv. Ser. Direct. High Energy Phys.*, 27:217–261. 45 p, 2017. (Cited on page 49.)

[21] Maurizio Vretenar. The radio-frequency quadrupole. In *CERN Accelerator School on High Power Hadron Machines*, pages 207–223, 3 2013. (Cited on page 50.)

[22] The CERN accelerator complex, layout in 2022. `http://cds.cern.ch/record/2800984`. (Cited on page 51.)

[23] S. Albright et al. Overview of the Beams from the Injectors. In *8th Evian Workshop on LHC beam operation*, pages 119–124, 2019. (Cited on pages 51 et 52.)

[24] H. Bartosik et al. Injectors Beam Performance Evolution during Run 2. In *9th LHC Operations Evian Workshop*, pages 51–58, 2019. (Cited on page 51.)

[25] Jorg Wenninger. The LHC collider. *Comptes Rendus Physique*, 16(4):347–355, 2015. Highlights of the LHC run 1 / Résultats marquants de la première période d'exploitation du GCH. (Cited on page 52.)

[26] Diagram of an LHC dipole magnet. `https://cds.cern.ch/record/40524`. (Cited on page 53.)

[27] Public ATLAS luminosity results for Run-2 of the LHC. `https://twiki.cern.ch/twiki/bin/view/AtlasPublic/LuminosityPublicResultsRun2`. (Cited on pages 54 et 150.)

[28] The HL-LHC project. `https://hilumilhc.web.cern.ch/content/hl-lhc-project`. (Cited on page 55.)

[29] ATLAS Collaboration. G. Aad et al. The ATLAS Experiment at the CERN Large Hadron Collider. *JINST*, 3:S08003, 2008. (Cited on pages 55, 65 et 70.)

[30] ATLAS experiment. https://cds.cern.ch/record/1505342. (Cited on page 56.)

[31] Experiment briefing: Keeping the ATLAS inner detector in perfect alignment. https://https://cds.cern.ch/record/2723878. (Cited on page 58.)

[32] ATLAS IBL Collaboration. B. Abbott et al. Production and Integration of the ATLAS Insertable B-Layer. *JINST*, 13(05):T05008, 2018, 1803.00844. FERMILAB-PUB-18-826-V. (Cited on pages 58 et 59.)

[33] ATLAS transition radiation tracker (TRT): Straw Tube Gaseous Detectors at High Rates. https://cds.cern.ch/record/1537991/. (Cited on page 59.)

[34] Janos Kirz. X-Ray Data Booklet: Section 3.1 SCATTERING of X-RAYS from ELECTRONS and ATOMS. http://xdb.lbl.gov/Section3/Sec_3-1.html. (Cited on page 61.)

[35] ATLAS Liquid Argon Calorimeter Collaboration. S. Stärz. Upgraded readout electronics for the ATLAS LAr calorimeter at the phase I of LHC. *Nucl. Instrum. Meth. A*, 718:115–117, 2013. (Cited on page 62.)

[36] H. Abreu et al. Performance of the electronic readout of the ATLAS liquid argon calorimeters. *JINST*, 5:P09003, 2010. (Cited on pages 63 et 73.)

[37] Signal Processing for the ATLAS Liquid Argon Calorimeter : studies and implementation. https://cds.cern.ch/record/1630826. (Cited on pages 63 et 74.)

[38] D. Fournier. "Liquid argon calorimetry". In: Workshop on large hadron collider. Aachen, Germany: Cern, Oct. 1990, pp. 356–359. https://cds.cern.ch/record/220650. (Cited on page 62.)

[39] Iro Koletsou. *Recherche du boson de Higgs dans le canal diphoton au LHC avec le détecteur ATLAS*. Thesis, Université Paris Sud - Paris XI, April 2008. (Cited on page 64.)

[40] Estelle Scifo. *Measurement of the Brout-Englert-Higgs boson couplings in its diphoton decay channel with the ATLAS detector at the LHC*. Theses, Université Paris Sud - Paris XI, July 2014. (Cited on page 64.)

[41] ATLASTechnicalPaperListOfFigures: Chapter 5 (Calorimetry) Fig. 5.1. https://twiki.cern.ch/twiki/bin/view/AtlasPublic/AtlasTechnicalPaperListOfFigures. (Cited on page 65.)

[42] Schematic of the ATLAS calorimeter. https://www.saske.sk/UEF/OSF/ATLAS/img/FGcalsys.png. (Cited on page 67.)

[43] ATLAS Liquid Argon Calorimeter Collaboration. Dag Gillberg. Performance of the ATLAS forward calorimeters in first LHC data. *J. Phys. Conf. Ser.*, 293:012041, 2011. (Cited on page 68.)

[44] ATLAS Collaboration. G. Aad et al. Commissioning of the ATLAS Muon Spectrometer with Cosmic Rays. *Eur. Phys. J. C*, 70:875–916, 2010, 1006.4384. (Cited on page 69.)

[45] ATLAS Collaboration. Morad Aaboud et al. Performance of the ATLAS Trigger System in 2015. *Eur. Phys. J. C*, 77(5):317, 2017, 1611.09661. CERN-EP-2016-241. (Cited on page 71.)

[46] ATLAS trigger schematic. https://twiki.cern.ch/twiki/pub/AtlasPublic/ApprovedPlotsDAQ/tdaq-run3-schematic-withoutFTK.pdf. (Cited on page 72.)

[47] W. E. Cleland and E. G. Stern. Signal processing considerations for liquid ionization calorimeters in a high rate environment. *Nucl. Instrum. Meth. A*, 338(2-3):467–497, 1994. (Cited on page 75.)

[48] ATLAS Collaboration. Georges Aad et al. Topological cell clustering in the ATLAS calorimeters and its performance in LHC Run 1. *Eur. Phys. J. C*, 77:490, 2017, 1603.02934. CERN-PH-EP-2015-304. (Cited on pages 75 et 135.)

[49] ATLAS Collaboration. Georges Aad et al. Electron and photon performance measurements with the ATLAS detector using the 2015–2017 LHC proton-proton collision data. *JINST*, 14(12):P12006, 2019, 1908.00005. CERN-EP-2019-145. (Cited on pages 76, 77, 78, 80, 81, 82, 83, 85, 135, 138, 140, 149, 154, 155, 168, 179, 182 et 183.)

[50] ATLAS Collaboration. Electron efficiency measurements with the ATLAS detector using the 2015 LHC proton-proton collision data. 6 2016. ATLAS-CONF-2016-024, ATLAS-CONF-2016-024. (Cited on page 79.)

[51] David W Scott. *Multivariate density estimation: theory, practice, and visualization*. John Wiley & Sons, 2015. (Cited on page 80.)

[52] Andreas Hocker et al. TMVA - Toolkit for Multivariate Data Analysis. 3 2007, physics/0703039. CERN-OPEN-2007-007. (Cited on page 80.)

[53] Matteo Cacciari, Gavin P Salam, and Gregory Soyez. The anti-kt jet clustering algorithm. *Journal of High Energy Physics*, 2008(04):063–063, apr 2008. (Cited on page 86.)

[54] ATLAS Collaboration. Morad Aaboud et al. Jet reconstruction and performance using particle flow with the ATLAS Detector. *Eur. Phys. J. C*, 77(7):466, 2017, 1703.10485. CERN-EP-2017-024. (Cited on page 86.)

[55] ATLAS Collaboration. Georges Aad et al. Jet energy scale and resolution measured in proton–proton collisions at $\sqrt{s} = 13$ TeV with the ATLAS detector. *Eur. Phys. J. C*, 81(8):689, 2021, 2007.02645. CERN-EP-2020-083. (Cited on page 86.)

[56] ATLAS Collaboration. Georges Aad et al. ATLAS b-jet identification performance and efficiency measurement with $t\bar{t}$ events in pp collisions at $\sqrt{s} = 13$ TeV. *Eur. Phys. J. C*, 79(11):970, 2019, 1907.05120. CERN-EP-2019-132. (Cited on page 87.)

[57] ATLAS Collaboration. Georges Aad et al. Search for Higgs boson pair production in the two bottom quarks plus two photons final state in pp collisions at $\sqrt{s} = 13$ TeV with the ATLAS detector. *Phys. Rev. D*, 106(5):052001, 2022, 2112.11876. CERN-EP-2021-180. (Cited on pages 87, 91, 92, 93, 94, 95, 100, 101, 102, 106, 116, 120, 122, 126 et 127.)

[58] High-Luminosity Large Hadron Collider (HL-LHC): Technical Design Report V. 0.1. 4/2017, 2017. CERN-2017-007-M. (Cited on page 88.)

[59] ATLAS highlights at ICHEP 2022 by G.Unal. https://agenda.infn.it/event/28874/contributions/171901. (Cited on pages 88 et 217.)

[60] ATLAS upgrade for high luminosity LHC. https://cds.cern.ch/record/2647063. (Cited on page 88.)

[61] ATLAS Collaboration. Technical Design Report for the ATLAS Inner Tracker Pixel Detector. 2017. CERN-LHCC-2017-021, ATLAS-TDR-030. (Cited on page 88.)

[62] ATLAS Collaboration. A High-Granularity Timing Detector for the ATLAS Phase-II Upgrade: Technical Design Report. CERN-LHCC-2020-007, ATLAS-TDR-031. (Cited on page 88.)

[63] CMS highlights at ICHEP 2022 by A.Rizzi. https://agenda.infn.it/event/28874/contributions/171902/. (Cited on page 88.)

[64] CMS Tracker Collaboration. Alessandro La Rosa. The Upgrade of the CMS Tracker at HL-LHC. *JPS Conf. Proc.*, 34:010006, 2021, 2102.06074. CMS-CR-2020-170. (Cited on page 88.)

[65] CMS Collaboration. Joel N. Butler and Tommaso Tabarelli de Fatis. A MIP Timing Detector for the CMS Phase-2 Upgrade. 2019. CERN-LHCC-2019-003, CMS-TDR-020. (Cited on page 88.)

[66] R. Frederix, S. Frixione, V. Hirschi, F. Maltoni, O. Mattelaer, P. Torrielli, E. Vryonidou, and M. Zaro. Higgs pair production at the LHC with NLO and parton-shower effects. *Phys. Lett. B*, 732:142–149, 2014, 1401.7340. CERN-PH-TH-2014-014, CP3-14-07, ZU-TH03-14, LPN14-055. (Cited on page 92.)

[67] Dihiggs graphic design department. https://twiki.cern.ch/twiki/bin/viewauth/AtlasProtected/HHGDD. (Cited on page 93.)

[68] G. C. Branco, P. M. Ferreira, L. Lavoura, M. N. Rebelo, Marc Sher, and Joao P. Silva. Theory and phenomenology of two-Higgs-doublet models. *Phys. Rept.*, 516:1–102, 2012, 1106.0034. (Cited on page 93.)

[69] ATLAS Collaboration. Combination of searches for Higgs boson pairs in pp collisions at 13 TeV with the ATLAS experiment. 9 2018. ATLAS-CONF-2018-043. (Cited on page 93.)

[70] J. Alison et al. Higgs boson potential at colliders: Status and perspectives. *Rev. Phys.*, 5:100045, 2020, 1910.00012. FERMILAB-CONF-19-468-E-T, LHCXSWG-2019-005. (Cited on page 94.)

[71] L.Cadamuro, Experimental summary and outlook , Higgs Pairs Workshop 2022 , Dubrovnik, . https://indico.cern.ch/event/1001391/contributions/4842925/attachments/2455652/4208916/HH_experimental_summary.pdf. (Cited on page 94.)

[72] ATLAS Collaboration. Search for resonant and non-resonant Higgs boson pair production in the $b\bar{b}\tau^+\tau^-$ decay channel using 13 TeV pp collision data from the ATLAS detector. 9 2022, 2209.10910. CERN-EP-2022-109. (Cited on pages 94 et 127.)

[73] ATLAS Collaboration. Georges Aad et al. Reconstruction and identification of boosted di-τ systems in a search for Higgs boson pairs using 13 TeV proton-proton collision data in ATLAS. *JHEP*, 11:163, 2020, 2007.14811. CERN-EP-2020-118. (Cited on page 94.)

[74] ATLAS Collaboration. Georges Aad et al. Search for resonant pair production of Higgs bosons in the $b\bar{b}b\bar{b}$ final state using pp collisions at $\sqrt{s} = 13$ TeV with the ATLAS detector. *Phys. Rev. D*, 105(9):092002, 2022, 2202.07288. CERN-EP-2021-229. (Cited on pages 94 et 127.)

[75] ATLAS Collaboration. Georges Aad et al. Search for the $HH \to b\bar{b}b\bar{b}$ process via vector-boson fusion production using proton-proton collisions at $\sqrt{s} = 13$ TeV with the ATLAS detector. *JHEP*, 07:108, 2020, 2001.05178. CERN-EP-2019-267. [Erratum: JHEP 01, 145 (2021), Erratum: JHEP 05, 207 (2021)]. (Cited on page 94.)

[76] ATLAS Collaboration. Search for non-resonant pair production of Higgs bosons in the $b\bar{b}b\bar{b}$ final state in pp collisions at $\sqrt{s} = 13$ TeV with the ATLAS detector. 2022. ATLAS-CONF-2022-035. (Cited on pages 94 et 127.)

[77] ATLAS Collaboration. Georges Aad et al. Search for non-resonant Higgs boson pair production in the $bb\ell\nu\ell\nu$ final state with the ATLAS detector in pp collisions at $\sqrt{s} = 13$ TeV. *Phys. Lett. B*, 801:135145, 2020, 1908.06765. CERN-EP-2019-143. (Cited on page 94.)

[78] CMS Collaboration. Albert M Sirunyan et al. Search for nonresonant Higgs boson pair production in final states with two bottom quarks and two photons in proton-proton collisions at $\sqrt{s}$ = 13 TeV. *JHEP*, 03:257, 2021, 2011.12373. CMS-HIG-19-018, CERN-EP-2020-222. (Cited on pages 94, 127 et 128.)

[79] CMS Collaboration. Search for nonresonant Higgs boson pair production in final states with two bottom quarks and two tau leptons in proton-proton collisions at $\sqrt{s} = 13\ \mathrm{TeV}$. 2022. CMS-PAS-HIG-20-010. (Cited on page 94.)

[80] CMS Collaboration. Armen Tumasyan et al. Search for a heavy Higgs boson decaying into two lighter Higgs bosons in the $\tau\tau$bb final state at 13 TeV. *JHEP*, 11:057, 2021, 2106.10361. CMS-HIG-20-014, CERN-EP-2021-094. (Cited on page 94.)

[81] CMS Collaboration. Armen Tumasyan et al. Search for Higgs boson pair production in the four b quark final state in proton-proton collisions at $\sqrt{s}$ = 13 TeV. 2 2022, 2202.09617. CMS-HIG-20-005, CERN-EP-2022-004. (Cited on page 94.)

[82] CMS Collaboration. Search for resonant Higgs boson pair production in four b quark final state using large-area jets in proton-proton collisions at $\sqrt{s} = 13\ \mathrm{TeV}$. 2021. CMS-PAS-B2G-20-004. (Cited on page 94.)

[83] CMS Collaboration. Armen Tumasyan et al. Search for heavy resonances decaying to a pair of Lorentz-boosted Higgs bosons in final states with leptons and a bottom quark pair at $\sqrt{s}$= 13 TeV. *JHEP*, 05:005, 2022, 2112.03161. CMS-B2G-20-007, CERN-EP-2021-226. (Cited on page 94.)

[84] CMS Collaboration. Search for nonresonant Higgs boson pair production in the 4 leptons plus 2 b jets final state in proton-proton collisions at $\sqrt{s}$ = 13 TeV. 2020. CMS-PAS-HIG-20-004, CMS-PAS-HIG-20-004. (Cited on page 94.)

[85] CMS Collaboration. Search for Higgs boson pairs decaying to WWWW, $\mathrm{WW}\tau\tau$, and $\tau\tau\tau\tau$ in proton-proton collisions at $\sqrt{s} = 13\ \mathrm{TeV}$. 2022. CMS-PAS-HIG-21-002. (Cited on page 94.)

[86] E.Mazzeo, EB request, ATLAS HH meeting, August 12th 2022. `https://indico.cern.ch/event/1188868/contributions/5000803/attachments/2492491/4280336/220812_bbyy_status_report_EB_request.pdf`. (Cited on page 94.)

[87] CMS Collaboration. A portrait of the Higgs boson by the CMS experiment ten years after the discovery. *Nature*, 607(7917):60–68, 2022, 2207.00043. CMS-HIG-22-001, CERN-EP-2022-039. (Cited on pages 94 et 129.)

[88] ATLAS Collaboration. Georges Aad et al. Measurement of isolated-photon pair production in pp collisions at $\sqrt{s} = 7$ TeV with the ATLAS detector. *JHEP*, 01:086, 2013, 1211.1913. CERN-PH-EP-2012-300. (Cited on pages 95 et 96.)

[89] S. Borowka, N. Greiner, G. Heinrich, S. P. Jones, M. Kerner, J. Schlenk, U. Schubert, and T. Zirke. Higgs Boson Pair Production in Gluon Fusion at Next-to-Leading Order with Full Top-Quark Mass Dependence. *Phys. Rev. Lett.*, 117(1):012001, 2016, 1604.06447. MPP-2016-80, NSF-KITP-16-040, ZH-TH-14-16. [Erratum: Phys.Rev.Lett. 117, 079901 (2016)]. (Cited on page 95.)

[90] ATLAS Collaboration. Validation of signal Monte Carlo event generation in searches for Higgs boson pairs with the ATLAS detector. 2019. ATL-PHYS-PUB-2019-007. (Cited on pages 95 et 97.)

[91] LHC Higgs cross section HH sub-group (a.k.a LHC-HH) twiki. `https://twiki.cern.ch/twiki/bin/view/LHCPhysics/LHCHWGHH?redirectedfrom=LHCPhysics.LHCHXSWGHH`. (Cited on page 95.)

[92] ATLAS Collaboration. M Beckingham, M. Duehrssen, E. Schmidt, M. Shapiro, M. Venturi, J. Virzi, I Vivarelli, M. Werner, S. Yamamoto, and T. Yamanaka. The simulation principle and performance of the ATLAS fast calorimeter simulation FastCaloSim. 10 2010. ATL-PHYS-PUB-2010-013. (Cited on page 96.)

[93] Internal note of the search for Higgs boson pair production in the two bottom quarks plus two photons final state. `https://https://cds.cern.ch/record/2752969`. (Cited on pages 99, 104, 107, 108, 114, 115, 117, 119 et 125.)

[94] ATLAS Collaboration. M. Aaboud et al. Search for Higgs boson pair production in the $\gamma\gamma b\bar{b}$ final state with 13 TeV pp collision data collected by the ATLAS experiment. *JHEP*, 11:040, 2018, 1807.04873. CERN-EP-2018-130. (Cited on pages 127 et 215.)

[95] ATLAS Collaboration. Combination of searches for non-resonant and resonant Higgs boson pair production in the $b\bar{b}\gamma\gamma$, $b\bar{b}\tau^+\tau^-$ and $b\bar{b}b\bar{b}$ decay channels using pp collisions at $\sqrt{s}$ = 13 TeV with the ATLAS detector. 2021. ATLAS-CONF-2021-052. (Cited on pages 129, 130 et 132.)

[96] ATLAS Collaboration. Constraining the Higgs boson self-coupling from single- and double-Higgs production with the ATLAS detector using pp collisions at $\sqrt{s} = 13$ TeV. 2022. ATLAS-CONF-2022-050. (Cited on pages 129 et 131.)

[97] ATLAS and CMS Collaborations. Snowmass White Paper Contribution: Physics with the Phase-2 ATLAS and CMS Detectors. 2022. ATL-PHYS-PUB-2022-018. (Cited on pages 132 et 133.)

[98] ATLAS, CMS Collaboration. Addendum to the report on the physics at the HL-LHC, and perspectives for the HE-LHC: Collection of notes from ATLAS and CMS. *CERN Yellow Rep. Monogr.*, 7:Addendum, 2019, 1902.10229. CERN-LPCC-2019-01, CMS-FTR-19-001, ATL-PHYS-PUB-2019-006, CERN-2019-007-ADD. (Cited on page 132.)

[99] ATLAS Collaboration. Projected sensitivity of Higgs boson pair production combining the $b\bar{b}\gamma\gamma$ and $b\bar{b}\tau^+\tau^-$ final states with the ATLAS detector at the HL-LHC. 2022. ATL-PHYS-PUB-2022-005. (Cited on pages 132, 133 et 134.)

[100] Richard Keith Ellis et al. Physics Briefing Book: Input for the European Strategy for Particle Physics Update 2020. 10 2019, 1910.11775. CERN-ESU-004. (Cited on page 134.)

[101] Andrea Dainese, Michelangelo Mangano, Andreas B. Meyer, Aleandro Nisati, Gavin Salam, and Mika Anton Vesterinen, editors. *Report on the Physics at the HL-LHC,and Perspectives for the HE-LHC*, volume 7/2019 of *CERN Yellow Reports: Monographs*. CERN, Geneva, Switzerland, 2019. (Cited on page 134.)

[102] ATLAS Collaboration. Georges Aad et al. Electron and photon energy calibration with the ATLAS detector using LHC Run 1 data. *Eur. Phys. J. C*, 74(10):3071, 2014, 1407.5063. CERN-PH-EP-2014-153. (Cited on page 135.)

[103] ATLAS Collaboration. Morad Aaboud et al. Electron and photon energy calibration with the ATLAS detector using 2015–2016 LHC proton-proton collision data. *JINST*, 14(03):P03017, 2019, 1812.03848. CERN-EP-2018-296. (Cited on pages 135, 137, 140, 146, 147, 151 et 179.)

[104] Paper draft: Electron and photon energy calibration with the ATLAS detector using LHC Run 2 data. https://cds.cern.ch/record/2816050. (Cited on pages 136, 138, 139, 140 et 141.)

[105] G.Lu and Y.Huang , Measurements of lateral energy leakage of electrons and photons in the second layer of EMC using full Run 2 p p collision data at $\sqrt{s} = 13$ TeV with the ATLAS detector. https://cds.cern.ch/record/2742736. (Cited on page 135.)

[106] O.Ducu and J.Maurer , Presampler energy scale calibration using muons. https://cds.cern.ch/record/2773097. (Cited on page 137.)

[107] M.Escalier and O.Kivernyk , Intercalibration of the first two layers of the liquid argon electromagnetic calorimeter using muons with the ATLAS detector using 2015-2018 LHC proton-proton collision data. https://cds.cern.ch/record/2770951. (Cited on page 137.)

[108] A.D'Onofrio, F.Alves, Y.Huang, S.Jin, J-B.De Vivie De Regie and M.Boonekamp , Intercalibration of the first two layers of the liquid argon electromagnetic calorimeter using electrons with the ATLAS detector using 2015-2018 LHC proton-proton collision data. https://cds.cern.ch/record/2784437. (Cited on page 138.)

[109] J.B De Vivie De Regie , EGamma Calibration meeting, 31 Mar 2022 , "E1/E2 combination, once again". https://indico.cern.ch/event/1145018/contributions/4806259/attachments/2418617/4147230/e1e2d310322Fix.pdf. (Cited on page 138.)

[110] L.Franco, Precision measurements of the Higgs Boson properties with the decay into two photons at the ATLAS experiment . https://cds.cern.ch/record/2805793/files/CERN-THESIS-2022-026.pdf. (Cited on page 140.)

[111] L.Guo, Electron energy in-situ calibration and linearity measurements from Z->e+e- events, ATL-COM-PHYS-2020-757. https://cds.cern.ch/record/2742791. (Cited on page 141.)

[112] Christophe Goudet. *Etalonnage du calorimètre électromagnétique de l'expérience ATLAS et application à la mesure des couplages du boson de (Brout-Englert-)Higgs dans le canal diphoton dans le cadre du Run 2 du LHC.* Theses, Université Paris Saclay (COmUE), September 2017. (Cited on pages 144 et 145.)

[113] Hicham Atmani. *Calibration of the ATLAS Electromagnetic Calorimeter and Measurement of W Boson Properties at $\sqrt{s} = 5$ and 13 TeV with the ATLAS Detector at the LHC.* PhD thesis, Université Paris-Saclay, U. Paris-Saclay, 2020. (Cited on page 145.)

[114] Internal note of: electron and photon energy calibration with the ATLAS detector using 2015-2017 LHC proton-proton collision data. `https://cds.cern.ch/record/2651890`. (Cited on pages 148 et 156.)

[115] Internal note of: Electron energy resolution corrections. `https://cds.cern.ch/record/2784105`. (Cited on page 152.)

[116] A.Lukianchuk, In-situ calibration of the liquid argon electromagnetic calorimeter with E/p method using 2018 LHC proton-proton collision data. `https://cds.cern.ch/record/2784107`. (Cited on page 168.)

[117] ATLAS Collaboration. Evaluating statistical uncertainties and correlations using the bootstrap method. 2021. ATL-PHYS-PUB-2021-011. (Cited on page 170.)

[118] R.Turra, Higgs Group Plenary and Approval Meeting , Thursday 26 Mar 2020 , "Global e/gamma energy calibration for Higgs mass measurement". `https://indico.cern.ch/event/902450/contributions/3798606/attachments/2009693/3357415/slides.pdf`. (Cited on page 179.)

[119] Scientific Symposium to celebrate the 10th anniversary of the Higgs boson discovery, Higgs boson properties: mass, width, spin and CP by Marco Delmastro. `https://indico.cern.ch/event/1135177/contributions/4788685/`. (Cited on page 217.)

[120] ATLAS Collaboration. Measurement of the Higgs boson mass in the $H \to ZZ^* \to 4\ell$ decay channel using 139 fb^{-1} of $\sqrt{s} = 13$ TeV pp collisions recorded by the ATLAS detector at the LHC. 7 2022, 2207.00320. CERN-EP-2022-135. (Cited on page 217.)

[121] ATLAS Collaboration. Georges Aad et al. Measurement of the Higgs boson mass from the $H \to \gamma\gamma$ and $H \to ZZ^* \to 4\ell$ channels with the ATLAS detector using 25 fb^{-1} of pp collision data. *Phys. Rev. D*, 90(5):052004, 2014, 1406.3827. CERN-PH-EP-2014-122. (Cited on page 217.)

[122] Supporting documentation ATL-COM-PHYS-2016-1784: Probing higgs production modes and couplings with the higgs to diphotons channel with the run 2 of LHC. `https://cds.cern.ch/record/2238687/files/ATL-COM-PHYS-2016-1784.pdf`. (Cited on page 217.)

[123] CMS Collaboration. Albert M Sirunyan et al. Measurements of properties of the Higgs boson decaying into the four-lepton final state in pp collisions at $\sqrt{s} = 13$ TeV. *JHEP*, 11:047, 2017, 1706.09936. CMS-HIG-16-041, CERN-EP-2017-123. (Cited on page 217.)

[124] CMS Collaboration. Vardan Khachatryan et al. Precise determination of the mass of the Higgs boson and tests of compatibility of its couplings with the standard model predictions using proton collisions

at 7 and 8 TeV. *Eur. Phys. J. C*, 75(5):212, 2015, 1412.8662. CMS-HIG-14-009, CERN-PH-EP-2014-288. (Cited on page 218.)

[125] Stephen P. Martin. Shift in the LHC Higgs Diphoton Mass Peak from Interference with Background. *Phys. Rev. D*, 86:073016, 2012, 1208.1533. FERMILAB-PUB-12-866-T. (Cited on page 218.)

[126] Cyril Pascal Becot. *Diphoton lineshape of the BEH boson using the ATLAS detector at the LHC: calibration, mass, width and interferences*. PhD thesis, Diderot U., Paris, 9 2015. (Cited on page 218.)

[127] ATLAS Collaboration. Estimate of the m_H shift due to interference between signal and background processes in the $H \rightarrow \gamma\gamma$ channel, for the $\sqrt{s} = 8$ TeV dataset recorded by ATLAS. 4 2016. ATL-PHYS-PUB-2016-009. (Cited on page 218.)

[128] LHC Higgs Cross Section Working Group Collaboration. D. de Florian et al. Handbook of LHC Higgs Cross Sections: 4. Deciphering the Nature of the Higgs Sector. 2/2017, 10 2016, 1610.07922. CERN-2017-002-M, CERN-2017-002. (Cited on page 218.)